Numerical Analysis of the Rainfall Infiltration Problem in Unsaturated Soil(Dissertation_全文)

AUTHOR(S):

GARCIA ARISTIZABAL, Edwin Fabian

CITATION:

GARCIA ARISTIZABAL, Edwin Fabian. Numerical Analysis of the Rainfall Infiltration Problem in Unsaturated Soil. 京都大学, 2010, 博士(工学)

ISSUE DATE:

2010-09-24

URL:

https://doi.org/10.14989/doctor.k15647

Numerical Analysis of the Rainfall Infiltration Problem in Unsaturated Soil

2010

Edwin Fabian GARCIA ARISTIZABAL

Abstract

Water infiltration into unsaturated soils is an important geotechnical problem related to large deformation and failure of natural slopes and soil structures. The failure of soils can be triggered by a wetting process from an unsaturated stage resulting from an increase in moisture content and a decrease in suction. Therefore, the study of water infiltration into unsaturated soils becomes and interesting topic due to the necessity of understanding the complex nonlinear interaction among the hydraulic and constitutive parameters of the unsaturated soils, the hydrological conditions, and the initial and boundary conditions of many practical geotechnical problems related to water infiltration. In order to simulate the water infiltration process into unsaturated soil, a series of simulations using a multiphase seepage-deformation method based on the theory of porous media were carried out.

A linear instability analysis was performed to investigate which variables have a significant effect on the instability of an unsaturated viscoplastic material subjected to water infiltration. It was found that the onset of instability of the material system mainly depends on the specific moisture capacity, the suction, and the hardening parameter. Numerical analysis of the one-dimensional infiltration problem is performed. The results of the numerical simulations are discussed with respect to the effect of the specific moisture capacity and the initial suction on the development of volumetric strain. It is found that rapid transitions from unsaturated to saturated states and higher levels of initial suction lead to the contractive behavior of the material and instability. The instability by the numerical results is consistent with the theoretical results obtained through the linear instability analysis.

In order to analyze the generation of pore water pressure and deformations when rainfall is applied to the soil, a parametric study including rainfall intensity, soil water characteristic curves, and permeability has been carried out in order to observe their influence on the changes in pore water pressure and volumetric strain. From the numerical results, it is shown that the generation of pore water pressure and volumetric strain is mainly controlled by material parameters that describe the soil water characteristic curve. In addition, the results of layered column tests are simulated and then presented as pore

water pressure profiles in order to compare them with the experimental results.

In recent years, frequent failure of natural slopes and river embankments have occurred in the world due to heavy rains. Heavy rainfalls bring about an increase of the ground water level within the soil as well as a rise in the water level of the rivers. As a result, soil slopes and embankments have been failed due to the rainfall infiltration and the generation of seepage flow. A series of two-dimensional numerical analyses of soil slopes and river embankments are carried out using a seepage-deformation coupled method for unsaturated soil. The mechanism of the surface deformation and the strain localization on these soil structures are discussed mainly with respect to the rainfall intensity and the saturated water permeability of the soil. From the numerical analysis, it is shown that both the rainfall patterns and the water permeability have a dominant effect on the generation of the pore water pressure and deformation. Results obtained by the simulations show that the finite element formulation describe very well the characteristics of the transient seepage flow into unsaturated soil structures due to rainfall infiltration.

Acknowledgments

I would like to acknowledge the people that have provided me support during the past years. This support was essential for the completion of this doctoral thesis, directly and indirectly.

First and foremost, I would like to express my deepest gratitude and appreciation to my supervisor, Professor Fusao Oka, for sharing with me his years of experience on Geomechanics and Geotechnical Engineering. His suggestions and directions have greatly shaped this study. His invaluable support and advice always inspired me and significantly have influenced my life as a researcher. I owe him not only for this study but also for extending his help on various aspects of my life in Japan.

During my research, I have received a lot of benefits from the valuable discussions and advices by Associate Professor Sayuri Kimoto. Her research work on multiphase analysis helped me successfully to develop my work. I have also received generous assistance from Assistant Professor Yosuke Higo. His research about instability of materials significantly contributed to my research. In addition, I would like to thank Ms. Chikako Itoh, secretary of the laboratory, for her unconditional help every time I had to do any paper work.

My appreciation is also extended to Professor Tetsuya Sumi, member of the advisory committee for his valuable suggestions, comments and criticisms to my work.

I appreciate the friendship and assistance of fellow students at the Geomechanics Laboratory. Especially, I would like to thank my friends Mr. Mojtaba Mirjalili and Mr. Baback Shahbodagh Khan; their valuable support and discussion every day about the research, their company and cooperation during this time are greatly appreciated. I would like to extend also my gratitude to the former foreign students: Dr. Feng Huaiping, Dr. Quoc Huy Nguyen, Ms. Ana Paula Ribeiro and Ms. Anne-Julie Tinet, with whom I shared a great time in Kyoto.

My friends in Colombian and in Japan have been an important part during the past years. It is hard to do justice to all of them, but I would like to mention the following

names: Manuel Builes, Carlos Riveros, Javier Ramirez, Ricardo Ramirez, Clara Kameda, Masakazu Kameda, Oliver Saavedra, Mauricio Castro, Yuri Kinose, Yuri Terada, Hernan Gonzalez, Jorge Patino, Raul Sanchez, Julio Saldarriaga, Carlos Palacio, Beatriz Wills, Diana Moreno, Carlos Gonzalez, Eugenio Duque, German Pardo.

I offer my most deeply-felt gratitude to my family in Colombia for their constant and lovely support in all my projects in my life. And most important of all, I owe my happiness to my lovely wife Nury. I am very much indebted to her for her support, patience understanding, and encouragement during this research.

This research and by extension doctoral degree would not have been possible without the financial aid of the Ministry of Education, Science, and Culture, Government of Japan (Mombusho).

Finally, I would like to express my thanks to the University of Antioquia, Colombia, for granting me leave to pursue my doctoral study at Kyoto University.

Kyoto, August 2010
Edwin Fabian Garcia Aristizabal

Table of Contents

List of Figures

List of Tables

Chapter 1

INTRODUCTION

1.1 Background and objectives

It has been well recognized that the behavior of unsaturated soil subjected to water infiltration plays an important role in Geomechanics. This is because the failure of natural slopes, embankments, and artificial soil structures is most often due to both short and long infiltrations caused by rainfall or melting snow. Water infiltrating into unsaturated soils results in an increase of saturation. This, in turn, leads to changes in pore water pressure (a reduction of suction) and a decrease in the shear strength of the soils. The study of water infiltration into unsaturated soils becomes an interesting topic due to the necessity of understanding the complex nonlinear interaction among the hydraulic and constitutive parameters of the unsaturated soils, the hydrological conditions, and the initial and boundary conditions of many practical geotechnical problems related to water infiltration.

To analyze unsaturated soils, it is necessary to choose the appropriate stress variables. Bishop (1960) proposed an effective stress equation for unsaturated soils; however, this effective stress concept cannot provide the explanation for the collapse phenomenon (Jennings and Burland, 1962). To reflect the collapse behavior, researchers (Bishop and Donald, 1961; Coleman, 1962; Matyas and Radhakrishna, 1968; Fredlund and Morgenstern, 1977) have suggested the independent stress variable approach, where two stresses are proposed for both the soil particles and the fluids. According to their studies any pair of stress fields among the following three stress states, $(\sigma_{ij} - u_a\delta_{ij})$, $(\sigma_{ij} - u_w\delta_{ij})$, and $(u_a - u_w)\delta_{ij}$, can be applied as a suitable stress framework to describe the stress-strain-strength behavior of partially saturated soils. The adoption of net stress $(\sigma_{ij} - u_a\delta_{ij})$ is

valid for dry soil and unsaturated soil only when the air pressure is thought to be constant. However, drained conditions for water and air cannot always be attained in engineering problems. Alternatively, other generalized effective stress formulations have also been used to explain the collapse phenomenon (e.g., Bolzon et al., 1996; Khalili and Khabbaz, 1998; Loret and Khalili, 2000; Kohgo et al., 2001). Most of these models are defined by the generalized effective stress concept with the introduction of a new constitutive parameter for the effective stress. Recently, the terms "effective stress" (Bolzon et al. 1996; Houlsby, 1997; Ehlers, 2004), "Average soil skeleton stress" (Jommi, 2000; Oka et al., 2006; Wheeler et al., 2003), "Generalized effective stress" (Laloui and Nuth, 2009), and "Skeleton stress" (Oka et al., 2008, 2010), that are consistent with a view point of the mixture theory have been used, where the skeleton stress averaged over the total mixture volume.

Many constitutive models have been proposed for unsaturated soils (e.g., Alonso et al., 1990; Wheeler and Sivakumar, 1995; Wheeler and Karube, 1995; Cui and Delage, 1996; Thomas and He, 1998; Sheng et al., 2003, Oka et al., 2008; Nuth and Laloui, 2008). Most of the models, however, are within the framework of rate-independent model, such as elasto-plastic models. A series of experiments on unsaturated silt was conducted by Kim (2004). From their results, the time-dependent property of unsaturated silt has been observed. It is also important to consider the time-dependent property of unsaturated soil in many civil engineering projects. Therefore, in the present study, an elasto-viscoplastic model for unsaturated soil that includes the effect of suction in the constitutive model is presented; it is an extension of the elasto-viscoplastic model for soil considering structure degradation proposed by Kimoto and Oka (2005).

In recent years, to reproduce the multiphase behavior of unsaturated soil, several researchers have described the unsaturated porous solid material within the well-founded Theory of Porous Media (TPM) (e.g., Atkin and Craine, 1976; Biot, 1962; Bowen, 1976; Coussy, 2004; Boer, 1998; Ehlers, 2003). To complete the coupled multiphase finite element formulation, the relationship between the degree of saturation and suction, namely, the soil water characteristic curve is required (Houlsby, 1997). In the model presented herein, a van Genuchten type of equation is employed as a constitutive equation between the saturation and the suction (van Genuchten, 1980). Based on these relations, an air-water-soil three-phase coupled model has been proposed (Oka et al., 2006, 2008).

The present study deals with the behavior of unsaturated materials subjected to an infiltration process. The analyses presented are based on the study of parameters and state variables on the one-dimensional deformation and unstable behavior of unsaturated materials when they are subjected to a wetting process, e.g., rainfall and flooding. The effects of the water infiltration due to rainfall and seepage flow into unsaturated slopes and embankments are also investigated. To do that, a multiphase coupled elasto-viscoplastic finite element analysis formulation is used to describe the water infiltration. Since the transport of water must be considered in the behavior of the unsaturated material, the problem is formulated within the framework of a macroscopic continuum mechanical approach through the use of the theory of porous media. The theory is considered to be a generalization of Biot's two-phase mixture theory for saturated soils. The unsaturated materials are assumed to be composed of solid, water and gas phases, which are assumed to be continuously distributed throughout the space at macroscopic level.

The instability of saturated porous media has been widely studied by many researchers (e.g., Ehlers and Volk, 1998; Higo et al., 2005; Loret and Prévost, 1991; Oka et al., 1994, 1995; Rice, 1975; Schrefler et al., 1995) from both experimental and analytical points of view. However, studies on the instability of unsaturated porous materials have not been completed. Many experimental and numerical researches have been conducted on the deformation behavior of unsaturated soil (e.g., Alonso et al., 2003; Cunningham et al., 2003; Feng, 2007; Khalili et al., 2004; Kimoto et al., 2007; Oka et al., 2010). Nevertheless, the deformation of unsaturated soil is an interesting topic that has not yet been fully investigated. And theoretical analyses, such as instability analyses, have not yet been performed. Recently, Buscarnera and Nova (2009a, 2009b) addressed the general problem of soil instability for partially saturated geomaterials with particular reference to the controllability of oedometric and triaxial conditions. They showed that unsaturated soil specimens are prone to instability when they are subjected to water infiltration. In the present study, the one-dimensional instability of an unsaturated material subjected to a wetting process has been theoretically and numerically performed.

Several researches have been conducted on the infiltration problem using column tests (Liakopoulos, 1964; Yang et al., 2004, 2006; Bathurst et al., 2007). Rainfall infiltration into unsaturated soils has also been analyzed by analytical solutions (Srivastava and Yeh, 1991; Zhan and Ng, 2004; Wu and Zhang, 2009). Recently, numerical solutions have been used to analyze the problem of unsaturated soil. Numerical analyses are necessary

because of the complicated initial and boundary conditions, the multi-layered soils, the different rainfall intensities, and the geometry of many engineering problems, whereas the analytical solutions cannot be obtained. Many numerical studies that can account for the inherent complexities of the infiltration problem into unsaturated soils have been presented (Pinder and Gray, 2008; Cai and Ugai, 2004; Griffiths and Lu, 2005; Ehlers et al., 2004; Oka et al., 2009). In spite of all the valuable works mentioned, the effect of the hydraulic parameters on the deformation behavior of unsaturated soils is an interesting topic that has not yet been fully studied. Seepage-deformation coupled analysis for unsaturated soil is necessary because changes in saturation and suction cause deformation of the soil and vice versa. In this study, the effects of the hydraulic parameters on the transient vertical infiltration problem and their effects on the deformation behaviour of unsaturated soils are studied.

Failure of unsaturated slopes and river embankments are a common phenomenon all over the world. Although, it can be attributed to many factors, such as geology, topography, hydrological conditions, material properties, and human action; it has been widely recognized that the water infiltration has a dominant effect on the slope instability. Many researchers have reported on the embankment and slope failure due to the rainfall infiltration (e.g., Yoshida et al., 1991; Matsushi et al., 2006; Yamagishi et al., 2004, 2005; Nakata et al., 2010; Chen et al., 2006; Au, 1998; Alonso et al. 2003). In addition, some studies have addressed the effect of the rainfall infiltration on the slope stability from the point of view of the statistical approach (e.g. Au, 1993; Okada and Sugiyama 1994). On the other hand, several researchers have been implementing numerical solutions to analyze the effect of the hydraulic characteristics on the instability of unsaturated slopes (e.g. Ng and Shi, 1998; Tsaparas et al., 2002, Cai and Ugai, 2004; Rahardjo et al., 2007). In these formulations, the effects of the rainfall infiltration on the generation of the pore water pressure and the instability of the slope are generally evaluated by a seepage analysis using the finite element method and followed by the slope stability analysis; thus, the study of the coupling of the deformation and the transient flow is disregarded. Numerical methods that can simultaneously consider the unsaturated seepage flow and the deformation of soil structures have been used to study the infiltration process (Cho and Lee, 2001; Alonso et al., 2003; Ehlers et al., 2004; Ye et al., 2005; Oka et al., 2009; Kato et al., 2009). In order to investigate the effects of the rainfall infiltration and seepage flow on the hydraulic and deformation behavior of unsaturated soil structures, various simulations of soil slopes and river embankments have been conducted. The method of numerical

simulation is an unsaturated seepage-deformation couple finite element method based on the finite deformation theory, using an elasto-viscoplastic model for the unsaturated soil. The results of the simulations are discussed mainly with respect to the saturated water permeability of the soil, the rainfall intensity, and their effects on the generation of the pore water pressures and the deformation within the unsaturated soil.

1.2 Scope and organization

The outline of the work presented in this doctoral thesis is briefly described in the followings.

In **Chapter 2**, an elasto-viscoplastic constitutive model and a seepage-deformation coupled method for unsaturated soils are presented. In the constitutive model, the skeleton stress and suction are adopted as the basic stress variables. The collapse behavior, which occurs with a decrease in suction, is considered with the shrinkage of the overconsolidation boundary surface, the static yield function, and the viscoplastic potential surface. In the finite element formulation the material is described within the framework of the macroscopic continuum mechanical approach through the use of the theory of porous media. Additionally, an updated Lagrangian method with the objective Jaumman rate of Cauchy stress is adopted.

In **Chapter 3**, a linear instability analysis is presented in order to investigate the effect of parameters on the onset of instability of the governing equations using a simplified one-dimensional viscoplastic model. In the analytical formulation, the material is assumed to be a triphasic material consisting of a soil skeleton, pore water, and pore air. Numerical simulations of the one-dimensional water infiltration problem are presented to discuss the effect of the specific moisture capacity and the initial suction on the development of volumetric strain.

In **Chapter 4**, parametric analyses, considering the hydraulic characteristics that control the unsaturated behavior (soil water characteristic curve and permeability function), are carried out in order to observe the influence of the characteristics on the changes in pore water pressure and volumetric strain. Additionally, the results of layered column tests are simulated and then presented as pore water pressure profiles in order to compare them with the experimental results. It is shown that the proposed multiphase coupled

model can capture very well many of the characteristics of transient vertical rainfall infiltration into layered soils.

In **Chapter 5**, two-dimensional numerical analyses, which focus on a parametric study considering different water levels, saturated water permeabilities, and rainfall patterns, are conducted in order to observe the influence of these hydraulic characteristics on the changes of the pore water pressure and the saturation, as well as in the progress of the lateral displacement and the viscoplastic shear strain during rainfall infiltration into unsaturated soil slopes. A discussion about the significance of the hydraulic parameters on the seepage-deformation process is presented.

In **Chapter 6**, two-dimensional numerical analyses at specific sites are performed for two river embankments. The first case study corresponds to a three layered river embankment which is subjected to both the effect of the rainfall infiltration and the seepage flow from the mountain side. The study of the effect of different water permeabilities for the upper layer on the seepage flow velocity and its effect on the strain localization are emphasized. Furthermore, the effects of horizontal drains and the degree of compaction on the generation of deformation are investigated. The second case study is for a controlled experiment performed in the field, and it corresponds to a river dike embankment used to protect the urban areas from the flooding triggered by the rainfall accumulation and the increase of the water level of the rivers. The results obtained by the numerical analyses for the pore water pressure are compared with the existing measured field data.

In **Chapter 7**, the conclusions of this dissertation and recommendations for future works are given.

Chapter 2

ELASTO-VISCOPLASTIC MODEL FOR UNSATURATED SOIL AND A SEEPAGE-DEFORMATION COUPLED ANALYSIS METHOD

2.1 Introduction

It has been recognized that the behavior of unsaturated soils plays an important role in Geomechanics. Many geotechnical problems, i.e., natural slopes, embankments, artificial structures, expansive soils, soil containing methane hydrates, etc., are related to unsaturated soils. To analyze the unsaturated soils, it is necessary to choose the appropriate stress variable for the soil as well as the appropriate constitutive model. This chapter presents a general review of the effective stress concept for unsaturated soils, the different constitutive models used for the unsaturated soil analysis, and the finite element formulation for the analysis of unsaturated soils.

A multiphase coupled elasto-viscoplastic finite element analysis formulation proposed by Oka et al. (2006) that is used for the analysis of unsaturated soils is presented. The numerical method presented here is based on the fundamental concept of the theory of porous media, (e.g., Atkin and Craine, 1976; Biot, 1962; Bowen, 1976; Coussy, 2004; Boer, 1998; Ehlers, 2003). The materials are assumed to be composed of solid, water, and air which are assumed to be continuously distributed throughout the space at macroscopic level. An elasto-viscoplastic constitutive model is adopted for the soil skeleton (Kimoto

and Oka, 2005). The skeleton stress (Oka et al., 2010), which is determined from the difference between the total stress and the average pore fluid pressure, is used for the stress variable in the governing equations. In addition, the constitutive parameters are functions of the matric suction, by which the shrinkage or the expansion of the overconsolidation boundary surface and the static yield surface can be described (Oka et al., 2006). In this formulation, an updated Lagrangian method with the objective Jaumann rate of Cauchy stress is adopted (Kimoto et al. 2004; Oka et al. 2006). The independent variables are the pore water pressure, the pore air pressure, and the nodal velocity. In the finite element formulation, an eight-node quadrilateral element with a reduced Gaussian integration is used for the displacement, and four nodes are used for the pore water pressure and the pore air pressure. The backward finite difference method is used for the time discretization.

2.2 Effective stress in unsaturated soil

Terzaghi (1936) introduced the effective stress concept to describe the deformation behaviour of water saturated soil. This concept was based on results of experiments on the strength and the deformation of soil. Terzaghi's effective stress in one-dimensional form is defined as:

$$\sigma^{'} = \sigma - u_w \tag{2.1}$$

where $\sigma^{'}$ is the effective stress, σ is the total stress and u_w is the pore-water pressure. Equation (2.1) is only effective for saturated soils with incompressible grains and a pore space completely filled with incompressible fluid. Figure 2.1 represents the effective stress principle introduced by Terzaghi for water saturated soils; this figure shows a conversion of a two-phase porous medium into a mechanically equivalent single-phase continuum.

Oka (1996) presented the validity and limits of the effective stress concept in Geomechanics describing that the behaviour of saturated soil depends on both the balance of forces and the compressibility of the constituents. Using constitutive equations of elastic solid-fluid mixtures for volumetric deformation and effective stress, the effective stress and the partial stresses under undrained conditions are presented as:

$$\sigma^{(f)} = nu^{'} \tag{2.2}$$

$$\sigma^{(s)} = \frac{((1/n)-1)\,C_b - (C_s/n) + C_l}{C_b - C_s} nu^{'} \tag{2.3}$$

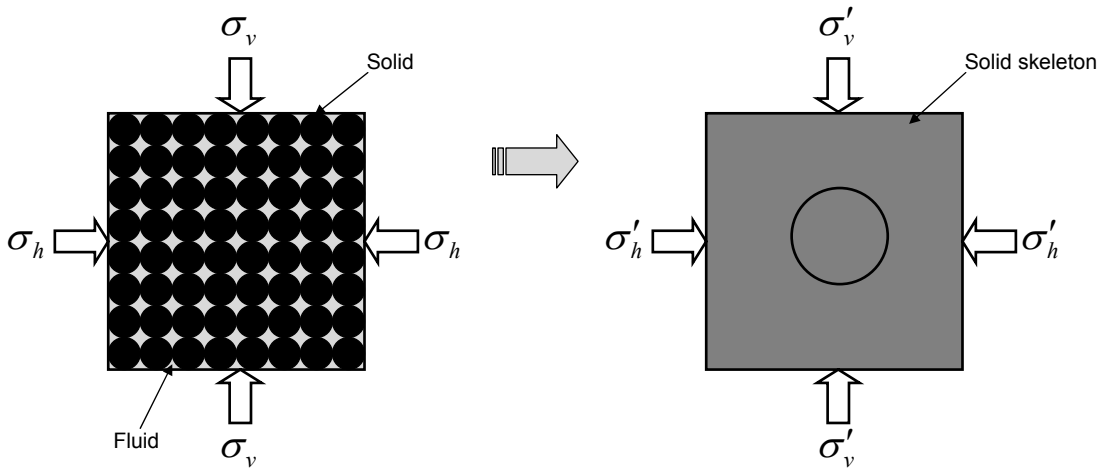

Figure 2.1 Representation of the effective stress concept for saturated soils

$$\sigma^I = \sigma^{(f)} + \sigma^{(s)} = mu^{'} \tag{2.4}$$

$$m = \frac{C_b - C_s + n\left(C_l - C_s\right)}{C_b - C_s} \tag{2.5}$$

where the inverse of m is equal to the Bishop's pore water pressure coefficient B (Bishop and Eldin, 1950). $\sigma^{(f)}$ is the partial stress for the fluid phase, $\sigma^{(s)}$ is the partial stress for the solid phase, σ^I is the surrounding applied total stress, n is the porosity, $u^{'}$ is the pore water pressure, C_b is the Bulk compressibility of the soil, C_s is the compressibility of the soil and C_l is the compressibility of the pore-water.

Owing to the low compressibility of the water, the isotropic deformation caused by the measured water pressure under the above condition can be disregarded. Under the general three-dimensional conditions, the effective stress tensor, σ^e_{ij} , is defined as:

$$\sigma^e_{ij} = \sigma_{ij} - \sigma^I \delta_{ij} \tag{2.6}$$

where σ_{ij} is the total stress tensor. On the other hand, under the unjacketed test conditions where only the pore water changes, we can use Therzaghi's definition of the effective stress exactly, it is,

$$\sigma^e_{ij} = \sigma_{ij} - \left\{nu + (1-n)\,u\right\}\delta_{ij} = \sigma_{ij} - u\delta_{ij} \tag{2.7}$$

Oka (1996) explained that in cases where m is almost equal to 1.0, the stress difference defined by (Equation 2.6) becomes Terzaghi's effective stress expressed by (Equation 2.7).

In addition, using different data of compressibility of various geological materials, Oka (1996) showed the relation between m and C_l/C_b for several values of porosity n (Figure 2.2). From this figure, it is seen that m is almost equal to unity in the case of soil or soft rock. However, the value of m increases with a decrease in the value of C_b. From the results, it was shown that Terzaghi's effective stress equation is applicable to cases where the ratio of the compressibility of pore fluid to that of the soil skeleton is small and the volumetric strain under the undrained conditions is negligible. Terzaghi's equation is meaningless, however, when the compressibility of the pore fluid is higher than the compressibility of the soil skeleton (i.e. unsaturated soil). In the case of unsaturated soil, the gas phase is highly compressible.

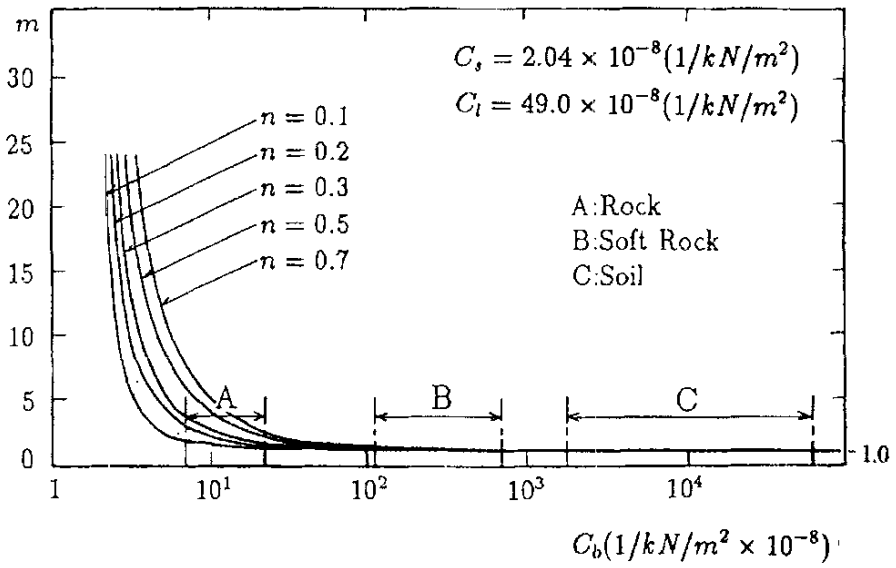

Figure 2.2 Relation between m and C_b(Oka, 1996)

Many researches have been discussing the effective stress for unsaturated soil (e.g. Simons and Menzies, 1974; Jennings and Burland, 1962; Lade and Boer, 1997; Nuth and Laloui, 2008). Bishop (1960) proposed an effective stress equation for unsaturated soils as:

$$\sigma_{ij}^{'} = (\sigma_{ij} - u_a\delta_{ij}) + \chi\,(u_a - u_w)\,\delta_{ij} \tag{2.8}$$

where, $\sigma_{ij}^{'}$ is the effective stress tensor or the Bishop stress tensor, σ_{ij} is the total stress tensor, u_a and u_w are the pore-air pressure and the pore-water pressure, respectively, δ_{ij} is the Kronecker's delta, and χ is a constitutive material parameter that ranges from zero for

dry soil to 1.0 for saturated soil depending on the degree of saturation. The term $(\sigma_{ij} - u_a)$ is called net stress, and the product $\chi\,(u_a - u_w)$ represents the interparticle effective stress due to capillary cohesion. The following considerations are mentioned about Equation (2.8):

1. The equation averages the stresses over a representative elementary volume containing all constituents: air, water and solid grains.

2. Bishop's effective stress tensor cannot be applied to explain the issues related to collapsible soil, such as the collapse behaviour, because suction $(u_a - u_w)$ and effective stress decrease during wetting (Jennings and Burland, 1962).

3. This expression does not consider the compressibility of the constituents because it relies solely on the balance force (Oka, 1996).

4. χ is implemented to scale down the influence of suction in the function of the volumetric ratios of the different fluid phases. But this parameter can be different for shear strength and volumetric deformation (Nuth and Laloui, 2008).

To reflect the collapse behavior of unsaturated soils, researchers (Bishop and Donald, 1961; Coleman, 1962; Matyas and Radhakrishna, 1968; Fredlund and Morgenstern, 1977) have suggested the independent stress variable approach, where two stresses are proposed for both the soil particles and the fluids. According to their studies any pair of stress fields among the following three stress states, $(\sigma_{ij} - u_a\delta_{ij})$, $(\sigma_{ij} - u_w\delta_{ij})$, and $(u_a - u_w)\,\delta_{ij}$, can be applied as a suitable stress framework to describe the stress-strain-strength behavior of partially saturated soils. For instance, two stress variables, $(\sigma_{ij} - u_a\delta_{ij})$ and suction $(u_a - u_w)\,\delta_{ij}$, have been adopted to describe the mechanical behavior of unsaturated soil by some researchers (Fredlund and Morgenstern, 1977; Alonso et al., 1990; Wheeler and Sivakumar, 1995; Gens, 1995; Cui and Delage, 1996). The limitations of the independent stress variables approach are:

1. Net stress and suction, could fail to provide straightforward transition between saturated and unsaturated states. That is, Terzaghi's effective stress cannot be recovered.

2. A double constitutive matrix is needed.

3. The adoption of net stress $\sigma_{ij} - u_a\delta_{ij}$ is valid for unsaturated soil only when the air pressure is thought to be constant. This is because the net stress is affected by the changes in air pressure and it is not an independent stress variable. However, drained conditions for water and air cannot always be attained in engineering problems. For example, the air pressure in river embankments or slopes increases during the seepage process or rainfall infiltration and may vary for soils during the soil compaction process.

Meanwhile, using the net stress and the suction as stress variables, it is very difficult to apply many constitutive models which have been developed for saturated soils, to unsaturated soils (Kohgo et al. 1993).

Recently, other generalized effective stress formulations have also been used to explain the collapse phenomenon (Bolzon et al., 1996; Khalili and Khabbaz, 1998; Loret and Khalili, 2000; Kohgo et al., 2001). Most of these models are defined by the generalized effective stress concept with the introduction of a new constitutive parameter for the effective stress. Recently, the terms "Effective stress" (Bolzon et al. 1996; Houlsby, 1997; Ehlers, 2004), "Average soil skeleton stress" (Jommi, 2000; Oka et al., 2006; Wheeler et al., 2003), "Generalized effective stress" (Laloui and Nuth, 2009), and "Skeleton stress" (Oka et al., 2008; 2010) have been used from a view point of the mixture theory; where the skeleton stress σ'_{ij} in Equation (2.9) is averaged over the total mixture volume as shown schematically in Figure (2.3). In this formulation the fluid pressure contributions are linked to their respective volumetric fraction.

$$\sigma'_{ij} = \sigma_{ij} - P^F\delta_{ij} \tag{2.9}$$

where P^F is the average pressure of the fluids surrounding the soil skeleton.

In the present model, the skeleton stress, which is the same as the average soil skeleton stress by Jommi (2000) and the generalized effective stress by Laloui and Nuth (2009), and suction are adopted as the basic stress variables. We use the "Skeleton stress" instead of "Average soil skeleton stress" to avoid confusing with the mean skeleton stress. In addition, suction is incorporated into the constitutive model to describe the collapse behavior of unsaturated soil.

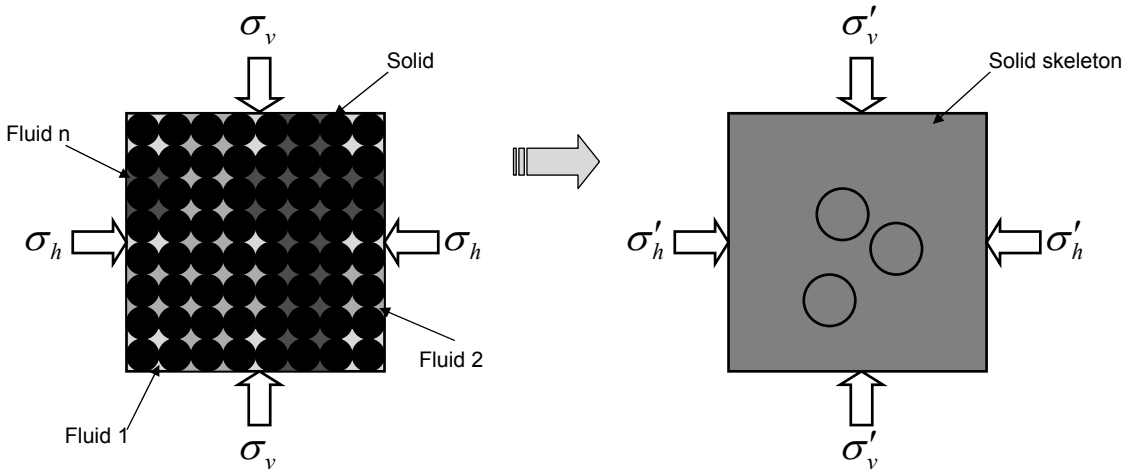

Figure 2.3 Representation of the effective stress concept for unsaturated soils. Conversion of multiphase and multistress medium (solid phase and pore space filled with n fluids) into single continuum.

Many constitutive models have been proposed for unsaturated soils (e.g., Alonso et al., 1990; Wheeler and Sivakumar, 1995; Wheeler and Karube, 1995; Cui and Delage, 1996; Thomas and He, 1998; Sheng et al., 2003; Oka et al., 2008; Nuth and Laloui, 2008). Most of the models, however, are derived within the framework of rate-independent model, such as elasto-plastic models. A series of experiments on unsaturated silt was conducted (Kim, 2004; Oka et al., 2010). From the results, the time-dependent property of unsaturated silt has been observed. It is also important to consider the time-dependent property of unsaturated soil in many civil engineering projects. Therefore, it is necessary to construct an elasto-viscoplastic model for unsaturated soil. By adopting the skeleton stress from the view point of the Mixture Theory, and by introducing the suction effect into an elasto-viscoplastic constitutive model for soil considering structure degradation (Kimoto and Oka, 2005), and elasto-viscoplastic model for unsaturated soil has been constructed to analyze the unsaturated soils (Kim et al., 2005; Oka et al., 2006, 2008).

To reproduce the multiphase behavior of unsaturated soil, a partially saturated porous solid material is described within the well-founded Theory of Porous Media (TPM) (e.g., Atkin and Craine, 1976; Biot, 1962; Bowen, 1976; Coussy, 2004; Schrefler and Gawin, 1996; Boer, 1998; Ehlers, 2003). To complete the coupled multiphase finite element formulation, the relationship between the degree of saturation and suction, namely, the soil water characteristic curve, is required (Houlsby, 1997). In the present model, a van Genuchten type of equation is employed as a constitutive equation between the saturation

and the suction (van Genuchten, 1980). Based on these relations, an air-water-soil three-phase coupled model has been proposed (Oka et al., 2006, 2008; Feng et al., 2006).

2.3 Elasto-Viscoplastic Constitutive Model for Unsaturated Soil

In the present study, an elasto-viscoplastic model based on the overstress-type of viscoplasticity theory with soil structure degradation for saturated soil (Kimoto et al. 2004; Kimoto and Oka 2005) has been extended to one for unsaturated soil using the skeleton stress and the suction effect in the constitutive model (Oka et al. 2006; Kimoto et al. 2007). The collapse behavior of unsaturated soil is macroscopic evidence of the structural instability of the soil skeleton, and it is totally independent of the stress variables adopted in the constitutive modeling (Oka, 1988; Jommi, 2000). In the model the collapse behavior is described by the shrinkage of the overconsolidation boundary surface, the static yield surface, and the viscoplastic surface due to the decrease in suction.

2.3.1 Multiphase mixture theory

Geomaterials usually fall into the field of multi-phase materials. It is considered that they are composed of soil particles, water and air. The behavior of multi-phase materials can be described by the macroscopic continuum mechanical approach through the use of the theory of porous media (e.g., Atkin and Craine, 1976; Bowen, 1976; Coussy, 2004; Schrefler and Gawin, 1996; Boer, 1998; Ehlers, 2003). The theory is considered to be a generalization of Biot's two-phase mixture theory for saturated soils (Biot, 1941; 1962).

2.3.2 General setting

The material to be modeled is composed of three phases, namely, solid (S), liquid (W), and gas (G), which are continuously distributed throughout space. Each constituent has a mass M^α and a volume V^α. The partial quantities used in the method and their relations to intrinsic quantities are defined here. The volume V is obtained from the sum of the partial volumes of the constituents, namely,

$$\sum_\alpha V^\alpha = V \qquad (\alpha = S, W, G) \tag{2.10}$$

The volume of void V^V, which is composed of water and gas, is given as follows:

$$\sum_{\beta} V^{\beta} = V^V \qquad (\beta = W, G) \tag{2.11}$$

Volume fraction n^α is defined as the local ratio of the volume element with respect to the total volume, namely,

$$n^\alpha = \frac{V^\alpha}{V} \qquad \sum_{\alpha} n^\alpha = 1 \qquad (\alpha = S, W, G) \tag{2.12}$$

The volume fraction of the void, n, is written as

$$n = \sum_{\beta} n^\beta = \frac{V^V}{V} = \frac{V - V^S}{V} = 1 - n^S \qquad (\beta = W, G) \tag{2.13}$$

In addition water saturation is required in the model,

$$s = \frac{V^W}{V^W + V^G} = \frac{V^W}{V^V} = \frac{n^W}{n} \tag{2.14}$$

Accordingly, the volume fraction can be given by

$$n^W = sn \qquad n^G = (1 - s)n \tag{2.15}$$

Finally, the partial mass density ρ^α and material (realistic or effective) density ρ_α are defined as

$$\rho^\alpha = \frac{M^\alpha}{V} \quad and \quad \rho_\alpha = \frac{M^\alpha}{V^\alpha} \qquad (\alpha = S, W, G) \tag{2.16}$$

where M^α is the mass of each constituent. The density of the mixture can be expressed as

$$\rho = \sum_{\alpha} \rho^\alpha = \sum_{\alpha} \rho_\alpha n^\alpha \tag{2.17}$$

2.3.3 Skeleton stress

In the theory of porous media, the concept of the effective stress tensor is related to the deformation of the soil skeleton and plays and important role. The effective stress tensor has been defined for water-saturated soil (Terzaghi, 1943). In the case of unsaturated soils, however, the concept needs to be redefined in order to consider compressible materials. In the present study, skeleton stress tensor σ'_{ij} is defined and then used for the stress variable in the constitutive relation for the soil skeleton (Jommi, 2000; Kimoto et al. 2007; Laloui and Nuth, 2009). Jommi calls it the average soil skeleton stress. Laloui and Nuth calls it generalised effective stress. The skeleton stress tensor is equivalent to the Bishop's stress tensor when degree of saturation s is taken as χ. Total stress tensor σ_{ij} is obtained from the sum of the partial stresses, σ^{α}_{ij}, namely,

$$\sum_{\alpha} \sigma^{\alpha}_{ij} = \sigma_{ij} \qquad (\alpha = S, W, G) \tag{2.18}$$

in which σ^{α}_{ij} represents the stress acting on each phase. It is assumed as the Cauchy stress tensor.

The partial stresses for water and air phases express as:

$$\sigma^{W}_{ij} = n^{W} P^{W} \delta_{ij} \tag{2.19}$$

$$\sigma^{G}_{ij} = n^{G} P^{G} \delta_{ij} \tag{2.20}$$

where P^W and P^G are the pore water pressure, and the pore air pressure, respectively. Tension is considered to be positive in this formulation. Then, P^W and P^G are negative.

The partial stress tensor for solid phase can be expressed by the analogy with the water-saturated one as:

$$\sigma^{S}_{ij} = \sigma'_{ij} + n^{S} P^{F} \delta_{ij} \tag{2.21}$$

where P^F is the average pressure of the fluids surrounding the soil skeleton obtained by the well-known Dalton's law via

$$P^{F} = sP^{W} + (1 - s)P^{G} \tag{2.22}$$

in which s is the degree of saturation.

These partial stresses values make up the total stress tensor of the mixture, σ_{ij}, as

$$\sigma_{ij} = \sum_{\alpha} \sigma_{ij}^{\alpha} = \sigma_{ij}^{'} + n^S P^F \delta_{ij} + n^W P^W \delta_{ij} + n^G P^G \delta_{ij} = \sigma_{ij}^{'} + P^F \delta_{ij} \tag{2.23}$$

$\sigma_{ij}^{'}$ is called the skeleton stress in the present study. It is used as the stress variable in the constitutive relation for the soil skeleton:

$$\sigma_{ij}^{'} = \sigma_{ij} - P^F \delta_{ij} \tag{2.24}$$

The definition of Equation (2.24) can be rewritten down as Bishop's definition for the effective stress of unsaturated soil. In addition to Equation (2.24), the effect of suction is also taken into account in the constitutive model. This assumption, which is included in the formulation presented here, leads to a reasonable consideration of the collapse behavior of unsaturated soil, which has been known as a behavior that cannot be described by only Bishop's definition for the effective stress of unsaturated soil.

From the point of view of the mixture theory, the adoption of the skeleton stress represents a natural application of the mixture theory to unsaturated soils. Therefore, it is possible to formulate a model for unsaturated soil starting from a model for saturated soil by substituting the skeleton stress for the effective stress.

2.3.4 Elastic stretching tensor

It is assumed that the total stretching tensor consists of elastic stretching tensor D_{ij}^e and viscoplastic stretching tensor D_{ij}^{vp} as

$$D_{ij} = D_{ij}^e + D_{ij}^{vp} \tag{2.25}$$

The elastic stretching tensor is given by a generalized Hooke type of law, i.e.

$$D_{ij}^e = \frac{1}{2G} \dot{S_{ij}} + \frac{\kappa}{3(1+e)} \frac{\dot{\sigma}_m^{'}}{\sigma_m^{'}} \delta_{ij} \tag{2.26}$$

where S_{ij} is the deviatoric stress tensor, $\sigma_m^{'}$ is the mean skeleton stress, G is the elastic shear modulus, e is the void ratio, κ is the swelling index, and the superimposed dot denotes the time differentiation.

2.3.5 Overconsolidation boundary surface

In this model, it is assumed that there is an overconsolidation (OC) boundary surface that delineates the normally consolidated (NC) region, $f_b \geq 0$, and the overconsolidated region (OC), $f_b < 0$, as follows:

$$f_b = \bar{\eta}^*_{(0)} + M^*_m \ln \frac{\sigma_m^{'}}{\sigma_{mb}^{'}} = 0 \tag{2.27}$$

$$\bar{\eta}^*_{(0)} = \sqrt{\left\{(\eta^*_{ij} - \eta^*_{ij(0)})(\eta^*_{ij} - \eta^*_{ij(0)})\right\}} \tag{2.28}$$

where $\eta^*_{ij} = \frac{S_{ij}}{\sigma_m^{'}}$ is the stress ratio tensor, and (0) denotes the state at the end of the consolidation, in other words, the initial state before deformation occurs. M^*_m is the value of $\eta^* = \sqrt{\eta^*_{ij}\eta^*_{ij}}$ when the volumetric strain increment changes from contraction to dilation, which is equal to ratio M^*_f at the critical state, $\sigma_{mb}^{'}$ is the hardening parameter, that controls the size of the boundary surface. In the present model, the hardening parameter is assumed to be a function of the viscoplastic strain ε^{vp}_{ij} and suction P^C. In order to describe the structure degradation on natural clay, strain-softening with viscoplastic strain is introduced into the hardening parameter in addition to the hardening with the viscoplastic volumetric strain. Meanwhile, to describe the suction effect on the unsaturated soil, suction is incorporated into the value of $\sigma_{mb}^{'}$ as

$$\sigma_{mb}^{'} = \sigma_{ma}^{'} \exp(\frac{1+e_0}{\lambda-\kappa}\varepsilon^{vp}_{kk}) \left[1 + S_I \exp\left\{-s_d(\frac{P^C_i}{P^C} - 1)\right\}\right] \tag{2.29}$$

where ε^{vp}_{kk} is the viscoplastic volumetric strain, λ and κ are the compression and the swelling indexes, respectively, and e_0 is the initial void ratio. $\sigma_{ma}^{'}$ is a strain-softening parameter used to describe the structure degradation effect, which is assumed to decrease with an increasing in viscoplastic strain, namely,

$$\sigma_{ma}^{'} = \sigma_{maf}^{'} + (\sigma_{mai}^{'} - \sigma_{maf}^{'}) \exp(-\beta z) \tag{2.30}$$

$$z = \int_0^t \dot{z} dt, \qquad \dot{z} = \sqrt{\dot{\varepsilon}^{vp}_{ij}\dot{\varepsilon}^{vp}_{ij}} \tag{2.31}$$

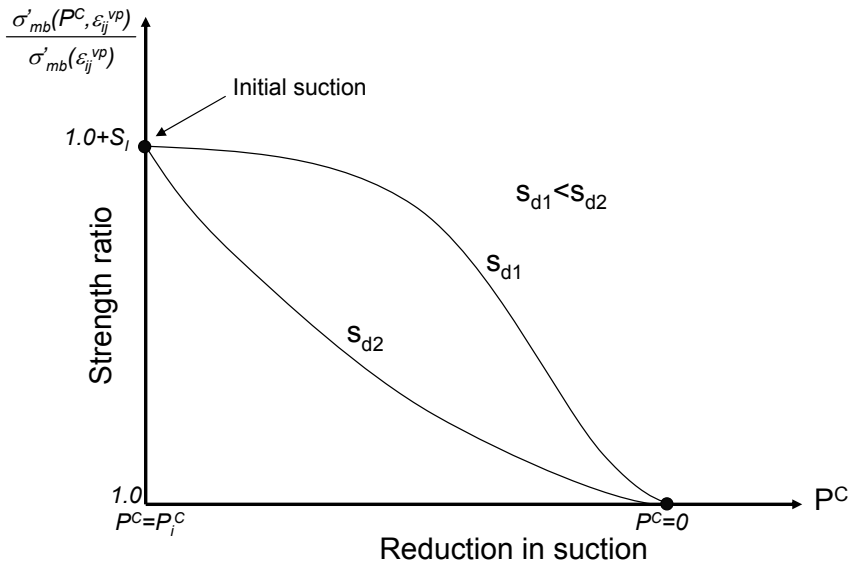

Figure 2.4 Strength degradation due to the reduction in suction

in which σ'_{mai} and σ'_{maf} are the initial and the final values for σ'_{ma}, respectively, β is a material parameter which controls the rate of structural changes, and z is the accumulation of the second invariant of viscoplastic strain rate $\dot{\varepsilon}^{vp}_{ij}$. Since the viscoplastic strain is equal to zero at the initial state, we can obtain the consolidation yield stress σ'_{mbi} equal to σ'_{mai}.

In the last term in Equation (2.29) S_I is the strength ratio of unsaturated soils when the value of suction P^C equals to P^C_i, and s_d controls the decreasing ratio of strength with decreasing suction. The term P^C_i is set to be the initial value of suction. At initial state when $P^C = P^C_i$, the strength ratio of the unsaturated soil to the saturated soil is $1 + S_I$ and decreases with a decline in suction. The change of hardening parameter with change in suction and the effect of parameter s_d is shown in Figure 2.4.

2.3.6 Static yield surface

To describe the mechanical behavior of clay at its static equilibrium state, a Cam-clay type of static yield function is assumed to be

$$f_y = \bar{\eta}^*_{(0)} + \tilde{M}^* \ln \frac{\sigma'_m}{\sigma'^{(s)}_{my}} = 0 \tag{2.32}$$

In the same way as the overconsolidation boundary surface, the suction effect is introduced in the value of $\sigma'^{(s)}_{my}$.

$$\sigma_{my}^{'(s)} = \frac{\sigma_{myi}^{'(s)}}{\sigma_{mai}^{'}}\sigma_{ma}^{'}\exp(\frac{1+e_0}{\lambda-\kappa}\varepsilon_{kk}^{vp})\left[1+S_I\exp\left\{-s_d(\frac{P_i^C}{P^C}-1)\right\}\right] = \frac{\sigma_{myi}^{'(s)}}{\sigma_{mai}^{'}}\sigma_{mb}^{'} \tag{2.33}$$

2.3.7 Viscoplastic potential surface

The viscoplastic potential surface is described as

$$f_p = \bar{\eta}_{(0)}^* + \tilde{M}^* \ln\frac{\sigma_m^{'}}{\sigma_{mp}^{'}} = 0 \tag{2.34}$$

where $\tilde{M}^*$ is assumed to be constant in the NC region and to vary with the current stress in the OC region as

$$\tilde{M}^* = \begin{cases} M_m^* & :\text{NC region} \\ -\frac{\sqrt{\eta_{ij}^*\eta_{ij}^*}}{\ln(\sigma_m^{'}/\sigma_{mc}^{'})} & :\text{OC region} \end{cases} \tag{2.35}$$

where M_m^* is the value of $\sqrt{\eta_{ij}^*\eta_{ij}^*}/\sigma_m^{'}$ at critical state, and $\sigma_{mc}^{'}$ denotes the mean skeleton stress at the intersection of the OC boundary surface and the $\sigma_m^{'}$ axis as

$$\sigma_{mc}^{'} = \sigma_{mb}^{'}\exp\frac{\sqrt{\eta_{ij(0)}^*\eta_{ij(0)}^*}}{M_m^*} \tag{2.36}$$

In the case of isotropic consolidation $\sigma_{mc}^{'}$ equals $\sigma_{mb}^{'}$. The effect of the decrease in the suction on the shrinkage of the overconsolidation boundary surface, f_b, the static yield function, f_y, and the viscoplastic potential function, f_p, for $\eta_{ij(0)}^* = 0$, are illustrated schematically in the $\sigma_m^{'} - \sqrt{2J_2}$ space, Figure 2.5. It can be seen that $\sigma_{mb}^{'}$ and $\sigma_{my}^{'(s)}$ decrease with decreasing suction owing to wetting. The increments in viscoplastic strain for the overstress type model depend on the difference between the current stress state and the static yield stress state, therefore, the shrinkage of f_y due to the wetting yields in the viscoplastic strain increments.

2.3.8 Viscoplastic flow rule

The viscoplastic stretching tensor is expressed by the following equation which is based on Perzyna's viscoplastic theory (Perzyna, 1963; Oka, 1982, 2004) as

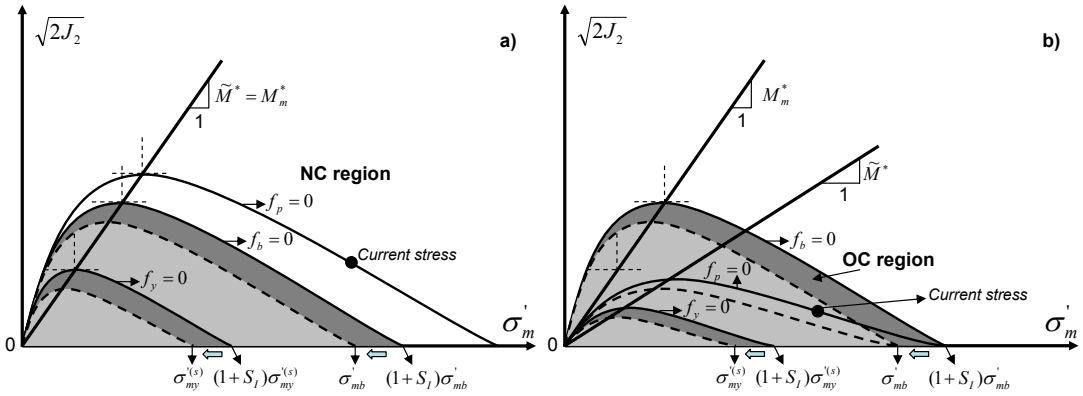

Figure 2.5 Shrinkage of the OC boundary surface, static yield function and potential function. a) In the NC region. b) In the OC region

$$D_{ij}^{vp} = \gamma \langle \Phi_1(f_y) \rangle \frac{\partial f_p}{\partial \sigma_{ij}^{'}} \tag{2.37}$$

in which $\langle\rangle$ are Macaulay's brackets; $\langle \Phi_1(f_y) \rangle = \Phi_1(f_y)$, if $f_y > 0$ and $\langle \Phi_1(f_y) \rangle = 0$, if $f_y \leq 0$. Φ_1 indicates strain rate sensitivity. Based on the experimental data from the strain rate constant triaxial tests, the material function is given as

$$\begin{aligned} \gamma \Phi_1(f_y) &= C^{'} \sigma_m^{'} \exp\left\{ m^{'} (\bar{\eta}_{(0)}^{*} + \tilde{M}^{*} \ln \frac{\sigma_m^{'}}{\sigma_{my}^{'(s)}}) \right\} \\ &= C^{'} \sigma_m^{'} \exp\left\{ m^{'} (\bar{\eta}_{(0)}^{*} + \tilde{M}^{*} \ln \frac{\sigma_{mai}^{'}}{\sigma_{myi}^{'(s)}} \frac{\sigma_m^{'}}{\sigma_{mb}^{'}}) \right\} \\ &= C \sigma_m^{'} \exp\left\{ m^{'} (\bar{\eta}_{(0)}^{*} + \tilde{M}^{*} \ln \frac{\sigma_m^{'}}{\sigma_{mb}^{'}}) \right\} \end{aligned} \tag{2.38}$$

$$C = C^{'} \exp\left\{ m^{'} \tilde{M}^{*} \ln \frac{\sigma_{mai}^{'}}{\sigma_{myi}^{'(s)}} \right\} \tag{2.39}$$

Finally, using the fourth rank isotropic tensor, C_{ijkl}, the viscoplastic stretching tensor is given by the following equations:

$$D_{ij}^{vp} = \begin{cases} C_{ijkl} \sigma_m^{'} \exp\left\{ m^{'} (\bar{\eta}_{(0)}^{*} + \tilde{M}^{*} \ln \frac{\sigma_m^{'}}{\sigma_{mb}^{'}}) \right\} \frac{\partial f_p}{\partial \sigma_{kl}^{'}} & : f_y > 0 \\ 0 & : f_y \leq 0 \end{cases} \tag{2.40}$$

where viscoplastic parameter C_{ijkl} is given by

$$C_{ijkl} = D \delta_{ij} \delta_{kl} + E(\delta_{ik} \delta_{jl} + \delta_{il} \delta_{jk}) \tag{2.41}$$

where D and E are material constants.

The viscoplastic stretching tensor can be written as follows:

$$D_{ij}^{vp} = C_1 \exp\left\{ m'(\bar{\eta}_{(0)}^{*} + \tilde{M}^{*} \ln \frac{\sigma_m^{'}}{\sigma_{mb}^{'}}) \right\} \frac{\eta_{ij}^{*} - \eta_{ij(0)}^{*}}{\bar{\eta}^{*}} + C_2 \exp\left\{ m'(\bar{\eta}_{(0)}^{*} + \tilde{M}^{*} \ln \frac{\sigma_m^{'}}{\sigma_{mb}^{'}}) \right\} \left\{ \tilde{M}^{*} - \frac{\eta_{mn}^{*}(\eta_{mn}^{*} - \eta_{mn(0)}^{*})}{\bar{\eta}^{*}} \right\} \frac{\delta_{ij}}{3} \tag{2.42}$$

$$C_1 = 2E, \tag{2.43}$$

$$C_2 = 3D + 2E \tag{2.44}$$

where C_1 and C_2 are the viscoplastic parameters for the deviatoric and the volumetric components, respectively.

2.4 Multiphase Finite Element Formulation for Analysis of Unsaturated Soil

Unsaturated soil is composed of three constituents, namely, solid particles, water and air, which in the context of the mixture theory, are viewed as three independent overlapping continua. The behavior of the multiphase materials can be described within the framework of a macroscopic continuum mechanical approach through the use of the theory of porous media. The theory is considered to be a generalization of Biot's two-phase mixture theory for saturated soil. The three phases represent the constituents as part of the mixture, also referred as the porous medium. For simplified and practical formulations, the grain particles and the water are assumed to be incompressible.

In the formulations, an updated Lagrangian method with the objective Jaumman rate of Cauchy stress is used for a weak form of the equilibrium equation. An eight-node quadrilateral element with a reduced Gaussian two-point integration is used for the displacement to eliminate shear locking and to reduce the appearance of a spurious hourglass mode. The pore water pressure and the gas pressure are defined at the four corner nodes, Figure 2.6.

Proceeding from the general geometrically non-linear formulation, the governing balance relations for multiphase materials can be obtained (e.g., Boer, 1998; Loret and

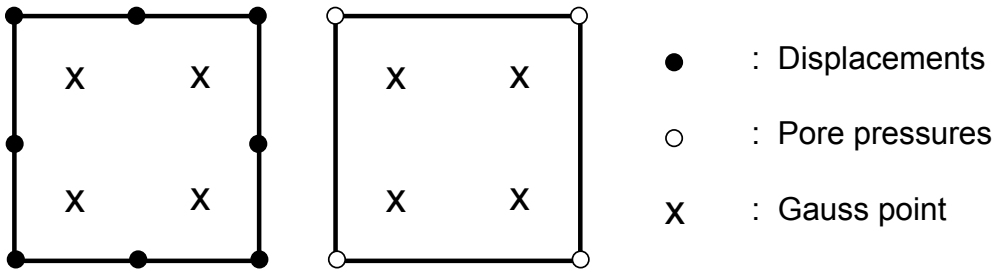

Figure 2.6 Isoparametric elements for the soil skeleton and the pore pressures

Khalili, 2000; Ehlers, 2003; Ehlers et al., 2004; Kimoto et al., 2007, 2010). Mass conservation laws for the gas phase as well as for the liquid phase are considered in those analyses.

2.4.1 Hydraulic Properties of Unsaturated Soils

2.4.1.1 Soil-water Characteristic Curve

The soil-water characteristic curve ($SWCC$) for soil is defined as the relationship between the volumetric water content or degree of saturation and suction of the soil. The $SWCC$ can be described as a measure of the water-holding capacity (i.e., the storage capacity) of the soil as the water content changes when it is subjected to various levels of suction. In the model, the following type of equation for the $SWCC$ is adopted (van Genuchten, 1980):

$$s_{re} = \left\{1 + (\alpha P^C)^{n'}\right\}^{-m} \tag{2.45}$$

where α, m and n' are material parameters and the relation $m = 1 - 1/n'$ is assumed. $P^C (= P^G - P^W)$ is the suction and s_{re} is the effective degree of saturation, namely,

$$s_{re} = \frac{(s - s_{min})}{(s_{max} - s_{min})} \tag{2.46}$$

where s_{min} and s_{max} are the minimum and maximum saturation values, respectively.

2.4.1.2 Unsaturated permeability

In the present model, k^W and k^G are the coefficients of permeability for water and for air, respectively. They are function of any two of three possible volume-mass properties,

namely, degree of saturation, void ratio, and water content (Lambe and Whitman, 1963; Lloret and Alonso, 1980). In the present analysis, the permeability is assumed to be affected by the degree of saturation and void ratio. Van Genuchten type of permeability functions are used. The effect of degree of saturation on permeability for water and air are assumed as

$$k^W = k_s^W s^a \left\{1 - (1 - s^{\frac{1}{m}})^m\right\}^2, \qquad k^G = k_s^G (1-s)^b \left\{1 - (s)^{\frac{1}{m}}\right\}^{2m} \tag{2.47}$$

However, Equations (2.47) leads to some numerical instability during the simulation process due to the large gradient presented when the saturation approaches to 1.0. To overcome this problem, in some of the simulation, the following equations were implemented.

$$k^W = k_s^W s^a \left\{1 - (1 - s^{\frac{1}{m}})^{n'}\right\}, \qquad k^G = k_s^G (1-s)^b \left\{1 - (s^{\frac{1}{m}})^{n'}\right\} \tag{2.48}$$

where a and b are the material parameters, and m and n' are the parameters in the van Genuchten equation (van Genuchten 1980). k_s^W is the coefficient of permeability for water under saturated conditions at a given void ratio, and k_s^G is the permeability of air under fully dry conditions. k_s^W and k_s^G depend on void ratio e in the following form:

$$k_s^W = k_{s0}^W \exp\left[(e - e_0)/C_k\right], \qquad k_s^G = k_{s0}^G \exp\left[(e - e_0)/C_k\right] \tag{2.49}$$

in which k_{s0}^W and k_{s0}^G are the initial value for k_s^W and k_s^G at $e = e_0$ respectively. C_k is the material constant governing the rate of changes in permeability subjected to changes in void ratio.

2.4.2 Conservation of Momentum

Based on the Truesdell's "Metaphysical Principles" of mixture theories (Truesdell, 1984), the momentum balance for each phase is given by,

$$n^\alpha \rho_\alpha \dot{v}_i^\alpha = \sigma_{ji,j}^\alpha + \rho_\alpha n^\alpha \bar{F}_i - \sum_\gamma D^{\alpha\gamma}(v_i^\alpha - v_i^\gamma) \qquad (\alpha = S, W, G) \tag{2.50}$$

in which $\bar{F}_i$ is the gravitational force per unit mass and $D^{\alpha\gamma}(D^{\alpha\gamma} = D^{\gamma\alpha})$ are parameters which describe the interaction between phase α and phase γ, which is defined as,

$$D^{WS} = \frac{(n^W)^2 \rho_W g}{k^W}, \qquad D^{GS} = \frac{(n^G)^2 \rho_G g}{k^G} \tag{2.51}$$

in which g is the acceleration of gravity, and k^W and k^G are the permeability coefficients for the liquid phase and gas phase, respectively. The momentum balance equation for solid (S), water (W), and gas (G) phases is respectively obtained with the following equations:

$$S \;:\; \sigma'_{ji,j} + (n^S P^F \delta_{ji})_{,j} + \rho_S n^S \bar{F}_i - D^{SW}(v_i^S - v_i^W) - D^{SG}(v_i^S - v_i^G) = n^S \rho_S \dot{v}_i^S \tag{2.52}$$

$$W \;:\; (n^W P^W \delta_{ji})_{,j} + \rho_W n^W \bar{F}_i - D^{WS}(v_i^W - v_i^S) - D^{WG}(v_i^W - v_i^G) = n^W \rho_W \dot{v}_i^W \tag{2.53}$$

$$G \;:\; (n^G P^G \delta_{ji})_{,j} + \rho_G n^G \bar{F}_i - D^{GS}(v_i^G - v_i^S) - D^{GW}(v_i^G - v_i^W) = n^G \rho_G \dot{v}_i^G \tag{2.54}$$

When we assume that the deformation is quasi-static process ($\dot{v}_i^\alpha$=0), the space derivative of volume fraction $n_{,i}^\beta$ is negligible, the sum of the momentum balance equations leads to

$$\begin{aligned}
&\sigma'_{ji,j} + (n^S P^F \delta_{ji})_{,j} + \rho_S n^S \bar{F}_i + (n^W P^W \delta_{ji})_{,j} + \rho_W n^W \bar{F}_i + (n^G P^G \delta_{ji})_{,j} + \rho_G n^G \bar{F}_i \\
&= \sigma'_{ji,j} + (P^F \delta_{ji})_{,j} + (\rho_S n^S + \rho_W n^W + \rho_G n^G)\bar{F}_i \\
&= \sigma'_{ji,j} + (P^F \delta_{ji})_{,j} + \rho \bar{F}_i = 0
\end{aligned} \tag{2.55}$$

Substituting Equation (2.24) into Equation (2.55) leads to the equilibrium equation for the whole mixture

$$\sigma_{ji,j} + \rho \bar{F}_i = 0 \tag{2.56}$$

Following the previous assumptions, disregarding the interaction between air and water phases, and using Equation (2.51), Equations (2.53) and (2.54) can be written as follows:

$$n^W (P^W \delta_{ji})_{,j} + \rho_W n^W \bar{F}_i - n^W \frac{\gamma_W}{k^W} V_i^W = 0 \tag{2.57}$$

$$n^G (P^G \delta_{ji})_{,j} + \rho_G n^G \bar{F}_i - n^G \frac{\gamma_G}{k^G} V_i^G = 0 \tag{2.58}$$

where the relative velocity vectors V_i^β of water and air with respect to the soil phase is defined as:

$$V_i^\beta = n^\beta(v_i^\beta - v_i^W) \qquad \beta = W, G \tag{2.59}$$

After manipulation of Equations (2.57) and (2.58), the relative velocity vector for the liquid to the soil skeleton and for the gas to the soil skeleton are written as:

$$V_i^W = \frac{k^W}{\gamma^W}\left\{(P^W\delta_{ji})_{,j} + \rho_W \bar{F}_i\right\} \tag{2.60}$$

$$V_i^G = \frac{k^G}{\gamma^G}\left\{(P^G\delta_{ji})_{,j} + \rho_G \bar{F}_i\right\} \tag{2.61}$$

2.4.2.1 Conservation of momentum for the boundary value problem

In the present study, an updated-Lagrangian method is employed to discretize the equilibrium equations.

When we take the initial configuration at current time t, nominal traction s_i is written as

$$s_i = \Pi_{ji} N_j \tag{2.62}$$

where Π_{ij} is the nominal stress and N_j is the unit normal vector to dS_0. dS_0 is the surface area in the initial configuration.

Using Nanson's theorem we have

$$\frac{\partial x_k}{\partial X_j}\Pi_{ji} = JT_{ki} \tag{2.63}$$

in which J is the Jacobian.

Differentiating Equation (2.63) with respect to time, we obtain

$$\dot{\Pi}_{ji} = J\dot{\hat{S}}_{ki}\frac{\partial X_q}{\partial x_k} \tag{2.64}$$

$$\dot{\hat{S}}_{ki} = \dot{T}_{ki} + L_{pp}T_{ki} - L_{kp}T_{pi} \tag{2.65}$$

where $\dot{\hat{S}}_{ij}$ is the nominal stress rate with respect to the current configuration.

Balance of linear momentum in the reference configuration is given by

$$\int_V \rho_0 a_i dV_0 = \int_V \Pi_{ji,j} dV_0 + \int_V \rho_0 b_i dV_0 \tag{2.66}$$

where a_i is the acceleration vector and b_i is the body force vector.

Taking a time derivative of the first term on the right hand side of Equation (2.66) and using Nanson's theorem and $\rho J = \rho_0$, we find

$$\begin{aligned} \frac{D}{Dt}\int_S \Pi_{ji} N_j dS_0 &= \int_S J\dot{\hat{S}}_{ki}\frac{\partial X_j}{\partial x_k} N_j dS_0 \\ &= \int_S J\dot{\hat{S}}_{ki}\frac{\partial X_j}{\partial x_k}\frac{1}{J}\frac{\partial x_p}{\partial X_j} n_p dS \\ &= \int_S \dot{\hat{S}}_{ki} n_k dS \end{aligned} \tag{2.67}$$

Hence a rate type of the balance of linear momentum with respect to the current configuration is obtained as:

$$\int_V \rho \dot{a}_i dV = \int_V \dot{\hat{S}}_{ki} n_k dV + \int_V \rho \dot{b}_i dV \tag{2.68}$$

Considering quasi static conditions with constant body force; i.e. constant gravitational force, the above equation becomes

$$\int_V \dot{\hat{S}}_{ji,j} dV = 0 \tag{2.69}$$

The above incremental equilibrium equation will be used for the updated Lagrangian formulation of the boundary value problem.

The rate type of conservation for the momentum by the material derivative of the equilibrium equations in the current configuration is give by

$$\dot{\hat{S}}_{ji,j} = 0 \tag{2.70}$$

in which changes in the material density are ignored. The total nominal stress rate tensor, $\dot{\hat{S}}_{ji}$, is defined as

$$\dot{\hat{S}}_{ji} = \dot{T}_{ij} + L_{pp}T_{ij} - T_{in}L_{jn} \tag{2.71}$$

where T_{ij} is the Cauchy stress tensor, $\dot{T}_{ij}$ is the rate type of the Cauchy stress tensor, and L_{ij} is the velocity gradient tensor. The relation between the Cauchy stress tensor and the skeleton Cauchy stress tensor is given as

$$T_{ij} = T^{'}_{ij} + P^F\delta_{ij} \tag{2.72}$$

The time rate of the Cauchy stress tensor is given as

$$\dot{T}_{ij} = \dot{T}^{'}_{ij} + \dot{P}^F\delta_{ij} \tag{2.73}$$

From the above equations, we have

$$\begin{aligned}\dot{\hat{S}}_{ji} &= (\dot{T}^{'}_{ij} + \dot{P}^F\delta_{ij}) + L_{pp}(T^{'}_{ij} + P^F\delta_{ij}) - (T^{'}_{in} + P^F\delta_{in})L_{jn} \\ &= (\dot{T}^{'}_{ij} + L_{pp}T^{'}_{ij} - T^{'}_{in}L_{jn}) + \dot{P}^F\delta ij + L_{pp}P^F\delta_{ij} - P^F\delta_{in}L_{jn} \\ &= \dot{\hat{S}}^{'}_{ij} + \dot{P}^F\delta_{ij} + L_{pp}P^F\delta_{ij} - P^F\delta_{in}L_{jn}\end{aligned} \tag{2.74}$$

in which, the nominal skeleton stress rate tensor, $\dot{\hat{S}}^{'}{}_{ij}$, is defined as

$$\dot{\hat{S}}^{'}{}_{ij} = (\dot{T}^{'}_{ij} + L_{pp}T^{'}_{ij} - T^{'}_{in}L_{jn}) \tag{2.75}$$

2.4.2.2 Weak form of the rate type of conservation for the momentum

The boundary conditions for the discretization for the rate type of conservation of momentum are given by

$$\dot{\hat{S}}_{ij}n_j = \dot{\bar{S}}_i \quad \text{on } \partial D_t \tag{2.76}$$

$$v_i = \bar{v}_i \quad \text{on } \partial D_u \tag{2.77}$$

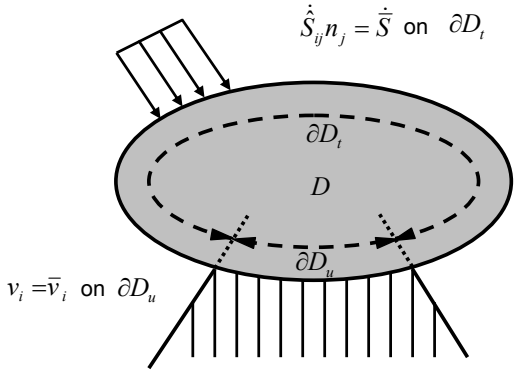

Figure 2.7 Boundary conditions for the whole fluid-solid mixture

As shown in Figure 2.7, ∂D_t and ∂D_u are the parts of the closed boundary ∂D, on which the stress rate and the displacement rate are prescribed as $\dot{\bar{S}}_i$ and $\bar{v}_i$, respectively. They satisfy the following relations:

$$\partial D_t \cup \partial D_u = \partial D \quad \texttt{and} \quad \partial D_t \cap \partial D_u = 0 \tag{2.78}$$

Considering the closed domain D at current time, $t = t$, the weak form of the rate type of equilibrium equation (2.70) is given as follows:

$$\int_D \dot{\hat{S}}_{ji,j}\, \delta v_i dV = 0 \tag{2.79}$$

in which δv_i is the virtual velocity.

From the relation

$$(\dot{\hat{S}}_{ji}\delta v_i)_{,j} = \dot{\hat{S}}_{ji,j}\, \delta v_i + \dot{\hat{S}}_{ji}\delta v_{i,j} \tag{2.80}$$

Equation (2.79) can be written as

$$\int_D (\dot{\hat{S}}_{ji}\delta v_i)_{,j}\, dV - \int_D \dot{\hat{S}}_{ji}\delta v_{i,j}\, dV = 0 \tag{2.81}$$

Applying the Gauss theorem and the compatibility conditions, i.e., $\delta v_{i,j} = \delta L_{ij}$, Equation (2.81) can be written as

$$\int_{\partial D}(\dot{\hat{S}}_{ji}\delta v_i)n_j dS - \int_D \dot{\hat{S}}_{ji}\delta L_{ij}dV = 0 \tag{2.82}$$

Incorporating Equation (2.74) into Equation (2.82) and considering the weak form of the following boundary condition

$$\dot{\bar{S}}_i = \dot{\hat{S}}_{ji}n_j \quad \text{on } \partial D_t \tag{2.83}$$

we have

$$\int_D \dot{\hat{S}}'_{ji}\delta L_{ij}dV + \int_D \dot{P}^F\delta_{ji}\delta L_{ij}dV + \int_D (L_{pp}P^F\delta_{ji} - P^F\delta_{jn}L_{in})\delta L_{ij}dV = \int_{\partial D_t}\dot{\bar{S}}_i\delta v_i dS \tag{2.84}$$

Since the stretching tensor D_{ij} is defined as

$$D_{ij} = \frac{1}{2}(L_{ij} + L_{ji}) \tag{2.85}$$

the following relation is used:

$$\delta_{ji}\delta L_{ij} = \delta D_{ii} = tr\delta D \tag{2.86}$$

From the symmetry of the effective Cauchy stress tensor,

$$\dot{T}_{ji}\delta L_{ij} = \frac{1}{2}\dot{T}_{ji}(\delta L_{ij} + \delta L_{ji}) = \dot{T}_{ji}\delta D_{ij} \tag{2.87}$$

Substituting Equations (2.86) and (2.87) and the nominal skeleton stress rate tensor, Equation (2.75), into Equation (2.84) gives

$$\begin{aligned}\int_D \dot{T}'_{ji}\delta D_{ij}dV \quad &- \int_D T'_{jk}L_{ik}\delta L_{ij}dV + \int_D T'_{ji}L_{kk}\delta L_{ij}dV + \int_D \dot{P}^F\delta D_{kk}dV \\ &+ \int_D (L_{pp}P^F\delta_{ji} - P^F\delta_{jn}L_{in})\delta L_{ij}dV = \int_{\partial D_t}\dot{\bar{S}}_i\delta v_i dS\end{aligned} \tag{2.88}$$

In this formulation, the finite deformation theory and the updated Lagrangian method is adopted. Thus, the Jaumann rate of effective Cauchy stress tensor $\hat{T}'_{ij}$ is adopted for the constitutive model (Oka et al., 2002; Higo, 2003; Higo et al., 2006; Kimoto, 2007). The Jaumann rate of the effective Cauchy stress tensor is the objective tensor; it is defined as

$$\hat{T}'_{ij} = \dot{T}'_{ij} - W_{ik}T'_{kj} + T'_{ik}W_{kj} \tag{2.89}$$

where W_{ij} is the spin tensor, namely,

$$W_{ij} = \frac{1}{2}(L_{ij} - L_{ji}) \tag{2.90}$$

The stretching tensor D_{ij} is assumed to be a composition of elastic stretching tensor D^e_{ij} and viscoplstic stretching tensor D^{vp}_{ij}, that is,

$$D_{ij} = D^e_{ij} + D^{vp}_{ij} \tag{2.91}$$

The relation between elastic stretching tensor D^e_{ij} and the Jaumann rate of Cauchy stress tensor $\hat{T}'_{ij}$ can be obtained as

$$\hat{T}'_{ij} = C^e_{ijkl}D^e_{kl} \tag{2.92}$$

where C^e_{ijkl} is the elastic stiffness matrix.

Herein, the tangent modulus method (as will be presented in the next section) is adopted in order to evaluate the viscoplastic stretching tensor D^{vp}_{ij} (Oka, 1992; Higo, 2003) as

$$\hat{T}'_{ij} = C^{tan}_{ijkl}D_{kl} - Q_{ij} \tag{2.93}$$

in which C^{tan}_{ijkl} is the tangential stiffness matrix, and Q_{ij} is the relaxation stress. Substituting Equation (2.93) into Equation (2.89) yields the following matrix form:

$$\left\{\dot{T}'\right\} = [C]\{D\} - \{Q\} + \{W^*\} \tag{2.94}$$

where $\{W^*\} = \{WT' - T'W\}$ is the vector related to the spin tensor.

According to Equation (2.22) the time derivative of P^F can be expressed as

$$\begin{aligned}\dot{P}^F &= \frac{\partial}{\partial t}\left\{sP^W + (1-s)P^G\right\} \\ &= \left\{\frac{\partial s}{\partial P^C}(P^W - P^G) + (1-s)\right\}\dot{P}^G + \left\{-\frac{\partial s}{\partial P^C}(P^W - P^G) + s\right\}\dot{P}^W \\ &= \left\{A_s + (1-s)\right\}\dot{P}^G + \left\{-A_s + s\right\}\dot{P}^W \end{aligned} \tag{2.95}$$

where

$$A_s = \frac{\partial s}{\partial P^C}(P^W - P^G) \tag{2.96}$$

From the soil water characteristic curve defined in Equations (2.45) and (2.46), we have,

$$c = \frac{\partial s}{\partial P^C} = -\alpha m n'(s_{max} - s_{min})(\alpha P^C)^{n'-1}\left\{1 + (\alpha P^C)^{n'}\right\}^{-m-1} \tag{2.97}$$

where c is the specific moisture capacity.

For the discretization of the weak form of the equilibrium equation, the following relations are defined:

$$\{v\} = [N]\{v^*\}, \qquad \{\delta v\} = [N]\{\delta v^*\} \tag{2.98}$$

$$\{D\} = [B]\{v^*\}, \qquad trD = \{B_v\}^T\{v^*\} \tag{2.99}$$

$$\{\delta D\} = [B]\{\delta v^*\}, \qquad tr\delta D = \{B_v\}^T\{\delta v^*\} \tag{2.100}$$

in which $\{v\}$ is the velocity vector in an element, $\{v^*\}$ is the nodal velocity vector, $[N]$ is a shape function of the eight-node quadrilateral element, $[B]$ is the matrix which transforms the nodal velocity vector $\{v^*\}$ to the stretching tensor $\{D\}$, and $\{B_v\}$ is the vector which transforms the nodal velocity into the trace of $\{D\}$.

$$P^W = [N_h]\left\{P^{W^*}\right\}, \qquad \dot{P}^W = [N_h]\left\{\dot{P}^{W^*}\right\} \tag{2.101}$$

$$P^G = [N_h]\left\{P^{G^*}\right\}, \qquad \dot{P}^G = [N_h]\left\{\dot{P}^{G^*}\right\} \tag{2.102}$$

in which $[N_h]$ represents the element shape function which transforms the nodal pore pressures $\left\{P^{W^*}\right\}$ and $\left\{P^{G^*}\right\}$ and the nodal pore pressure rate vectors $\left\{\dot{P}^{W^*}\right\}$ and $\left\{\dot{P}^{G^*}\right\}$ into the pore pressure P^W and P^G and the rate pressures $\dot{P}^W$ and $\dot{P}^G$.

$$\left\{P^W_{,i}\right\} = [N_{h,i}]\left\{P^{W^*}\right\} = [B_h]\left\{P^{W^*}\right\} \tag{2.103}$$

$$\left\{P^G_{,i}\right\} = [N_{h,i}]\left\{P^{G^*}\right\} = [B_h]\left\{P^{G^*}\right\} \tag{2.104}$$

in which $[B_h]$ is the matrix that transforms the nodal pore pressure vector to the vector form of pore pressure gradient.

$$\{L\} = [B_M]\{v^*\} \tag{2.105}$$

where $[B_M]$ is the matrix which transform the nodal velocity vector into the velocity gradient vector $\{L\}$. Meanwhile, the other two items in Equation (2.88) are expressed as

$$\left\{-T^{'}_{ik}L_{jk}\right\} = [D^{'}_s][B_M]\{v^*\} \tag{2.106}$$

$$U = \left\{L_{pp}P^F\delta_{ji} - P^F\delta_{jn}L_{in}\right\} = [U][B_M]\{v^*\} \tag{2.107}$$

By all the matrices and vector relations obtained previously, Equation (2.88) can be expressed as

$$\begin{aligned} & \int_D \{\delta v^*\}^T [B]^T[C][B]\{v^*\}\, dV \\ - & \int_D \{\delta v^*\}^T [B]^T \{Q\}\, dV + \int_D \{\delta v^*\}^T [B]^T \{W^*\}\, dV \\ + & \int_D \{\delta v^*\}^T [B_M]^T[D^{'}_s][B_M]\{v^*\}\, dV + \int_D \{\delta v^*\}^T [B_M]^T\{T^{'}\}\{B_v\}^T\{v^*\}\, dV \end{aligned}$$

$$+ \int_D \{\delta v^*\}^T (-A_s + s) \{B_v\} \{N_h\} \left\{\dot{P}^{W^*}\right\} dV \tag{2.108}$$
$$+ \int_D \{\delta v^*\}^T \{A_s + (1-s)\} \{B_v\} \{N_h\} \left\{\dot{P}^{G^*}\right\} dV$$
$$+ \int_D \{\delta v^*\}^T [B_M]^T [U] [B_M] \{v^*\} dV = \int_{\partial Dt} \{\delta v^*\}^T [N]^T \left\{\dot{\bar{S}}\right\} dS$$

Since nodal virtual velocity $\{\delta v^*\}^T$ is arbitrary, from Equation (2.108) we have

$$[K] \{v^*\} + [K_L] \{v^*\} + (-A_s + s)[K_v] \left\{\dot{P}^{W^*}\right\} + \{A_s + (1-s)\} [K_v] \left\{\dot{P}^{G^*}\right\} = \{V\} + \{F\} \tag{2.109}$$

in which

$$[K] = \int_D [B]^T [C] [B] dV \tag{2.110}$$
$$[K_L] = \int_D [B_M]^T [D_s^{'}] [B_M] dV + \int_D [B_M]^T \{T^{'}\} \{B_v\}^T dV + \int_D [B_M]^T [U] [B_M] dV \tag{2.111}$$
$$[K_v] = \int_D \{B_v\} \{N_h\} dV \tag{2.112}$$
$$\{V\} = \int_{\partial Dt} [N]^T \left\{\dot{\bar{S}}\right\} dS \tag{2.113}$$
$$\{F\} = \int_D [B]^T \{Q\} dV - \int_D [B]^T \{W^*\} dV \tag{2.114}$$

The relation between the nodal velocity vector $\{v^*\}$ and the nodal displacement increment vector $\{\Delta u^*\}$ can be obtained by using Euler's approximation as

$$\{v^*\} = \frac{\{\Delta u^*\}}{\Delta t} \tag{2.115}$$

Similarly, the pore water pressure and the pore air pressure can be obtained as

$$\left\{\dot{P}^W\right\} = \frac{\left\{P^{W^*}\right\}_{t+\Delta t} - \left\{P^{W^*}\right\}_t}{\Delta t}, \qquad \left\{\dot{P}^G\right\} = \frac{\left\{P^{G^*}\right\}_{t+\Delta t} - \left\{P^{G^*}\right\}_t}{\Delta t} \tag{2.116}$$

Incorporating Equations (2.115) and (2.116) into Equation (2.109) the weak form of the equilibrium equations is obtained, that is,

$$\begin{aligned} &([K] + [K_L]) \{\Delta u^*\} + (-A_s + s)[K_v] \left\{P^{W^*}\right\}_{t+\Delta t} + \{A_s + (1-s)\} [K_v] \left\{P^{G^*}\right\}_{t+\Delta t} \\ &= \Delta t(\{V\}_t + \{F\}_t) + (-A_s + s)[K_v] \left\{P^{W^*}\right\}_t + \{A_s + (1-s)\} [K_v] \left\{P^{G^*}\right\}_t \end{aligned} \tag{2.117}$$

2.4.3 Tangent Modulus Method

In this section, we will derive the relation between Jaumann rate of Cauchy's stress and the stretching tensor using the tangent modulus method (Pierce et al., 1984; Oka et al., 1992a). As shown in Equation (2.91), the total stretching tensor is being divided between the elastic stretching tensor D_{ij}^{e} and the viscoplastic stretching tensor D_{ij}^{vp}. The elastic stretching tensor has been defined in Equation (2.26). The viscoplastic stretching tensor is defined as

$$D_{ij}^{vp} = \gamma \left\langle \Phi(f_y) \right\rangle \frac{\partial f_p}{\partial T_{ij}^{'}} \tag{2.118}$$

Material function $\Phi(f_y)$ depends only on the Cauchy stress tensor $T_{ij}^{'}$ and the viscoplastic volumetric strain tensor v^{vp}. Then, the time derivative of $\Phi(f_y)$ can be written as

$$\dot{\Phi}(f_y) = \frac{\partial \Phi}{\partial T_{ij}^{'}} \dot{T}_{ij}^{'} + \frac{\partial \Phi}{\partial v^{vp}} \dot{v}^{vp} \tag{2.119}$$

The rate of Cauchy stress can be derived from the Jaumann rate of Cauchy stress as

$$\hat{T}_{ij}^{'} = \dot{T}_{ij}^{'} - W_{ik} T_{kj}^{'} + T_{ik}^{'} W_{kj} \tag{2.120}$$

where W_{ij} is the spin tensor.

Using two scalars, A and B, and a symmetric tensor U_{ij}, we can write

$$\begin{aligned} \frac{\partial \Phi}{\partial T_{ij}^{'}} \hat{T}_{ij}^{'} &= \frac{\partial \Phi}{\partial T_{ij}^{'}} (\dot{T}_{ij}^{'} - W_{ik} T_{kj}^{'} + T_{ik}^{'} W_{kj}) \\ &= \frac{\partial \Phi}{\partial T_{ij}^{'}} \dot{T}_{ij}^{'} + \frac{\partial \Phi}{\partial T_{ij}^{'}} (-W_{ik} T_{kj}^{'} + T_{ik}^{'} W_{kj}) \\ &= \frac{\partial \Phi}{\partial T_{ij}^{'}} \dot{T}_{ij}^{'} + (AU_{ij} + B\delta_{ij})(-W_{ik} T_{kj}^{'} + T_{ik}^{'} W_{kj}) \end{aligned} \tag{2.121}$$

we then have

$$AU_{ij}(-W_{ik} T_{kj}^{'} + T_{ik}^{'} W_{kj}) = A(U_{ki} T_{ij}^{'} - U_{ki} T_{ji}^{'}) W_{kj} = 0 \tag{2.122}$$

$$B\delta_{ij}(-W_{ik} T_{kj}^{'} + T_{ik}^{'} W_{kj}) = B(-W_{ki} T_{ik}^{'} + T_{ik}^{'} W_{ki}) = 0 \tag{2.123}$$

Substituting Equations (2.122) and (2.123) into Equation (2.121), we obtain

$$\frac{\partial \Phi}{\partial T'_{ij}} \hat{T}'_{ij} = \frac{\partial \Phi}{\partial T'_{ij}} \dot{T}'_{ij} \tag{2.124}$$

Then, substituting Equation (2.124) into Equation (2.119), we have

$$\dot{\Phi}(f_y) = \frac{\partial \Phi}{\partial T'_{ij}} \hat{T}'_{ij} + \frac{\partial \Phi}{\partial v^{vp}} \dot{v}^{vp} \tag{2.125}$$

Using the tangent modulus parameter θ yields

$$\Phi = (1-\theta)\Phi_t + \theta \Phi_{t+\Delta t} \tag{2.126}$$

where

$$\Phi_{t+\Delta t} = \Phi_t + \Delta\Phi = \Phi_t + \Delta t \dot{\Phi}_t \tag{2.127}$$

Applying Equations (2.125), (2.126), and (2.127), we obtain

$$\Phi = (1-\theta)\Phi_t + \theta \left\{ \Phi_t + \frac{\partial \Phi}{\partial T'_{ij}} \hat{T}'_{ij} + \frac{\partial \Phi}{\partial v^{vp}} \dot{v}^{vp} \right\} \Delta t \tag{2.128}$$

Using Equations (2.92) and (2.118), the Jaumann rate for Cauchy stress can be written as

$$\begin{aligned} \hat{T}'_{ij} &= C^e_{ijkl}(D_{kl} - D^{vp}_{kl}) \\ &= C^e_{ijkl}(D_{kl} - \gamma \Phi \frac{\partial f_p}{\partial T'_{kl}}) \end{aligned} \tag{2.129}$$

We can derivate Δv^{vp} from Equation (2.118) as follows

$$\Delta v^{vp} = \dot{v}^{vp} \Delta t = D^{vp}_{kk} \Delta t = \gamma \Phi \frac{\partial f_p}{\partial T'_{kk}} \Delta t \tag{2.130}$$

Substituting Equations (2.129) and (2.130) into Equation (2.128) yields

$$\begin{aligned}\Phi &= (1-\theta)\Phi_t + \theta\left\{\Phi_t + \frac{\partial\Phi}{\partial T'_{ij}}C^e_{ijkl}(D_{kl} - \gamma\Phi\frac{\partial f_p}{\partial T'_{kl}})\Delta t + \frac{\partial\Phi}{\partial v^{vp}}\gamma\Phi\frac{\partial f_p}{\partial T'_{kk}}\Delta t\right\} \\ &= \frac{1}{1+\xi'}\left\{\Phi_t + (\theta\Delta t)\frac{\partial\Phi}{\partial T'_{ij}}C^e_{ijkl}D_{kl}\right\} \qquad (2.131)\end{aligned}$$

$$\xi' = \gamma\left\{\frac{\partial\Phi}{\partial T'_{ij}}C^e_{ijkl}\frac{\partial f_p}{\partial T'_{kl}} - \frac{\partial\Phi}{\partial v^{vp}}\frac{\partial f_p}{\partial T'_{kk}}\right\}(\theta\Delta t) \qquad (2.132)$$

Thus, substituting Equation (2.132) into Equation (2.118) leads to

$$D^{vp}_{ij} = \gamma\frac{1}{1+\xi'}\left\{\Phi_t + (\theta\Delta t)\frac{\partial\Phi}{\partial T'_{pq}}C^e_{pqrs}D_{rs}\right\}\frac{\partial f_p}{\partial T'_{ij}} \qquad (2.133)$$

From Equations (2.133) and (2.129), we obtain

$$\begin{aligned}\hat{T}'_{ij} &= C^e_{ijkl}\left\{D_{kl} - \gamma\frac{1}{1+\xi'}\left(\Phi_t + (\theta\Delta t)\frac{\partial\Phi}{\partial T'_{pq}}C^e_{pqrs}D_{rs}\right)\frac{\partial f_p}{\partial T'_{kl}}\right\} \qquad (2.134) \\ &= \left[C^e_{ijkl} - C^e_{ijrs}\gamma\frac{\partial f_p}{\partial T'_{rs}}\frac{1}{1+\xi'}(\theta\Delta t)\frac{\partial\Phi}{\partial T'_{pq}}C^e_{pqkl}\right]D_{kl} - C^e_{ijkl}\gamma\frac{\partial f_p}{\partial T'_{kl}}\frac{1}{1+\xi'}\Phi_t\end{aligned}$$

Tangential stiffness matrix C^{tan}_{ijkl} and relaxation stress Q_{ij} are defined as

$$\begin{aligned}C^{tan}_{ijkl} &= C^e_{ijkl} - C^e_{ijrs}\gamma\frac{\partial f_p}{\partial T'_{rs}}\frac{1}{1+\xi'}(\theta\Delta t)\frac{\partial\Phi}{\partial T'_{pq}}C^e_{pqkl} \qquad (2.135) \\ Q_{ij} &= C^e_{ijkl}\gamma\frac{\partial f_p}{\partial T'_{kl}}\frac{1}{1+\xi'}\Phi_t\end{aligned}$$

Then, substituting Equation (2.135) into Equation (2.134) yields

$$\hat{T}'_{ij} = C^{tan}_{ijkl}D_{kl} - C^e_{ijkl}\gamma\frac{\partial f_p}{\partial T'_{kl}}\frac{1}{1+\xi'}\Phi_t \qquad (2.136)$$

2.4.4 Conservation of Mass

2.4.4.1 Continuity equation for water and air

The conservation law of mass for each phase, i.e., solid, liquid, and gas phases, is given in the following equation (Schrefler, 2002) as

$$\frac{D}{Dt}(n^\alpha \rho_\alpha) + n^\alpha \rho_\alpha v^\alpha_{i,i} = 0 \qquad \alpha = (S, W, G) \tag{2.137}$$

The conservation laws for three phases are expressed as

$$S \quad : \quad \rho_S \frac{Dn^S}{Dt} + n^S \frac{D\rho_S}{Dt} + n^S \rho_S v^S_{i,i} = 0 \tag{2.138}$$

$$W \quad : \quad \rho_W \frac{Dn^W}{Dt} + n^W \frac{D\rho_W}{Dt} + n^W \rho_W v^W_{i,i} = 0 \tag{2.139}$$

$$G \quad : \quad \rho_G \frac{Dn^G}{Dt} + n^G \frac{D\rho_G}{Dt} + n^G \rho_G v^G_{i,i} = 0 \tag{2.140}$$

Considering the fact that the soil particles and water are incompressible, namely, $\frac{D\rho_S}{Dt} = 0$, $\frac{D\rho_W}{Dt} = 0$, and using Equations (2.13) and (2.14) the conservation law for each phase can be expressed with degree of saturation s and the volume fraction of void n, as follows:

$$S \quad : \quad -\dot{n}\rho_S + (1-n)\rho_S v^S_{i,i} = 0 \tag{2.141}$$

$$W \quad : \quad \dot{n}s\rho_W + n\dot{s}\rho_W + ns\rho_W v^W_{i,i} = 0 \tag{2.142}$$

$$G \quad : \quad (1-s)\dot{n}\rho_G - n\dot{s}\rho_G + n(1-s)\dot{\rho_G} + n(1-s)\rho_G v^G_{i,i} = 0 \tag{2.143}$$

where the superimposed dot denotes the material time derivative.

Multiplying both sides of Equation (2.141) by $s\frac{\rho_W}{\rho_S}$ yields

$$-\dot{n}s\rho_W + (1-n)s\rho_W v^S_{i,i} = 0 \tag{2.144}$$

Adding both sides of Equation (2.142) and Equation (2.144) and then dividing by ρ_W, we get

$$n\dot{s} + sv^S_{i,i} + ns(v^W_i - v^S_i)_{,i} = 0 \tag{2.145}$$

The relative velocity vector V^β_i of water and air with respect to the solid phase is defined as:

$$V_i^\beta = n^\beta (v_i^\beta - v_i^S) \qquad \beta = W, G \tag{2.146}$$

Substituting Equation (2.85) and apparent velocity V_i^W in Equation (2.146) into Equation (2.145), the conservation law for water can finally be defined as

$$sD_{ii} + \dot{s}n = -V_{i,i}^W \tag{2.147}$$

where the assumption, $\frac{\partial n^W}{\partial x_i} \approx 0$, is used. Next the conservation law for gas is obtained from Equations (2.141) and (2.143), by multiplying both sides of Equation (2.141) by $(1-s)\frac{\rho_G}{\rho_S}$ yields

$$-\dot{n}(1-s)\rho_G + (1-n)(1-s)\rho_G v_{i,i}^S = 0 \tag{2.148}$$

Adding both sides of Equation (2.143) and Equation (2.148) and then dividing by ρ_G, we get

$$-n\dot{s} + n(1-s)\frac{\dot{\rho}_G}{\rho_G} + (1-s)v_{i,i}^S + n(1-s)(v_i^G - v_i^S)_{,i} = 0 \tag{2.149}$$

Substituting Equation (2.85) and apparent velocity V_i^G in Equation (2.146) into Equation (2.149), the conservation law for gas can finally be defined as

$$(1-s)D_{ii} - \dot{s}n + (1-s)n\frac{\dot{\rho}_G}{\rho_G} = -V_{i,i}^G \tag{2.150}$$

where the assumption, $\frac{\partial n^G}{\partial x_i} \approx 0$, is used.

2.4.4.2 Weak form of the continuity equation for the liquid phase

The boundary conditions for the discretization of the continuity equation of liquid phase are given by

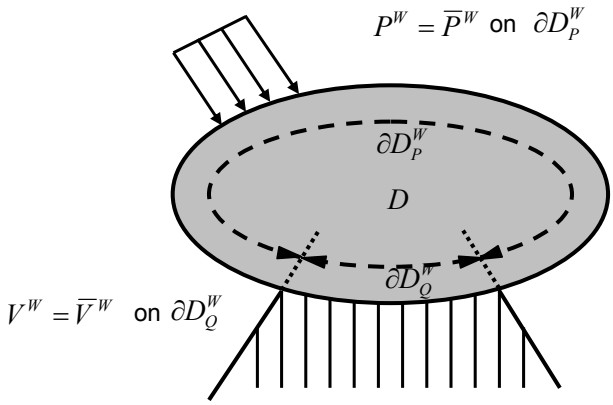

Figure 2.8 Boundary conditions for the liquid phase

$$P^W = \bar{P}^W \qquad \texttt{on} \quad \partial D_P^W \tag{2.151}$$

$$V^W = \bar{V}^W \qquad \texttt{on} \quad \partial D_Q^W \tag{2.152}$$

As Figure 2.8 shows, $\bar{P}^W$ is the water pressure applied on the pressure boundary ∂D_P^W, and $\bar{V}^W$ is the velocity of the water through the boundary surface ∂D_Q^W. ∂D_P^W and ∂D_Q^W are the parts of the closed boundary ∂D, which satisfies the following relations:

$$\partial D_P^W \cup \partial D_Q^W = \partial D \quad \texttt{and} \quad \partial D_P^W \cap \partial D_Q^W = 0 \tag{2.153}$$

Following the Galerkin Method, using the shape function as weighting $\bar{W} = \{N_h\}$, the weak form of the continuity equation for water is given from Equation (2.147) as

$$\int_D (V_{,i}^W + sD_{ii} + \dot{s}n)\bar{W} dV = 0 \tag{2.154}$$

Employing the relation

$$V_{,i}^W \bar{W} = (V_i^W \bar{W})_{,i} - V_i^W \bar{W}_{,i} \tag{2.155}$$

and applying the Gauss theorem, Equation (2.154) can be rewritten as

$$-\int_D \bar{W}_{,i} V_i^W dV + \int_D \bar{W} s D_{ii} dV + \int_D \bar{W} n \dot{s} dV + \int_{\partial D_Q^W} \bar{W} \bar{V}_i^W n_i dS = 0 \tag{2.156}$$

Considering the fact that the degree of saturation, s, is the single-variation function of suction, P^C, $\dot{s}$ can be given as

$$\dot{s} = \frac{\partial s}{\partial P^C}\frac{DP^C}{Dt} = c\frac{DP^C}{Dt} = c(\dot{P}^G - \dot{P}^W) \tag{2.157}$$

Substituting Equations (2.60) and (2.157) into Equation (2.156) yields

$$\begin{aligned} - & \int_D \bar{W}_{,i}\frac{k^W}{\gamma^W}(P^W_{,i} + \rho_W \bar{F}_i)dV + \int_D \bar{W} s D_{ii} dV + \int_D \bar{W} nc(\dot{P}^G - \dot{P}^W)dV \\ + & \int_{\partial D^W_Q} \bar{W}\bar{V}^W_i n_i dS = 0 \end{aligned} \tag{2.158}$$

Incorporating Equations (2.99), (2.101), (2.102), and (2.103) into Equation (2.158), we obtain

$$\begin{aligned} - & \int_D [B_h]^T \frac{k^W}{\gamma^W}[B_h]\left\{P^{W^*}\right\}dV - \int_D [B_h]^T \frac{k^W}{\gamma^W}\rho_W\left\{\bar{F}\right\}dV \\ + & \int_D \{N_h\}^T s\{B_v\}^T\{v^*\}dV \\ + & \int_D \{N_h\}^T nc\{N_h\}\left(\left\{\dot{P}^{G^*}\right\} - \left\{\dot{P}^{W^*}\right\}\right)dV \\ + & \int_{\partial D^W_Q} \{N_h\}^T\{n\}^T\left\{\bar{V}^W\right\}dS = 0 \end{aligned} \tag{2.159}$$

The previous equation is reorganized as follows

$$\begin{aligned} - & \int_D \{N_h\}^T s\{B_v\}^T\{v^*\}dV + \frac{k^W}{\gamma^W}\int_D [B_h]^T[B_h]\left\{P^{W^*}\right\}dV \\ + & \int_D \{N_h\}^T nc\{N_h\}\left\{\dot{P}^{W^*}\right\}dV - \int_D \{N_h\}^T nc\{N_h\}\left\{\dot{P}^{G^*}\right\}dV \\ = & \int_{\partial D^W_Q} \{N_h\}^T\{n\}^T\left\{\bar{V}^W\right\}dS - \frac{k^W}{\gamma^W}\int_D [B_h]^T\rho_W\left\{\bar{F}\right\}dV \end{aligned} \tag{2.160}$$

Finally, the discretization of the continuity equation for the liquid phase is obtained as

$$\begin{aligned} & -s[K_v]^T\{v^*\} + \frac{k^W}{\gamma^W}[K_h]\left\{P^{W^*}\right\} + nc[K_n]\left\{\dot{P}^{W^*}\right\} - nc[K_n]\left\{\dot{P}^{G^*}\right\} \\ & = \left\{V^W\right\} + \left\{F^W\right\} \end{aligned} \tag{2.161}$$

where

$$[K_v]^T = \int_D \{N_h\}^T \{B_v\}^T dV \tag{2.162}$$

$$[K_h] = \int_D [B_h]^T [B_h] dV \tag{2.163}$$

$$[K_n] = \int_D \{N_h\}^T \{N_h\} dV \tag{2.164}$$

$$\{V^W\} = \int_{\partial D_Q^W} \{N_h\}^T \{n\}^T \{\bar{V}^W\} dS \tag{2.165}$$

$$\{F^W\} = -\frac{k^W}{\gamma^W} \int_D [B_h]^T \rho_W \{\bar{F}\} dV \tag{2.166}$$

Substituting the Euler's approximation Equation (2.115) and Equation (2.116) into Equation (2.161), the final discretization equation of the continuity equation for the liquid phase is obtained as

$$\begin{aligned} &-s [K_v]^T \{\Delta u^*\} + \Delta t \frac{k^W}{\gamma^W} [K_h] \{P^{W^*}\}_{t+\Delta t} + nc [K_n] \{P^{W^*}\}_{t+\Delta t} - nc [K_n] \{P^{G^*}\}_{t+\Delta t} \\ &= \Delta t \left(\{V^W\}_t + \{F^W\}_t\right) + nc [K_n] \{P^{W^*}\}_t - nc [K_n] \{P^{G^*}\}_t \end{aligned} \tag{2.167}$$

2.4.4.3 Weak form of the continuity equation for the gas phase

The boundary conditions for the discretization of the continuity equation of gas phase are given by

$$P^G = \bar{P}^G \qquad \texttt{on} \quad \partial D_P^G \tag{2.168}$$

$$V^G = \bar{V}^G \qquad \texttt{on} \quad \partial D_Q^G \tag{2.169}$$

As Figure 2.9 shows, $\bar{P}^G$ is the air pressure applied on the boundary ∂D_P^G, and $\bar{V}^G$ is the velocity of the air through the boundary surface ∂D_Q^G. ∂D_P^G and ∂D_Q^G are the parts of the closed boundary ∂D, which satisfies the following relations:

$$\partial D_P^G \cup \partial D_Q^G = \partial D \quad \texttt{and} \quad \partial D_P^G \cap \partial D_Q^G = 0 \tag{2.170}$$

Following the Galerkin Method, using the shape function as weighting $\bar{W} = \{N_h\}$, the weak form of the continuity equation for gas if given from Equation (2.150) as

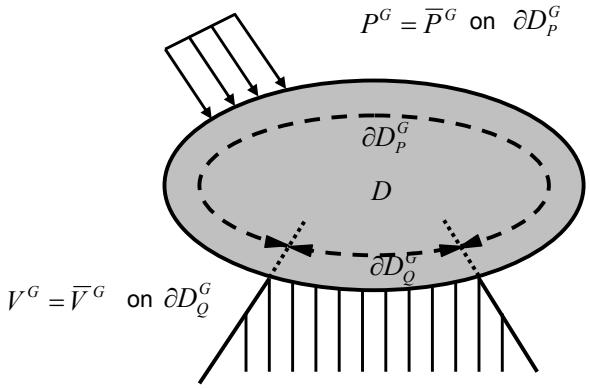

Figure 2.9 Boundary conditions for the gas phase

$$\int_D \left((1-s)\, D_{ii} - \dot{s}n + (1-s)\, n\frac{\dot{\rho}_G}{\rho_G} + V_{i,i}^G \right) \bar{W} dV = 0 \tag{2.171}$$

Employing the relation

$$V_{i,i}^G \bar{W} = \left(V_i^G \bar{W} \right)_{,i} - V_i^G \bar{W}_{,i} \tag{2.172}$$

Applying the Gauss theorem, Equation (2.171) can be written as

$$\begin{aligned} &\int_D \bar{W}\,(1-s)\, D_{ii} dV - \int_D \bar{W}\dot{s}n dV + \int_D \bar{W}\,(1-s)\, n\frac{\dot{\rho}_G}{\rho_G} dV \\ &+ \int_{\partial D_Q^G} \bar{W}\bar{V}_i^G n_i dS - \int_D \bar{W}_{,i} V_i^G dV = 0 \end{aligned} \tag{2.173}$$

Substituting Equation (2.157) into Equation (2.173) yields

$$\begin{aligned} &\int_D \bar{W}\,(1-s)\, D_{ii} dV - \int_D \bar{W} nc \left(\dot{P}^G - \dot{P}^W \right) dV + \int_D \bar{W}\,(1-s)\, n\frac{\dot{\rho_G}}{\rho_G} dV \\ &- \int_D \bar{W}_{,i} V_i^G dV + \int_{\partial D_Q^G} \bar{W}\bar{V}_i^G n_i dS = 0 \end{aligned} \tag{2.174}$$

To describe the changes in gas density, the equation for ideal gases is used as

$$\rho_G = \frac{M\left(-P^G\right)}{R\theta} = -\frac{MP^G}{R\theta} \tag{2.175}$$

$$\dot{\rho}_G = -\frac{M}{R}\left(\frac{\dot{P}^G}{\theta} - \frac{P^G\dot{\theta}}{\theta^2}\right) \tag{2.176}$$

in which M is the molecular weight of gas, R is the gas constant, θ is the temperature, and tension is positive in the equations.

Dividing Equation (2.176) by Equation (2.175) yields

$$\frac{\dot{\rho_G}}{\rho_G} = \frac{\dot{P}^G}{P^G} - \frac{\dot{\theta}}{\theta} \tag{2.177}$$

In this analysis, the temperature is assumed to be constant, namely, $\dot{\theta}$ =0. Equation (2.177) becomes

$$\frac{\dot{\rho_G}}{\rho_G} = \frac{\dot{P}^G}{P^G} \tag{2.178}$$

Substituting Equations (2.61) and (2.178) into Equation (2.174) yields

$$\begin{aligned}
&-\int_D \bar{W}_{,i}\frac{k^G}{\gamma_G}\left(P^G_{,i} + \rho_G\bar{F}_i\right)dV + \int_D \bar{W}\left(1-s\right)D_{ii}dV - \int_D \bar{W}nc\left(\dot{P}^G - \dot{P}^W\right)dV \\
&+\int_D \bar{W}\left(1-s\right)n\frac{\dot{P}^G}{P^G}dV + \int_{\partial D^G_Q}\bar{W}\bar{V}^G_i n_i dS = 0
\end{aligned} \tag{2.179}$$

Incorporating Equations (2.99), (2.101), (2.102), and (2.104) into Equation (2.179), we have

$$\begin{aligned}
&-\int_D \left[B_h\right]^T\frac{k^G}{\gamma_G}\left[B_h\right]\left\{P^{G^*}\right\}dV - \int_D \left[B_h\right]^T\frac{k^G}{\gamma_G}\rho_G\left\{\bar{F}\right\}dV \\
&+\int_D \left\{N_h\right\}^T\left(1-s\right)\left\{B_v\right\}^T\left\{v^*\right\}dV \\
&-\int_D \left\{N_h\right\}^T nc\left\{N_h\right\}\left(\left\{\dot{P}^{G^*}\right\} - \left\{\dot{P}^{W^*}\right\}\right)dV \\
&+\int_D \left\{N_h\right\}^T\left(1-s\right)n\frac{\left\{N_h\right\}\left\{\dot{P}^{G^*}\right\}}{\bar{P}^G_m}dV \\
&+\int_{\partial D^G_Q}\left\{N_h\right\}^T\left\{n\right\}^T\left\{\bar{V}^G\right\}dS = 0
\end{aligned} \tag{2.180}$$

where $\bar{P}_m^G$ is the average pore air pressure in D. The previous equation can be reorganized as follows

$$
\begin{aligned}
&+\int_D [B_h]^T \frac{k^G}{\gamma_G} [B_h] \left\{P^{G^*}\right\} dV - \int_D \{N_h\}^T (1-s) \{B_v\}^T \{v^*\} dV \\
&+\int_D \{N_h\}^T nc \{N_h\} \left(\left\{\dot{P}^{G^*}\right\} - \left\{\dot{P}^{W^*}\right\}\right) dV - \int_D \{N_h\}^T (1-s)\, n \frac{\{N_h\}\left\{\dot{P}^{G^*}\right\}}{\bar{P}_m^G} dV \\
&= \int_{\partial D_Q^G} \{N_h\}^T \{n\}^T \left\{\bar{V}^G\right\} dS - \int_D [B_h]^T \frac{k^G}{\gamma_G} \rho_G \left\{\bar{F}\right\} dV
\end{aligned} \tag{2.181}
$$

Finally, the discretization of the continuity equation for the gas phase is obtained as

$$
\begin{aligned}
&-(1-s)[K_v]^T \{v^*\} + \frac{k^G}{\gamma_G} [K_h] \left\{P^{G^*}\right\} - nc [K_n] \left\{\dot{P}^{W^*}\right\} + nc [K_n] \left\{\dot{P}^{G^*}\right\} \\
&-(1-s)\, n \left[K_c^P\right] \left\{\dot{P}^{G^*}\right\} = \left\{V^G\right\} + \left\{F^G\right\}
\end{aligned} \tag{2.182}
$$

where

$$[K_v]^T = \int_D \{N_h\}^T \{B_v\}^T dV \tag{2.183}$$

$$[K_h] = \int_D [B_h]^T [B_h] dV \tag{2.184}$$

$$[K_n] = \int_D \{N_h\}^T \{N_h\} dV \tag{2.185}$$

$$\left[K_c^P\right] = \int_D \frac{\{N_h\}^T \{N_h\}}{\bar{P}_m^G} dV \tag{2.186}$$

$$\left\{V^G\right\} = \int_{\partial D_Q^G} \{N_h\}^T \{n\}^T \left\{\bar{V}^G\right\} dS \tag{2.187}$$

$$\left\{F^G\right\} = -\frac{k^G}{\gamma_G} \int_D [B]^T \rho_G \left\{\bar{F}\right\} dV \tag{2.188}$$

Substituting the Euler's approximations in Equations (2.115) and (2.116) into Equation (2.182), the final discretization equation for the continuity equation of the gas phase is obtained as

$$
\begin{aligned}
&-(1-s)[K_v]^T \{\Delta u^*\} + \Delta t \frac{k^G}{\gamma_G} [K_h] \left\{P^{G^*}\right\}_{t+\Delta t} - nc [K_n] \left\{P^{W^*}\right\}_{t+\Delta t} \\
&+nc [K_n] \left\{P^{G^*}\right\}_{t+\Delta t} - (1-s)\, n \left[K_c^P\right] \left\{P^{G^*}\right\}_{t+\Delta t} \\
&= \Delta t \left(\left\{V^G\right\}_t + \left\{F^G\right\}_t\right) - nc [K_n] \left\{P^{W^*}\right\}_t + nc [K_n] \left\{P^{G^*}\right\}_t \\
&-(1-s)\, n \left[K_c^P\right] \left\{P^{G^*}\right\}_t
\end{aligned} \tag{2.189}
$$

2.4.5 Discretized Governing Equations for the Multiphase Finite Element Analysis

Combining the discretization of the equilibrium equation (2.117), and the continuity equations for the liquid phase (2.167) and the gas phase (2.189) gives the governing equation for the multiphase finite element formulation as

$$\left(\Delta t\left[K_1\right]+\left[K_2\right]\right)\left\{X\right\}_{t+\Delta t}=\Delta t\left(\left\{\mathtt{F}\right\}+\left\{\mathtt{V}\right\}\right)+\left[K_2\right]\left\{Y\right\}_t \tag{2.190}$$

in which $\{X\}_{t+\Delta t}$ and $\{Y\}_t$ are unknown values at time $t+\Delta t$, and the values at the last step, respectively, which are defined as

$$\left\{X\right\}_{t+\Delta t}=\left\{\begin{array}{c}\{\Delta u^*\}\\ \left\{P^{W^*}\right\}_{t+\Delta t}\\ \left\{P^{G^*}\right\}_{t+\Delta t}\end{array}\right\},\qquad \left\{Y\right\}_t=\left\{\begin{array}{c}\{0\}\\ \left\{P^{W^*}\right\}_t\\ \left\{P^{G^*}\right\}_t\end{array}\right\} \tag{2.191}$$

where $[K_1]$ and $[K_2]$ in Equation (2.190) are given as

$$\left[K_1\right]=\left[\begin{array}{ccc}0 & 0 & 0\\ 0 & \frac{k^W}{\gamma_W}\left[K_h\right] & 0\\ 0 & 0 & \frac{k^G}{\gamma_G}\left[K_h\right]\end{array}\right] \tag{2.192}$$

$$\left[K_2\right]=\left[\begin{array}{ccc}\left[K\right]+\left[K_L\right] & \left(-A_s+s\right)\left[K_v\right] & \left\{A_s+(1-s)\right\}\left[K_v\right]\\ -s\left[K_v\right]^T & nc\left[K_n\right] & -nc\left[K_n\right]\\ -\left(1-s\right)\left[K_v\right]^T & -nc\left[K_n\right] & nc\left[K_n\right]-n\left(1-s\right)\left[K_c^P\right]\end{array}\right] \tag{2.193}$$

$\{\mathtt{F}\}$ and $\{\mathtt{V}\}$ in Equation (2.190) are given as

$$\left\{\mathtt{F}\right\}=\left\{\begin{array}{c}\{F\}\\ \{F^W\}\\ \{F^G\}\end{array}\right\},\qquad \left\{\mathtt{V}\right\}=\left\{\begin{array}{c}\{V\}\\ \{V^W\}\\ \{V^G\}\end{array}\right\} \tag{2.194}$$

Chapter 3

INSTABILITY ANALYSIS AND SIMULATION OF WATER INFILTRATION INTO AN UNSATURATED ELASTO-VISCOPLASTIC MATERIAL

3.1 Introduction

It has been well recognized that the behavior of unsaturated soil subjected to water infiltration plays an important role in Geomechanics. This is because the failure of natural slopes, embankments, and artificial soil structures is most often due to water infiltration. The failure of soil structures can be triggered by a wetting process from an unsaturated stage resulting from an increase in moisture content and a decrease in suction. Jennings and Burland (1962) conducted a series of consolidation tests and showed that partly saturated soil upon wetting undergoes additional settlement or "collapses"; this phenomenon is commonly referred to as collapse behavior. To study this behavior in unsaturated soil, several constitutive models have been developed (e.g., Alonso et al., 1990; Cui and Delage, 1996; Oka et al., 2006; Sheng et al., 2003; Thomas and He, 1998; Wheeler and Karube, 1996; Wheeler and Sivakumar, 1995). Simultaneously, unsaturated seepage-deformation

coupled methods have been developed in order to solve practical geotechnical problems for unsaturated soil (e.g., Alonso et al., 2003; Cho and Lee, 2001; Ehlers et al., 2004; Kato et al., 2009; Oka et al., 2009).

The instability of saturated porous media has been widely studied by many researchers (e.g., Ehlers and Volk, 1998; Higo et al., 2005; Loret and Prévost, 1991; Oka et al., 1994, 1995; Rice, 1975; Schrefler et al., 1995) from both experimental and analytical points of view. However, studies on the instability of unsaturated porous materials have not been completed. Many experimental and numerical researches have been conducted on the deformation behavior of unsaturated soil (e.g., Alonso et al., 2003; Cunningham et al., 2003; Feng, 2007; Khalili et al., 2004; Kimoto et al., 2007; Oka et al., 2010). Nevertheless, the deformation of unsaturated soil is still a subject of research. And theoretical analyses, such as instability analyses, have not yet been performed. Recently, Buscarnera and Nova (2009a, 2009b) addressed the general problem of soil instability for partially saturated geomaterials with particular reference to the controllability of oedometric and triaxial conditions. They showed that the onset of instability can be identified by several hydro-mechanical tests, in which wetting processes may explain the main cause of soil instability. In addition, Garcia et al. (2010) studied the effect of hydraulic parameters on the transient vertical infiltration problem and their effect on the deformation behavior of elasto-viscoplastic unsaturated soil. Among the hydraulic parameters studied, it has been found that the generation of pore water pressure and volumetric strain is significantly controlled by the material parameters that describe the soil water characteristic curve.

The main objective of the present paper is to study the effect of parameters and state variables on the unstable behavior of unsaturated materials when they are subjected to a wetting process, e.g., rainfall and flooding. Then, before conducting the numerical analysis, the material parameters and the conditions that contribute to the growth rate of the fluctuation are examined via a linear instability analysis. From this analysis, it is found that the onset of the instability of the material system depends on the specific moisture capacity (slope of the soil water characteristic curve), the suction, and the hardening parameter.

The multiphase coupled elasto-viscoplastic finite element analysis formulation proposed by Oka et al. (2006) is used to describe the water infiltration into a one-dimensional column and the transition of the porous material from an unsaturated state to a satu-

rated state. The numerical analyses presented here are based on the fundamental concept of the theory of porous media (e.g., Atkin and Craine, 1976; Biot, 1962; Bowen, 1976; Coussy, 2004; Boer, 1998; Ehlers, 2003). The materials are assumed to be composed of solid, water, and air which are thought to be continuously distributed throughout space at a macroscopic level. An elasto-viscoplastic constitutive model is adopted for the soil skeleton (Kimoto and Oka, 2005). The skeleton stress, which is determined from the difference between the total stress and the average pore fluid pressure, is used for the stress variable in the governing equations. In addition, the constitutive parameters are functions of the matric suction, by which the shrinkage or the expansion of the overconsolidation boundary surface and the static yield surface can be described (Oka et al., 2006).

The organization of this chapter is outlined as follows: In Section 3.2, a linear instability analysis is presented in order to investigate the effect of parameters on the onset of the instability of the governing equations using a simplified one-dimensional viscoplastic model. In the analytical formulation, the material is assumed to be a triphasic material consisting of a soil skeleton, pore water, and pore air. In Section 3.3, numerical simulations of the one-dimensional water infiltration problem are presented to discuss the effect of the specific moisture capacity and the initial suction on the development of volumetric strain. For the numerical simulation, an updated Lagrangian method with the objective Jaumman rate of Cauchy stress is adopted (Kimoto et al., 2004; Oka et al., 2006). It is shown that the instability obtained by the numerical analyses is consistent with the theoretical results obtained by the linear instability analysis.

3.2 1D instability analysis of an unsaturated viscoplastic material

Jennings and Burland (1962) conducted a series of consolidation tests on unsaturated soils and showed that upon wetting, the soil samples collapsed; this phenomenon is commonly referred to as collapse behavior, i.e., instability problem. In recent years, many researches have been oriented to study the behavior of unsaturated soils (e.g., Alonso et al., 2003; Buscarnera and Nova, 2009b; Cunningham et al., 2003; Ehlers et al., 2004; Khalili et al., 2004; Kimoto et al., 2007; Oka et al., 2010).

In spite of the above-mentioned valuable works, the effects of the constitutive parameters on the deformation of an unsaturated material have not yet been fully investigated.

Hence, the deformation behavior of unsaturated soils has to be studied with both numerical simulations and an instability analysis. In the present section, a linear instability analysis is conducted on an unsaturated material in a viscoplastic state in order to examine which constitutive parameters and conditions lead to the onset of a growing instability during a wetting process.

Due to the high nonlinearity of the hydraulic and the constitutive equations involved in the unsaturated coupled seepage-deformation analysis method, only simplified one-dimensional analytical solutions for the infiltration problem can be obtained for elastic materials (e.g., Wu and Zhang, 2009). Therefore, the linear instability analysis will be applied to a one-dimensional viscoplastic unsaturated material based on the multiphase coupled seepage-deformation framework presented in Section 2.4. The results by the instability analysis obtained here will be discussed with the numerical simulation results in Section 3.3.

3.2.1 Governing equations

3.2.1.1 Stress variable

Following the elasto-viscoplstic constitutive model and the multiphase finite element formulation presented in Sections 2.3 and 2.4, respectively, one-dimensional stress variables are defined in the followings. From Equations (2.18) $\sim$ (2.21), the one-dimensional total and partial stresses can be rewritten as:

$$\sigma^W = n^W P^W \tag{3.1}$$

$$\sigma^G = n^G P^G \tag{3.2}$$

$$\sigma^S = \sigma' + n^S P^F \tag{3.3}$$

$$\sigma = \sigma^S + \sigma^W + \sigma^G \tag{3.4}$$

where σ is the total stress, σ^α (α=S,W,G) are the partial stresses, and P^W and P^G are the pore water pressure and the pore air pressure, respectively. Tension is considered to be positive in this formulation. Then, P^G and P^W are neagtive. σ' is called the skeleton stress in the present study; it acts only on the solid phase and is used as the stress variable in the constitutive equation for the soil skeleton. Substituting Equations (3.1) $\sim$ (3.3) into Equation (3.4), and considering Equations (2.12) $\sim$ (2.14), the skeleton stress is obtained as:

$$\sigma' = \sigma - P^F \tag{3.5}$$

in which P^F is the average fluid pressure acting on the solid phase given by

$$P^F = sP^W + (1-s)P^G \tag{3.6}$$

where s is the saturation.

3.2.1.2 Constitutive equation

A simplified viscoplastic constitutive model is used in this analysis. The stress-strain relation can be written as:

$$\sigma' = H\varepsilon + \mu\dot{\varepsilon} \tag{3.7}$$

where σ' is the skeleton stress, ε is the viscoplastic strain, the superimposed dot denotes the differentiation with respect to time t, H is the strain-hardening -softening parameter, which is a function of the suction P^C, and μ is the viscoplastic parameter.

Suction P^C is included in the constitutive model as the difference between the pore air pressure and the pore water pressure, when tension is assumed to be positive, and P^W and P^G are negative. Then, the suction is defined by

$$P^C = -(P^G - P^W) \tag{3.8}$$

3.2.1.3 Equation of equilibrium

The one-dimensional equilibrium equation can be written from Equation (2.56) as follows:

$$\frac{\partial \sigma}{\partial x} + \rho\bar{F} = \frac{\partial \sigma'}{\partial x} + \frac{\partial P^F}{\partial x} + \rho\bar{F} = 0 \tag{3.9}$$

3.2.1.4 Continuity equations

In the one-dimensional analysis the continuity equations for the water and the air phases, can be written from Equations (2.147) and (2.150), respectively,

$$s\dot{\varepsilon} + n\dot{s} = -\frac{\partial V^W}{\partial x} \tag{3.10}$$

$$(1-s)\dot{\varepsilon} - n\dot{s} + n(1-s)\frac{\dot{\rho_G}}{\rho_G} = -\frac{\partial V^G}{\partial x} \tag{3.11}$$

where $\dot{\varepsilon}$ is the strain rate, n is the porosity, V^α (α=W,G) is the relative velocity of the fluid (2.146), ρ_G is the air density, and the superimposed dot denotes the time differentiation.

3.2.1.5 Darcy's law

Darcy's type of equations for the flow of water and air, can be obtained from Equations (2.60) and (2.61), namely,

$$V^W = \frac{k^W}{\gamma_W}\left\{\frac{\partial P^W}{\partial x} + \rho_W \bar{F}\right\} \tag{3.12}$$

$$V^G = \frac{k^G}{\gamma_G}\left\{\frac{\partial P^G}{\partial x} + \rho_G \bar{F}\right\} \tag{3.13}$$

where k^W and k^G are the water and the air permeabilities, respectively, γ_W and γ_G are the unit weight of the water and the air, respectively, and ρ_W and ρ_G are the densities of the water and the air, respectively.

3.2.2 Perturbed governing equations

In the following, the perturbation of the pore water pressure P^W, pore air pressure P^G and strain ε in a one-dimensional form is considered for the governing equations. Disregarding the changes in material density and considering the body force constant, the perturbation of the equilibrium equation (3.9) is given by

$$\frac{\partial \tilde{\sigma}}{\partial x} = \frac{\partial \tilde{\sigma'}}{\partial x} + \frac{\partial \tilde{P}^F}{\partial x} = 0 \tag{3.14}$$

where the perturbed variables are indicated by a tilde. In Equation (3.14), the perturbation of the skeleton stress σ' can be written from Equation (3.7) as:

$$\tilde{\sigma'} = \tilde{H}\varepsilon + H\tilde{\varepsilon} + \mu\dot{\tilde{\varepsilon}} \tag{3.15}$$

In Equation (3.15), the strain hardening parameter H is a function of the suction; hence, the perturbation of H is given as:

$$\tilde{H} = \frac{\partial H}{\partial P^C}\tilde{P}^C = A\tilde{P}^C \tag{3.16}$$

where A $(= \partial H/\partial P^C)$ indicates the slope of the $H - P^C$ curve.

The perturbation of the terms in periodic form for Equations (3.15) and (3.16), can be written as:

$$\begin{aligned}
\tilde{P}^C &= -(\tilde{P}^G - \tilde{P}^W) && (3.17)\\
\tilde{P}^G &= P^{G^*}\mathtt{exp}(iqx + \omega t) && (3.18)\\
\tilde{P}^W &= P^{W^*}\mathtt{exp}(iqx + \omega t) && (3.19)\\
\tilde{\varepsilon} &= \varepsilon^*\mathtt{exp}(iqx + \omega t) && (3.20)\\
\dot{\tilde{\varepsilon}} &= \omega\varepsilon^*\mathtt{exp}(iqx + \omega t) && (3.21)
\end{aligned}$$

where q is the wave number $(= 2\pi/l$, l: wave length), ω is the growth rate of the fluctuation and the superscript * indicates the amplitude of each variable.

Using Equations (3.15) $\sim$ (3.21), we have a space differentiation of the perturbed skeleton stress as:

$$\frac{\partial\tilde{\sigma}'}{\partial x} = (A\varepsilon P^{W^*} - A\varepsilon P^{G^*} + H\varepsilon^* + \mu\omega\varepsilon^*)iq\mathtt{exp}(iqx + \omega t) \tag{3.22}$$

Similarly, in Equation (3.14), the perturbation of the average pore pressure P^F can be written by means of Equation (3.6) as:

$$\tilde{P}^F = \tilde{s}P^W + s\tilde{P}^W + (1 - s)\tilde{P}^G - \tilde{s}P^G \tag{3.23}$$

In Equation (3.23), the degree of saturation, s, is a function of the suction; then, the perturbation of the degree of saturation is given as:

$$\tilde{s} = \frac{\partial s}{\partial P^C}\tilde{P}^C = B\tilde{P}^C \tag{3.24}$$

where B $(= \partial s/\partial P^C)$ indicates the slope of curve $s - P^C$. B is called the specific moisture capacity.

Using Equations (3.17) $\sim$ (3.19), and Equations (3.23) and (3.24), we have a gradient of the perturbed average pore pressure as:

$$\frac{\partial \tilde{P}^F}{\partial x} = ((BP^W + s - BP^G)P^{W^*} + (-BP^W + 1 - s + BP^G)P^{G^*})iq\texttt{exp}(iqx + \omega t) \tag{3.25}$$

By substituting Equations (3.22) and (3.25) into Equation (3.14) and rearranging the terms, we obtain:

$$(A\varepsilon + BP^C + s)P^{W^*} - (A\varepsilon + BP^C + s - 1)P^{G^*} + (H + \mu\omega)\varepsilon^* = 0 \tag{3.26}$$

The perturbation of the continuity equation for the water phase (3.10) is given by

$$\tilde{s}\dot{\varepsilon} + s\dot{\tilde{\varepsilon}} + n\dot{\tilde{s}} = -\frac{\partial \tilde{V}^W}{\partial x} \tag{3.27}$$

where $\dot{\varepsilon}$ is the current strain rate.

The perturbation of the rate of the degree of saturation is

$$\dot{\tilde{s}} = \omega B\tilde{P}^C \tag{3.28}$$

The perturbation of the spatial differentiation of a Darcy type of Equation (3.12) for the water can be written as:

$$\frac{\partial \tilde{V}^W}{\partial x} = \frac{\partial}{\partial x}\left[\frac{k^W}{\gamma_W}\left\{\frac{\partial \tilde{P}^W}{\partial x} + \rho_W \bar{F}\right\}\right] = \frac{k^W}{\gamma_W}\frac{\partial^2 \tilde{P}^W}{\partial x^2} \tag{3.29}$$

Substituting Equations (3.17) $\sim$ (3.19), (3.21), (3.24), (3.28) and (3.29) into Equation (3.27) and rearranging the terms, we obtain

$$\left(B\dot{\varepsilon} + n\omega B - q^2\frac{k^W}{\gamma_W}\right)P^{W^*} - (B\dot{\varepsilon} + n\omega B)\,P^{G^*} + s\omega\varepsilon^* = 0 \tag{3.30}$$

For the sake of simplicity, it is considered that the time rate of the air density is equal to zero in the present state; as a result, the perturbation of the continuity equation for the air phase (3.11) is given by

$$(1 - s)\dot{\tilde{\varepsilon}} - \tilde{s}\dot{\varepsilon} - n\dot{\tilde{s}} = -\frac{\partial \tilde{V}^G}{\partial x} \tag{3.31}$$

The perturbation of the spatial differentiation of a Darcy type of Equation (3.13) for the air can be written as:

$$\frac{\partial \tilde{V}^G}{\partial x} = \frac{\partial}{\partial x}\left[\frac{k^G}{\gamma_G}\left\{\frac{\partial \tilde{P}^G}{\partial x} + \rho_G \bar{F}\right\}\right] = \frac{k^G}{\gamma_G}\frac{\partial^2 \tilde{P}^G}{\partial x^2} \tag{3.32}$$

Substituting Equations (3.17) $\sim$ (3.19), (3.21), (3.24), (3.28) and (3.32) into Equation (3.31) and rearranging the terms, we obtain

$$-\left(B\dot{\varepsilon} + n\omega B\right) P^{W^*} + \left(B\dot{\varepsilon} + n\omega B - q^2\frac{k^G}{\gamma_G}\right) P^{G^*} + (1-s)\omega\varepsilon^* = 0 \tag{3.33}$$

We can rewrite the perturbation of the equilibrium and the continuity equations for water and air, Equations (3.26), (3.30), and (3.33), in matrix form as:

$$[A]\{y\} = \{0\}$$

$$\begin{bmatrix} (A\varepsilon + BP^C + s) & -(A\varepsilon + BP^C + s - 1) & (H + \mu\omega) \\ \left(B\dot{\varepsilon} + Bn\omega - q^2\frac{k^W}{\gamma_W}\right) & -(B\dot{\varepsilon} + Bn\omega) & s\omega \\ -(B\dot{\varepsilon} + Bn\omega) & \left(B\dot{\varepsilon} + Bn\omega - q^2\frac{k^G}{\gamma_G}\right) & (1-s)\omega \end{bmatrix} = \begin{Bmatrix} P^{W^*} \\ P^{G^*} \\ \varepsilon^* \end{Bmatrix} = \{0\} \tag{3.34}$$

For nonzero values of P^{W^*}, P^{G^*}, and ε^*, the determinant of matrix $[A]$ has to be equal to zero. From det$[A]$=0, we have a polynomial function of ω as:

$$\begin{aligned} &\frac{1}{\gamma_G\gamma_W}\left[\left\{-B\dot{\varepsilon}\left(\gamma_W k^G + \gamma_G k^W\right) + k^G k^W q^2\right\} q^2 H\right. \\ &+\left\{q^2\left\{\gamma_W k^G s^2 + \left(A\varepsilon + BP^C\right)\left(\gamma_W k^G s - \gamma_G k^W(1-s)\right) + \gamma_G k^W\left(s^2 - 2s + 1\right)\right.\right. \\ &\left.\left.-B\left(\gamma_W k^G + \gamma_G k^W\right)(nH + \mu\dot{\varepsilon}) + k^W k^G \mu q^2\right\} - B\dot{\varepsilon}\gamma_W\gamma_G\right\}\omega \\ &\left.-Bn\left\{\gamma_G\gamma_W + \left(\gamma_W k^G + \gamma_G k^W\right) q^2\mu\right\}\omega^2\right] = 0 \end{aligned} \tag{3.35}$$

Equation (3.35) can be rewritten as follows:

$$\omega^2 + \alpha_1\omega + \alpha_2 = 0 \tag{3.36}$$

in which

$$\alpha_1 = \frac{1}{-Bn\left\{\gamma_G\gamma_W + \left(\gamma_W k^G + \gamma_G k^W\right) q^2\mu\right\}} \left[q^2 \left\{\gamma_W k^G s^2 + (A\varepsilon + BP^C)(\gamma_W k^G s - \gamma_G k^W(1-s))\right.\right.$$

$$\left.\left. + \gamma_G k^W \left(s^2 - 2s + 1\right) - B\left(\gamma_W k^G + \gamma_G k^W\right)(nH + \dot{\varepsilon}\mu) + k^W k^G \mu q^2\right\} - B\dot{\varepsilon}\gamma_W\gamma_G\right] \quad (3.37)$$

$$\alpha_2 = \frac{1}{-Bn\left\{\gamma_G\gamma_W + \left(\gamma_W k^G + \gamma_G k^W\right) q^2\mu\right\}} \left\{-B\dot{\varepsilon}\left(\gamma_W k^G + \gamma_G k^W\right) + k^G k^W q^2\right\} q^2 H \quad (3.38)$$

In the following, we discuss the instability of the material system. If the growth rate of perturbation ω, which is the root of Equation (3.36), is positive, the material system is unstable. On the contrary, if ω is negative, the material system is stable. In order to estimate whether ω is negative or positive, we adopt the Routh-Hurwitz criteria. The roots of Equation (3.36) have negative real parts when the coefficients of the characteristic polynomial satisfy

$$\alpha_1 > 0, \qquad \alpha_2 > 0 \quad (3.39)$$

The first factor in Equations (3.37) and (3.38) is positive. Thus, it is sufficient to consider the sign of the variables in the second factor for the analysis, namely,

$$\alpha_1^* = \left[q^2 \left\{\gamma_W k^G s^2 + (A\varepsilon + BP^C)(\gamma_W k^G s - \gamma_G k^W(1-s)) + \gamma_G k^W \left(s^2 - 2s + 1\right)\right.\right.$$

$$\left.\left. - B\left(\gamma_W k^G + \gamma_G k^W\right)(nH + \dot{\varepsilon}\mu) + k^W k^G \mu q^2\right\} - B\dot{\varepsilon}\gamma_W\gamma_G\right] > 0 \quad (3.40)$$

$$\alpha_2^* = \left\{-B\dot{\varepsilon}\left(\gamma_W k^G + \gamma_G k^W\right) + k^G k^W q^2\right\} q^2 H > 0 \quad (3.41)$$

In Equations (3.40) and (3.41), the terms q, s, n, μ, k^W, k^G, γ_W, and γ_G are all positive, as well as the term $(s^2 - 2s + 1)$, because $s < 1$. Considering that the unit weight of the air is much smaller than the unit weight of the water ($\frac{\gamma_G}{\gamma_W} \approx 0.001$), we can reasonably assume that the term $(\gamma_W k^G s - \gamma_G k^W(1-s))$, is always positive for the typical permeabilities of the soils. This condition is satisfied by the water and air permeabilities used in the simulations.

The possibility for α_1^* and α_2^* to be negative depends on strain-hardening -softening parameter H, the values of A and B, strain ε, and strain rate $\dot{\varepsilon}$. Firstly, the hardening parameter decreases when the suction decreases; consequently, the slope of curve $H - P^C$ is positive, i.e., $A > 0$. Secondly, the saturation increases when the suction decreases, this means that the slope of curve $s - P^C$ is negative, i.e., $B < 0$. Then, the negative terms including B in α_1^* and α_2^* become positive and term BP^C in α_1^* becomes negative. Thirdly, strain ε is positive in tension and negative in compression, and strain rate $\dot{\varepsilon}$ can be positive or negative.

Now, let us consider the model when parameter H is positive, i.e., viscoplastic hardening. In this case, it is possible that α_1^* is negative. Thus, the onset of the instability of the material system appears. α_1^* and α_2^* can be negative in the following cases:

1. *Large B.* B is negative, hence when when B increases, term BP^C in α_1^* becomes negative more easily; namely, the possibility of instability is higher. In addition, if strain rate $\dot{\varepsilon}$ is negative, terms $-B\dot{\varepsilon}$ included in α_1^* and α_2^* become negative, and this increases the potential for instability.

2. *Large suction.* If P^C increases, term BP^C becomes more negative; consequently, α_1^* becomes negative more easily. The system is more unstable.

3. *Large A and negative strain* $\varepsilon < 0$. In this case, when A increases while the strain is negative, $\varepsilon < 0$ (compression), term $A\varepsilon$ is more negative. Consequently, there is a possibility for α_1^* to become more negative.

4. *Viscoplastic parameter* μ *and negative strain rate* $\dot{\varepsilon} < 0$. If the strain rate is negative, namely, compressive, term $\dot{\varepsilon}\mu$ in α_1^* becomes negative. Moreover, term α_1^* becomes more negative if the viscoplastic parameter is larger.

5. *Negative H.* In the case of viscoplastic softening, α_1^* and α_2^* can also be negative. Then, similar conditions exist for the onset of the instability of the material system.

Until now, the conditions for the onset of the instability of an unsaturated material system have been shown by means of an analytical analysis using a viscoplastic model and the linear instability analysis. From the analysis, it can be said that in both hardening and softening ranges, the onset of the instability of a material in a viscoplastic state mainly depends on terms BP^C and $A\varepsilon$, as well as strain rate $\dot{\varepsilon}$. In Section 3.3, the results of

various simulations of the one-dimensional infiltration problem will be presented in order to study the material instability by the model proposed in Section 2.3. The numerical analyses are based on the effect of the variation in parameters α and n', which controls the soil water characteristic curve as well as specific moisture capacity B (slope of the $SWCC$) and initial suction P_i^C. The effect of these parameters on the generation of volumetric strain ε is presented.

3.3 Numerical analysis by an elasto-viscoplastic model

3.3.1 Simulation of the one-dimensional infiltration problem

The finite element mesh and the boundary conditions for the simulations are shown in Figure 3.1. A homogeneous soil column with a depth of 1 m is employed in the simulations. An undrained boundary for water is assigned at the bottom and on the lateral sides of the column. Air flux is allowed both at the bottom and at the top of the column. The top of the column is subjected to a pore water pressure equal to 4.9 kPa. The simulations of the infiltration process start from an unsaturated condition where initial suction P_i^C is the same along the column. At t=0, water starts to infiltrate due to the pore water pressure applied at the top until a hydrostatic condition is attained in the column. Different values for parameter α, from α=0.1 to α=10 (1/kPa), and for parameter n', from n'=1.01 to n'=9.0, as well as two different levels of initial suction, P_i^C=25.5 (Case 1) and 100 kPa (Case 2), were considered to study the instability of the unsaturated material system. The material parameters required by the constitutive model introduced here are listed in Table 3.1. Figure 3.2 shows an example of the results for a time history of the pore water pressure distribution obtained by the simulations. This figure shows a transition of the soil from an initial unsaturated state (P_i^C=25.5 kPa) to a saturated state corresponding to the hydrostatic condition.

In the following sections, the discussion intends to show a trend in the deformation behavior of unsaturated soil as well as the consistency between the numerical results and the theoretical results obtained in Section 3.2. It is worth noting that the onset of the instability of the unsaturated viscoplastic material subjected to a wetting process can be interpreted as the sudden increase in compressive volumetric deformation during the numerical analysis. This compressive behavior (collapse behavior) can be attained if the soil presets an open potentially unstable unsaturated structure which can also be

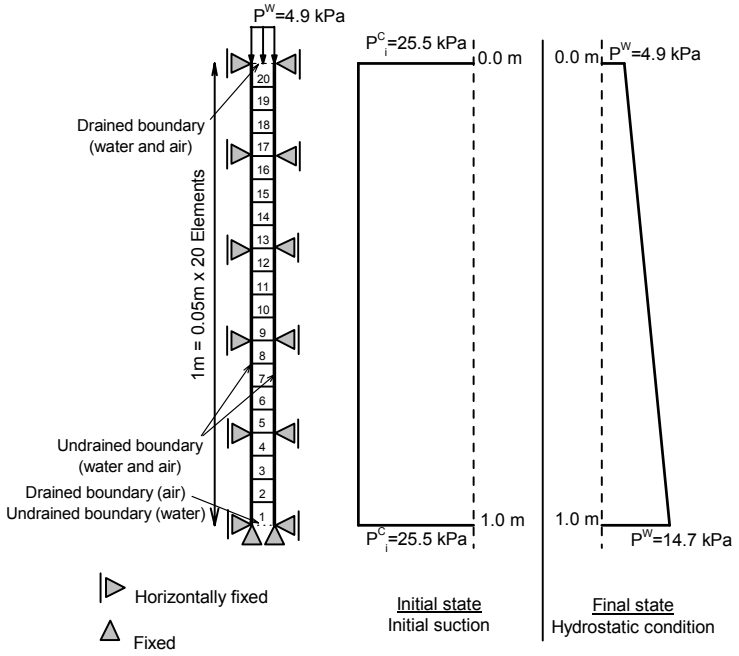

Figure 3.1 Finite element mesh and boundary conditions

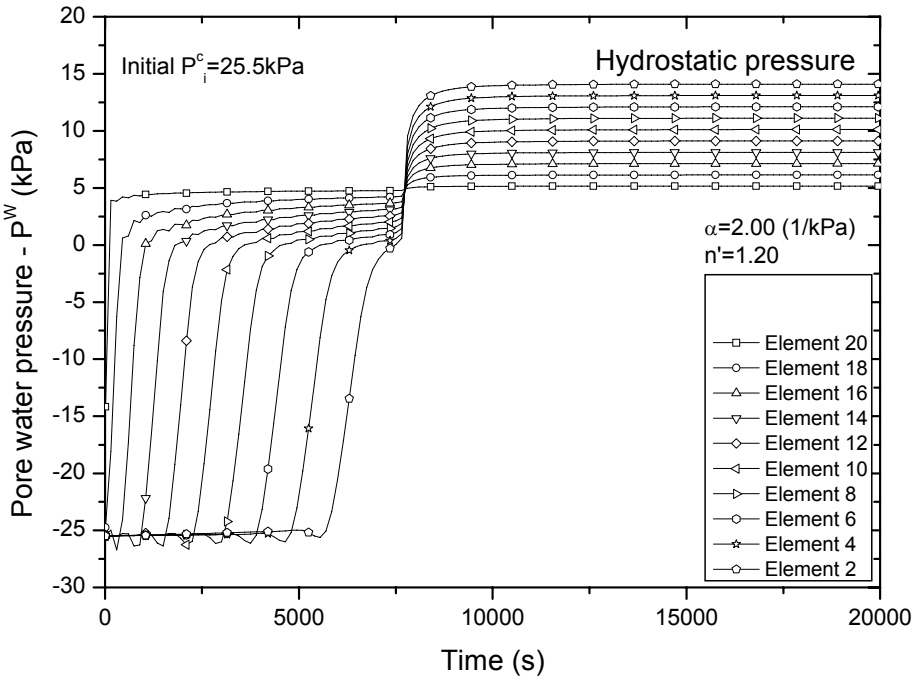

Figure 3.2 Time history of pore water pressure (α=2.00 1/kPa, n'=1.20, P_i^C=25.5 kPa)

Table 3.1 Material parameters for the simulations

Viscoplastic parameter	$m^{'}$	23.0
Viscoplastic parameter (1/s)	C_1	1.0 x 10^{-8}
Viscoplastic parameter (1/s)	C_2	1.0 x 10^{-8}
Stress ratio at critical state	M_m^*	0.947
Coefficient of water permeability at s=1.0 (m/s)	k_s^W	1.83 x 10^{-5}
Coefficient of air permeability at s=0.0 (m/s)	k_s^W	1.83 x 10^{-3}
Compression index	λ	0.136
Swelling index	κ	0.0175
Initial shear elastic modulus (kPa)	G_0	4000
Initial void ratio	e_0	0.5983
Structural parameter	β	0.0
Suction parameter	S_I	0.20
Suction parameter	S_d	0.25
Minimum saturation	s_{min}	0.0
Maximum saturation	s_{max}	0.99
Shape parameter of water permeability	a	3.0
Shape parameter of air permeability	b	2.3

attained when relatively high suction or applied stress exists (Barden et al., 1973; Lloret and Alonso, 1980; Wheeler and Sivakumar, 1995). Finally, in order to show the potentially stable and unstable regions of the one-dimensional infiltration problem, the results of the simulation will be plotted in the $\alpha - n'$ space, where the effect of the initial suction is also included.

3.3.2 Significance of the values for BP^C and $A\varepsilon$ on the onset of the instability of the unsaturated material

In Section 3.2, it was shown that the instability of the material system depends mainly on values BP^C and $A\varepsilon$ and strain rate $\dot{\varepsilon}$. Among these terms, $\dot{\varepsilon}$ depends on the deformation pattern of the soil during the infiltration process, and its effect on the onset of the instability of the unsaturated material will be addressed later (Section 3.3.5). To estimate which of the other two terms has a more significant effect on the onset of the instability of the material, the values corresponding to $A\varepsilon$ and BP^C, included in Equation (3.40),

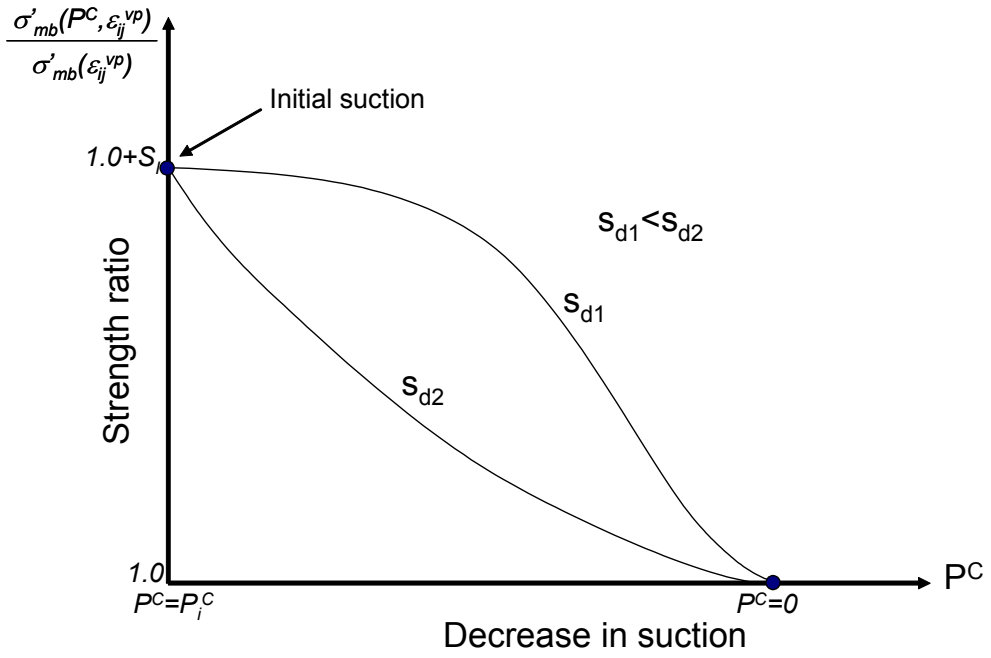

Figure 3.3 Strength degradation due to the decrease in suction

are investigated during the infiltration process. Firstly, the strength degradation due to the decrease in suction is shown schematically in Figure 3.3, and the relation between the strain-hardening parameter and the suction is given by Equation (2.29). From this equation, A is obtained as

$$A = \frac{\partial \sigma'_{mb}}{\partial P^C} = \sigma'_{ma} \exp\left(\frac{1+e_0}{\lambda-\kappa}\varepsilon_{kk}^{vp}\right) \left[S_I \exp\left\{-s_d\left(\frac{P_i^C}{P^C}-1\right)\right\}\right] \left[S_d \frac{P_i^C}{P^{C2}}\right] \tag{3.42}$$

In the same manner, the slope of the $SWCC$ can be obtained from Equations (2.45) and (2.46) as

$$B = \frac{\partial s}{\partial P^C} = -\alpha m n'(s_{max}-s_{min})(\alpha P^C)^{n'-1}\left\{1+(\alpha P^C)^{n'}\right\}^{-m-1} \tag{3.43}$$

In the analysis of the one-dimensional soil column, strain ε in Equation (3.40) corresponds to both the axial strain and the volumetric strain (ε=ε_x=ε_v). Using Equations (3.42) and (3.43), values $A\varepsilon_v$ and BP^C can be calculated. Figures 3.4 and 3.5 show comparisons of the time histories of values $A\varepsilon_v$ and BP^C, respectively, for different parameters α, namely, α=0.5. 1.0, 2.0, and 3.0 (1/kPa), with the same parameter n'=1.4 and with the

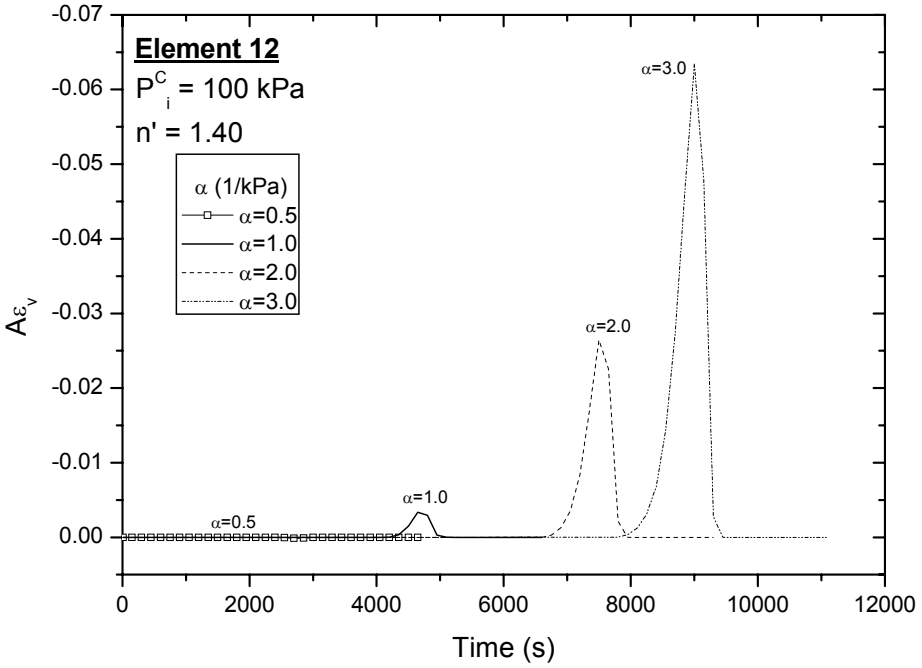

Figure 3.4 Time history of value $A\varepsilon_v$ for different parameters α

same initial suction P_i^C=100 kPa during the infiltration process. Figure 3.4 shows negative values for $A\varepsilon_v$ because the calculated volumetric strain is negative $\varepsilon_v < 0$ (compression). Similarly, Figures 3.6 and 3.7 show comparisons of the time histories of values $A\varepsilon_v$ and BP^C, respectively, for different parameters n', namely, n'=1.1, 1.2, 1.3, 1.4, 1.5, and 1.6, with the same parameter α=1.0 (1/kPa) and with the same initial suction P_i^C=100 kPa. In Figure 3.6 positive values for $A\varepsilon_v$ indicate positive volumetric strain $\varepsilon_v > 0$ (expansion) and negative values for $A\varepsilon_v$ when $\varepsilon_v < 0$ (compression). Figures 3.4 and 3.6 show that negative values for $A\varepsilon_v$ increase when parameters α and n' increase. However, they are smaller than the negative values obtained for BP^C (see Figures 3.5 and 3.7). This means that the effect of term BP^C on the onset of the instability of the material is more significant. Accordingly, it can be said that the onset of the stability of the unsaturated elasto-viscoplastic material in an infiltration process depends mainly on specific moisture capacity B and suction P^C.

In the following section, the effect of B and P^C on the development of volumetric strain will be studied.

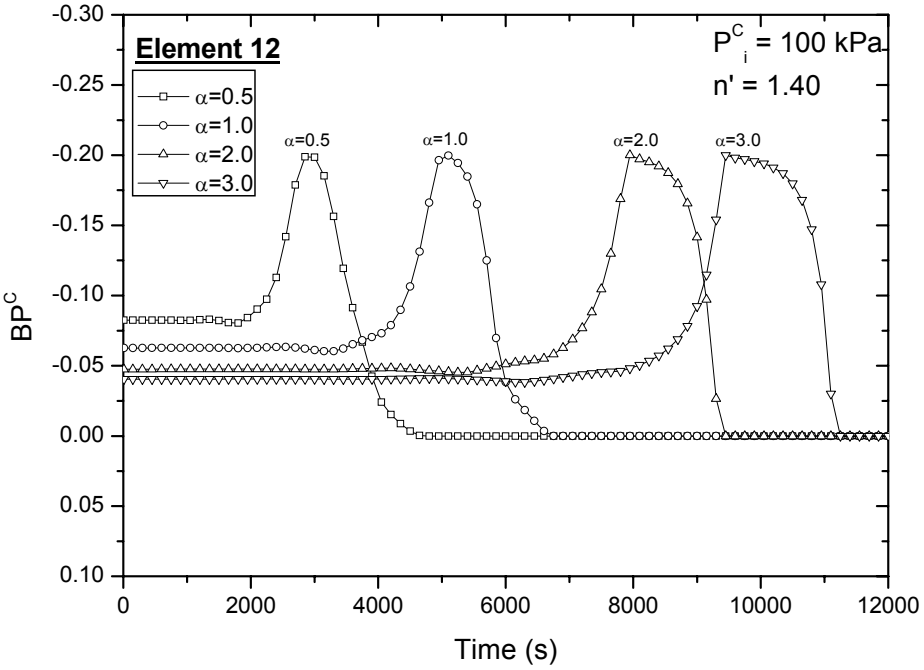

Figure 3.5 Time history of value BP^C for different parameters α

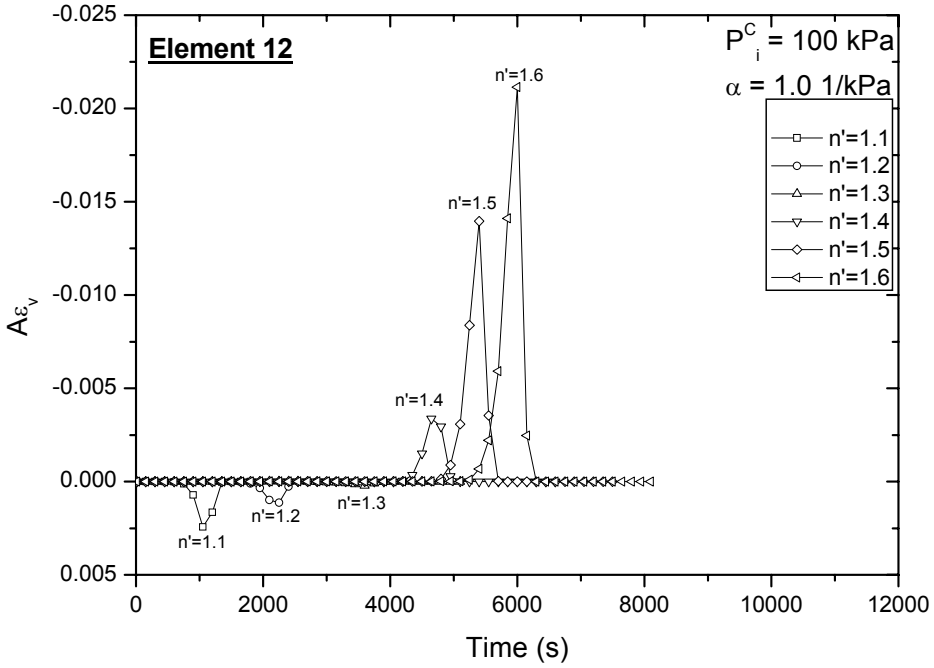

Figure 3.6 Time history of value $A\varepsilon_v$ for different parameters n'

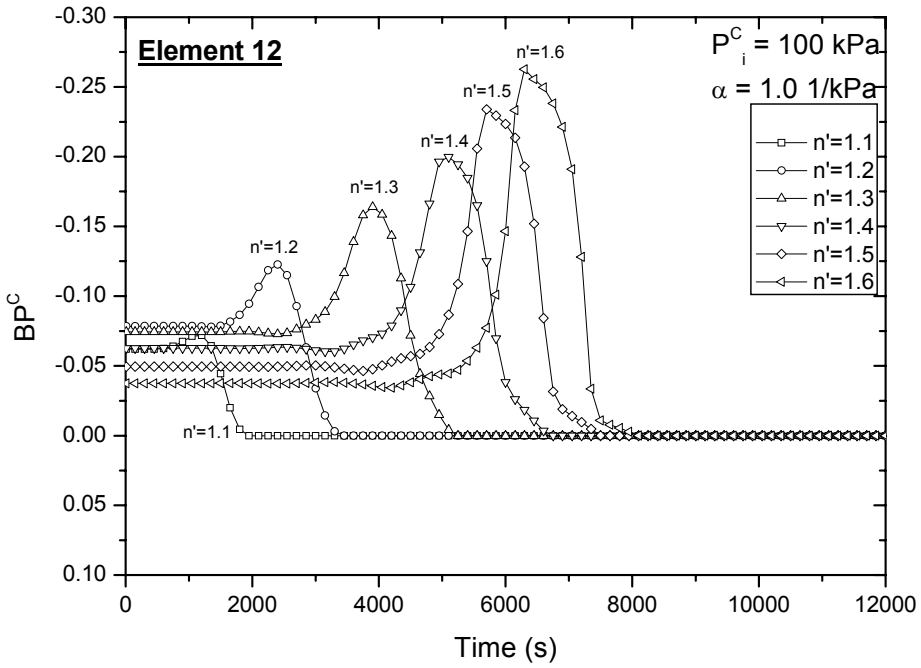

Figure 3.7 Time history of value BP^C for different parameters n'

3.3.3 Effect of specific moisture capacity B on the instability of the unsaturated material

From Equations (2.45) and (2.46), it is seen that the $SWCC$ is mainly controlled by parameters α and n'. These parameters control the shape of the $SWCC$. Parameter α is related to the air-entry value condition, which is the suction value at which the maximum saturation (99% is assumed in the simulations) starts to decrease due to the incoming of air into the soil. Parameter n' is related to the pore size distribution of the soil. Figure 3.8 illustrates the effect of parameter α on the air-entry value and the $SWCC$ for constant parameter n'. This figure shows that when parameter α increases, the air-entry value decreases. Soils with relatively high air-entry values, e.g., clays, are characterized by smaller values for α. Similarly, Figure 3.9 illustrates the effect of parameter n' on the $SWCC$ for constant parameter α. In this figure, it is seen that the soil water characteristic curve becomes steeper for the larger values of n'; soils with steeper curves, e.g., sands, are represented by larger parameters n'.

According to the instability analysis presented in Section 3.2 and using a multiphase viscoplastic model, the material system can be unstable if the magnitude of B, which corresponds to the slope of the soil water characteristic curve ($B = \partial s/\partial P^C$), increases.

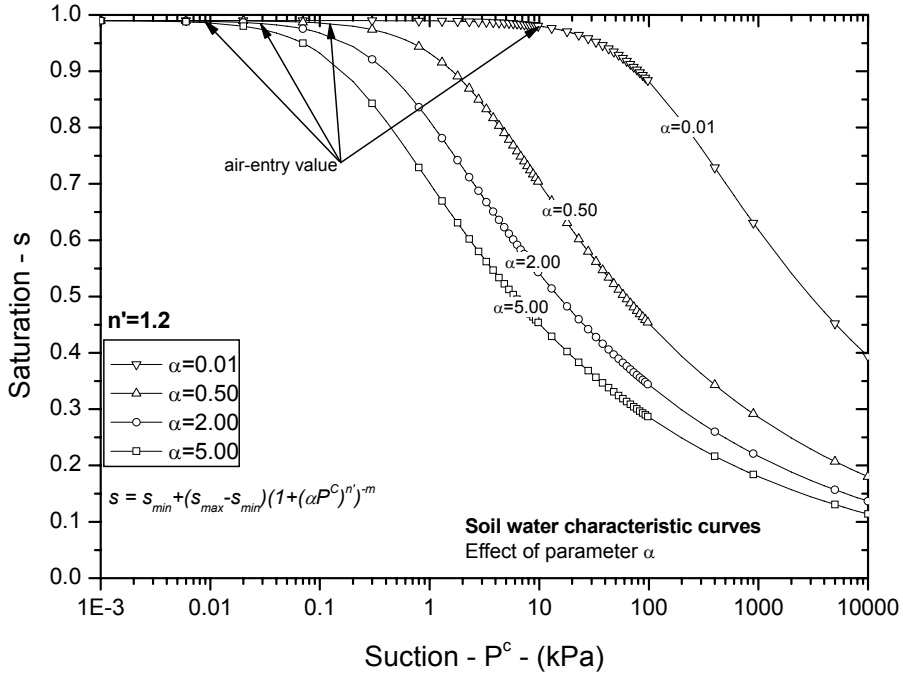

Figure 3.8 Effect of parameter α on the soil water characteristic curve

In the formulation presented in Section 2.3, B plays an important role in the continuity equations for both water and air phases. In addition to the $SWCC$, B (in Equation 3.43) is also mainly controlled by parameters α and n' and current suction P^C.

In the following, a discussion on the effect of parameters α and n' and suction P^C on the development of the volumetric strain is presented. It is worth noting that the potential for the instability of the unsaturated viscoplastic material subjected to infiltration will be interpreted as the increase and divergence of the deformation.

3.3.3.1 Effect of parameter α on specific moisture capacity B and volumetric strain ε_v

Figure 3.10 shows the variation in B due to the changes in suction for different α values when n'=1.4. This figure shows that the value of B is smaller for the higher values of suction. However, when the suction starts to decrease, the value of B increases until it reaches a maximum peak that depends on the α value; the larger the parameter α, the greater the peak for B. After this peak, the value of B starts to decrease toward zero for P^C=0.

Five different values are considered for parameter α to show its effect on the water

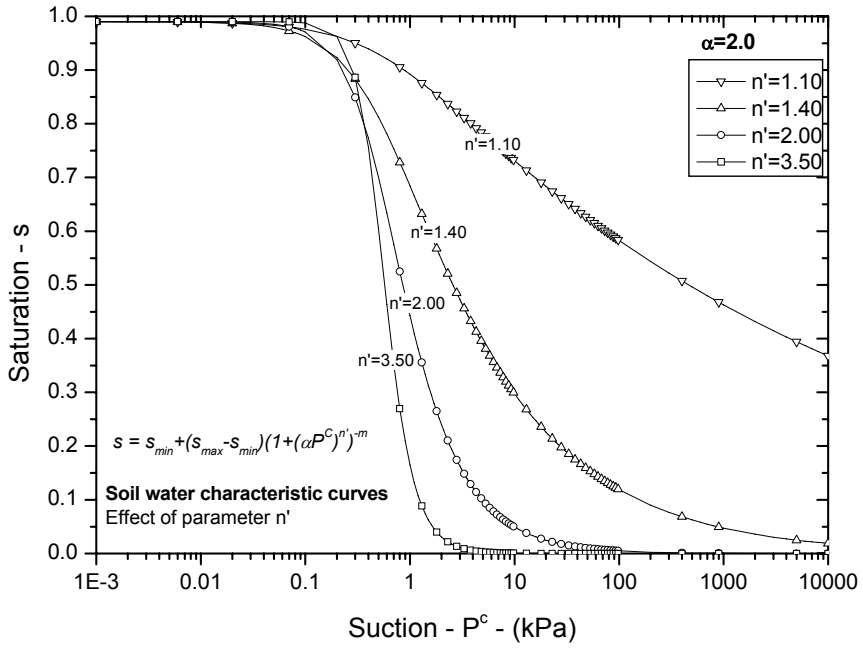

Figure 3.9 Effect of parameter n' on the soil water characteristic curve

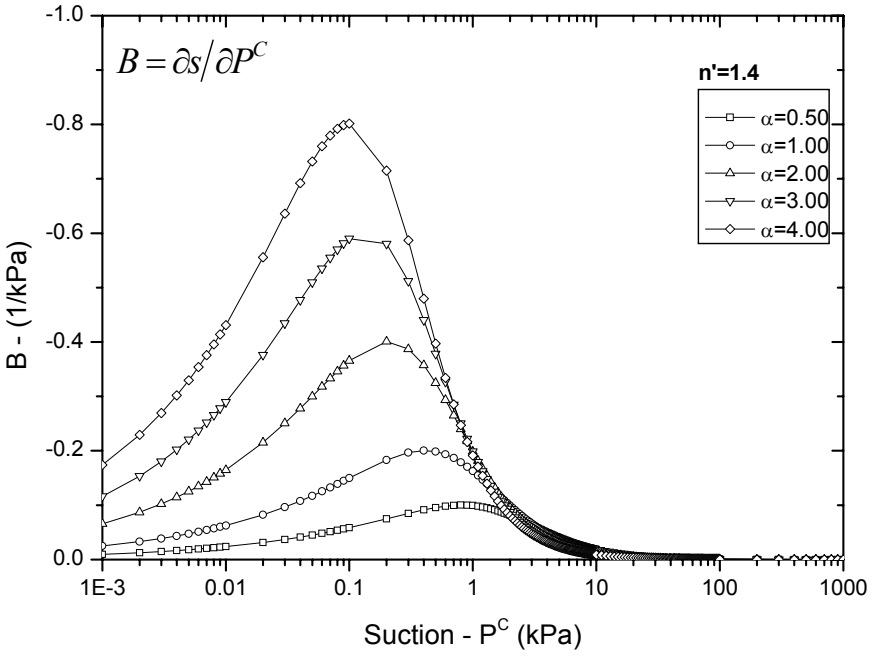

Figure 3.10 The influence of parameter α on the variation in B $(\partial s/\partial P^C)$

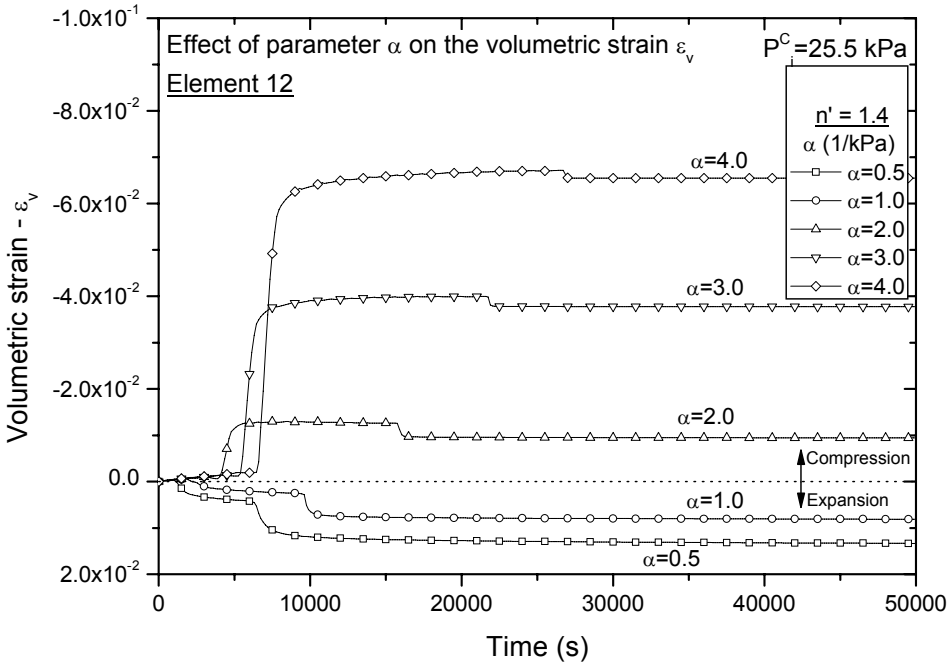

Figure 3.11 The influence of parameter α on the development of volumetric strain (P_i^C=25.5 kPa)

infiltration process and the development of volumetric strain (α=0.5, 1.0, 2.0, 3.0, and 4.0 1/kPa). Figure 3.11 shows the effect of parameter α on the development of volumetric strain ε_v for Element 12 (in Figure 3.1) when the material is subjected to infiltration from an initial suction, P_i^C=25.5 kPa (Case 1). From this figure, it is seen that the volumetric strain changes from expansive to compressive when parameter α increases. A similar trend is observed for Case 2 (Figure 3.12), in which the initial suction is P_i^C= 100 kPa. The increase in parameter α means an increase in B and an increase in the compressive (contractive) behavior of the soil, and therefore, the potential for instability. These numerical results are consistent with the theoretical results obtained in the linear instability analysis in Section 3.2, where it was shown that the onset of instability increases when B and the compressive strain increase. This means that soils with greater parameters α are potentially more unstable than soils with smaller parameters α.

3.3.3.2 Effect of parameter n' on specific moisture capacity B and volumetric strain ε_v

The effect of parameter n' on the variation in B is similar to the effect of parameter α. Figure 3.13 shows the variation in the specific moisture capacity due to the changes in suction for different n' values at the same value of α=1.0 (1/kPa). From the figure, it is

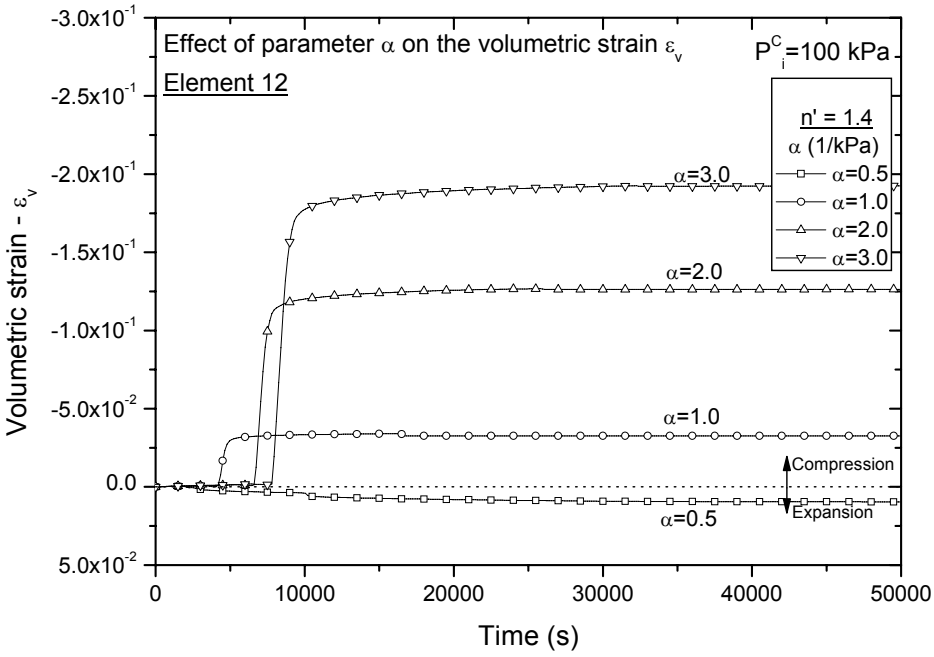

Figure 3.12 The influence of parameter α on the development of volumetric strain (P_i^C=100 kPa)

seen that the value of B is smaller for higher values of suction. However, when the suction starts to decrease, the value of B increases and reaches a maximum peak that depends on the n' value; the greater parameter n', the greater the peak of B. After this peak, the value of B starts to decrease toward zero for P^C=0.

Figures 3.14 and 3.15 describe the effect of parameter n' on the development of volumetric strain ε_v in Element 12 in Figure 3.1 during the infiltration process for the two different cases, P_i^C=25.5 and 100 kPa, respectively. Five different values for parameter n' are used in order to observe their effect on the water infiltration process, namely, n'=1.2, 1.3, 1.4, 1.5, and 1.6, with α=1.0 (1/kPa). In the case of P_i^C=25.5 kPa (Figure 3.14), the volumetric strain is changing from positive volumetric strain (expansion) at smaller values of n' to negative volumetric strain (compression) at greater values of n'. The same trend is observed in the case of P_i^C=100 kPa (Figure 3.15). Similarly to the effect of parameter α, the trend for greater compressive deformations is obtained for the greater n' values. An increase in parameter n' means an increase in B and the compressive behavior of the soil, thus, the potential for instability. This is consistent with the theoretical results obtained in the linear instability analysis in Section 3.2, where it was shown that the instability increases when B increases and the volumetric strain is compressive. It can

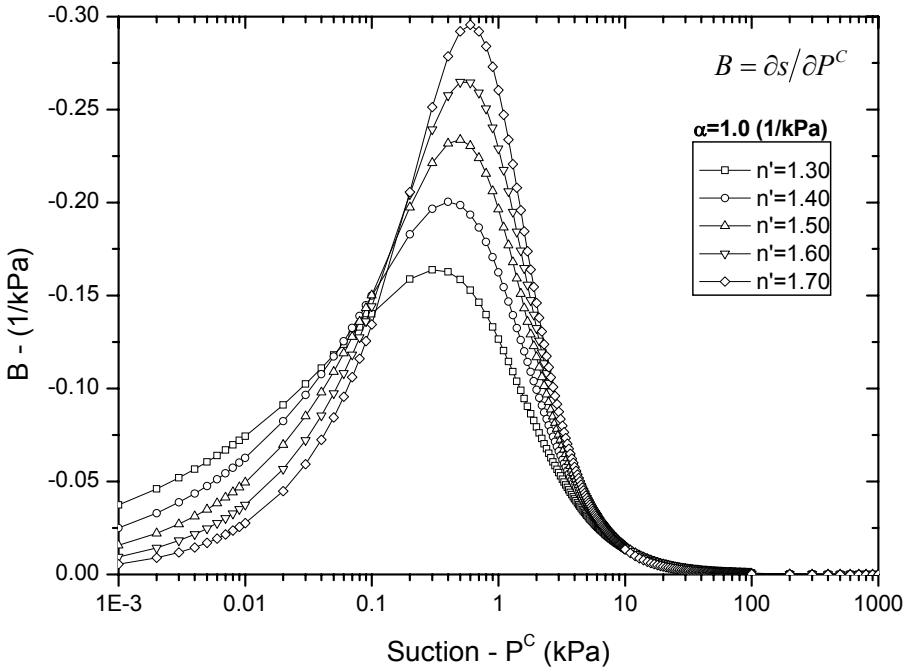

Figure 3.13 The influence of parameter n' on the variation in B ($\partial s/\partial P^C$)

be said that, during the infiltration process, unsaturated materials with smaller n' values are less unstable than those with greater n' values.

3.3.4 Effect of initial suction P_i^C on volumetric strain ε_v

Suction is a main variable related to unsaturated soils. It has a direct effect on the stress variables, the soil water characteristic curve, the hydraulic conductivity, and the deformation characteristics. From the instability analysis presented in Section 3.2, it is seen that suction P^C has an additional effect on the stability since it is included in A and B. The results of the instability analysis shown in Equation (3.40) suggest that a material with a greater initial suction P_i^C is expected to contribute more to the onset of instability than a material with a smaller initial suction.

Figures 3.16 and 3.17 show the time histories of volumetric strain for two different parameters, α=1.0, 2.0 (1/kPa), respectively. On these graphs, a comparison is made for the two different levels of initial suction (P_i^C=25.5 and 100 kPa), while parameter n' is increased. From the figures, it is seen that the trend for greater compressive volumetric strain is obtained for the greater initial suction (P_i^C=100 kPa) when the same parameter n' is compared. This implies that the compressive strain develops prominently during the

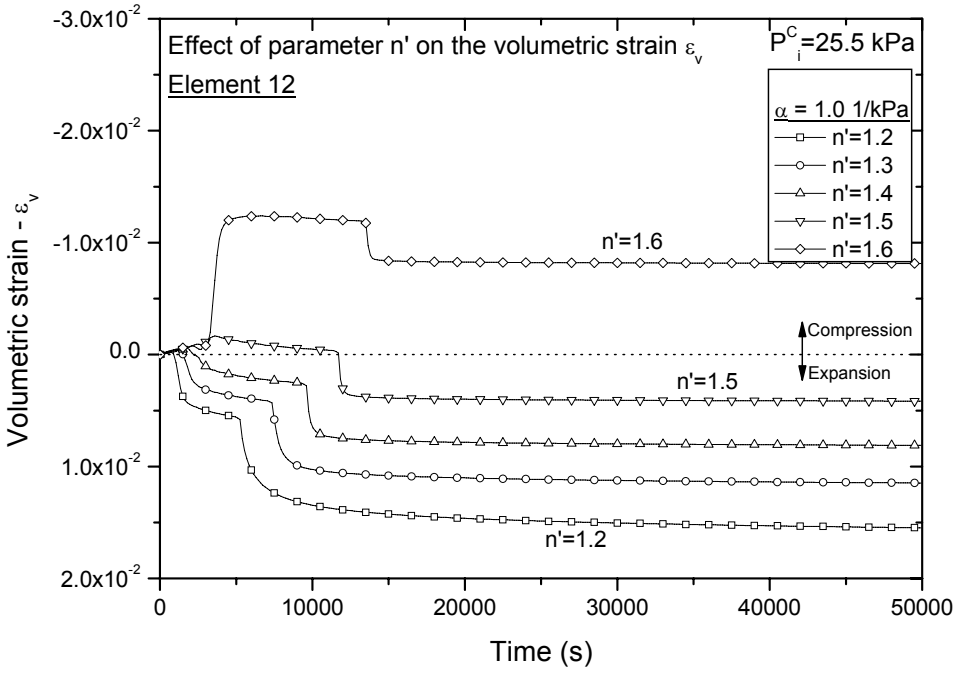

Figure 3.14 The influence of parameter n' on the development of volumetric strain (P_i^C=25.5 kPa)

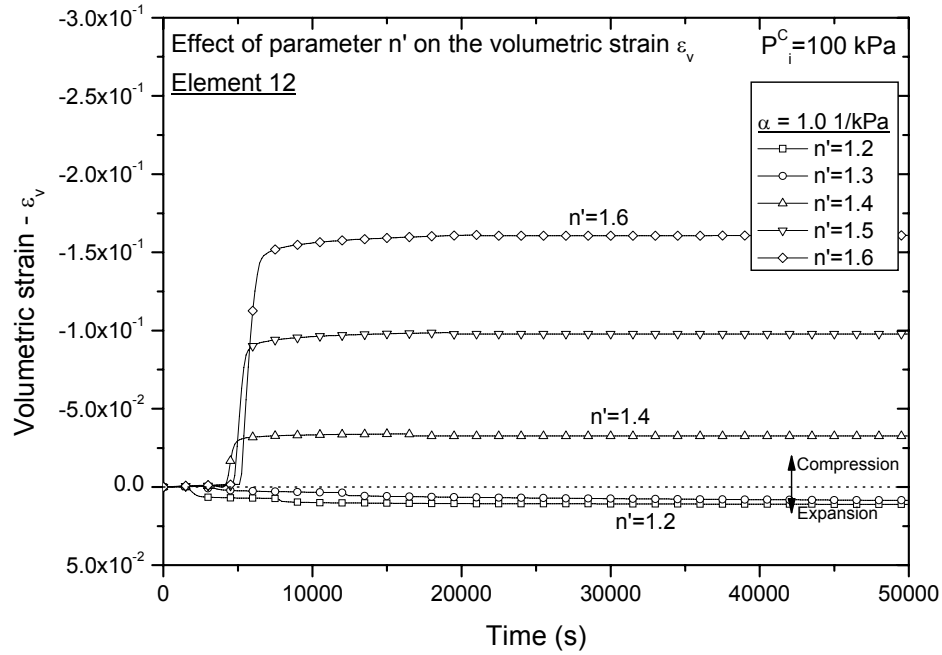

Figure 3.15 The influence of parameter n' on the development of volumetric strain (P_i^C=100 kPa)

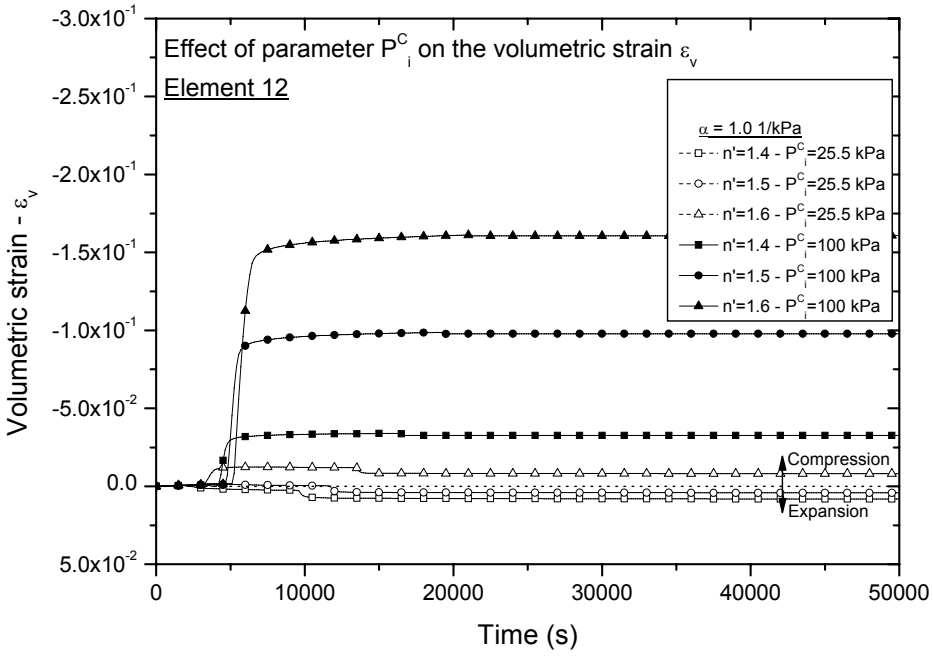

Figure 3.16 The influence of initial suction P_i^C on the development of volumetric strain (α=1.0 1/kPa)

wetting process when unsaturated materials present higher suctions. This is consistent with the theoretical results obtained in the instability analysis, namely, an increase in suction leads to an increase in the onset of the instability of the material system. It can be said that in a wetting process, the unsaturated materials with smaller suction values are less unstable than those with greater suction values.

3.3.5 Summary of the simulation results

Firstly, the results of the calculated settlements at the top of the soil-column and at the end of the infiltration process for different parameters α and n' and initial suction P_i^C=25.5 kPa are shown in Figure 3.18. Figure 3.18 indicates that for each parameter α, the initial behavior of the soil is expansive for the smaller n' values. When parameter n' is large, however, the behavior changes to be compressive (except for α=0.10 (1/kPa)). Two different types of numerical instability are observed during the simulation process for the cases when P_i^C=25.5 kPa:

1. For the cases when α=0.10 to 4.00 (1/kPa), the settlement increases with the increase in parameter n' until the peak where the settlement starts to decrease and changes to swelling. The rate of change from compressive to expansive behavior is

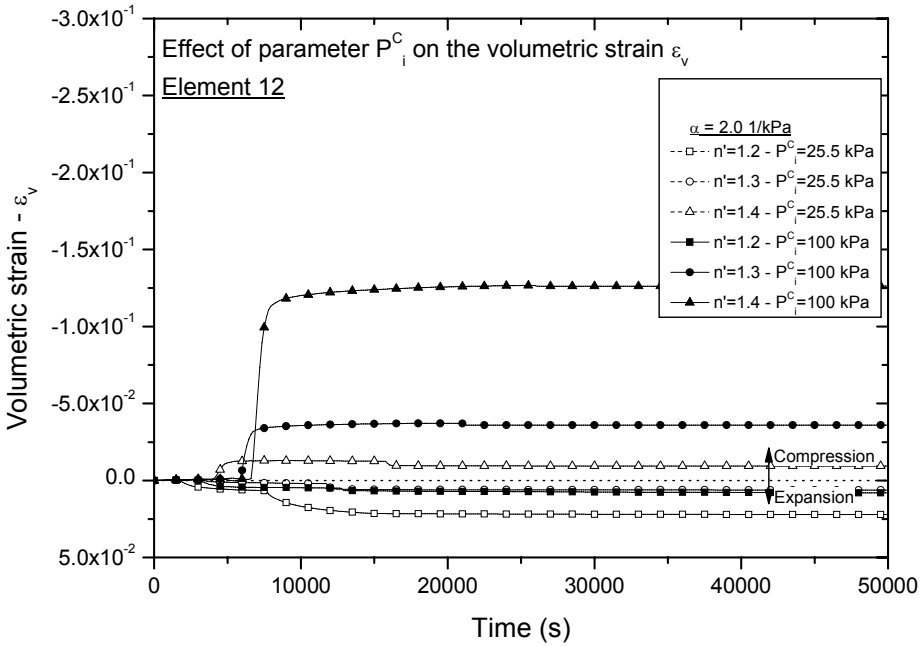

Figure 3.17 The influence of initial suction P_i^C on the development of volumetric strain (α=2.0 1/kPa)

larger for the larger α values. For n' values larger than those shown by the solid square (■) in Figure 3.18, the numerical instability emerged due to an abrupt transition from the unsaturated to the saturated state presented at the very beginning of the calculation. In these cases, the numerical instability is apparently triggered by the rapid saturation in the soil column due to the larger values of the specific moisture capacity (owing to the larger n' values) which leads to the generation of a large expansive deformation in the soil column. The numerical instability for the simulation with constant α=0.1 (1/kPa) was attained when n'=8.5.

2. In the cases of greater parameters, namely, α=6.0, 8.0 and 10.0 (1/kPa), the numerical instability occurred at the compressive side after the settlement reached a value between 0.15 and 0.20 m. From Figure 3.18, it is also possible to see that the rate of deformation increases when parameter α increases.

Similarly, Figure 3.19 shows the calculated settlements for the case of the initial suction P_i^C=100 kPa; similar behavior to that observed in the case of initial suction P_i^C=25.5 kPa for the larger parameters α is shown. The numerical instability is attained after the settlement reached values in between 0.15 and 0.20m, the settlement increases with an increase in parameters α and n'. In this case, however, the deformation rates are larger

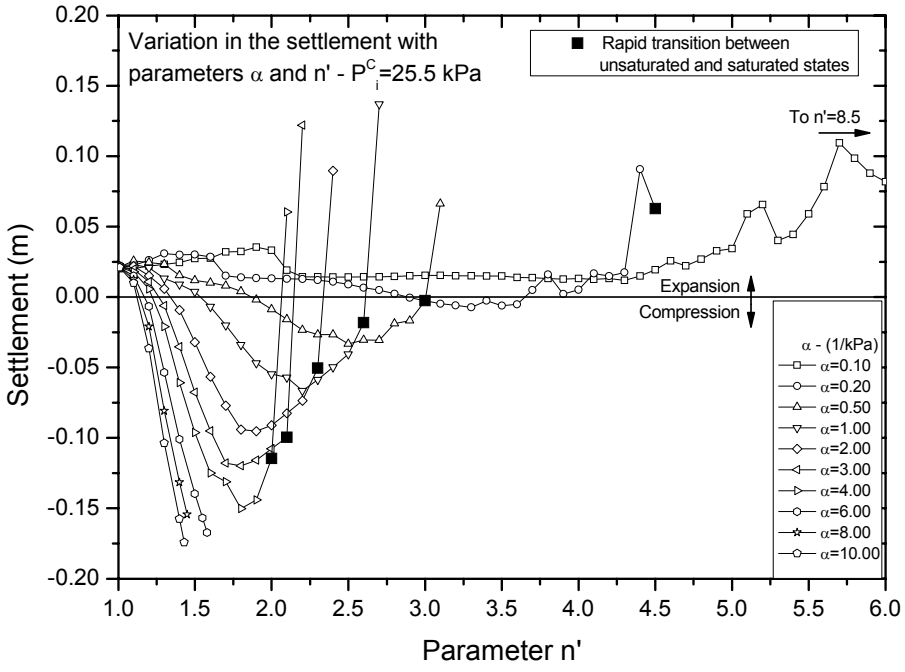

Figure 3.18 Variation in the settlement with parameters α and n' (P_i^C=25.5 kPa)

and the instability always occurred at the compressive side. This suggests that soils with higher levels of suction are prone to be unstable due to the highly compressive behavior triggered by a wetting process. In this case, where the compressive behavior increases, both volumetric strain ε_v and strain rate $\dot{\varepsilon}$ are negative. As a result, and according to Equations (3.40) and (3.41), the potential for instability increases. The results in Figures 3.18 and 3.19 are consistent with the instability results obtained in Section 3.2, where it was found that the onset of instability increases if the behavior of the material is compressive and both specific moisture capacity B and suction P^C increase.

In the simulations, the numerical instability is reached after a large compressive deformation is obtained. As a result, the numerical calculation abruptly ends due to the large increase in the deformation.

The results of the simulations described in Subsection 3.3.1 are summarized in a stability chart in order to observe the potentially stable region for the one-dimensional water infiltration problem. Figures 3.20 and 3.21 show the results of the simulation for different values of parameters α and n' and for the initial levels of suction P_i^C=25.5 and 100 kPa, respectively. In these figures, the solid circle (•) indicates the stable simulation results, while the **x** indicates the numerically unstable simulation results (large increase

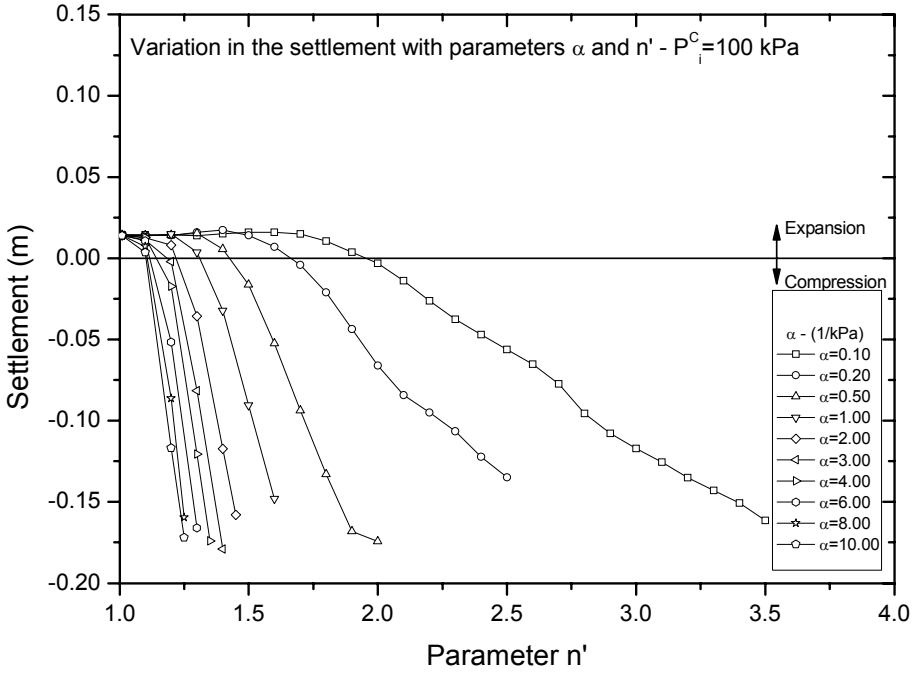

Figure 3.19 Variation in the settlement with parameters α and n' (P_i^C=100 kPa)

in the compressive volumetric deformation). On the graphs, the boundaries between the numerically-stable and -unstable regions (continuous line) and the boundary between expansive and compressive behaviors (dashed line) are shown. From Figures 3.20 and 3.21, the following characteristics can be understood:

1. The expansive behavior is presented for materials with smaller parameters α and n', but the compressive behavior is obtained when these parameters increase.

2. For the same parameter α, the potential for instability increases when parameter n' is large. A larger parameter n' leads to an increase in B and an increase in the deformation.

3. For the same parameter n', the instability potential increases when parameter α becomes large. This larger parameter α leads to an increase in B; and consequently, to an increase in the deformation.

4. It is possible to see that the material stable-unstable boundaries and the expansive-compressive boundaries shrink as the suction increases. It happens when P_i^C is changed from 25.5 kPa to 100 kPa.

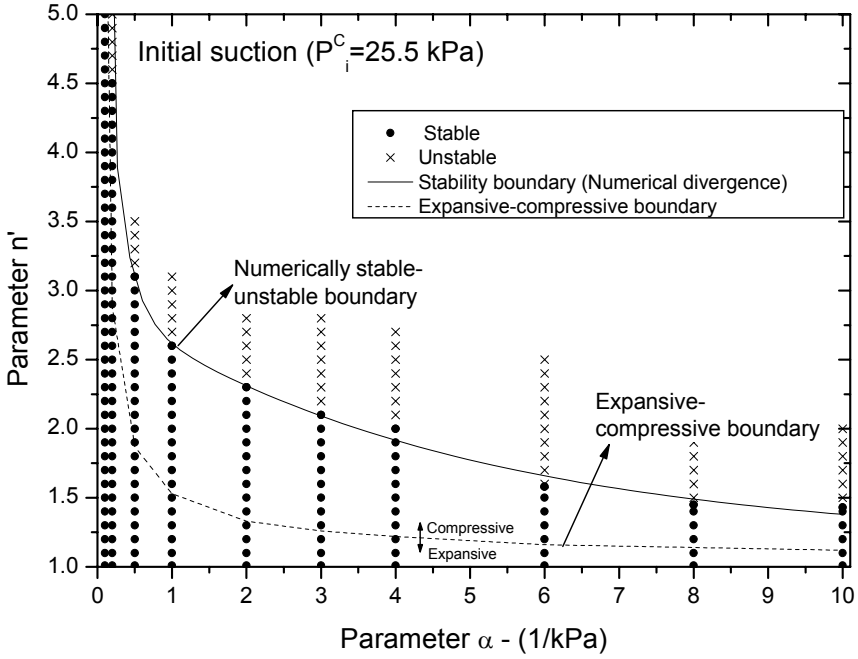

Figure 3.20 Stable and unstable regions for parameter α and n' during the infiltration process (P_i^C=25.5 kPa)

5. The instability obtained by the numerical analyses is consistent with the theoretical results obtained by the linear instability analysis presented in Section 3.2.

According to the instability results, it can be said that unsaturated soils that are prone to instability during a wetting process are those with higher levels of initial suction, e.g., clays, as well as soils that are represented by a steeper soil water characteristic curve, e.g., sands.

3.3.6 Stress paths and strain-time responses during wetting

In the simulation of the one-dimensional infiltration problem, the soil column is considered to be in its initial state with constant suction. The initial mean skeleton stress and the initial saturation are different, however, because different van Genuchten parameters (α and n') are used in each simulation. Now, in Figure 3.22, we will examine the effect of n' in detail by the stress paths ($\sqrt{2J_2} - \sigma'_m$) for Element 12, for three values of parameter n', n'=1.4, 2.0, and 2.9, with the other parameters being held constant, namely, α=1.0 1/kPa and P_i^C=25.5 kPa. The cases of n'=1.4 and 2.0 correspond to the stable region, while the case of n'=2.9 is on the unstable region, in Figure 3.20. In the case of n'=1.4, it is seen

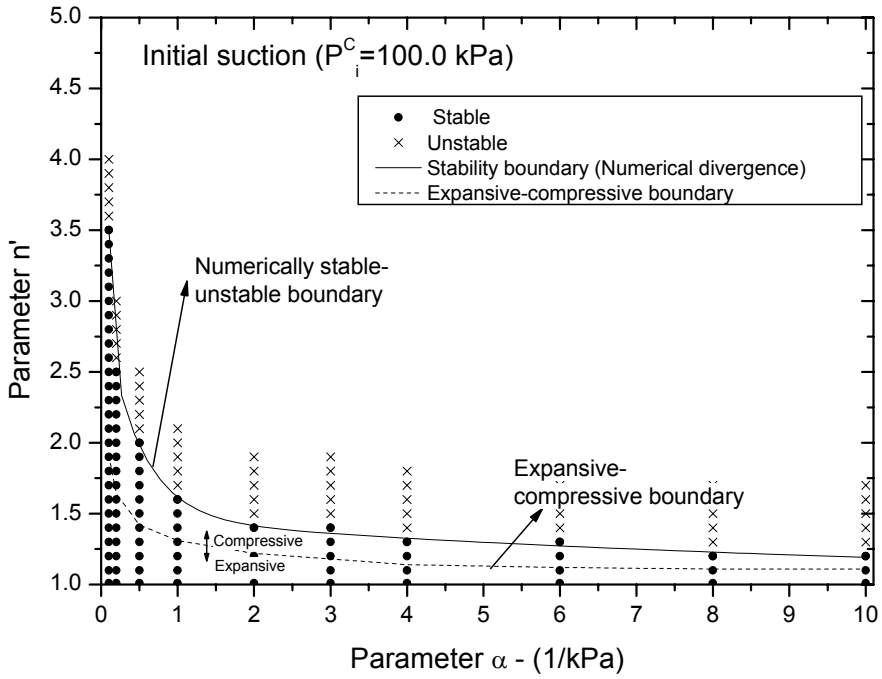

Figure 3.21 Stable and unstable regions for parameter α and n' during the infiltration process (P_i^C=100 kPa)

that the stress path follows a direction toward the critical state line (A-A'-A"), whereas for n'=2.0, the stress path initially goes in the opposite direction during the unsaturated state (B-B') and then returns toward the critical state line in the saturated state (B'-B"). When n'=2.9, it is seen that the stress path approaches the critical state line and reaches the state with almost zero deviator stress. After that, the path goes to C" (C-C'-C").

The saturation-mean skeleton stress relations, which correspond to Figure 3.22, are presented in Figure 3.23. This figure shows that the larger the parameter n', the smaller the initial saturation, namely, points A, B, and C. The initial saturation significantly affects the initial mean skeleton stress because the mean skeleton stress depends on the saturation that is included in the calculation of the average pore pressure, as shown in Equations (2.22) and (2.24). For the same suction, the larger the saturation, the smaller the average pore pressure; hence, the initial mean skeleton stress is large. Figure 3.23 also shows that for the case of n'=2.9, once full saturation has been attained, the mean skeleton stress decreases and then increases (C'-C"). Figure 3.24 illustrates the suction-mean skeleton stress relations. As shown in Figure 3.24, for the same initial suction, the values for the initial mean skeleton stress are different at points A, B, and C. The larger the value of n', the smaller the initial mean skeleton stress. During the infiltration

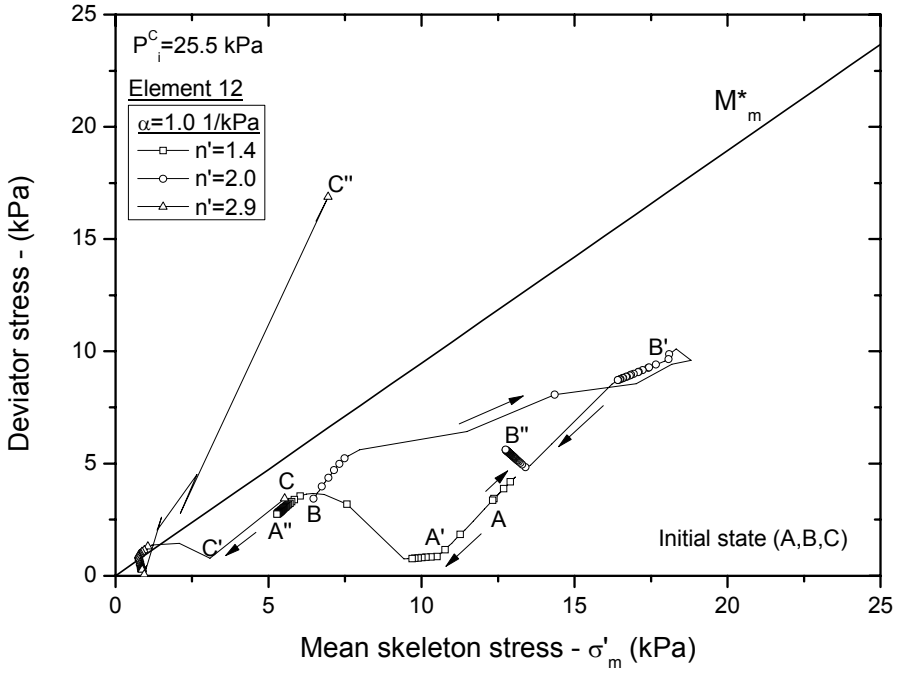

Figure 3.22 Stress path during the wetting process - $\sqrt{2J_2} - \sigma'_m$ space (P_i^C=25.5 kPa)

process, when the water reaches the element, the suction starts to decrease and the mean skeleton stress decreases or increases depending on the value of n'. For n'=1.4, the mean skeleton shows a small decrease in the unsaturated state (A-A'), while for n'=2.0, the mean skeleton stress increases (B-B'). In the case of n'=2.9, the mean skeleton stress reduces with the reduction in suction and then finally increases (C-C'-C").

The accumulated viscoplastic shear strain (γ^{vp})-time histories are shown in Figure 3.25. It is observed that the development of irrecoverable deformation is very small for the parameter n'=1.4. For the larger value of n'=2.0, however, the accumulated viscoplastic shear strain develops prominently during the transition of the material from the unsaturated state to the saturated state up to γ^{vp}=10.3%. For the case of n'=2.9, the accumulated viscoplastic shear strain develops from the beginning of the process until it reaches a value of 3%, and it remains almost constant before suddenly increasing. This indicates that large irrecoverable deformation has developed in the soil column. Similarly, the time histories of the volumetric strain are shown in Figures 3.26. The development of the volumetric deformation in time indicates that different responses of the column are obtained during the wetting process for different parameters n'. For n'=1.4, the volume increases slightly due to the decrease in mean skeleton stress, mainly because of the

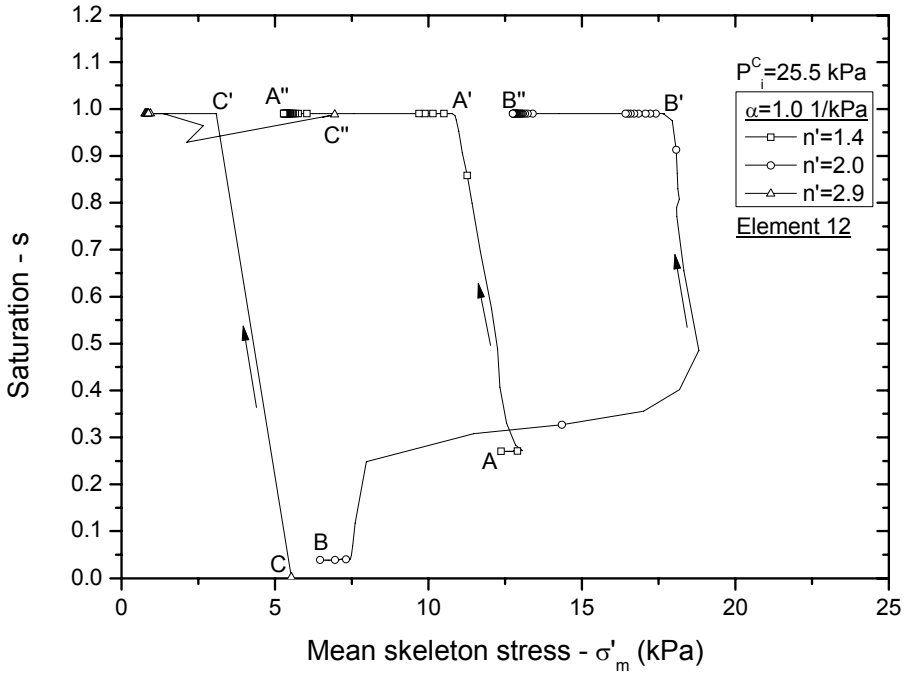

Figure 3.23 Saturation - mean skeleton stress relation - $s - \sigma'_m$ space (P_i^C=25.5 kPa)

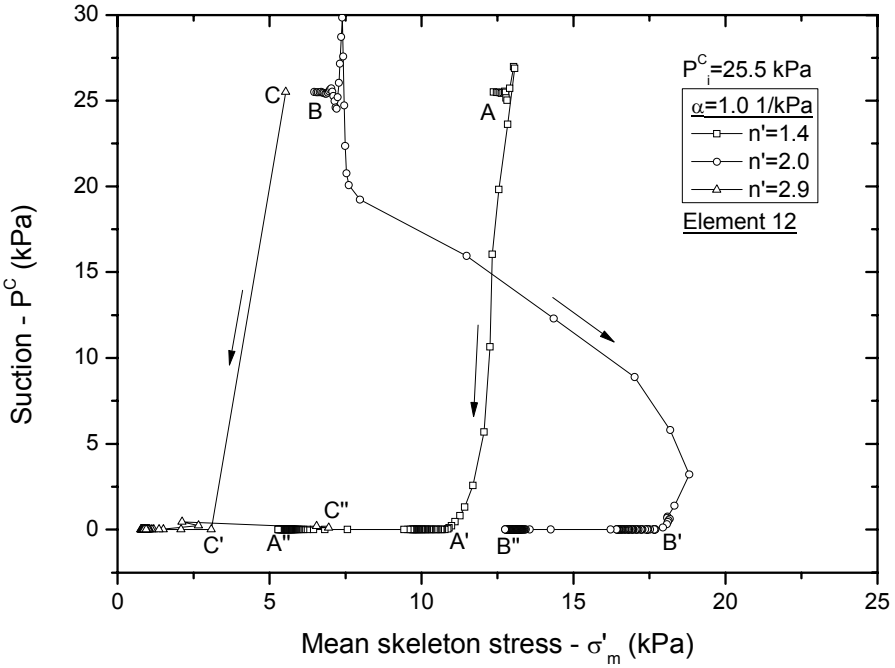

Figure 3.24 Suction - mean skeleton stress relation - $P^C - \sigma'_m$ space (P_i^C=25.5 kPa)

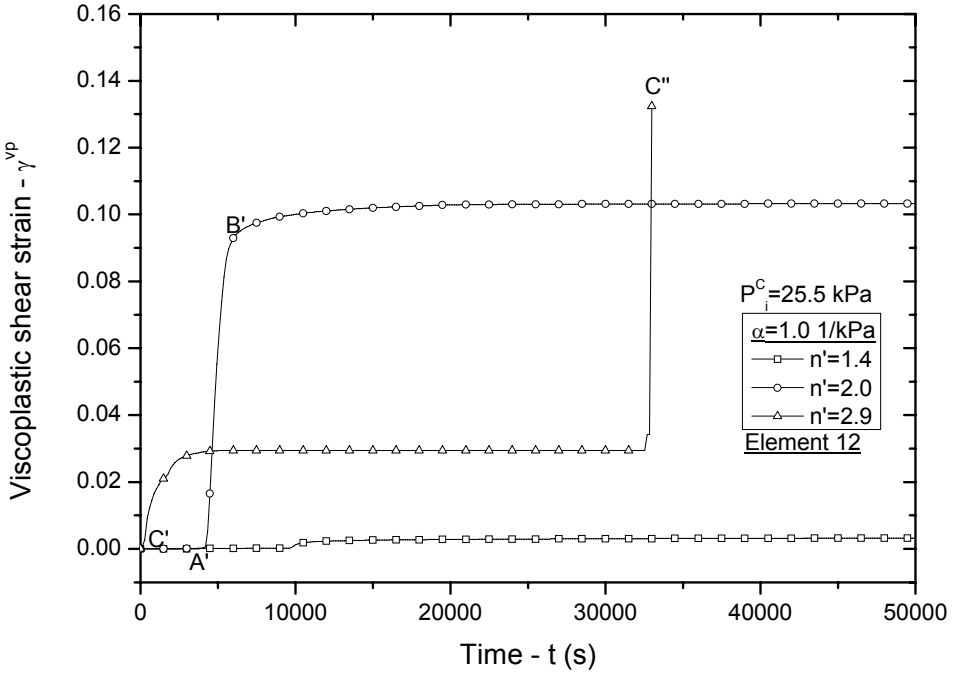

Figure 3.25 Time history of viscoplastic shear strain (P_i^C=25.5 kPa)

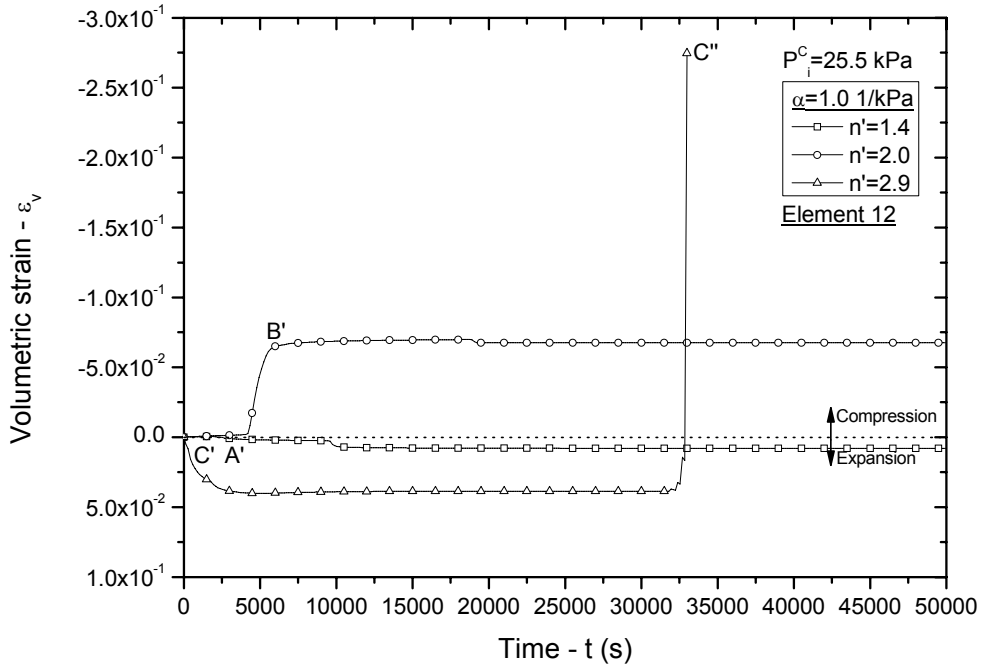

Figure 3.26 Time history of volumetric strain (P_i^C=25.5 kPa)

increase in pore water pressure. For n'=2.0, however, the volume decreases due to the increase in mean skeleton stress, mainly because of the increase in the total stress. In the case of n'=2.9, it is seen that the volume increases at the beginning of the process, and it remains constant for some time before an abrupt change to large compression. The increase in volumetric strain at the beginning of the simulation can be explained by the rapid saturation of the soil owing to a steeper soil water characteristic curve represented by the larger parameter n'. This significant transition also leads to the diminution of the mean skeleton stress with suction, namely, C-C' in Figure 3.24.

From the above discussion using Figures 3.22-3.26, it is seen that a larger value of n', i.e., a steeper suction-saturation characteristic curve, leads to the development of larger strain. This result is consistent with the instability analysis presented in Section 3.2. In addition, it is worth noting that compressive volume strain occurs when large strain develops, namely, for the case of relatively unstable behavior (Barden et al., 1973; Lloret and Alonso, 1980; Wheeler and Sivakumar, 1995).

3.3.7 Summary

In order to study the effects of parameters and state variables on the instability of an unsaturated material system during a wetting process, a theoretical analysis was conducted with a simplified viscoplastic model. It was found that in both hardening and softening ranges, the occurrence of the instability of an unsaturated material system is more likely (the rate of the fluctuation grows) if suction P^C and specific moisture capacity $B = \partial s/\partial P^C$ increase. Moreover, the onset of instability can be increased if the strain rate is negative ($\dot{\varepsilon} < 0$), and the behavior of the material is compressive ($\varepsilon < 0$), while the slope of curve $\sigma'_{mb} - P^C$ ($A = \partial\sigma'_{mb}/\partial P^C$) increases. It was also found that the effect of the specific moisture capacity and the suction is more significant than the effect of the slope of curve $\sigma'_{mb} - P^C$.

From the numerical study on the one-dimensional infiltration problem, it was found that the elasto-viscoplastic material system is more unstable when parameters α and n' are large, namely, for large values of the slope of the soil water characteristic curve (specific moisture capacity). For the effect of the suction, it is observed that the instability significantly increased when the initial suction of the unsaturated material is increased (P_i^C=25.5 to 100 kPa). These trends are consistent with the theoretical results obtained by the linear instability analysis.

The simulated settlements show that for smaller parameters α and n', the material behavior is expansive. Nevertheless, when these parameters become large, the expansive behavior of the soils changed to a compressive one. Parameters α and n' indicate a great effect on the development of the deformation. The greater the parameters α and n', the larger the settlements obtained. Larger rates of settlement were also obtained for higher levels of initial suction. This suggests that rapid transitions from unsaturated to saturated states and higher levels of suction lead to compressive behavior and instability; e.g., a wetting-induced collapse.

Chapter 4

NUMERICAL ANALYSIS OF A 1D INFILTRATION PROBLEM IN UNSATURATED SOIL

4.1 Introduction

Recently, increasing attention is being given to numerical coupled analyses for unsaturated soils. This is mainly because many geotechnical problems are related to unsaturated soils such as rain-induced slope failures and expansive soils. Embankment and slope failures occur frequently due to both short and long infiltration caused by rainfall or melting snow. Water, infiltrating into unsaturated soils, results in an increase in saturation. This, in turn, leads to changes in pore water pressure (a reduction in suction) and a decrease in the shear strength of the soils. One-dimensional infiltration into unsaturated soils becomes an interesting topic due to the necessity of understanding the complex nonlinear response of unsaturated soils.

Several researches have been conducted on the infiltration problem using column tests. Liakopoulos (1964) reported on the column tests used to investigate the leakage in sandy materials as a result of downward drainage from an initially saturated state, Yang et al. (2004) used a soil column apparatus to simultaneously measure all the variables in an infiltration process, Yang et al. (2006) presented the results of laboratory tests on vertical infiltration into two soil columns of finer-over-coarser soils subjected to simultaneous rainfall under conditions of no-ponding at the surface and constant head at the bottom, and Bathurst et al. (2007) reported the results of column tests used to investigate the tran-

sient unsaturated-saturated hydraulic response of sand and sand-geotextile layers under conditions of one-dimensional constant head infiltration.

Rainfall infiltration into unsaturated soils has also been analyzed by analytical solutions. For instance, Srivastava and Yeh (1991) derived analytical solutions to describe the seepage flow for one-dimensional rainfall infiltration toward the water table through homogeneous and two-layer soils. Zhan and Ng (2004) used the analytical solution obtained by Srivastava and Yeh (1991) to investigate the effect of hydraulic parameters and rainfall conditions on the infiltration of unsaturated ground. Among the hydraulic parameters studied, it was found that the response of negative pore water pressure due to rainfall infiltration is meanly governed by the saturated permeability and the desaturation coefficient which controls the rate of decrease in water content and the unsaturated permeability with an increase of suction. Wu and Zhang (2009) are the first to have the analytical solution to a one-dimensional coupled water infiltration and deformation problem applying a Fourier integral transform. In their formulation, Fredlund's incremental-linear elastic constitutive model for unsaturated soil is implemented (Fredlund and Rahardjo 1993). The results showed that the volume change due to a change in soil suction and the ratio of rainfall intensity to saturated permeability (q/k_s) have a significant effect on the distribution of the negative pore water pressure and deformations along the soil profile. It also demonstrated that the coupling of seepage and deformation plays an important role in water infiltration in unsaturated soil.

Recently, numerical solutions have been used to analyze the problem of unsaturated soil. Numerical analyses are necessary because of the complicated initial and boundary conditions, the multi-layered soils, the different rainfall intensities, and the geometry of many engineering problems, whereas the analytical solutions cannot be obtained. Many numerical studies that can account for the inherent complexities of the infiltration problem into unsaturated soils have been presented in the past years, e.g., Pinder and Gray (2008) analyzed the infiltration and drainage behaviors of air-water and dense nonaqueous phase-water flows in homogeneous and heterogeneous layered soils. Their results showed the effects of primary and secondary infiltration and drainage processes on the saturation and the negative pore water pressure distributions, as well as the impact of the nonaqueous phase density on the one-dimensional transient flow. Cai and Ugai (2004) investigated effects of the hydraulic characteristics on the transient water flow through unsaturated-saturated soil slopes and their stability. Griffiths and Lu (2005) analyzed

the unsaturated slope stability due to water infiltration using the Bishop's definition for the effective stress of unsaturated soils combined with the 1-D suction theory. Ehlers et al. (2004) used a seepage-deformation coupled approach that includes the effective pore-pressure and the effective stress concept to analyze the deformation and the localization of strains on unsaturated soils due to seepage flow. Cho and Lee (2001) employed the net stress concept in a seepage-deformation coupled method to analyze the instability of unsaturated soil slopes. In addition, using the net stress concept, Alonso et al. (2003) computed deformations and the variation of the safety factor with time of an unstable slope in a profile of weathered overconsolidated clay by means of an unsaturated coupled hydromechanical model. Oka et al. (2009), and Kato et al. (2009) investigated the coupled seepage-deformation characteristics of unsaturated river embankments under seepage conditions; in their formulations the skeleton stress is incorporated using the average pore pressure, as well as the suction effect in the constitutive model.

In spite of all the valuable works mentioned above, the effect of the hydraulic parameters on the deformation behavior of unsaturated soils is an interesting topic that has not yet been fully studied. Seepage-deformation coupled analysis for unsaturated soil is necessary because changes in saturation and suction cause deformation of the soil and vice versa. The main purpose of the present paper is to study the effect of the hydraulic parameters on the transient vertical infiltration problem and their effects on the deformation behaviour of unsaturated soils. To do that, a multiphase coupled elasto-viscoplastic finite element analysis formulation proposed by Oka et al. (2006) is used to describe the rainfall infiltration into a one-dimensional column. The numerical analyses presented here are based on Biot's theory (Biot 1941, 1962) extended by the theory of porous media, e.g., Atkin and Craine, 1976; Bowen, 1976; Coussy, 2004; Boer, 1998; Ehlers, 2003. The materials are assumed to be composed of solid, water, and gas phases, which are assumed to be continuously distributed throughout space at macroscopic level. An elasto-viscoplastic constitutive model is adopted for the soil skeleton. The skeleton stress, which is determined from the difference between the total stress and the average pore fluid pressure, is used for the stress variable in the constitutive model. In addition, the effect of suction is expressed as the shrinkage or the expansion of the overconsolidation (OC) boundary surface and the static yield surface (Oka et al. 2006).

The computed results of the pore water pressure, saturation, and volumetric strain show that the coupled method can completely describe the reduction in suction and

the increase in saturation within the unsaturated soil when it is subjected to rainfall infiltration, as well as the development of strain and the reduction in shear strength due to the generation of pore water pressure. Subsequently, a complete parametric study, including the main hydraulic characteristics that control the unsaturated behavior (soil water characteristic curve and permeability function), is carried out in order to observe the influence of the characteristics on the changes in pore water pressure and volumetric strain. From the parametric study, it is shown that the generation of pore water pressure and volumetric strain is controlled by material parameters α and n' that describe the soil water characteristic curve. This shows that the deformation behavior of unsaturated soils is strongly dependent on the hydraulic behavior, which emphasizes the importance of seepage-deformation coupled methods for the analysis of rainfall infiltration. Finally, the results of layered column tests are simulated and then presented as pore water pressure profiles in order to compare them with the experimental results. It is shown that the proposed multiphase coupled model can capture very well many of the characteristics of transient vertical rainfall infiltration into layered soils.

4.2 Simulation of a one-dimensional rainfall infiltration problem

Wu and Zhang (2009) derived the analytical solution to a one-dimensional seepage-deformation coupled problem in unsaturated soil considering a homogeneous elastic material, and showed the significance of the coupling of seepage and deformation during the infiltration process. Analytical solutions are simple and easy to implement, but cannot account for the complex initial and boundary conditions, the soil heterogeneities, the non-linear stress-strain and hydraulic relations involved in practical geotechnical problems (e.g., layered soils, elasto-plastic and elasto-viscoplastic stress-strain relations), whereas the numerical solutions are more practical due to their flexibility. In the followings, a general description of the methodology and boundaries used for the numerical analysis of a one-dimensional infiltration problem and the parametric study are presented.

The elasto-viscoplastic model for unsaturated soil described in Section 2.3 and the multiphase finite element formulation described in Section 2.4 are used to simulate the one-dimensional infiltration problem. In this formulation, an updated Lagrangian method with the objective Jaumann rate of Cauchy stress is adopted (Kimoto et al. 2004; Oka

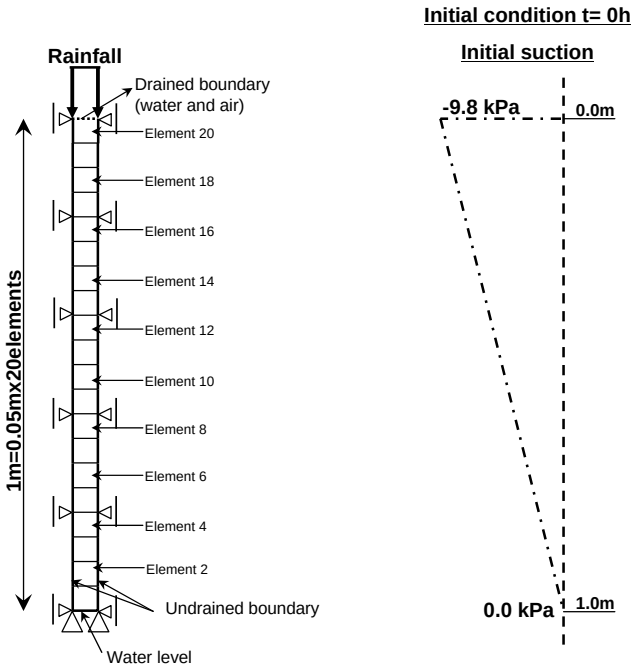

Figure 4.1 Finite element mesh and boundary conditions

et al. 2006). The independent variables are the pore water pressure (P^W), the pore air pressure (P^G), and the nodal velocity (v). In the finite element formulation, an eight-node quadrilateral element with a reduced Gaussian integration is used for the displacement, and four nodes are used for the pore water pressure and the pore air pressure. The backward finite difference method is used for the time discretization.

The finite element mesh and the boundary conditions for the simulations are shown in Figure 4.1. A 1-m homogeneous soil column is employed in the simulation. The initial pore water pressure distribution (suction) is considered to be linear. The water level in the soil is assumed to be located at the bottom of the column where the boundary conditions for water are permeable and the pore water pressure is equal to zero. An impermeable boundary is assigned at the lateral sides of the column. The top of the column is subjected to rainfall infiltration during 30 hours. The rainfall intensity is constant and smaller than the saturated permeability of the soil ($I/k_s^W < 1.0$). The initial air pressure P_i^G is assumed to be zero. The flux of air is allowed at the top of the column. The material parameters required by the constitutive model introduced here are listed in Table 4.1. The parameters have basically been determined from fully drained triaxial tests (drained for air and water) using silty clay, referred to as DL clay.

Table 4.1 Material parameters of the DL Clay

Viscoplastic parameter	$m^{'}$	23.0
Viscoplastic parameter (1/s)	C_1	1.3 x 10^{-11}
Viscoplastic parameter (1/s)	C_2	2.3 x 10^{-11}
Stress ratio at critical state	M_m^*	1.01
Coefficient of saturated permeability (m/s)	k_s^W	1.00 x 10^{-6}
Compression index	λ	0.144
Swelling index	κ	0.0186
Initial elastic shear modulus (kPa)	G_0	20000
Initial void ratio	e_0	1.03
Structural parameter	β	0.0
Suction parameter	S_I	0.20
Suction parameter	s_d	5.00
Minimum saturation	s_{min}	0.0
Shape parameter of gas permeability	b	1.0

Table 4.2 Hydraulic parameters used for the numerical simulations

$\alpha(1/kPa)$	n'	s_{max}	a	$I(m/s)$	k_s^W
0.07	1.30	0.96	0.50	$0.2k_s^W$	1.0 x 10^{-6}
0.10	2.00	0.97	1.00	$0.4k_s^W$	1.0 x 10^{-6}
0.12	**4.00**	0.98	2.00	$0.6k_s^W$	1.0 x 10^{-6}
0.14	8.00	**0.99**	**3.00**	$\mathbf{0.8}k_s^W$	1.0 x 10^{-6}

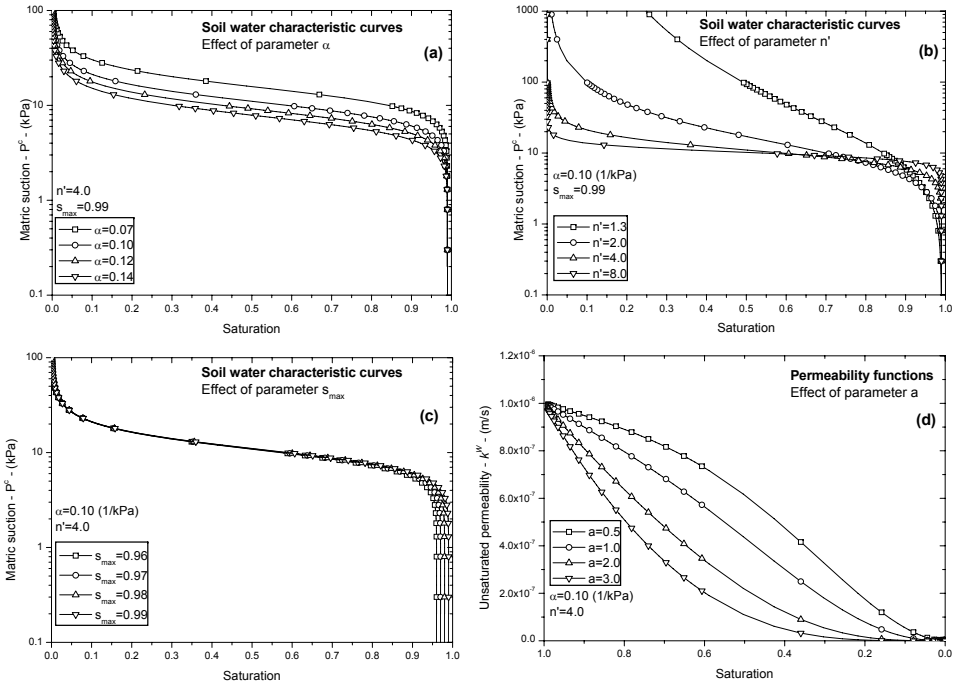

Figure 4.2 Effect of the hydraulic parameters α and n', s_{max} and parameter a on the soil water characteristic curve and permeability function

In order to study the effect of the hydraulic characteristics on the coupled formulation, different values for the hydraulic parameters, rainfall intensity I, van Genuchten parameter α, n', s_{max}, and coefficient of water permeability a, were used in the simulations. The parameters for the soil water characteristic curve, α and n', were chosen based on Lu and Likos (2004) and they are shown in Table 4.2; these parameters describe different typical soils as sands (α =0.10, 0.12, and 0.14 and n'=4.0 and 8.0), silts(α =0.07 and 0.10 and n'=2.0 and 4.0), and clayey silts (α =0.07 and n'=1.3 and 2.0). In Table 4.2 numbers in bold are held constant while a series is being simulated. e.g. when series n' is simulated (parameter n'=1.2, 2.0, 4.0 and 8.0), parameters α=0.10 1/kPa, s_{max}=0.99, a=3.0 and I=0.8k_s^W; when series of parameter a is simulated (parameter a=0.5, 1.0, 2.0 and 3.0), parameters α=0.10 1/kPa, n'=4.0, s_{max}=0.99 and I=0.8k_s^W.

The effect of the hydraulic parameters used in the simulations on the soil water characteristic curve and the permeability function is shown in Figure 4.2.

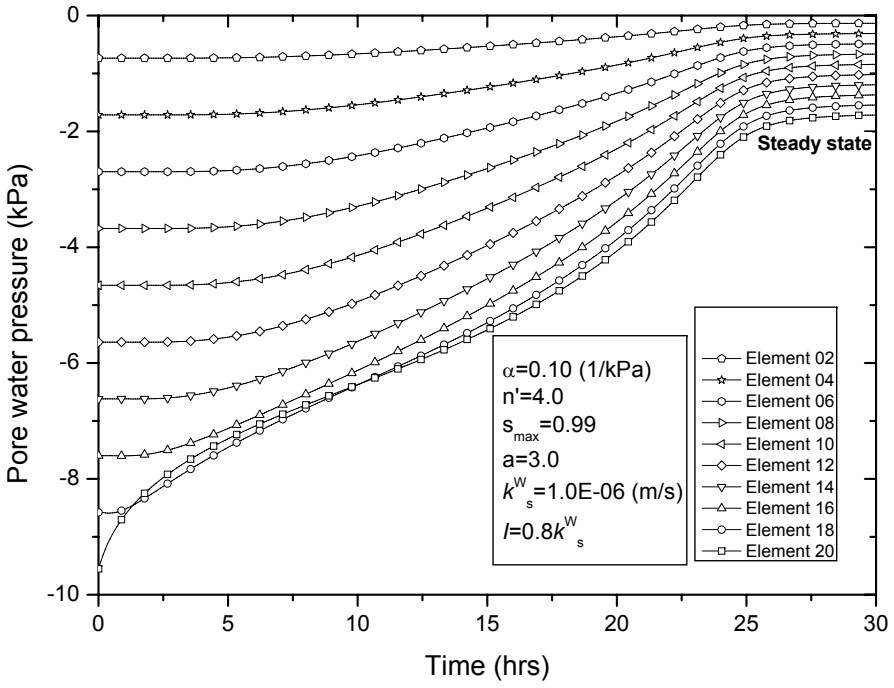

Figure 4.3 Time history of pore water pressure

4.2.1 Numerical results

4.2.1.1 Pore water pressure, saturation and strain histories

Figures 4.3 and 4.4 show the calculated pore water pressure and saturation for the elements of the mesh shown in Figure 4.1. The results are obtained at the center of each element and represent the transition from the initial unsaturated state for each element to their final state corresponding to the unsaturated steady state. Both graphs show that the changes in pore water pressure and saturation are sequential from the top (element 20) to the bottom (element 2), according to the advancing water front. Figure 4.5 shows the volumetric strain and stress histories for the element 10, located in the middle of the soil column (see Figure 4.1). This figure also includes the pore water pressure calculated for the element. It can be seen that when the pore water pressure starts to increase due to the water infiltration, both the skeleton stress and the volumetric strain change. Diminution of the skeleton stress is observed when the pore water pressure is negative (suction); this is due to the effect of the decrease in suction included in the constitutive model and the increase in the average pressure of the fluids. Negative volumetric strain develops at the beginning of the infiltration process; however, it changes to positive volumetric strain, i.e., expansion, while the pore water pressure increases.

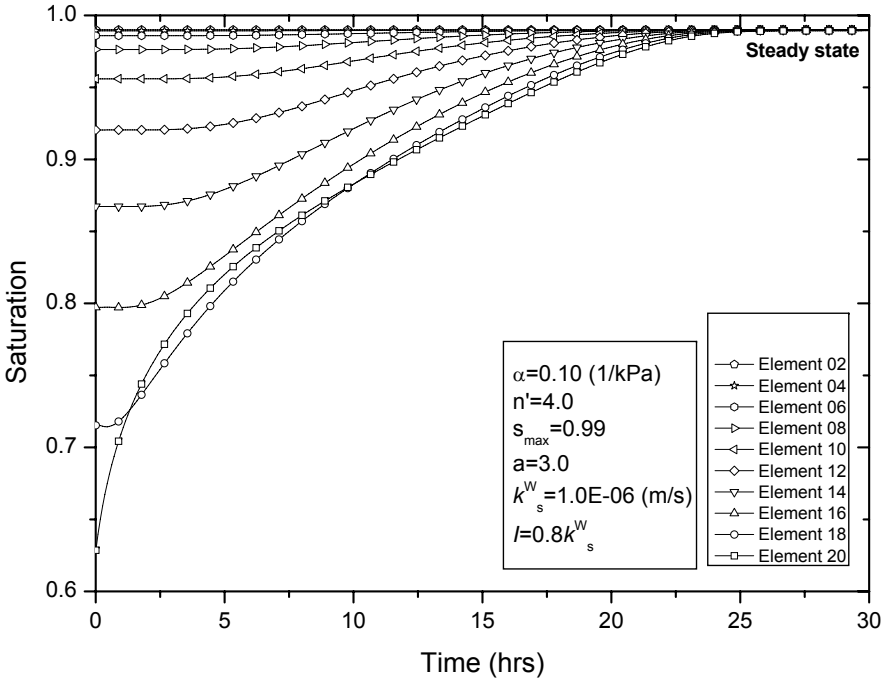

Figure 4.4 Time history of saturation

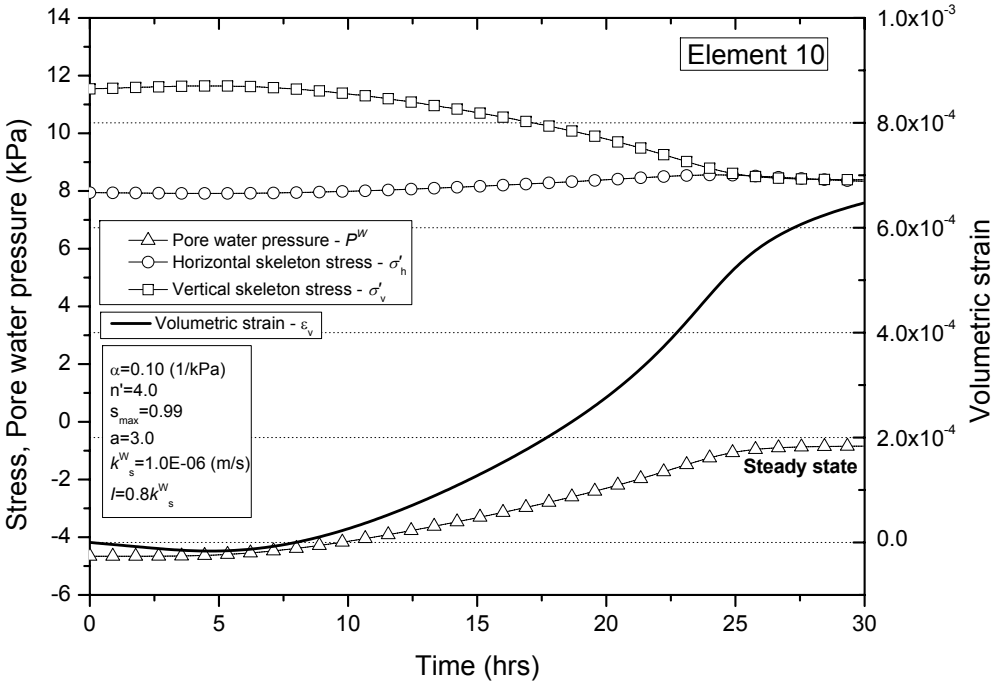

Figure 4.5 Time history of skeleton stress and volumetric strain

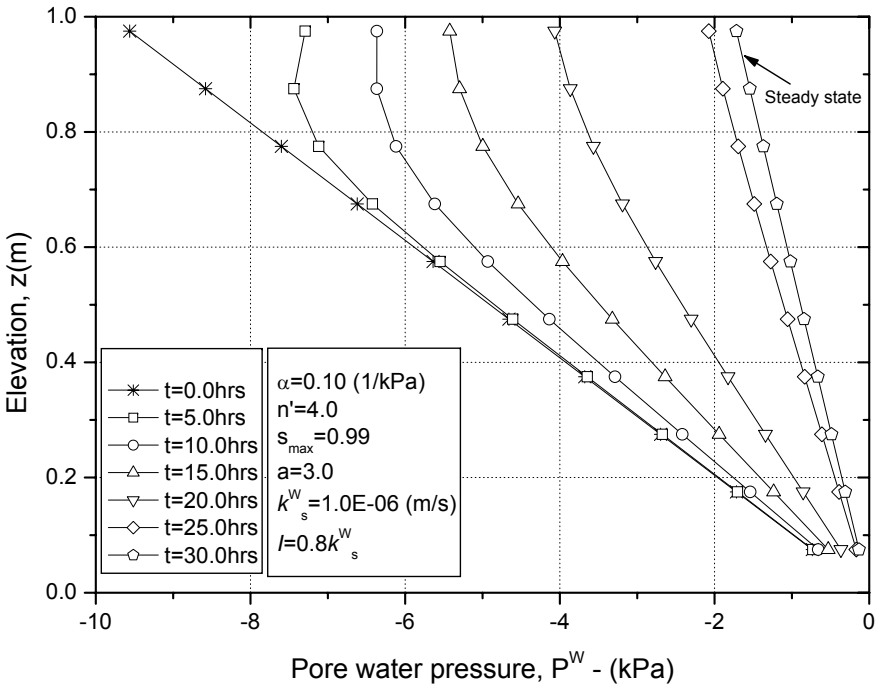

Figure 4.6 Pore water pressure profile

Figure 4.6 shows the calculated pore water pressure profiles at time intervals 0h, 5h, 10h, 15h, 20h, 25h, and 30h during the infiltration process. The initial state of t=0h corresponds to a linear distribution when the water table is at the bottom of the column. Next, when time t is greater than zero, the rainfall intensity increases to $0.8k_s^W$ and the pore water pressure is generated in the column during the rainfall infiltration (30 hours). A steady state is reached after 28 hours. The corresponding saturation profile is shown in Figure 4.7. When infiltration starts, both the pore water pressure and the saturation increase notably in depths relatively close to the soil surface (suction becomes less negative); this trend gradually progresses downward toward the water table as the wetting front advances. The effect of the water infiltration on the volumetric deformation of the soil column is shown in Figure 4.8. The calculation of the deformation is based on the changes in the skeleton stress due to the reduction in suction. In this particular case, it is mostly positive, indicating the swelling of the ground. During the simulations the calculated pore air pressures were close to zero, meaning that $P^C = -P^W$.

4.2.1.2 Effect of rainfall intensity I

Pore water pressure and saturation profiles, corresponding to four different intensities less than the saturated permeability (i.e., I=$0.2k_s^W$, I=$0.4k_s^W$, I=$0.6k_s^W$, and I=$0.8k_s^W$),

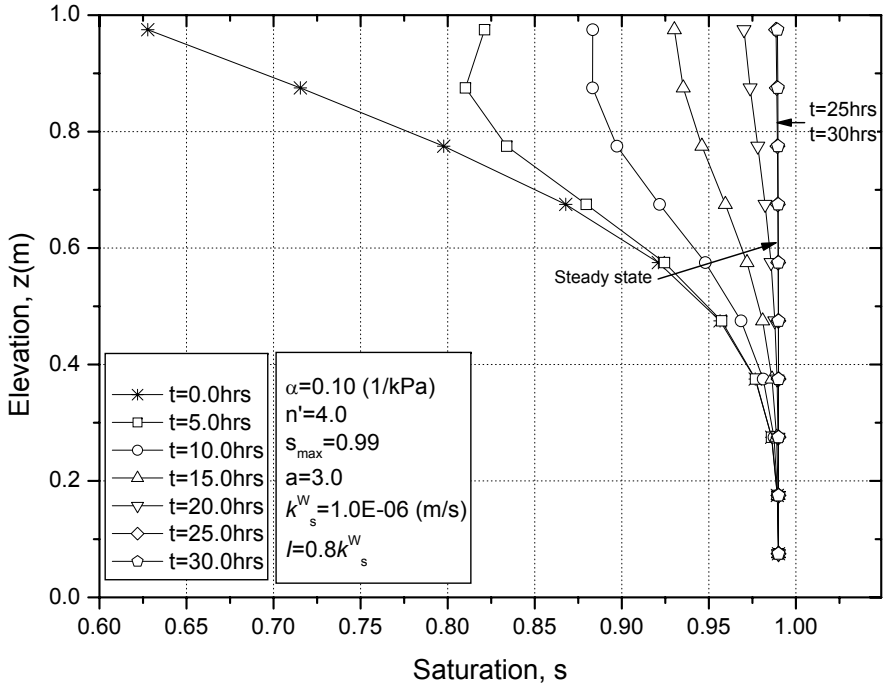

Figure 4.7 Saturation profile

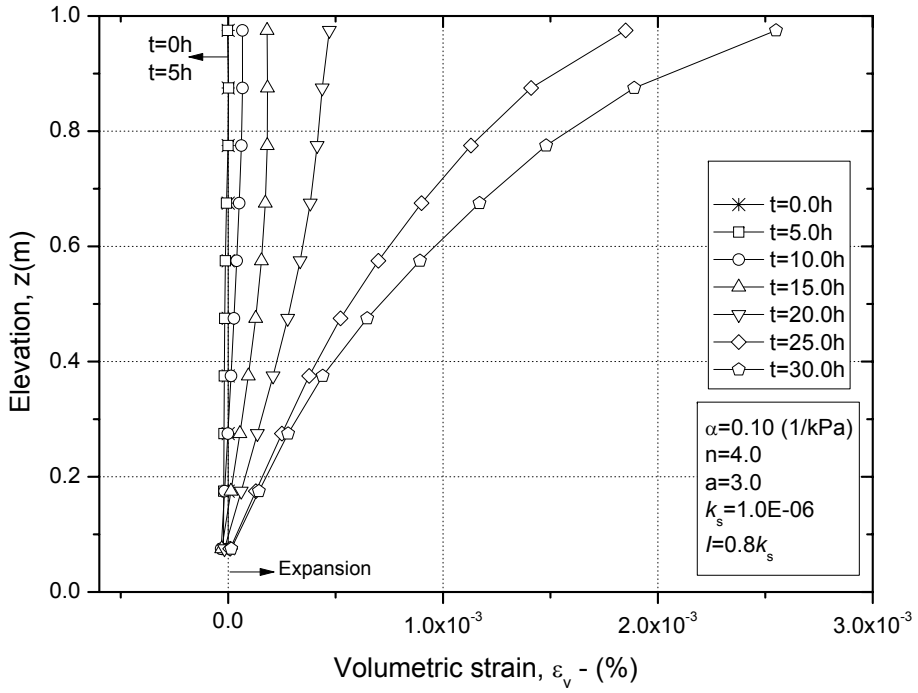

Figure 4.8 Volumetric strain profile

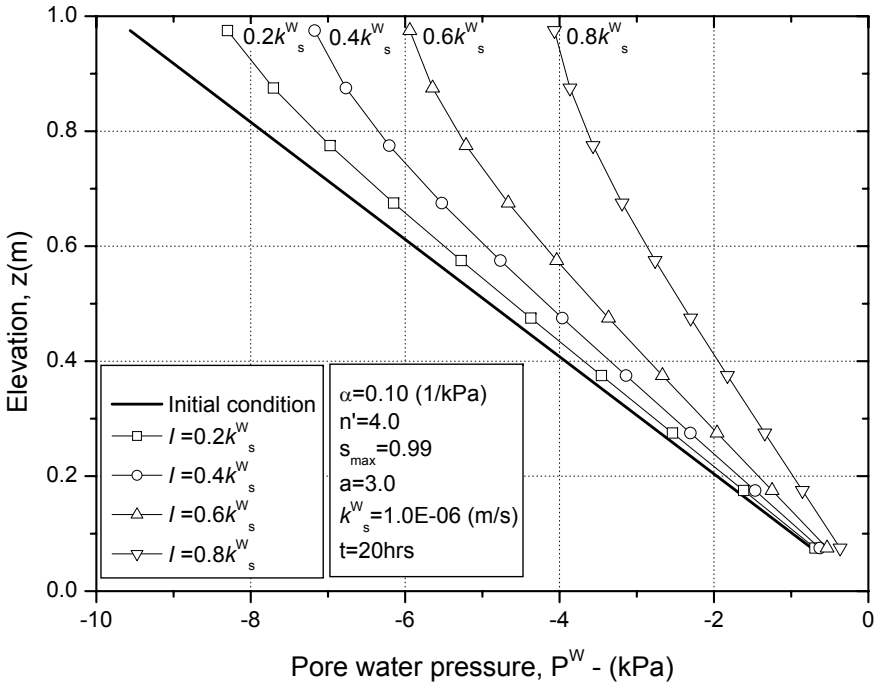

Figure 4.9 Pore water pressure profiles for different rainfall intensities at t=20hrs.

and for a rainfall infiltration time equal to 20 hours are shown in Figures 4.9 and 4.10, respectively. It can be seen from the figures that the higher the rainfall intensity, the more the reduction of suction (negative pore water pressure) and the greater the saturation after 20 hours. This is similar to the result obtained experimentally by Yang et al. (2006) on the effect of rainfall infiltration in one-dimensional layered soils columns. In addition, this result was confirmed analytically by Wu and Zhang (2009); who investigated the influence of the rainfall intensity on the pore-water pressure and the volumetric water content distributions in a homogeneous soil profile in both coupled and uncoupled conditions. Figures 4.9 and 4.10 show the nonlinear relation between the pore water pressure (suction) and the saturation assumed in the calculation (van Genuchten equation). The influence of the rainfall intensity on the volumetric strain is shown in Figure 4.11. When the intensity is lower (I=$0.2k_s^W$), the soils show a compressive behavior at the top of the column, but this behavior changes to swelling when the rainfall intensity is increased. The higher the rainfall intensity, the greater the volumetric strain after 20 hours. This effect is more marked as the rainfall intensity gets higher. The intensity has a significant influence on the increase in saturation and the generation of pore water pressure.

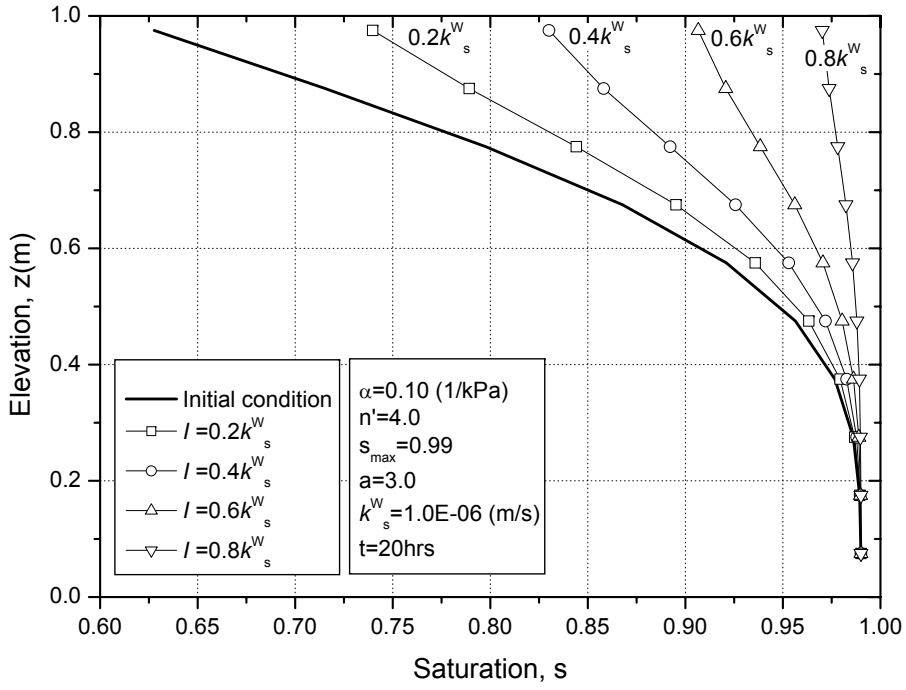

Figure 4.10 Saturation profiles for different rainfall intensities at t=20hrs.

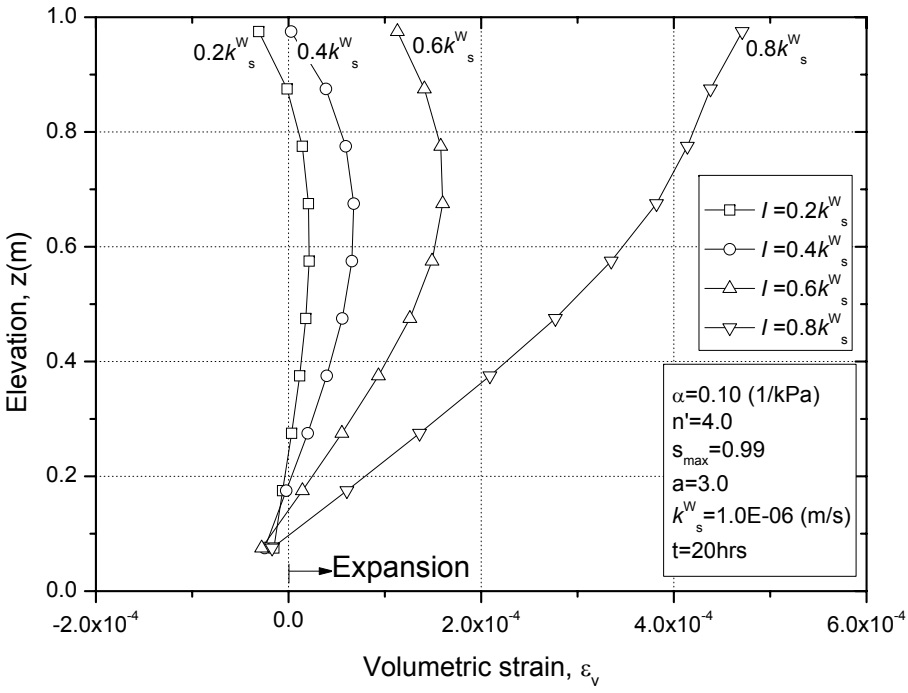

Figure 4.11 Volumetric strain profiles for different rainfall intensities at t=20hrs.

4.2.1.3 Effect of parameter α

Parameter α is very important in the soil water characteristic curve. Parameter α approximates the inverse of the air entry pressure in the soil water characteristic curve (Lu and Likos, 2004). Large values of the air entry pressure are associated with the smaller pore sizes and the smaller values of air entry pressures are associated with the larger pore sizes; consequently, larger values for parameter α represent sands and smaller values represent silts and clays. In Figure 4.2(a), it can be seen that when parameter α increases, the saturation decreases for the same given initial suction and the same parameter n'. This means that soils with larger values for parameter α (i.e., sands) are expected to be less saturated than those with smaller α values (i.e., silts and clays) at the same suction. Four different values are considered for parameter α to show its effect in the water infiltration problem (α=0.07, 0.10, 0.12, and 0.14 1/kPa in Figure 4.2(a)). Pore water pressure and saturation profiles for the different α are shown in Figure 4.12 and 4.13, respectively. From the figures, it is possible to see a similar trend for pore water pressure and saturation. In general, the greater the parameter α , the smaller the pore water pressure and saturation reached after 20 hours. In the simulations, the steady state was reached after 11 hours when parameter α=0.07; this is because of the higher initial saturation for the given initial suction, as explained previously. As a result, for the same intensity and permeability, faster infiltrations and steady states can be expected for finer soils (silts and clays) where parameter α is smaller. The volumetric strain profiles for these series of simulations are shown in Figure 4.14. From the graph, two different responses can be observed after 20 hours of rainfall, namely, a trend toward compressive behavior for coarser materials when parameter α is greater (α=0.12 and 0.14 1/kPa) and a trend toward swelling behavior for finer materials when α is smaller (α=0.07 and 0.10 1/kPa).

4.2.1.4 Effect of parameter n'

Parameter n' plays a more significant role in the soil water characteristic curve as well as in the permeability function. In addition, parameter n' is frequently used to constrain the parameter m, which is related to the overall symmetry of the soil water characteristic curve ($m = 1 - 1/n'$). The n' parameter is related to the pore size distribution of the soil (Lu and Likos, 2004); then, the grain size distribution of the soil has an important effect on the suction-saturation relationship. Pinder and Gray (2008) explained that for well-sorted soils, soils that have a narrow range of grains, the suction-saturation relationship is relatively flat signifying that drainage occurs rather sharply over a narrow range of

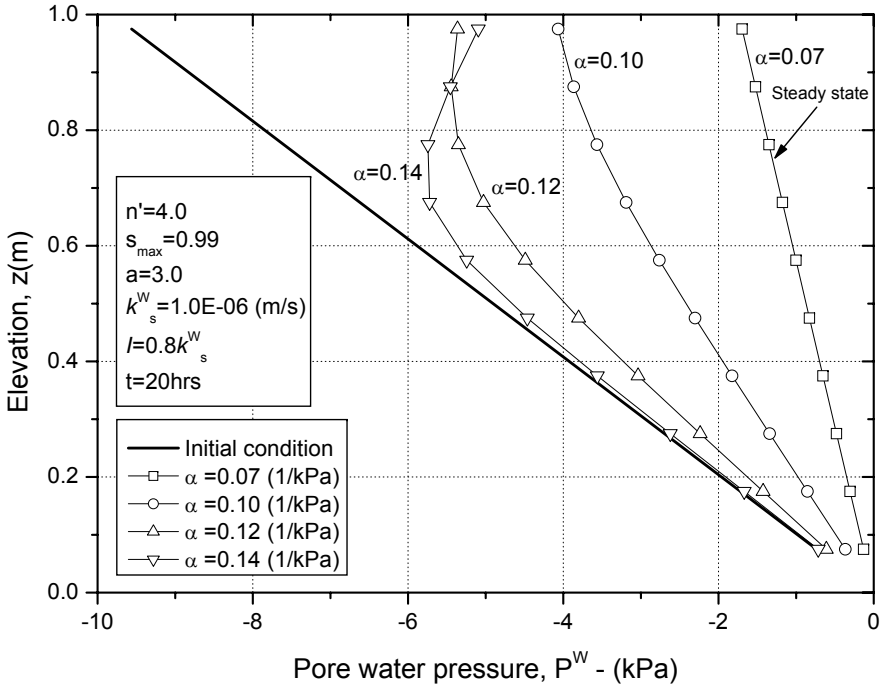

Figure 4.12 Pore water pressure profiles for different values of parameter α at t=20hrs.

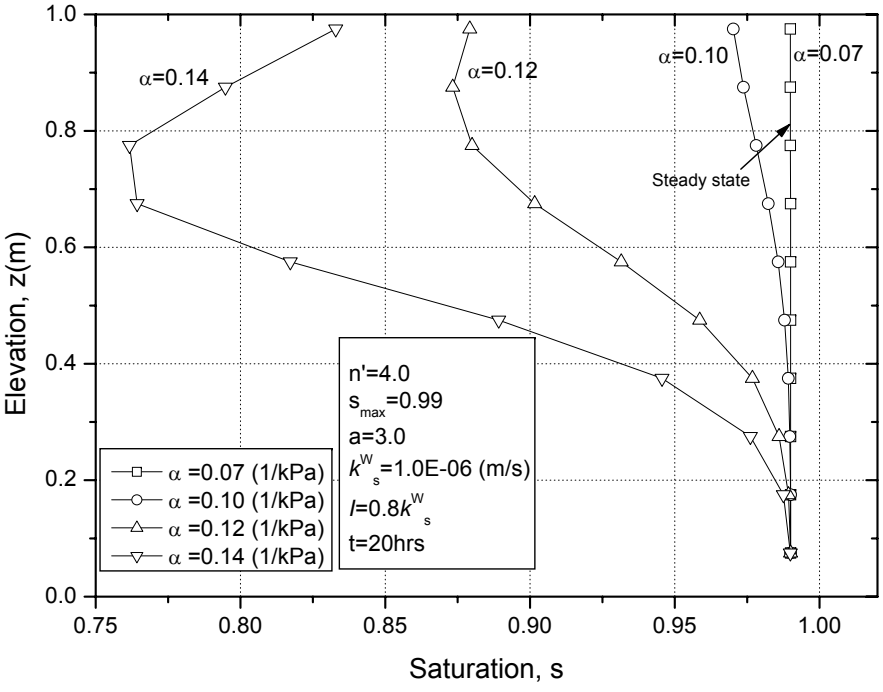

Figure 4.13 Saturation profiles for different values of parameter α at t=20hrs.

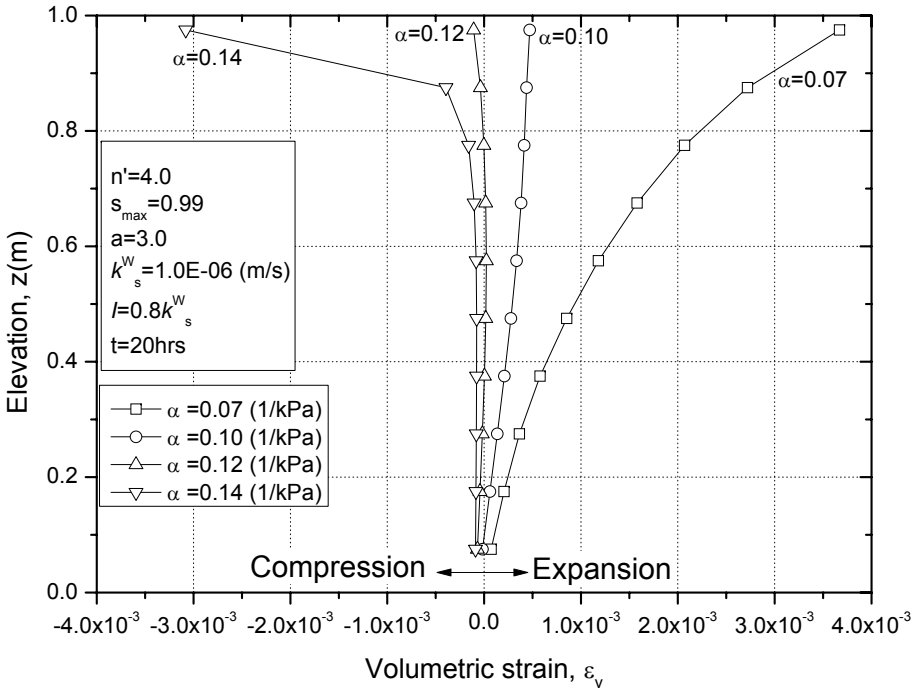

Figure 4.14 Volumetric strain profiles for different values of parameter α at t=20hrs.

suction; however, for a well-graded soil a mild transition is obtained from unsaturated to saturated state since drainage occurs over a greater range of suctions. The effect of different values for parameter n' in the soil water retention characteristic curve can be seen in Figure 4.2(b). In this figure, smaller values for parameter n' represent both, finer soils (i.e., silts and clays) and well-graded soils. On the contrary, larger values represent both, coarser soils (i.e., sands) and well-sorted soils. Figures 4.15 and 4.16 describe the pore water pressure and the saturation profiles, respectively, obtained during the infiltration process at t=20 hours for different values of parameter n' (n'=1.3, 2.0, 4.0, and 8.0). A complex response in the profiles is obtained. For smaller n' values, the pore water pressure decreases when n' increases (n'= 1.3 to 4.0). For larger n' values, however, the response is reversed and the pore water pressure increases when n' increases (n'= 8.0). A similar trend is observed in the saturation profiles, in which the saturation decreases when n'=1.3 and 2.0 and increases when n'=4.0 and 8.0. These two different responses can be explained by the initial saturation at the beginning of the infiltration process, namely, t=0h. Both processes are controlled by the initial saturation as follows:

1. For smaller n' values (i.e., silts and clays, n'=1.3 and 2.0), the initial saturation along the column is higher for the smaller n' value (n'=1.3) and decreases for n'=2.0 (see the profiles in Figure 4.17). Then, the saturation rate is faster for soils with the

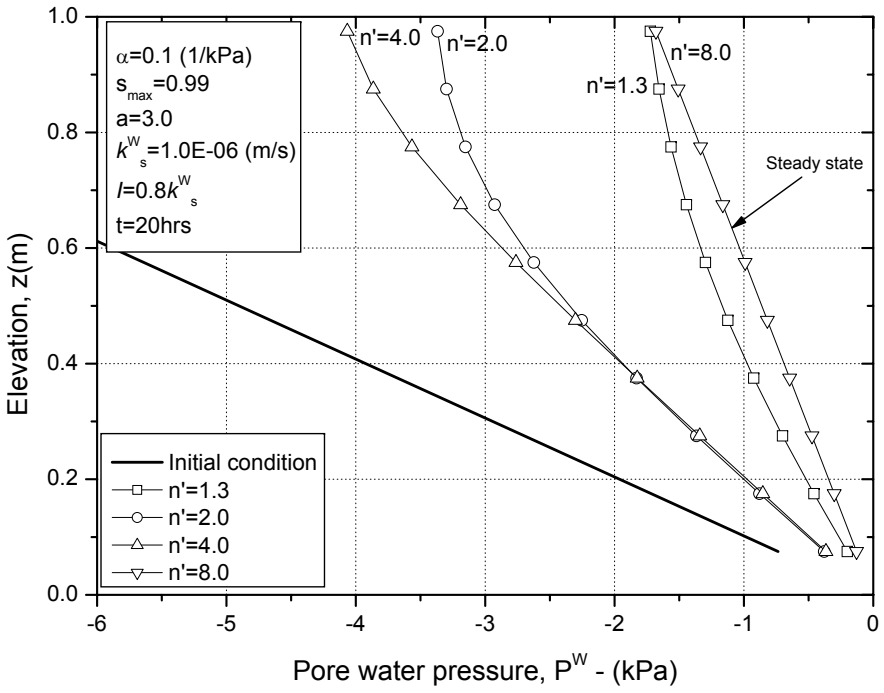

Figure 4.15 Pore water pressure profiles for different values of parameter n' at t=20hrs.

smaller n' value where the initial saturation distribution along the column is higher; as a result, the pore water pressure is higher.

2. For greater n' values (i.e., sands, n'=4.0 and 8.0), the initial saturation is higher at the bottom and the middle of the column, but lower at the top (see Figure 4.17). Contrary to the last case, the initial saturation distribution along the column increases when n' increases. The saturation of the column is faster in this case because of the higher saturation at the bottom and the middle of the column. Parameter n' has a significant influence on the initial saturation distribution.

Additionally, the effect of parameter n' on the volumetric strain is also important; it is shown in Figure 4.18. Generally, a similar trend as that shown for the pore water pressure profile is presented. The positive volumetric strain (expansion) decreases when n' changes from 1.3 to 4.0; conversely, it increases when n'= 8.0.

4.2.1.5 Effect of parameter s_{max}

From experimental data, e.g. Yang et al. (2006), Garcia et al. (2007), it is observed that the maximum saturation during the infiltration process is less than 1.0. s_{max} indicates the maximum saturation which the soil can reach in the infiltration process. The maximum

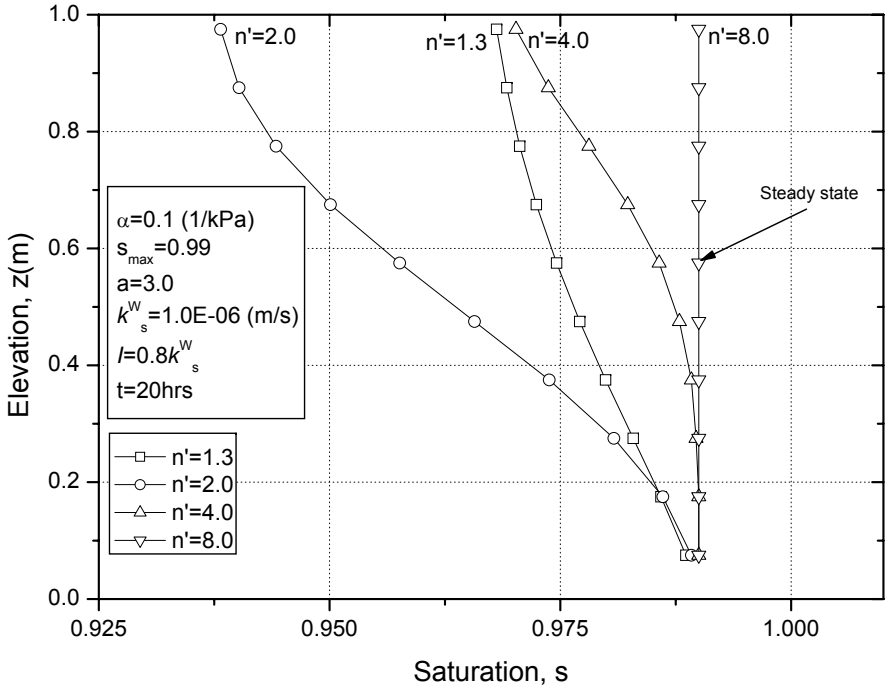

Figure 4.16 Saturation profiles for different values of parameter n' at t=20hrs.

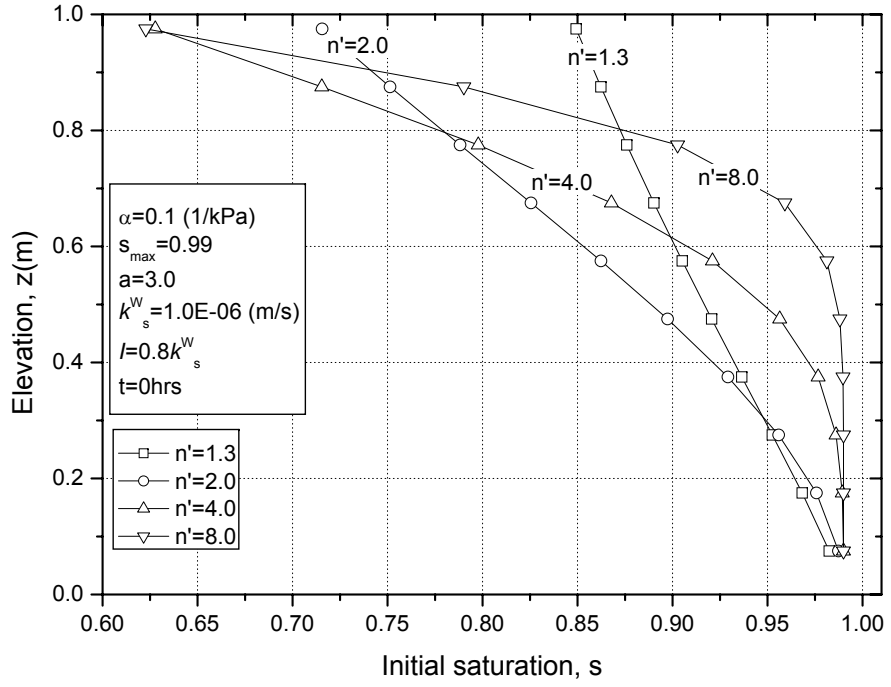

Figure 4.17 Initial saturation profiles for different values of parameter n' at t=0hrs.

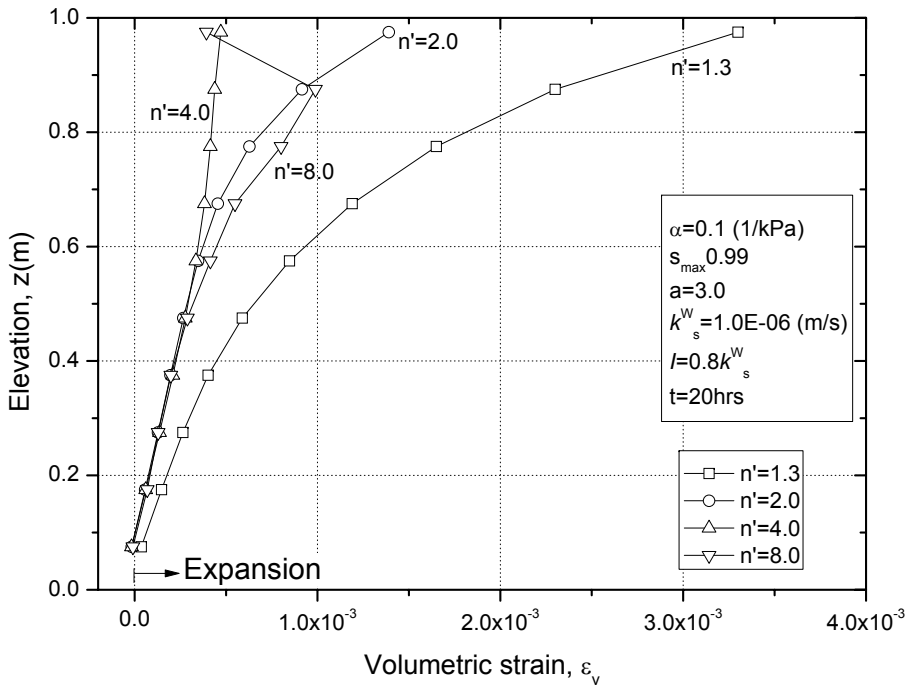

Figure 4.18 Volumetric strain profiles for different values of parameter n' at t=20hrs.

saturation s_{max} is also related to the water storage capacity of a soil (i.e., the maximum amount of water that the soil can store during an infiltration process). The larger the parameter s_{max}, the larger the amount of water the soil can retain. Four values for the maximum saturations, s_{max}, were assumed in order to observe their effect in the infiltration process, namely, s_{max}=0.96, 0.97, 0.98, and 0.99 (see Figure 4.2(c)). Comparisons of the pore water pressure, saturation, and volumetric strain profiles at t=20 hours are shown in Figures 4.19, 4.20, and 4.21, respectively. The pore water pressure profiles show that the larger the maximum saturation (s_{max}), the smaller the pore water pressure after 20 hours of rainfall infiltration. This result is comparable to the result obtained by Zhan and Ng (2004), where the larger the water storage capacity ($\theta_s - \theta_r$, θ_s and θ_r = saturated and residual volumetric water content of the soil), the smaller the pore water pressure along the soil profile. The volumetric strain profiles show that the maximum positive volumetric strain (expansion) is attained for the smallest s_{max} value.

4.2.1.6 Effect of parameter a

Parameter a is an essential parameter in the definition of the permeability function, Equation (2.48). Larger a values bring about faster permeability decay in the unsaturated state, that is, the case of sands. Conversely, smaller a values represent permeability functions

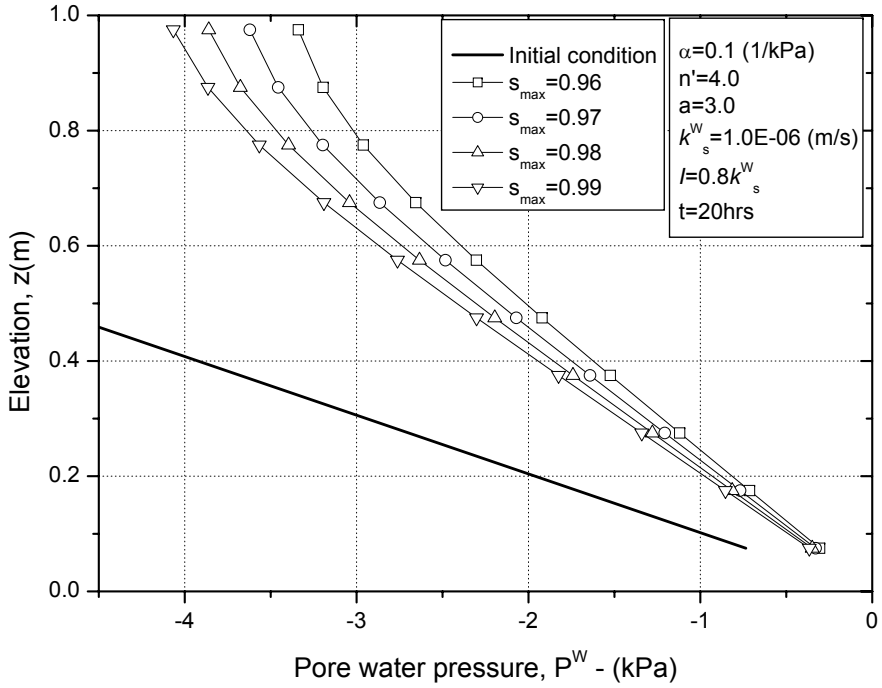

Figure 4.19 Pore water pressure profiles for different values of parameter s_{max} at t=20hrs.

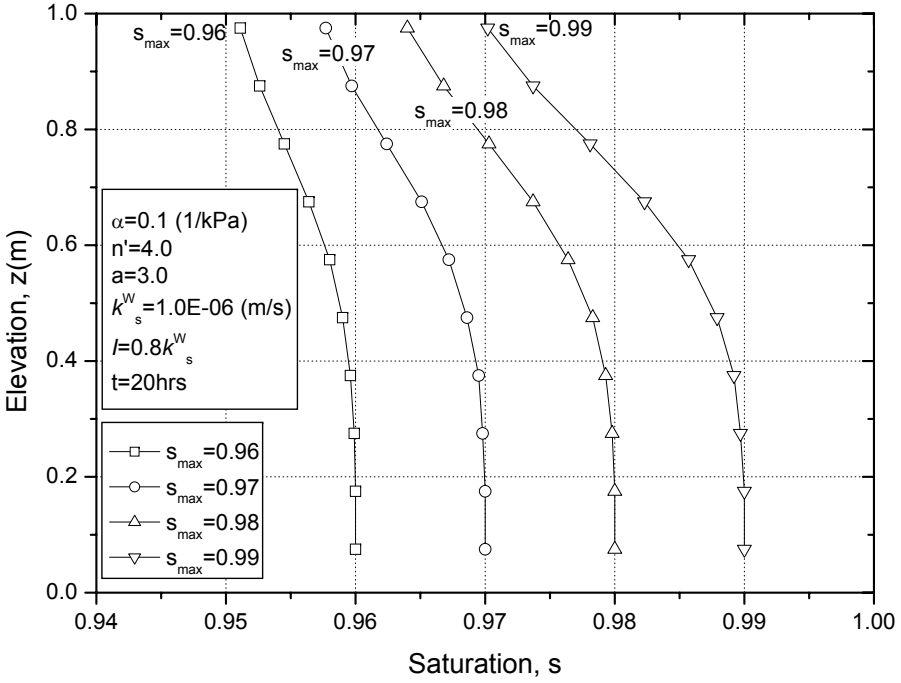

Figure 4.20 Saturation profiles for different values of parameter s_{max} at t=20hrs.

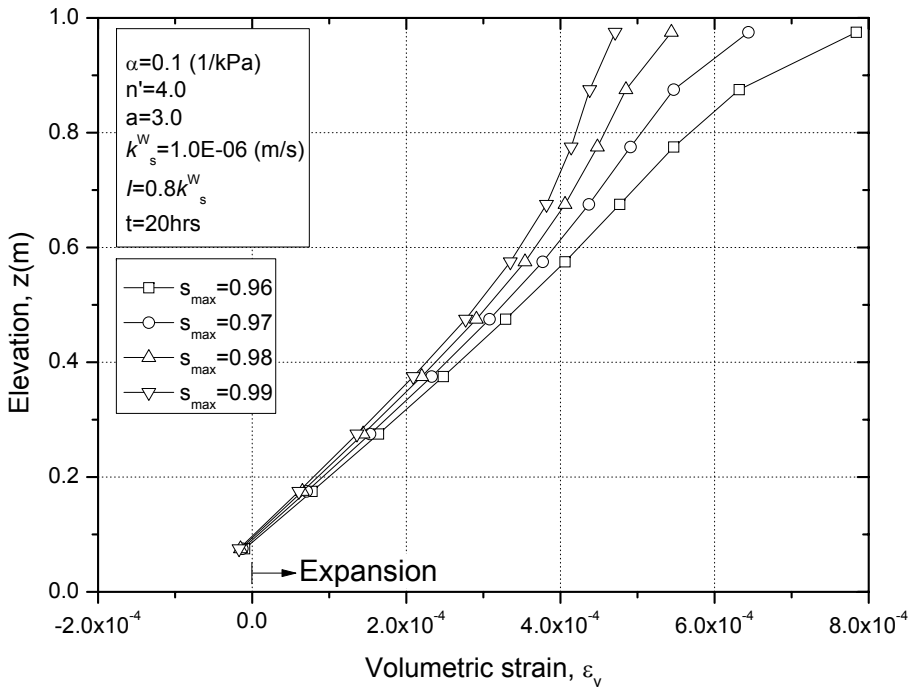

Figure 4.21 Volumetric strain profiles for different values of parameter s_{max} at t=20hrs.

for silts and clays, and the effect of parameter a on the permeability function can be seen in Figure 4.2(d). The influence of parameter a, i.e., a=0.5, 1.0, 2.0, and 3.0, on the pore water pressure, saturation, and volumetric strain profiles at t=20 hours, are shown in Figures 4.22, 4.23, and 4.24, respectively. As shown in Figure 4.22, when parameter a increases, the pore water pressure increases along the column. Similarly, Figures 4.23 and 4.24 show an increase in the saturation and the positive volumetric strain for larger values of parameter a.

4.2.1.7 Comparison of the results

The effect of the material parameters on the infiltration process is shown by means of the time required to reach the steady state (see Figure 4.25). This figure shows that parameters α and n' have a greater effect on the rate for the steady state when they are compared to parameters s_{max} and a. In the case of parameter α, the steady state is reached faster when α is smaller; this is because smaller parameters α represent soils with higher initial saturations (silts and clays). As parameter α increases, the time needed to reach the steady state is longer. Parameter n' presents a more complex influence on the time it takes the soil to reach the steady state. Initially, the time needed for the steady state increased when n' changed from 1.3 to 2.0. After that, this time decreased while

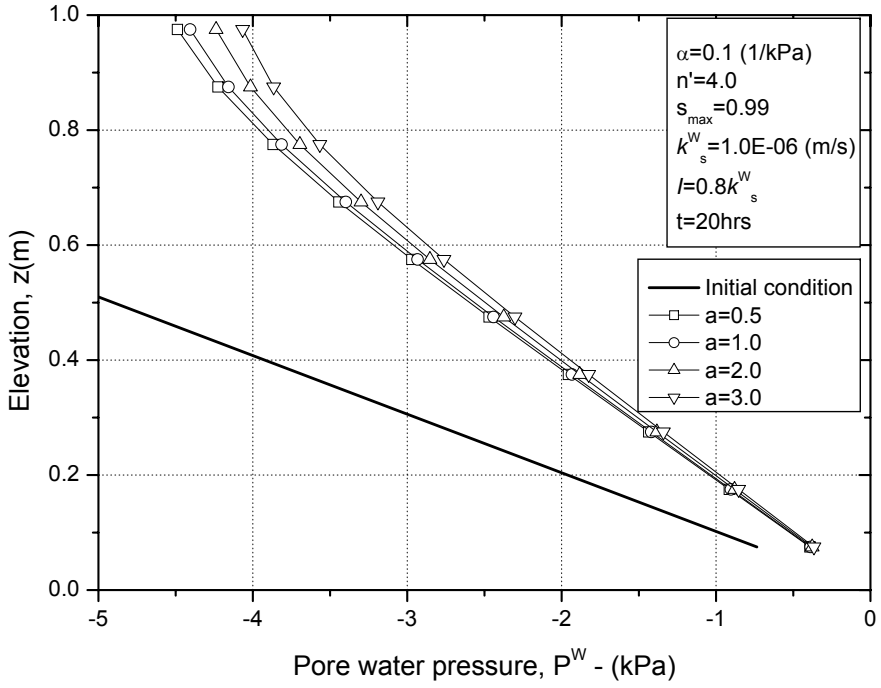

Figure 4.22 Pore water pressure profiles for different values of parameter a at t=20hrs.

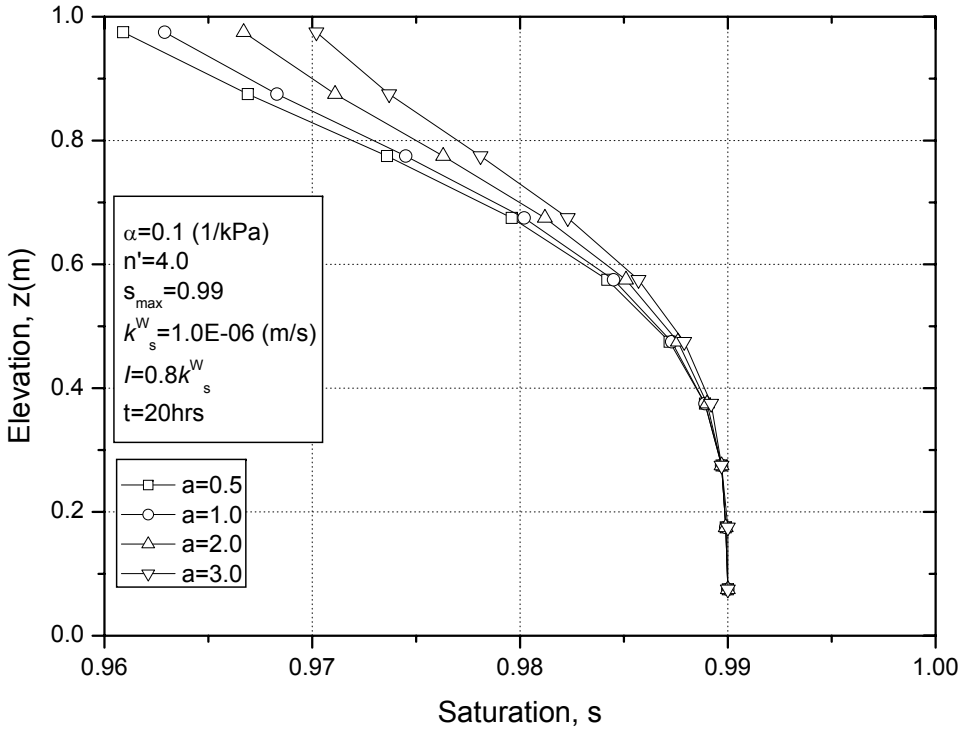

Figure 4.23 Saturation profiles for different values of parameter a at t=20hrs.

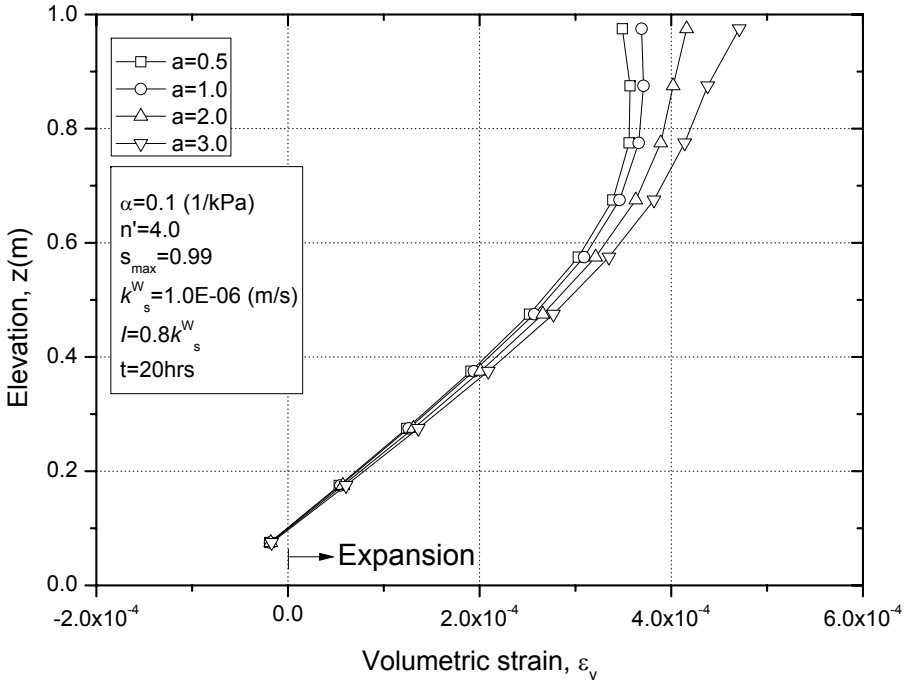

Figure 4.24 Volumetric strain profiles for different values of parameter a at t=20hrs.

parameter n' increased from 4.0 to 8.0. Larger values for n' (sands) describe a faster transition between unsaturated and saturated states. Parameters s_{max} and a do not have a great effect on the rate for the steady state.

The influence of the hydraulic parameters on the one-dimensional rainfall infiltration problem is also estimated by the responses of the pore water pressure and the volumetric strain at the middle of the column (element 12) after 20 hours of rainfall infiltration. The effect of the parameters in the generation of pore water pressure is presented in Figure 4.26. In this figure, when parameter a increases, the pore water pressure increases. In contrast, when maximum saturation s_{max} and parameter α increase, the pore water pressure decreases. This effect is more significant for parameter α. Parameter n' has a combined effect, namely, for smaller values of parameter n' (n'=1.3 to 4.0), the pore water pressure decreases, but as n' becomes larger, the pore water pressure starts to increase. The effect of the parameters on the volumetric strain is shown in Figure 4.27. For parameter α, the positive volumetric strain decreases while parameter α increases, and it changes from a positive to a negative volumetric strain when α=0.14 1/kPa. Similar behavior for decreasing positive volumetric strain can be observed for parameter s_{max}. On the contrary, parameter a shows an increase in positive volumetric strain when it increases.

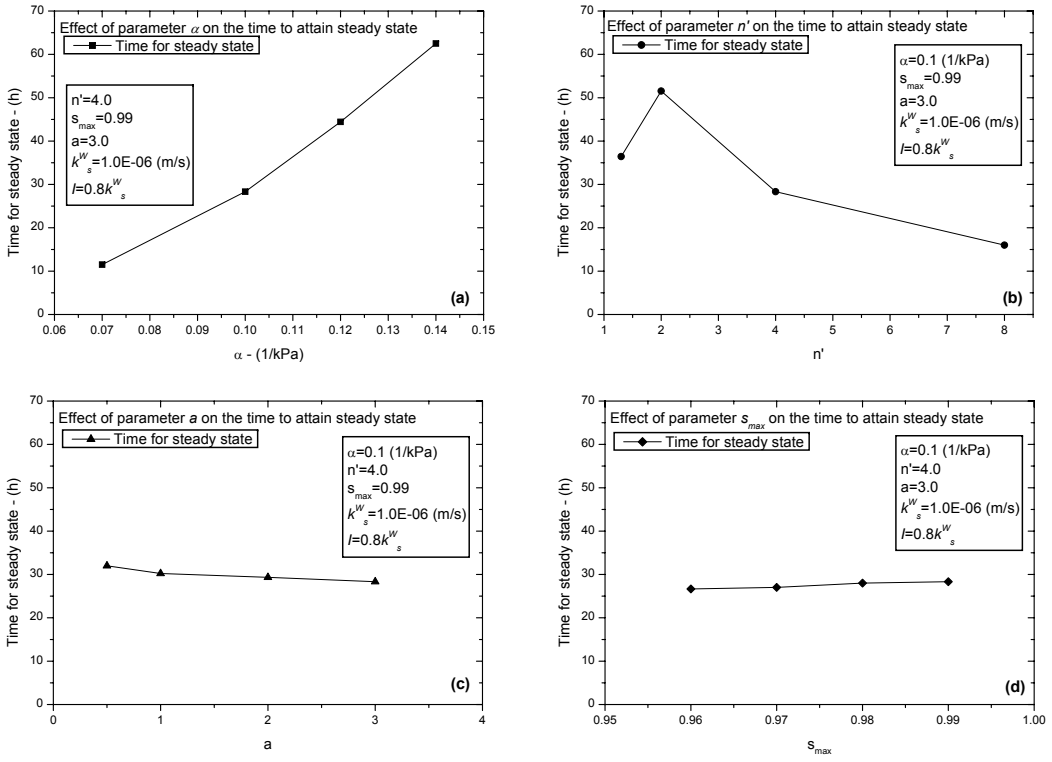

Figure 4.25 Effect of parameters (α, n', a and s_{max}) on the time to attain the steady state

Once more, parameter n' shows a combined effect, namely, the positive volumetric strain decreases for smaller values of n' and it later increases for larger values. The greatest positive volumetric strain was obtained for the smallest α value (α=0.07 1/kPa) and for the greatest n' value (n'=8.0) in which the steady states were reached faster.

The parameter n', presented in the van Genuchten model (Equation 2.45), is related to the pore size distribution of the soil (Lu and Likos 2004). The parameter n' corresponds to the desaturation coefficient used by Zhan and Ng (2004). Zhan and Ng (2004) assumed an exponential function for the volumetric water content-suction relationship, in which the dasaturation coefficient controls the rate of reduction in hydraulic conductivity or moisture content as the pore water pressure becomes more negative. Their results provided that between the hydraulic parameters related to the soil water characteristic curve studied (i.e., dasaturation coefficient and water storage capacity) the effect of the dasaturation coefficient on the pore water pressure profile is much more significant than the effect of the water storage capacity. As mentioned before, these two parameters are directly related to the parameters n' and s_{max} in the van Genuchten model.

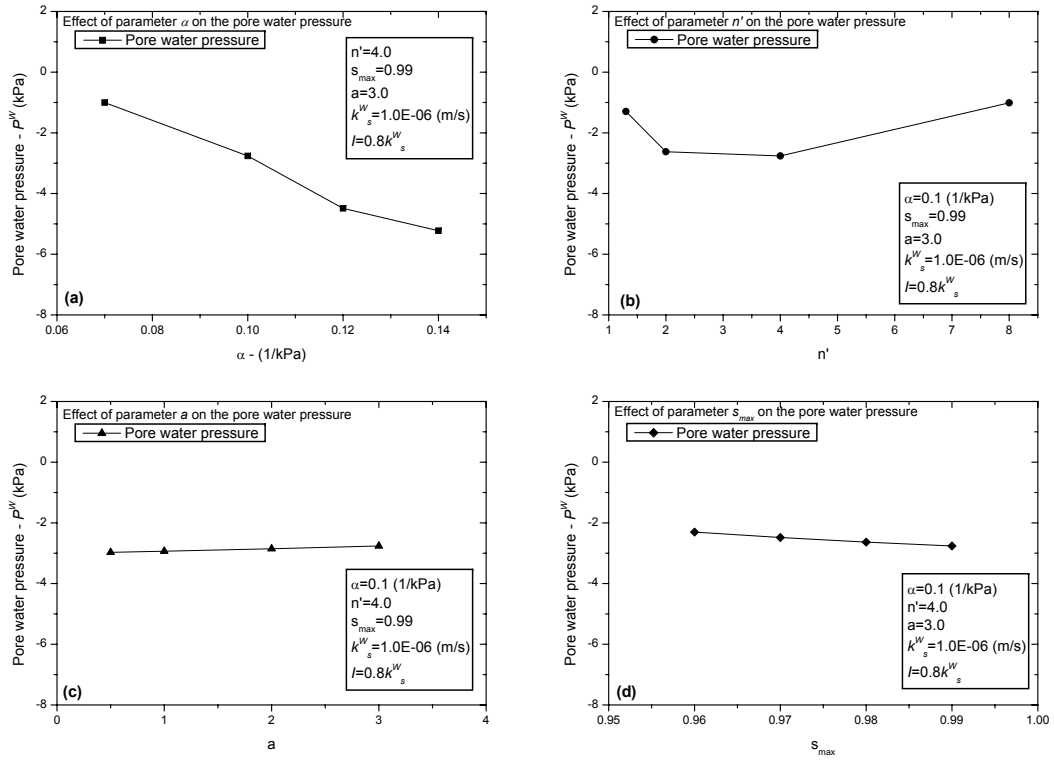

Figure 4.26 Effect of parameters (α, n', a and s_{max}) on the pore water pressure (Element 12). t=20hrs.

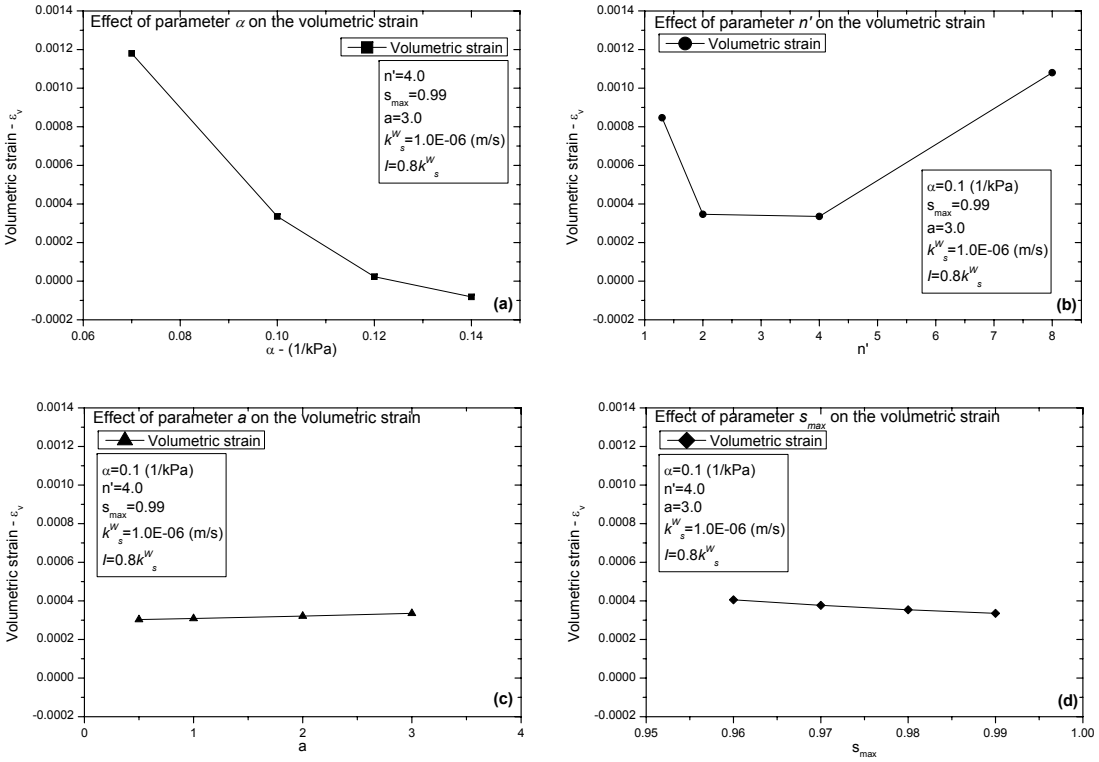

Figure 4.27 Effect of parameters (α, n', a and s_{max}) on the volumetric strain (Element 12). t=20hrs.

When Figures 4.26 and 4.27 are compared, it is possible to see the relationship between the pore water pressure and the volumetric strain. The results show a trend in larger positive volumetric strain (expansion) for higher pore water pressure values (lower suctions). On the contrary, when the pore water pressure is lower, either the positive volumetric strain is smaller or it changes to negative.

The results herein estimate the effect of the hydraulic parameters in the infiltration problem based on the pore water pressure-saturation relation and the volumetric strain. The material parameters of the soil related to the deformation showed in Table 4.1 were kept constant during all the simulations. Despite the fact that the material parameters related to the deformation may not be consistent with some hydraulic parameters assumed for some of the simulations, they do show a trend that provides useful information on the coupled hydraulic-deformation behavior of soils, which is the main object of this parametric study. Furthermore,the results of the parametric analysis show the dependency of the deformation behaviour of unsaturated soil on the hydraulic parameters.

In this study the effect of the hydraulic parameters on the deformation of the soil due to the rainfall infiltration was investigated. In the future, it is necessary to study the effects of the constitutive parameters of the soil, e.g., viscoplastic parameters, by the proposed numerical method.

4.2.2 Comparison with experimental results

Experimental results of infiltration into unsaturated soils are scarce, costly; valuable and useful input data for simulations. They allow the calibration and verification of numerical models used to investigate the behaviour of unsaturated soils. Yang et al. (2006) performed an interesting experimental work and provided measurements of rainfall intensity, pore water pressure, volumetric water content, and drainage rate instantaneously and continuously during rainfall infiltration. The results showed that rainfall intensity and its duration had an important effect on the rainfall infiltration in the finer soil layer. In addition, from the measurement of the negative pore water pressures and water contents, it was shown different paths for the wetting and drying processes during the rainfall infiltration, i.e. the soil exhibited hysteretic behaviour.

Some of these laboratory test results of vertical infiltration into a layered soil are used in order to compare with the numerical results obtained by a multiphase coupled finite

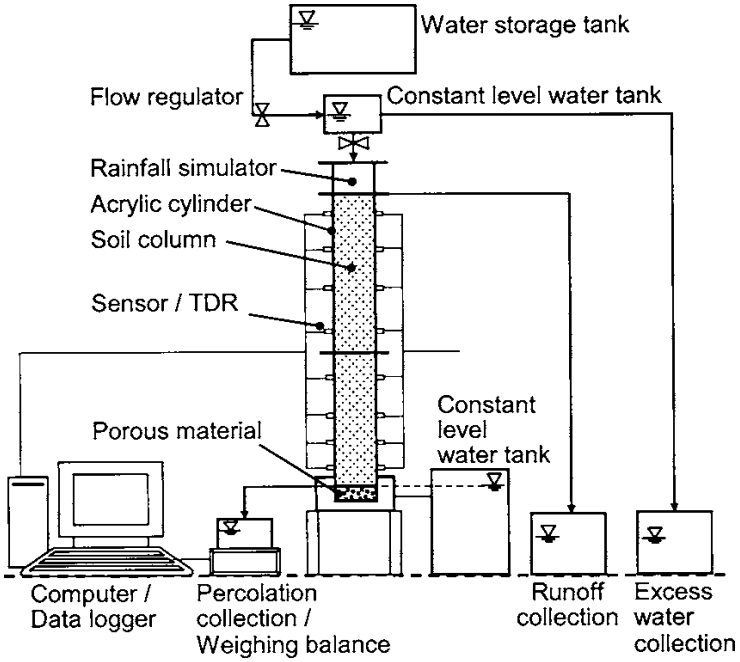

Figure 4.28 Sketch of the infiltration apparatus (Yang et al. 2006)

element analysis method. The results were obtained by Yang et al. (2006) by performing column tests of finer over coarser soil subjected to simulated rainfalls under conditions of no-ponding at the surface and constant head at the bottom. The infiltration tests were conducted in a soil column apparatus described by Yang (2004). The apparatus comprised a transparent acrylic cylinder 1.0 m high and 0.19 m internal diameter for containing the soils (Figure 4.28). Tensiometer transducers to measure pore water pressure, time-domain reflectometry for water contents and weighing balance for drainage water were used in the experiments. Simulated rainfalls of desired intensity (q) and duration were applied to the surface of the soil from dropping water from four outlets. The water table was maintained constant at the bottom of the column, which formed the lower boundary condition during the infiltration tests.

Results of layered soil column composed of clayey sand over fine sand are presented here. Laboratory tests started from a hydrostatic condition where the water level is located at the bottom of the soil column; constant rainfall intensities lower than the permeability of the clayey sand are applied to the top of the column for 24 hours; results of the experiments for two different rainfall intensities (CF-R1:q=1.6x10^{-7}m/s, CF-R2:q=3.3x10^{-7}m/s) are shown in Figure 4.29.

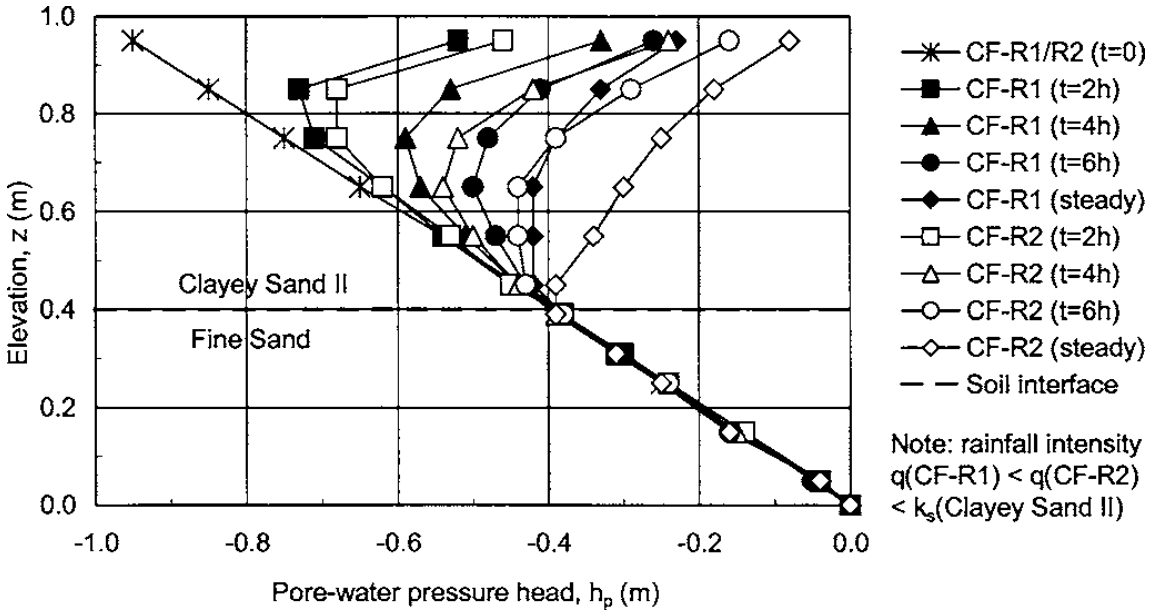

Figure 4.29 Pore-pressure head profiles, clayed sand over fine sand during rainfall (Yang et al. 2006)

4.2.2.1 Simulation of a layered soil column

Same boundary conditions as those used in the experiments are used for the simulations. A 20-element column mesh with two soil layers and drained boundary at the top is used as the space discretization. The horizontal dimension of the column is irrelevant because the flow pattern is one-dimensional. The finite element mesh of the soil column is shown in Figure 4.30. The main parameters for the material properties of the soil particles, water and gas required by the constitutive model as well as those describing the suction-saturation relation that are used in the simulation are listed in Table 4.3, parameters that are not listed in this table remain the same to those used in the verification of a one-dimensional infiltration problem shown in Table 4.1.

4.2.2.2 Results of the simulations

The calculated pore water pressure profiles obtained in the simulation at similar elevation as shown in the experimental results are shown in Figures 4.31 and 4.32. Both figures show the water front advancing with the time from the initial pressure head profile at t=0.0h. When infiltration starts the pore water pressure increases for the clayey sand notably in depths relatively close to the soil surface (suction becomes less negative); this trend gradually progresses downward toward the fine sand layer as the wetting front advances. When results of the experiment are compared with the results of the simulations, it is

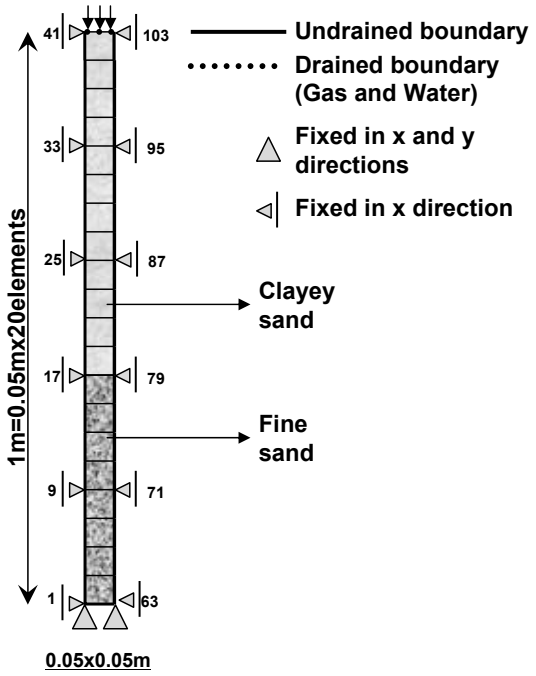

Figure 4.30 Finite element mesh for the boundary conditions

Table 4.3 Material parameters

		Clayey sand	Fine sand
Compression index	λ	0.03	
Swelling index	κ	0.002	
Initial shear elastic modulus (kPa)	G_0	28700	
Initial void ratio	e_0	0.762	
Permeability of water at s=1.0 (m/s)	k_s^W	8.8 x 10^{-7}	2.7 x 10^{-4}
Maximum saturation	s_{max}	0.99	
Minimum saturation	s_{min}	0.00	
van Genuchten parameter (1/kPa)	α	2.0	1.0
van Genuchten parameter	$n^{'}$	1.14	5.00

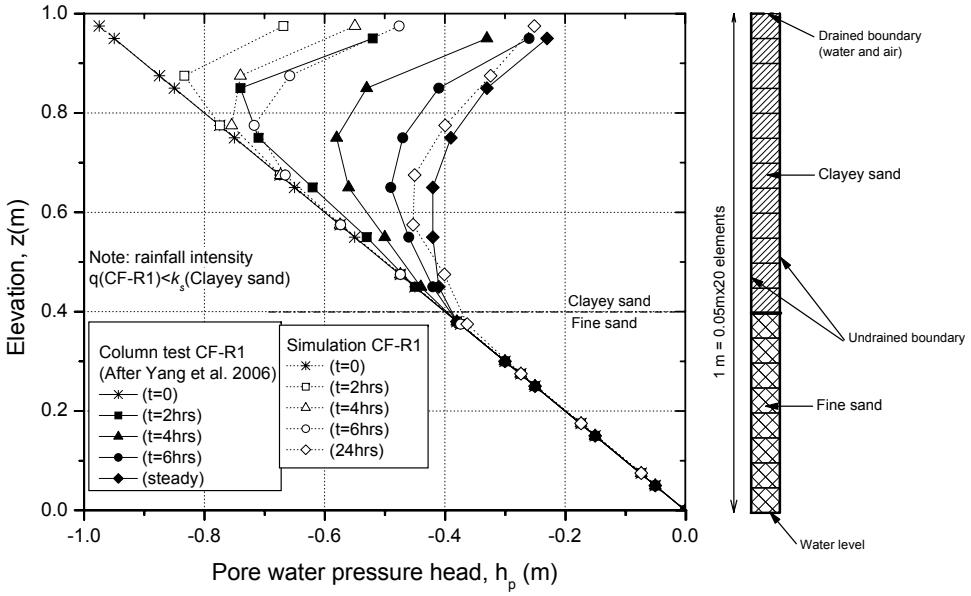

Figure 4.31 Pore-water head profile CF-R1 (Test and simulation)

seen that the following features observed in the experiments are captured by the numerical calculation:

1. Pore water pressure increases initially at the surface of the clayey sand and gradually increases downward the soil column while the water infiltrates.

2. Pore water pressure is higher and infiltration is faster when the intensity of the rainfall is higher (CF-R2).

3. Pore water pressures were always negative even after 24h of rainfall infiltration and they did not develop in the fine sand layer.

4. Although the infiltration during the simulation was slower compared with the experiments, the final results were very close to the steady state measured.

Despite that the same rainfall intensities, permeabilities and soil water characteristic curves similar to those reported on the experiments were used for the numerical analysis, a time delay in the simulated infiltration is observed. This time delay can be explained mainly by the uncertainty in the soil water characteristic curve and permeabilities which are highly dependent of the void ratio. More accurate information about the soil water

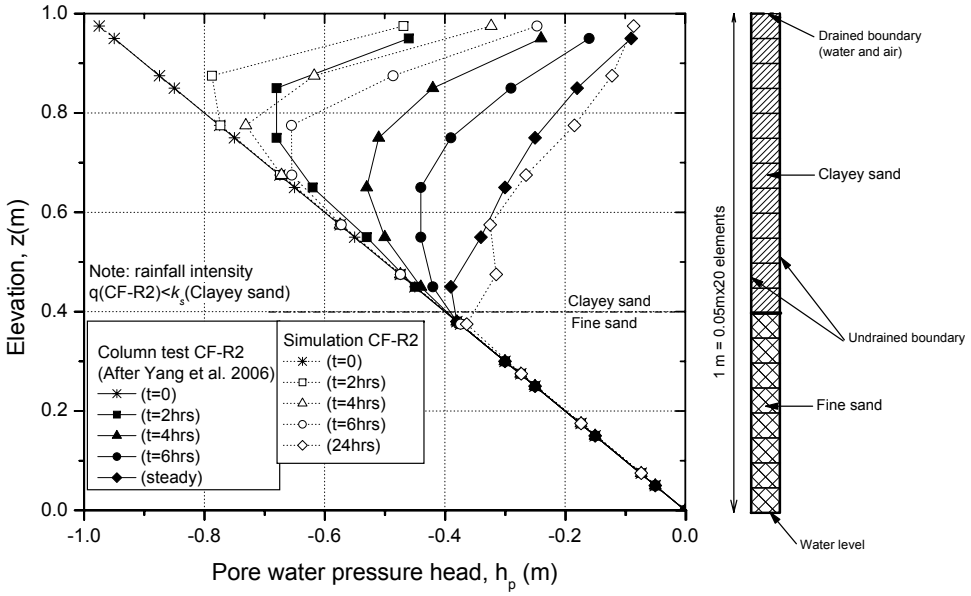

Figure 4.32 Pore-water head profile CF-R2 (Test and simulation)

characteristic curve and permeabilities are necessary to improve the simulation. It emphasizes the significance of the experimental data related to infiltration and deformation of unsaturated soils in the improvement of the numerical models in order to understand the complex response of unsaturated soils.

4.2.3 Summary

A multiphase coupled elasto-viscoplastic finite element analysis formulation based on the theory of porous media (Oka et al. 2006; Kimoto et al. 2007) is used to describe the rainfall infiltration process into a one-dimensional soil column. This formulation includes the effect of suction by the shrinkage or expansion of the OC boundary surface as well as the usage of the skeleton stress by taking into account the average fluid pressure (water and gas phases). This three phase-coupled analysis model can describe very well the reduction in suction, the increase in saturation, and the development of strain over space and time when a soil is subjected to rainfall infiltration.

From the parametric analyses, it is observed that parameters α and n' have a significant effect on the one-dimensional infiltration process. The steady states are reached faster for soils where parameter α is smaller, as well as for soils where parameter n' is larger.

It can be seen that the initial saturation in the column is important in regards to the time it takes to attain the steady state and it is controlled by these two parameters. Rainfall intensity also has a significant effect on the infiltration process; the higher the rainfall infiltration, the greater the pore water generated (a reduction in suction) along the column. Parameters s_{max} and a do not show a significant effect on the infiltration process.

The effect of the hydraulic parameters on the soil deformation is shown through the pore water pressure and the volumetric strain profiles obtained for all the simulations after 20 hours of rainfall infiltration. The results show a trend in larger positive volumetric strains for the higher pore water pressures. In contrast, when the pore water pressure is lower, either the positive volumetric strain is smaller or it changes to negative. Moreover, it is shown that the generation of the pore water pressure and the volumetric strain is mainly controlled by material parameters α and n' that describe the soil water characteristic curve. This shows that the deformation behavior of unsaturated soils is strongly dependent on the hydraulic behavior, which emphasizes the importance of seepage-deformation coupled methods for the analysis of rainfall infiltration.

From the results obtained through the simulations, it can be seen that the proposed multiphase finite element analysis can describe very well the characteristics observed during the experiments of the one-dimensional water infiltration into layered unsaturated columns. The model is useful for the study of the unsaturated response of multiple layered soils that are commonly found in practical geotechnical problems related to water infiltration such a rainfall- and seepage-induced instability.

In the future, it is necessary for the full validation of the seepage-coupled methods to perform tests on infiltration in unsaturated soils with complete measurement of the hydraulic and the deformation characteristics.

Chapter 5

SIMULATION OF RAINFALL INFILTRATION ON UNSATURATED SOIL SLOPES

5.1 Introduction

Failure of unsaturated slopes is a common phenomenon all over the world. Although, it can be attributed to many factors, such as geology, topography, hydrological conditions, material properties, and human action; it has been widely recognized that the water infiltration has a dominant effect on the slope instability. Many researchers have reported on the embankment and slope failure due to the rainfall infiltration. For instance, Yoshida et al. (1991) and Matsushi et al. (2006) presented a series of shallow-depth slope failures occurred in Japan as a result of heavy torrential rainfalls. In the same manner, Yamagishi et al. (2004, 2005) described different landslides in Niigata Japan induced by heavy-rainfall and melting snow. Nakata et al. (2010) investigated the failure mechanics of an expressway embankment due to the heavy rainfall cause by the passage of a typhoon in Yamaguchi prefecture in Japan. Similarly, Chen et al. (2006) discussed the factors triggering landslide-induced debris flows by the passage of a typhoon in Taiwan. Au (1998); reviewed some of the slope failures that have occurred in Hong Kong and showed that most of the slope failure were rain-induced. Alonso et al. (2003) presented a case study of an unsaturated slope in overconsolidated clays in Italy and showed its deformation and stability responses due to rainfall infiltration.

Failure of soil structures can be triggered by a wetting process (e.g. both short and

long infiltration caused by rainfall or melting snow) from an unsaturated state as a result of the increase of the moisture content and the reduction of suction. This, in turn, leads to a decrease in the shear strength of the soil and the development of deformations. The study of the rainfall infiltration-deformation behavior on unsaturated soils is very complex because it is controlled by many variables associated to the non-linear hydraulic and constitutive properties of the soil, as well as the rainfall characteristic. Rainfall infiltration becomes an interesting subject due to the need of understanding its effects on the increase of the pore water pressure and the generation of deformation in unsaturated slopes.

Some studies have addressed the effect of the rainfall infiltration on the slope stability from the point of view of the statistical approach (e.g. Au, 1993; Okada and Sugiyama 1994). On the other hand, several researchers have been implementing numerical solutions to analyze the effect of the hydraulic characteristics on the instability of unsaturated slopes (e.g. Ng and Shi, 1998; Tsaparas et al., 2002; Cai and Ugai, 2004; Rahardjo et al., 2007). In these formulations, the effects of the rainfall infiltration on the generation of the pore water pressure and the instability of the slope are generally evaluated by a seepage analysis using the finite element method and followed by the slope stability analysis; thus, the study of the coupling of the deformation and the transient flow is disregarded. However, the deformation behavior of unsaturated soil is strongly dependent on the seepage flow and vice versa. Accordingly, rainfall infiltration-deformation problems are better formulated by the use of coupled seepage-deformation methods. Numerical methods that can simultaneously consider the unsaturated seepage flow and the deformation of soil structures have been used to study the infiltration process. For instance, Cho and Lee (2001) studied the effect of rainfall on the development of pore water pressure, shear strain and the stability of homogeneous and non-homogeneous slopes. Alonso et al. (2003) investigated the displacements and safety factors for weathered overconsolidated clay. Ehlers et al. (2004) analyzed the deformation and localization of strains on unsaturated embankments and excavations due to seepage infiltration. Ye et al. (2005) analyzed a large-scale progressive failure in a soft-rock slope due to heavy rainfall. Oka et al. (2009) and Kato et al. (2009) investigated the coupled seepage-deformation characteristics of unsaturated river embankments due to the increase of the water level. Although the seepage-deformation coupled methods have become more popular for the study of unsaturated seepage flow; the particular case of the rainfall infiltration problem and its effects on the development of deformations in unsaturated slopes has not yet been fully

addressed or understood.

In this chapter, the multiphase coupled elasto-viscoplastic finite element formulation proposed by Oka et al. (2006) is used to describe the rainfall infiltration process and its effect on the development of pore water pressure and deformation into an unsaturated slope. A significant feature of the analysis presented herein is the use of a coupled seepage-deformation model which allows the calculation of the displacements along with the reduction of suction or increase of the pore water pressure. The numerical analysis are base on Biot's theory (1941, 1962) extended by the theory of porous media, e.g., Atkin and Craine, 1976; Bowen, 1976; Coussy, 2004; Boer, 1998; Ehlers, 2003. The materials are assumed to be composed of solid, water, and gas phases, which are assumed to be continuously distributed throughout space at macroscopic level. An elasto-viscoplastic constitutive model is adopted for the soil skeleton. The skeleton stress, which is determined from the difference between the total stress and the average pore fluid pressure, is used for the stress variable in the constitutive model. In addition, the effect of suction is expressed as the shrinkage or the expansion of the overconsolidation (OC) boundary surface and the static yield surface (Oka et al. 2006).

A numerical analysis, which focuses on a parametric study including different water levels, saturated water permeabilities and rainfall patterns, is carried out to observe the influence of these hydraulic characteristics on the changes of the pore water pressure and the saturation, as well as on the progress of the lateral displacement and the viscoplastic shear strain during the rainfall infiltration into unsaturated slopes. From the parametric study, it is shown that both the saturated water permeability and the rainfall patterns have a dominant effect on the generation of the pore water pressure and deformation. It is also shown that the rainfall infiltration-deformation process is significantly controlled by the relation between the rainfall intensity to the saturated water permeability. Results obtained by the simulations show that the finite element formulation describes very well the characteristics of the transient seepage flow due to rainfall into unsaturated slopes.

5.2 Numerical analysis of an unsaturated slope

The elasto-viscoplastic model for unsaturated soil described in Section 2.3 and the multiphase finite element formulation described in Section 2.4 are used to simulate the rainfall infiltration into the unsaturated slopes. In this formulation, an updated Lagrangian

method with the objective Jaumann rate of Cauchy stress is adopted (Kimoto et al. 2004; Oka et al. 2006). The independent variables are the pore water pressure, the pore air pressure, and the nodal velocity. In the finite element formulation, an eight-node quadrilateral element with a reduced Gaussian integration is used for the displacement, and four nodes are used for the pore water pressure and the pore air pressure. The backward finite difference method is used for the time discretization.

The finite element mesh and the boundary conditions for the simulation of the rainfall infiltration into the unsaturated slopes are shown in Figure 5.1. The mesh is finer close to the surface where the high hydraulic gradients due to the rainfall infiltration are expected. For the displacement, the slope is fixed at the bottom in both horizontal and vertical directions, the laterals boundaries are fixed only in horizontal direction. The initial negative pore water pressure distribution (suction) is considered to be linear. The water level in the soil is assumed to be located at different heights from 2.0 to 5.0 m measured from the bottom impermeable boundary. The flux of air is allowed for the entire boundaries and the initial air pressure, P_i^G, is assumed to be zero. The boundary conditions for water flux are described in this manner: an impermeable boundary is assigned to the bottom or soil foundation; for the lateral sides of the slope below the water level the boundary is considered permeable; and above the water level the boundary is initially impermeable, but it changes to permeable if the pore water pressure turns positive; the toe, slope and crest of the slope are assumed to be rainfall boundaries. The rainfall boundary is described more in detail in the followings.

5.2.1 Rainfall boundary

When a rainfall starts on an unsaturated soil the infiltrated water increases the saturation and the pore water pressure within the slope. Horton (1933) described the concepts of infiltration rate and infiltration capacity and showed that the rate of infiltration decreases with time and approaches to a constant and minimum infiltration rate (see Figure 5.2). The minimum infiltration rate, k_0 , is often assumed to be equal to the saturated water permeability, k_s^W (Lu and Likos, 2004). Assuming that there is always water available on the soil surface due to the rainfall, at the initial stage of the infiltration, the unsaturated soil has the enough capacity to allow the whole water to infiltrate into the soil; however, once the soil surface is saturated, ponding occurs and the excess of water either accumulates on the surface or dissipates as runoff. Figures (5.3) and (5.4) show the sketches of the

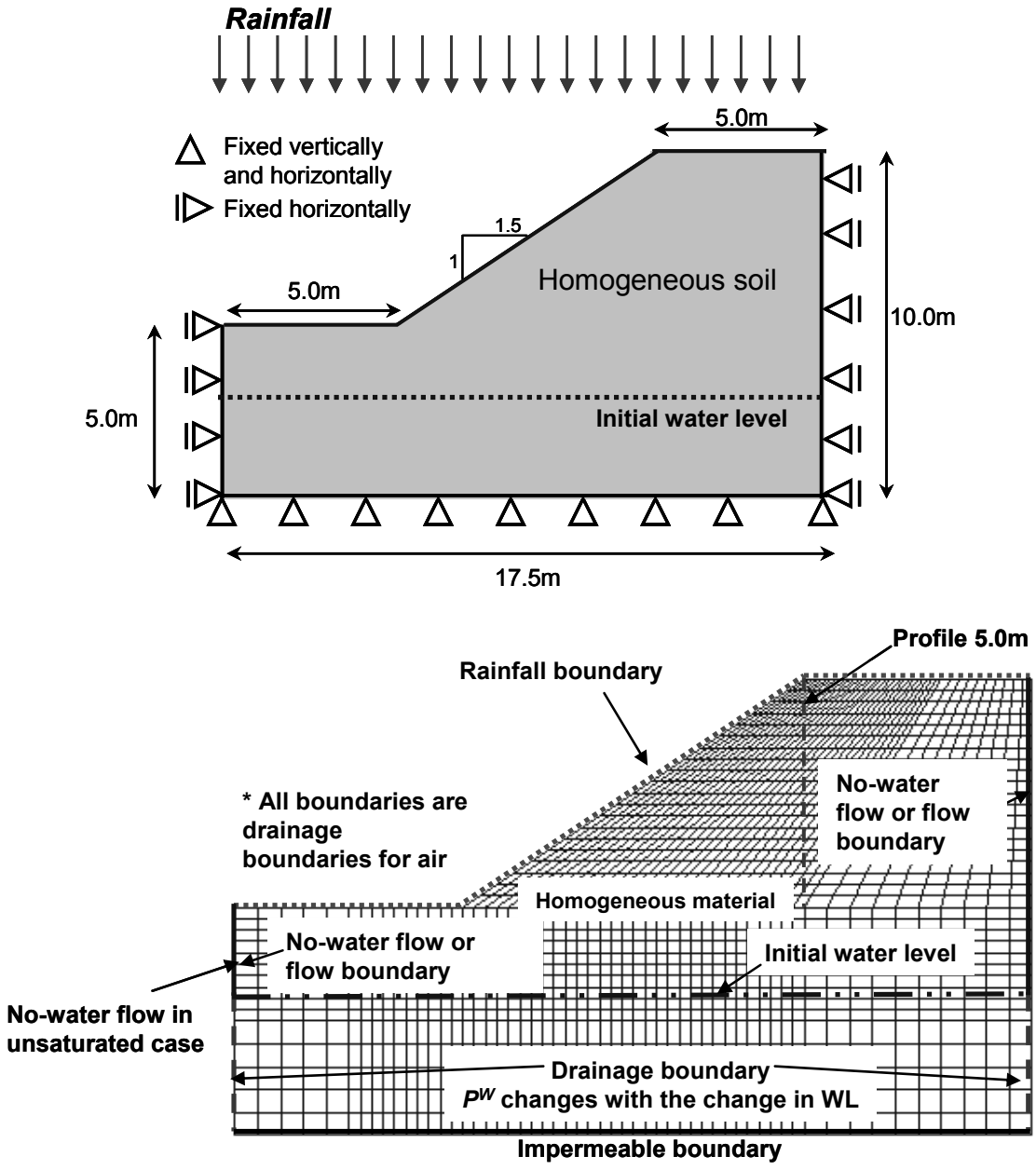

Figure 5.1 Finite element mesh and boundary conditions

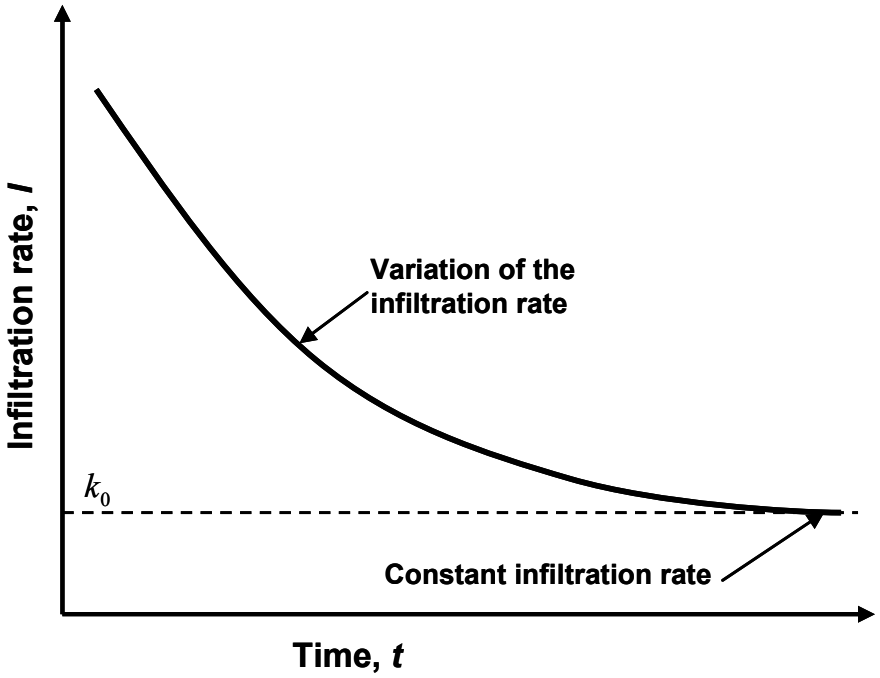

Figure 5.2 Variation of the infiltration rate with respect to the time (Horton, 1993)

rainfall boundary used to simulate this kind of behavior, the rainfall boundary is switched from a flow boundary to a pore water pressure boundary and vice versa according to the rainfall intensity and the saturation of the soil surface, as follows:

- *Case 1*: Unsaturated soil and rainfall intensity smaller or equal than the minimum infiltration rate, i.e., $s < s_{max}$ and $I \leq k_0 = k_s^W$. A prescribed flow boundary is used and the whole water infiltrates into the soil (Figure 5.3(a))

- *Case 2*: Unsaturated soil and rainfall intensity larger than the minimum infiltration rate, i.e., $s < s_{max}$ and $I > k_0 = k_s^W$. A prescribed pore water pressure boundary is used on the surface; in this case, the incoming of water within the soil is controlled by the gradient of the matric suction. The pore water pressure assigned on the surface is calculated according with the rainfall intensity. In the simulation it is assumed that the excess of water is dissipated as runoff (Figure 5.3(b)).

- *Case 3*: Unsaturated soil without rainfall intensity (rainfall stops), i.e., $s < s_{max}$ and $I = 0$. An impermeable boundary is assigned on the surface. In this case, water will drain down and the saturation of the soil close to the surface decreases (Figure 5.3(c)).

- *Case 4*: Saturated soil without rainfall intensity (rainfall stops), i.e., $s = s_{max}$ and $I = 0$. A drained boundary is prescribed on the saturated surface. In addition, if the pore water pressure on this boundary turns positive, the excess of water within the slope is drained out as shown in Figure 5.4(a).

- *Case 5*: Combined Saturated and unsaturated soil and rainfall intensity smaller or equal than the minimum infiltration rate, i.e., $s \leq s_{max}$ and $I \leq k_0 = k_s^W$. For this case, a flow boundary is prescribed for the unsaturated soil and a drained boundary is precribed for the saturated soil. When the pore water pressure turns positive inside the slope, drainage of water is allowed in the saturated side as shown in Figure 5.4(b)).

- *Case 6*: Combined saturated and unsaturated soil and rainfall intensity larger than the minimum infiltration rate, i.e., $s \leq s_{max}$ and $I > k_0 = k_s^W$. A prescribed pore water pressure boundary is used on the surface. It is assumed that the excess of water within the slope is drained out as shown in Figure 5.4(c).

Similar rainfall boundaries controlled by the rainfall intensity and the saturation of the soil have been used for the analysis of rainfall infiltration and slope stability (Gitirana et al., 2005; Alonso et al., 2003; Tsaparas et al., 2002; Cho and Lee, 2001).

The material parameters required by the constitutive model described in Section 2.3 are listed in Table 5.1. The parameters have basically been determined from fully drained triaxial tests using silty clay (drained test for water and air), referred to as DL clay. The soil water characteristic curve for the DL clay is shown in Figure 5.5. In order to study the effect of the initial suction, the saturated water permeability of the soil, and the rainfall pattern on the hydraulic and deformation behaviour of the unsaturated slopes, different combinations of initial water levels, (WL=2.0, 3.0, 4.0 and 5.0 m), saturated water permeabilities ($k_{sv}^W = k_s^W$, $2k_s^W$, $5k_s^W$ and $10k_s^W$) and rainfall intensities ($R-1$, $R-2$, and $R-3$) were chosen for the simulations and they are shown in Table 5.2. The rainfall patterns used for the analysis are shown in Figure 5.6. The rainfall pattern $R-1$ corresponds to the rainfall pattern recommended by the Japan Institute of Construction Engineering (2002) for the seepage analysis of river embankments. This rainfall pattern consists of two different minor and major rainfalls; the minor rainfall event of 200 mm total rainfall is distributed evenly over a period of time equal to 200 h (I= 1.00 mm/h), and a major rainfall event of 300 mm total rainfall is distributed evenly over a period

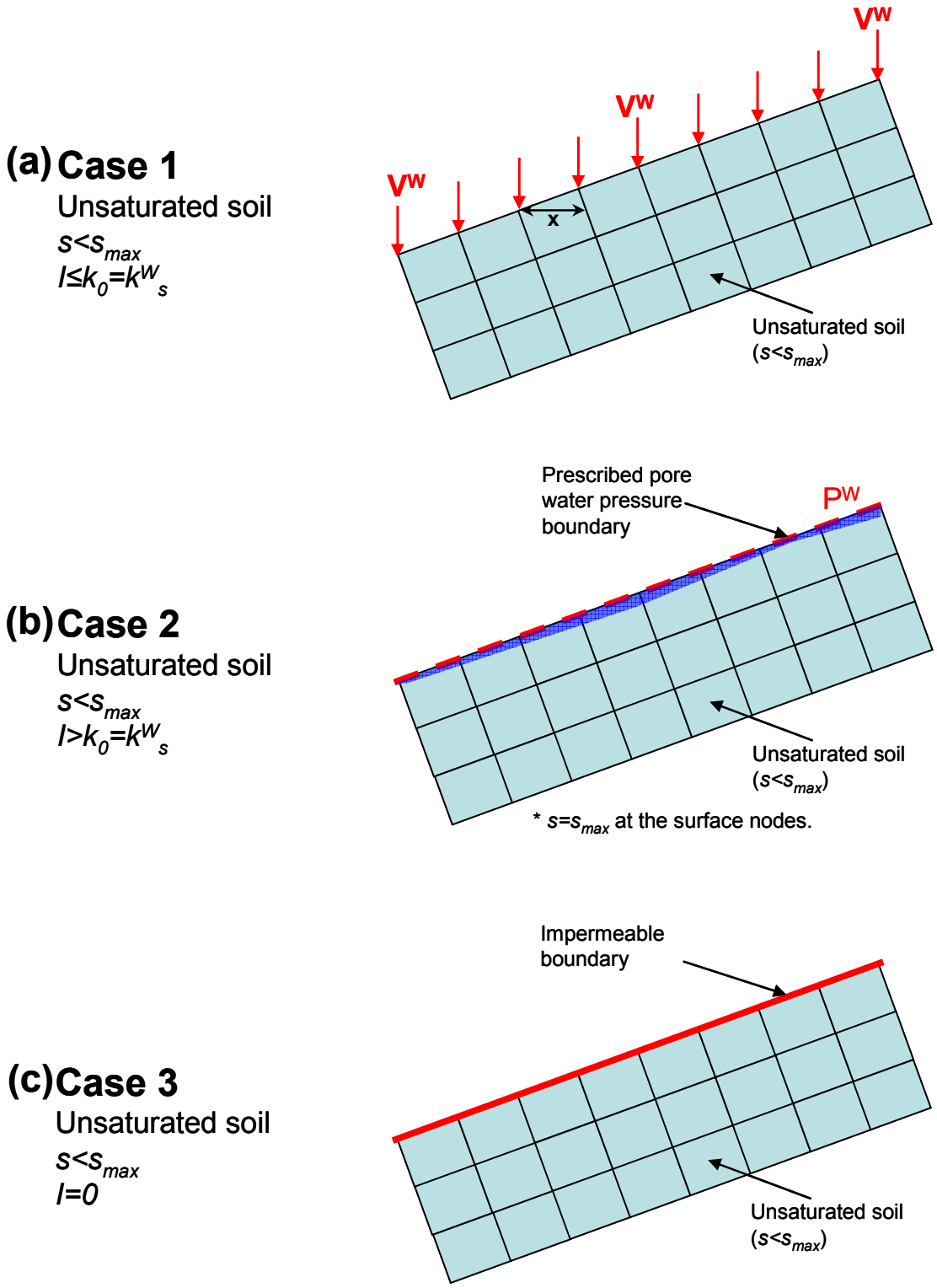

Figure 5.3 Rainfall boundary conditions applied on the surface of the slope. Unsaturated cases.

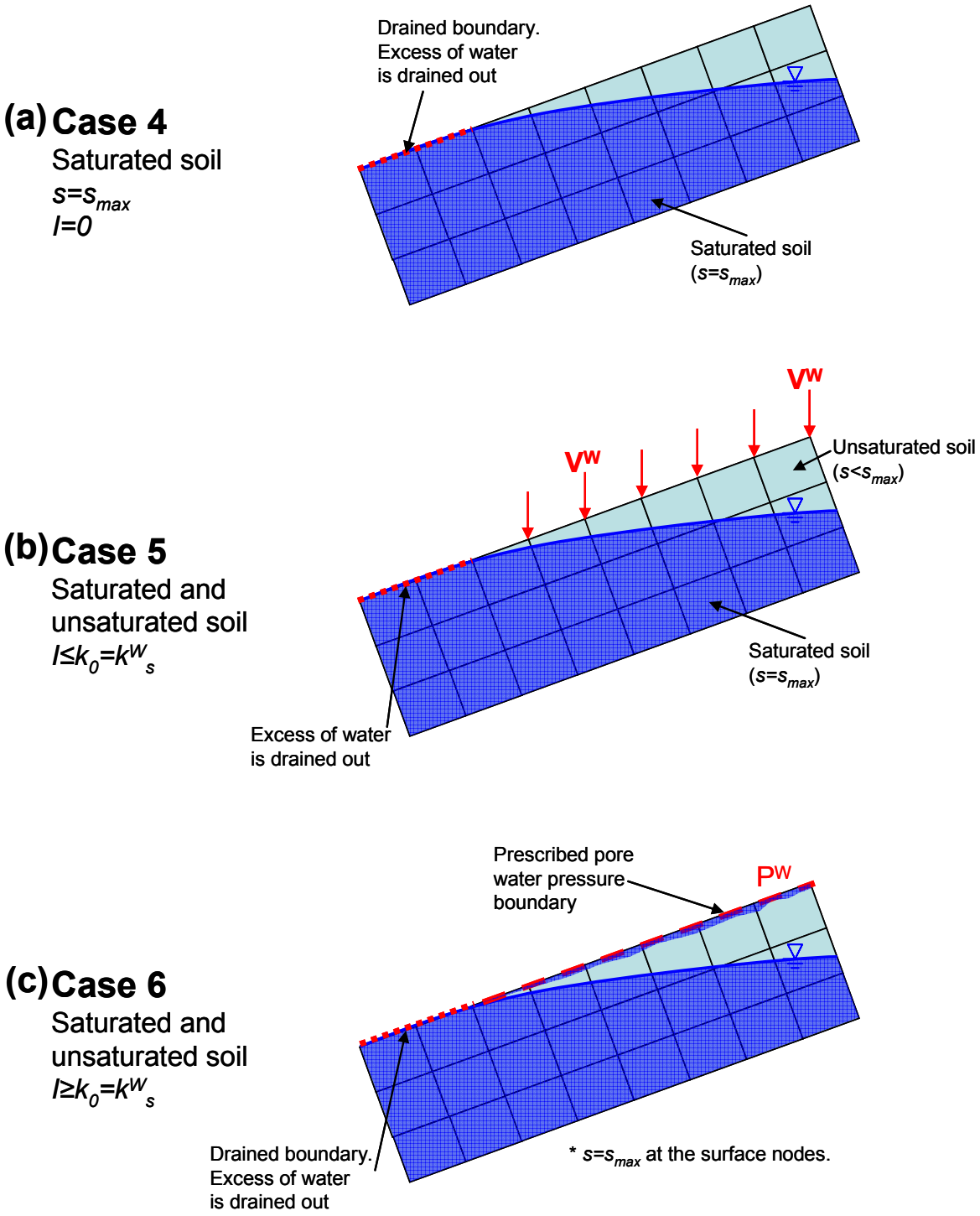

Figure 5.4 Rainfall boundary conditions applied on the surface of the slope. Combined saturated and unsaturated cases.

Table 5.1 Material parameters of the DL Clay

Viscoplastic parameter	$m^{'}$	23.0
Viscoplastic parameter (1/s)	C_1	1.3 x 10^{-11}
Viscoplastic parameter (1/s)	C_2	2.3 x 10^{-11}
Stress ratio at critical state	M_m^*	1.01
Coefficient of gas permeability at s=0 (m/s)	k_s^G	1.00 x 10^{-3}
Compression index	λ	0.144
Swelling index	κ	0.0186
Initial elastic shear modulus (kPa)	G_0	4000
Initial void ratio	e_0	1.03
Structural parameter	β	0.0
Van Genuchten parameter (1/kPa)	α	0.13
Van Genuchten parameter	n'	1.65
Suction parameter	S_I	0.20
Suction parameter	s_d	5.00
Minimum saturation	s_{min}	0.0
Maximum saturation	s_{max}	0.99
Shape parameter of water permeability	a	3.0
Shape parameter of gas permeability	b	1.0

of time equal to 30 h (I= 10.00 mm/h). For the rainfalls patterns $R-2$ and $R-3$, the major rainfall is distributed evenly along smaller periods of time ($R-2$: 15 h, $R-3$: 5 h, respectively), which leads to higher rainfall intensities ($R-2$: I= 20.00 mm/h, $R-3$: I= 60.00 mm/h, respectively), as shown in Figure 5.6.

5.3 Numerical results

An example of the numerical results obtained for the saturation distribution corresponding to the rainfall pattern $R-1$, the water level 5.0 m, the saturated water permeability k_{sv}^W=k_s^W=1.0 x 10^{-6} m/s, and for the rainfall infiltration times t=100h, 200 h, 215h, and 230h are shown in Figure 5.7. In this figure, it is seen that when the rainfall is applied, the saturation of the slope increases notably in depths relatively close to the soil surface, and gradually the wetting front progresses inside the slope when the time increases. For times t=100 h and t=200 h, when the rainfall intensity is smaller than the saturated water

Table 5.2 Studied cases for the unsaturated slopes

Effect of initial suction	Effect of saturated permeability	Effect of rainfall pattern
Initial water level (m)	Vertical permeability (m/s)	Rainfall pattern
2.0	k_{sv}^W=k_s^W=1.0 x 10^{-6}	$R-1$
3.0	k_{sv}^W=$2k_s^W$=2.0 x 10^{-6}	$R-2$
4.0	k_{sv}^W=$5k_s^W$=5.0 x 10^{-6}	$R-3$
5.0	k_{sv}^W=$10k_s^W$=1.0 x 10^{-5}	

*The horizontal permeability is 10 times the vertical permeability $k_{sh}^W = 10k_{sv}^W$

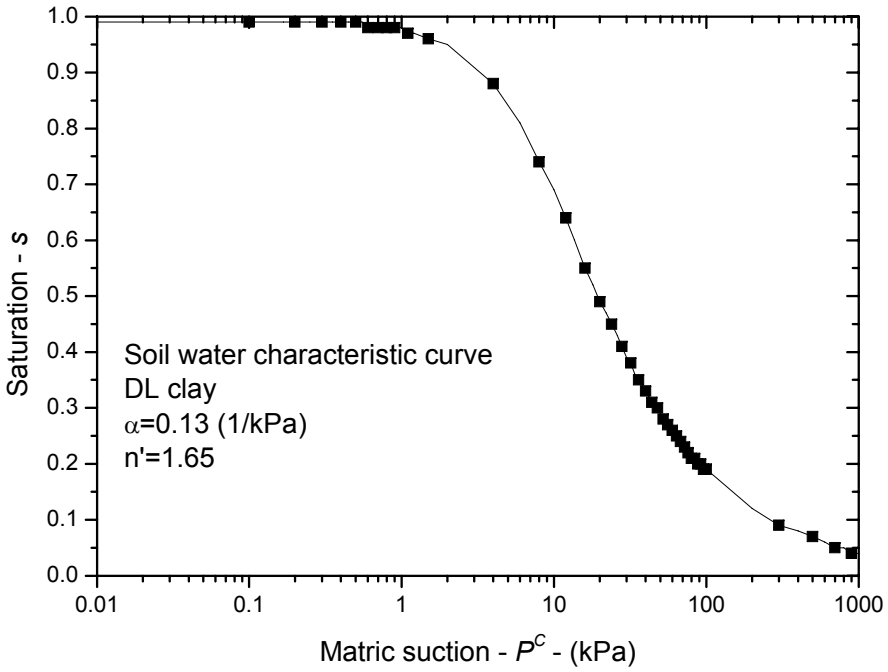

Figure 5.5 Soil water characteristic curve for the DL Clay

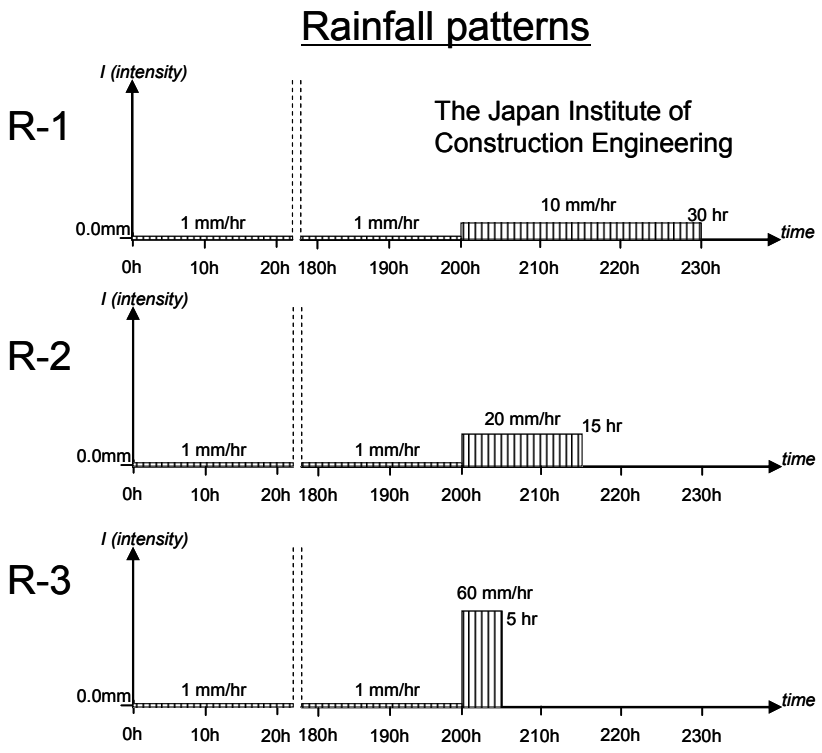

Figure 5.6 Rainfall patterns for the infiltration analyses

permeability, $I < k_{sv}^{W}$, the soil above the water level remains unsaturated and the wetting front reaches a maximum saturation about 0.70. At the time t=200 h, the major rainfall starts to be applied on the slope surface (I= 10.00 mm/h) for a total period of time t=30 h. In this case, the rainfall intensity is larger than the saturated water permeability of the soil, $I > k_{sv}^{W}$; the surface of the slope starts to saturate, as well as the depth of saturation increases with the advancing of time due to the sufficient amount of water provided on the slope surface.

Pore water pressure and saturation profiles below the crest of the slope, corresponding to the time intervals 0, 100, 200, 215, and 230 h during the rainfall infiltration process are shown in Figures 5.8 and 5.9, respectively. The initial state of t=0h corresponds to a linear distribution for the pore water pressure when the water table is at the toe of the slope (5.0 m from the bottom). When t is greater than zero, a rainfall with the intensity equal to 1.00 mm/hr is applied on the slope surface and the pore water pressure and saturation are increased in the soil. After 100 h of rainfall infiltration, the pore water pressure and saturation increased especially close to the soil surface; and they grow downward as the wetting front advances. At the time t=200h, the rainfall intensity is increased to 10.00

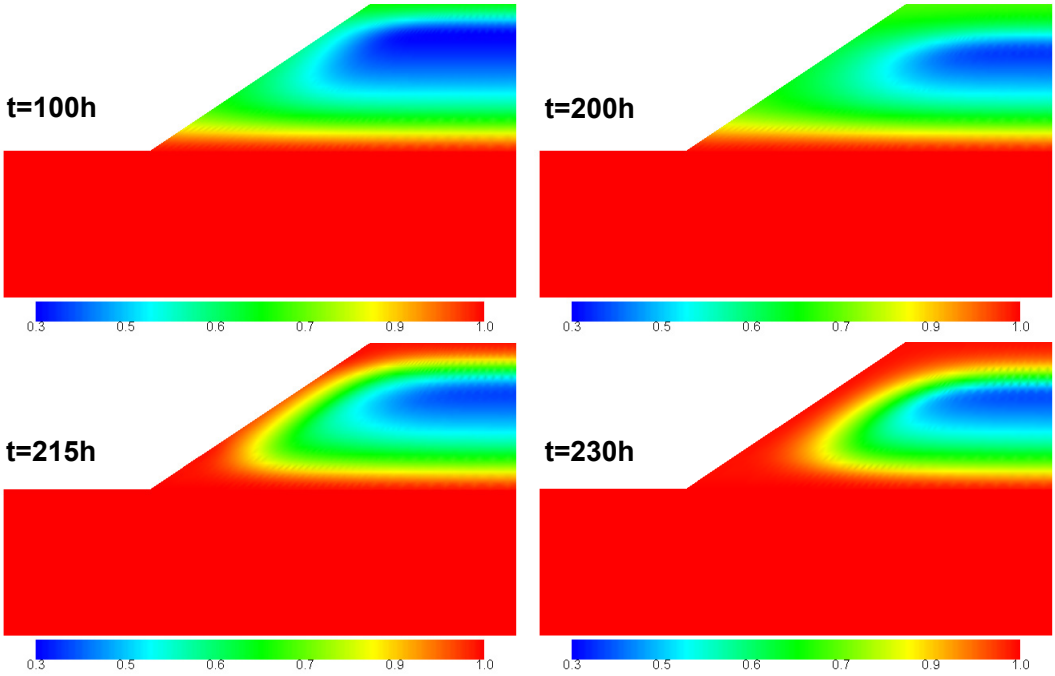

Figure 5.7 Saturation distribution (WL=5.0 m, $R-1$, $1k_s^W$)

mm/hr; after 215 h of rainfall, the negative pore water pressure on the surface is reduced to zero and the saturation reaches its maximum value.

The effect of the rainfall infiltration on the lateral displacement below the crest of the slope is shown in Figure 5.10. The pattern of deformation is associated with the volume change of the soil as the suction reduces (pore water pressure increases) due to the water infiltration. It is seen from the figure that the lateral displacement increases with time as the pore water pressure increases (see Figure 5.8). The lateral displacement is larger around the crest of the slope and it decreases with the increase in depth. Similarly, Figure 5.11 shows the calculated viscoplastic shear strain profiles. The viscoplastic shear strain is smaller in the soil close to the surface but suddenly starts to increases with the increase in depth. A maximum value for the viscoplastic strain is obtained at the middle height of the slope (z=7.5 m), afterward the viscoplastic strain decreases with the increase in depth (z from 7.5 to 5.0 m).

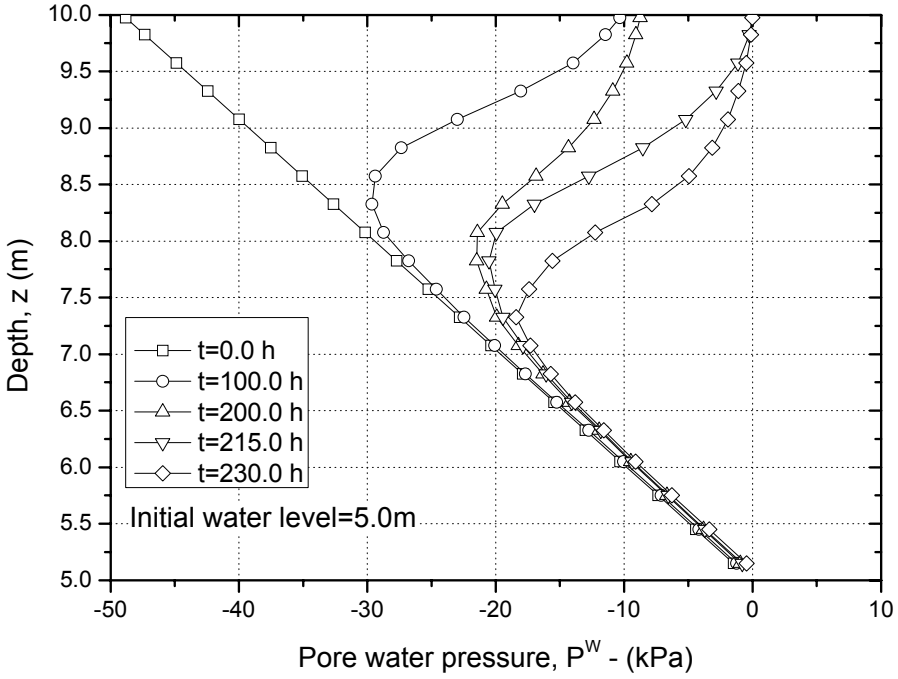

Figure 5.8 Pore water pressure profile (WL=5.0 m, $R-1$, $1k_s^W$)

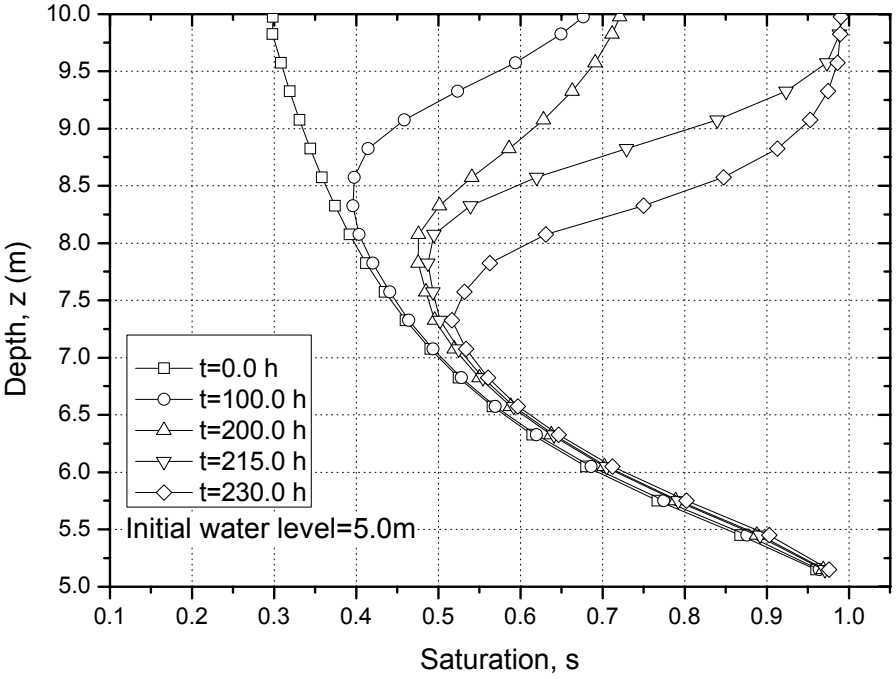

Figure 5.9 Saturation profile (WL=5.0 m, $R-1$, $1k_s^W$)

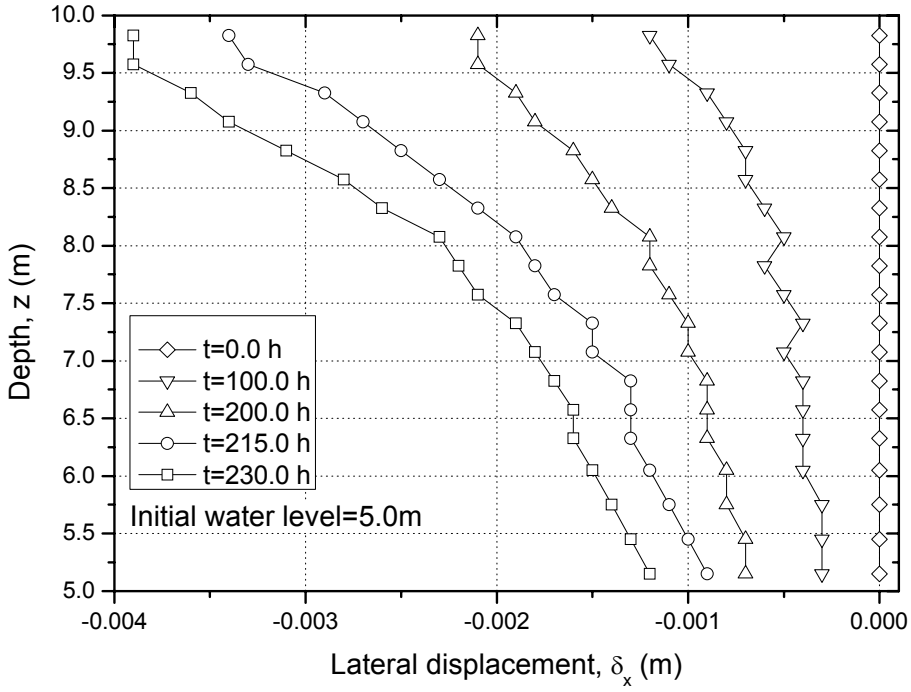

Figure 5.10 Lateral displacement profile (WL=5.0 m, $R-1$, $1k_s^W$)

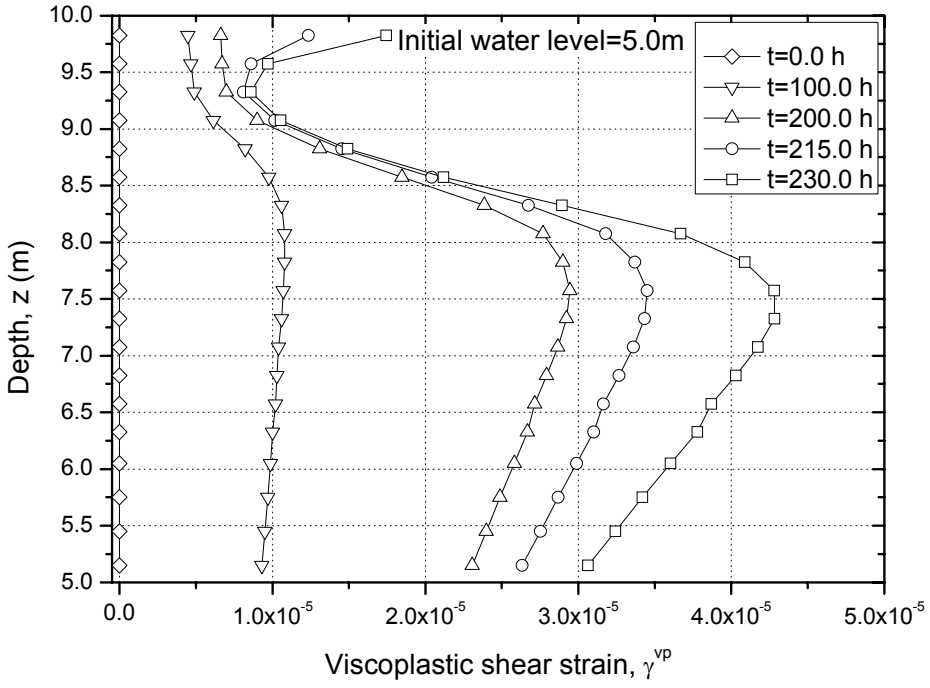

Figure 5.11 Viscoplastic shear strain profile (WL=5.0 m, $R-1$, $1k_s^W$)

5.3.1 Effect of initial suction

5.3.1.1 Pore water pressure and saturation profiles

The comparisons of the pore water pressure and saturation profiles at the times intervals t=200 and t=230 h for the four different initial water levels (i.e. WL= 2.0, 3.0, 4.0 and 5.0 m), the rainfall pattern $R-1$, and the saturated water permeability $k_{sv}^W = k_s^W$ are shown comparatively in Figure 5.12. This figure also includes the initial pore water pressure and saturation profiles at t=0 h. Figure 5.12(a) shows that after 200 h of rainfall, the pore water pressure are slightly different at shallow depths, but this difference increases with the increase in depth; the larger pore water pressures profiles are obtained for the higher initial water levels. Figure 5.12(b) shows the pore water profile after 230 h (30 h after the major rainfall); in this case, it is observed that the pore water pressures close to the surface are the same, regardless of the initial water level (Depth from 9.0 to 10.0 m), afterward the difference in pore water pressure starts to increase and the larger pore water pressures are obtained for the higher water levels. It suggests that the effect of the initial water level on a slope has either a minimum or negligible effect on the shallow depths; nevertheless, there is a great effect on the pore water distributions at the deeper soil. This result is the same result obtained by Tsaparas et al. (2002), who analyzed the development of pore water pressure in time at the crest of unsaturated slopes with different initial suction profiles. Similar conclusions can be obtained from the saturation profiles at times t=200 and t=230 h that are shown comparatively in Figures 5.12(c) and 5.12d), respectively.

5.3.1.2 Lateral displacement and viscoplastic shear strain profiles

Figures 5.13(a) and (b) show the comparisons of the lateral displacement and viscoplastic shear strain profiles, respectively, corresponding to the four different initial water levels (i.e. WL= 2.0, 3.0, 4.0 and 5.0 m), the rainfall pattern $R-1$, the saturated water permeability $k_{sv}^W = k_s^W$, and for the time interval t=230 h (after the major rainfall). From Figure 5.13(a) it is possible to see that the lateral displacements are larger for the case where the initial water level is 5.0 m and smaller for the case with initial water level 2.0 m. The maximum displacement takes place at the crest of the slope and it is approximately 4 mm. It suggests that unsaturated slopes with higher initial water levels are potentially more unstable due to the larger development of displacements during and infiltration process. This result can be compared to that obtained by Ng and Shi (1998) who showed that lower initial water levels have a significant influence on the increase of the safety

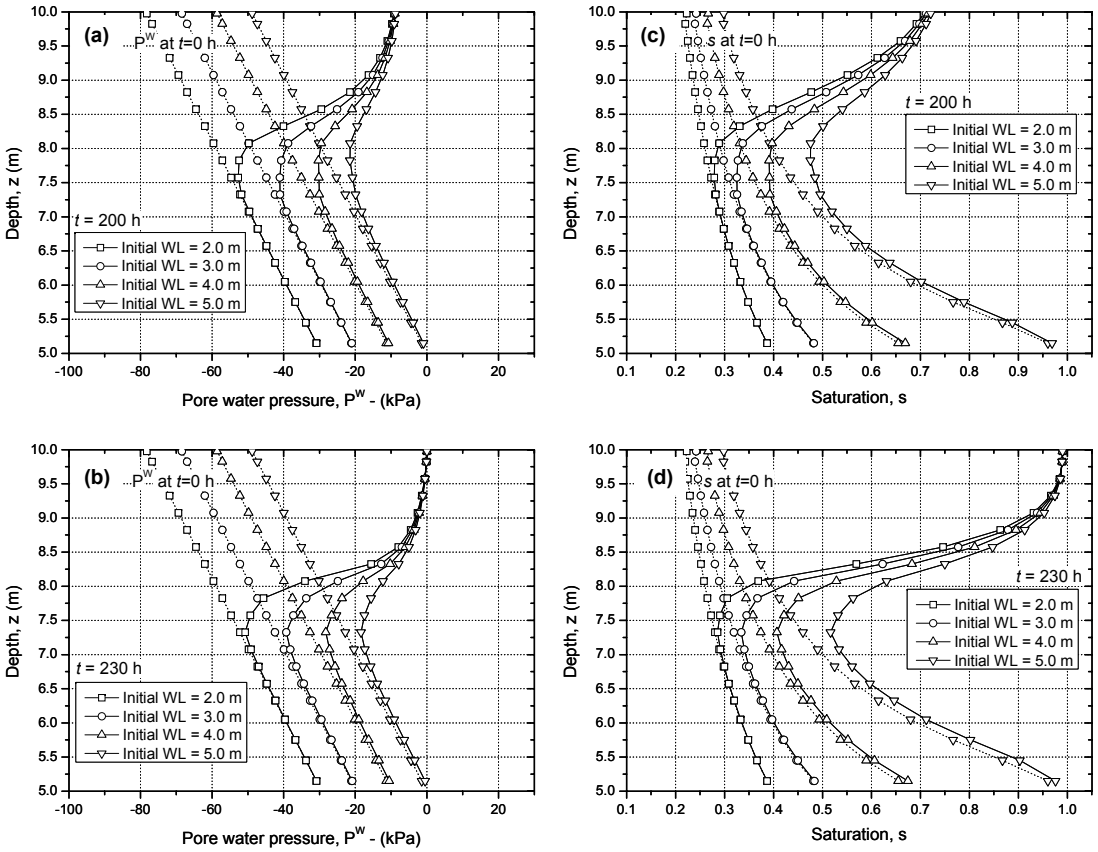

Figure 5.12 Comparisons for different initial water levels. (a) Pore water pressure profiles at t=200 h. (b) Pore water pressure profiles at t=230 h. (c) Saturation profiles at t=200 h. (d) Saturation profiles at t=230 h.

factor of unsaturated slopes subjected to rainfall infiltration. Figure 5.13(b) shows that the shear viscoplastic strains are very similar between the depths z=10.0 and z=8.0 m. The maximum viscoplastic shear strain is observed around the middle high of the slope (z=7.5 m) and it corresponds to the higher initial water level, WL=5.0 m; beyond this depth, the viscoplastic shear strain decreases with an increases in depth. The results of the deformation comparisons show that the larger deformation is obtained for the higher initial water level; that is, for the lower initial suction and the greater initial saturation.

5.3.2 Effect of the saturated water permeability

5.3.2.1 Pore water pressure and saturation profiles

Figure 5.14(a) presents the comparison of the pore water pressure profiles for the different water saturated permeabilities used for the simulations, namely, $k_{sv}^W = k_s^W$, $2k_s^W$, $5k_s^W$ and $10k_s^W$, at the end of the rainfall $(R-1)$, with maximum rainfall intensity I=10 mm/h

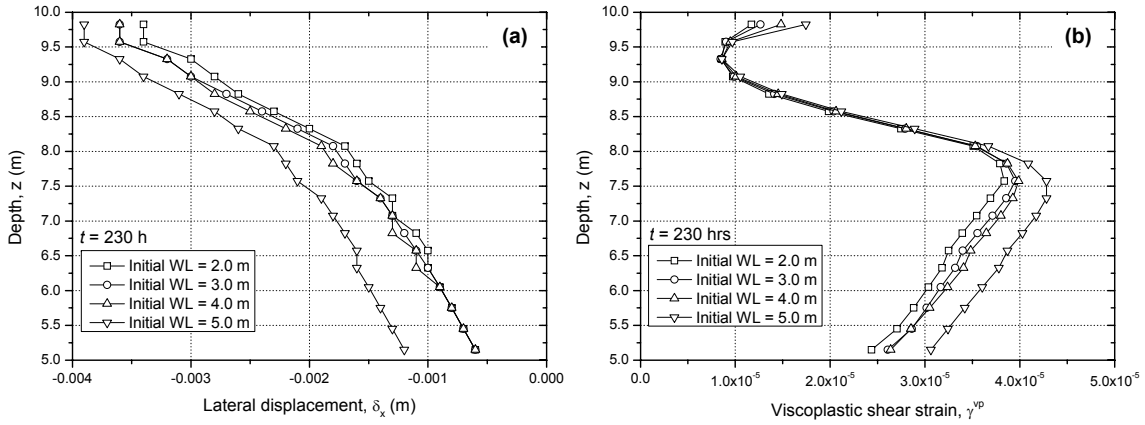

Figure 5.13 Comparisons for different initial water levels. (a) Lateral displacement profiles at t=230 h. (b) Viscoplastic shear strain profiles at t=230 h.

(2.78 x 10^{-6} m/s), and for a rainfall infiltration time equal to 230 h. From this figure, it is possible to see two different responses in the pore water pressure distributions along the selected profile below the crest of the slope (see Figure 5.1). In the cases when the rainfall intensity is larger than the permeabilities of the soil, i.e. I=2.78 x 10^{-6} m/s $> 2k_s^W$=2.00 x 10^{-6} m/s $> k_s^W$=1.00 x 10^{-6} m/s, the pore water pressures on the slope surface reach a value equal to zero. On the contrary, for the cases when the rainfall intensity is smaller than the permeabilities of the soil, I=2.78 x 10^{-6} m/s $< 5k_s^W$=5.00 x 10^{-6} m/s $< 10k_s^W$=1.00 x 10^{-5} m/s, the slope surface remains unsaturated (negative pore water pressure); the higher the saturated water permeability, the smaller the pore water pressure developed on the surface. These different behaviors can be explained by the relation between the infiltration rate and the saturated water permeability of the soil as shown schematically in Figure 5.2. During the infiltration process, if the saturated water permeability of the soil is smaller than the intensity of the rainfall, the infiltration capacity of the soil is exceeded after some time and only certain amount of water infiltrates into the soil; the excess of water accumulates on the surface or moves freely as runoff, it makes that the surface of the slope remains saturated. However, if the rainfall intensity is smaller than the saturated water permeability of the soil, the infiltration capacity of the soil is larger than the rainfall intensity, the whole water infiltrates the soil and not accumulation or excess of water appears on the surface, maintaining the slope surface unsaturated.

Figure 5.14(a) also shows an additional considerable difference in the pore water pressure results obtained for the different saturated water permeabilities. The pore water pres-

sures are larger at shallow depths for the permeabilities that are smaller that the rainfall intensity; and the pore water pressures are smaller for the cases when the permeabilities are larger than the rainfall intensity, between z=10.0 m and z=8.5 m. Nevertheless, when the depth increases, between z=8.5 m and z=7.5 m, this behavior is inverted and the pore water pressure becomes larger for the permeabilities that are larger than the rainfall intensity. These results can be explained in terms of the saturated water permeability. In the case of soil with low permeability, although the surface remains saturated during the rainfall, the water cannot be drained down quickly toward the water table, as a consequence, the pore water pressure develops closer to the slope surface. In contrast, for the high permeable soil the water does not accumulate on the surface and it can be drained down faster toward the water table, increasing the depth of the wetting front, as well as the pore water pressures at greater depths.

The results of the pore water pressure profiles obtained for the rainfalls $(R-2)$ and $(R-3)$, with maximum rainfall intensities I=20 mm/h and I=60 mm/h and for rainfall infiltration times equal to t=215 and t=205 h, respectively, are shown in Figures 5.14(b) and 5.14(c), respectively. The entire characteristics described above for the rainfall infiltration process into unsaturated slopes with different permeabilities are also obtained for these two different rainfall patterns. In the case of rainfall $(R-3)$, where the intensity I=60 mm/hr is larger than the four permeabilities used in the simulations, the pore water pressure at the surface becomes zero for all the simulated cases.

These results discussed above are consistent with the results obtained by Tsaparas et al. (2002) who investigated the influence of the saturated permeability and the rainfall distribution on the stability of unsaturated slopes; and the results by Zhan and Ng (2004) who studied the effect of hydraulic parameters and rainfall conditions on the one-dimensional infiltration into unsaturated ground.

The influence of the saturated water permeability on the saturation distribution along the selected profile for the same series of permeabilities and the rainfall patterns described above are shown in Figures 5.15(a) to (c). Generally, the same characteristics explained by the pore water pressure profiles can be understood from these figures. Larger saturations are obtained at the surface for soils where saturated permeabilities are smaller than the rainfall intensity; however, in the case of permeabilities larger than the rainfall intensities, the saturations at the surface are smaller. This trend for larger saturations is inverted

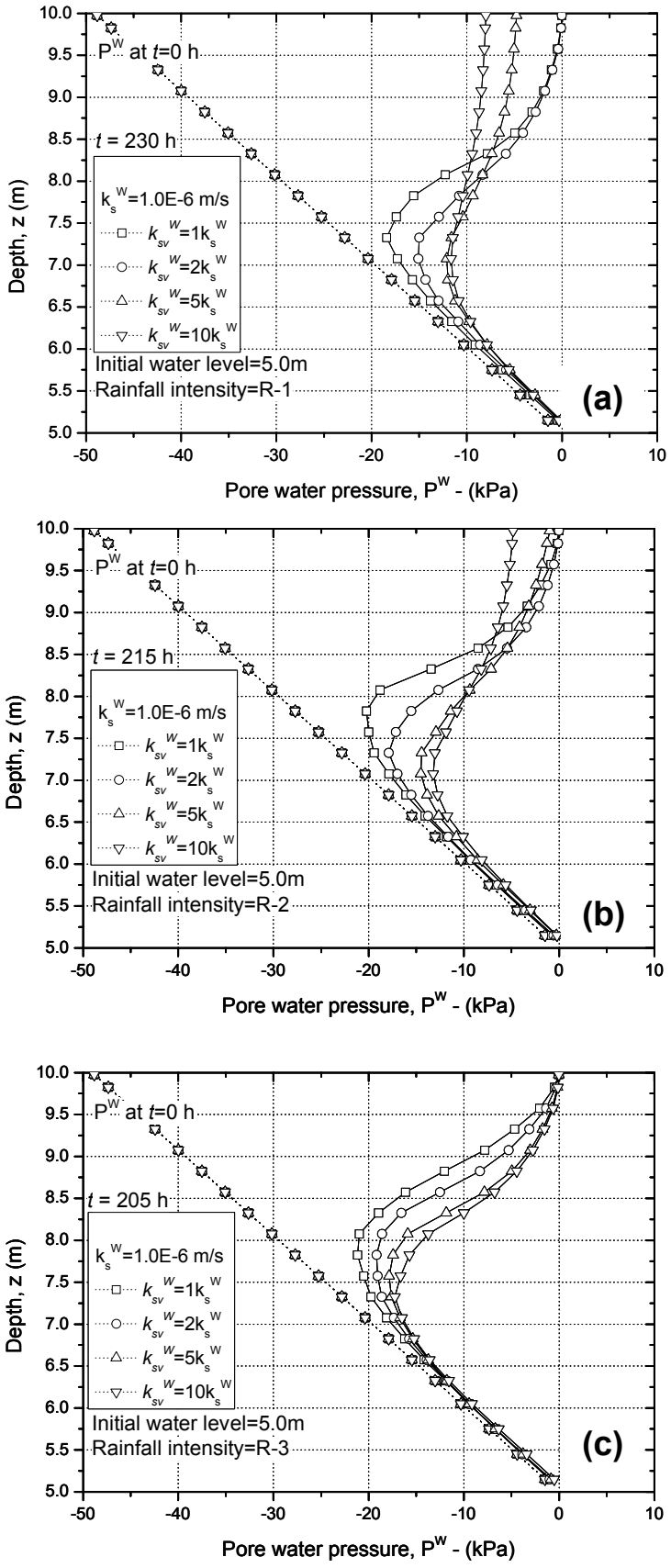

Figure 5.14 Pore water pressure profiles for different permeabilities. (a) Rainfall pattern $R-1$. (b) Rainfall pattern $R-2$. (c) Rainfall pattern $R-3$.

when the soil depth increases showing the higher saturation at greater depths for the larger permeabilities; correspondingly to the trend shown in the pore water pressure profiles. The similar results presented by both the pore water pressure and saturation profiles are explained by their relation in the unsaturated state (soil water characteristic curve); the larger the saturation, the larger the pore water pressure (reduction of suction) and vice versa.

5.3.2.2 Lateral displacement and viscoplastic shear strain profiles

The influence of the saturated water permeability on the deformation of the unsaturated slopes during the infiltration process is estimated by the comparison of the lateral displacement and viscoplastic shear stain profiles at the end of the rainfall infiltrations below the crest of the slope. The effect of the saturated permeabilities, namely, $k_{sv}^W = k_s^W$, $2k_s^W$, $5k_s^W$ and $10k_s^W$, on the lateral displacement of the unsaturated slope is shown in Figure 5.16(a) for the rainfall $(R-1)$ and the initial water level 5.0 m. From this Figure, it is seen that the maximum lateral displacements are obtained for the saturated water permeability k_{sv}^W=$2k_s^W$=2.00 x 10^{-6} m/s, which suggests that for a given rainfall intensity, there is a critical saturated water permeability which leads to the maximum deformation. This permeability value is the closest to the applied rainfall intensity (I=10 mm/hr = 2.78 x 10^{-6} m/s). The computed displacements are small, in the order or a few millimeters. The displacement profile along the depth shows that the motion of the slope reduces when the depth increases. Similarly, Figures 5.16(b) and (c) show the lateral displacement profiles for the cases of rainfalls $(R-2)$ and $(R-3)$, respectively. In these Figures, the maximum lateral displacements are obtained for the saturated permeabilities k_{sv}^W=$5k_s^W$=5.00 x 10^{-6} m/s and k_{sv}^W=$10k_s^W$=1.00 x 10^{-5} m/s, respectively. These permeabilities are also the closest to the applied rainfall intensities (I=20 mm/hr = 5.56 x 10^{-6} m/s and I=60 mm/hr = 1.67 x 10^{-5} m/s, respectively); which confirms that for given rainfall intensity, there is a critical saturated water permeability that develops the largest lateral deformations. As shown by Figures 5.16(a) to (c), the saturated water permeability has a significant influence in the slope deformation.

Zhan and Ng (2004) pointed out a similar observation about the critical rainfall intensity, indicating that the critical rainfall infiltration rate which leads to the largest total increase of the pore water pressure may be close to the saturated permeability of the soil. However, in the analysis presented by Zhan and Ng (2004), the deformation behavior of the soil was not investigated. Alonso et al. (2003) studied the rainfall infiltration process

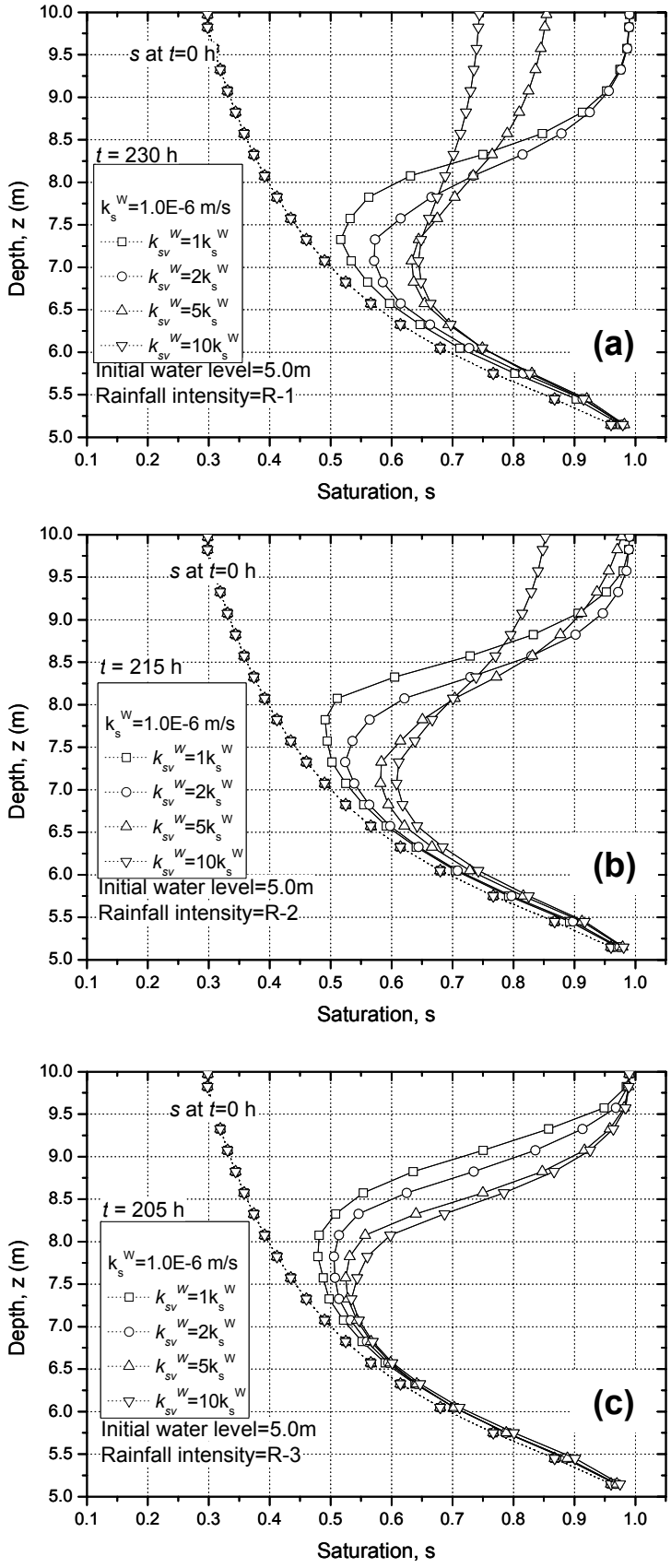

Figure 5.15 Saturation profiles for different permeabilities. (a) Rainfall pattern $R-1$. (b) Rainfall pattern $R-2$. (c) Rainfall pattern $R-3$.

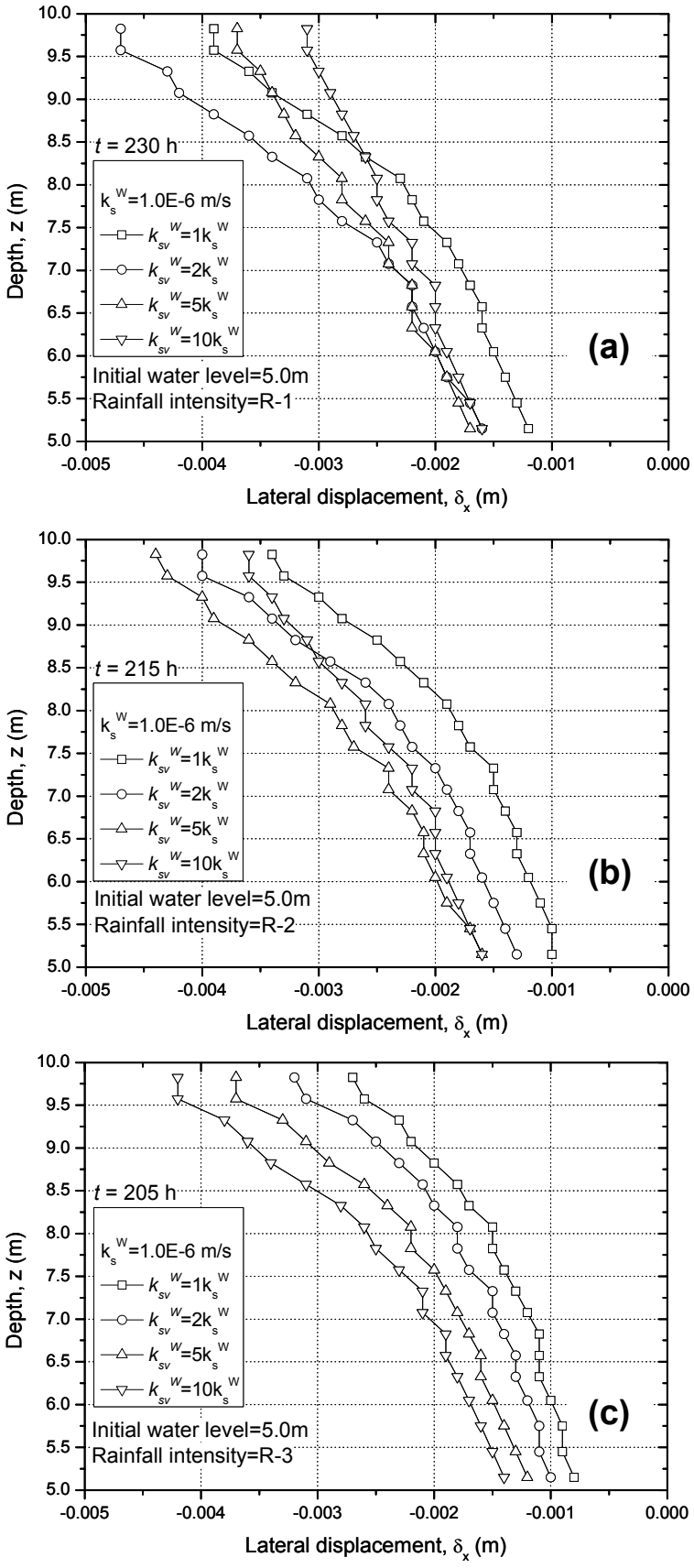

Figure 5.16 Lateral displacement profiles for different permeabilities. (a) Rainfall pattern $R-1$. (b) Rainfall pattern $R-2$. (c) Rainfall pattern $R-3$.

in an unsaturated layered slope compose of overconsolidated clays and found that there is a combination of soil saturated water permeabilities that leads to the larger generated pore water pressures for a given rainfall record.

The comparison of the viscoplastic shear strain profiles for the same saturated permeabilities as described above, and for the rainfall infiltrations $R-1$, $R-2$, and $R-3$ are shown in Figures 5.17(a) to (c), respectively. Generally, the viscoplastic shear profiles show that the larger values along depth are obtained at the middle high of the profile, and there is a trend for larger values of viscoplastic shear strains for the lower permeabilities than for the larger permeabilities. In addition, comparison of Figures 5.17(a) to (c) shows that the magnitudes of the shear strain are larger for the case when the rainfall intensity is smaller (i.e. Figure 5.17(a), rainfall $R-1$, I=10 mm/hr for 30 h). This may be explained by the longer time of infiltration during $R-1$, which developes the larger pore water pressures (larger reduction of suction) inside the soil slope as shown in Figure 5.14(a).

5.3.3 Effect of rainfall patterns

5.3.3.1 Pore water pressure and saturation profiles

Three different rainfall patterns are considered to show their effect of the rainfall intensity on the water infiltration problem into an unsaturated slope ($R-1$, $R-2$ and $R-3$ in Figure 5.6). The comparison of the pore water pressure profiles at the end of the different rainfall patterns (i.e. $R-1$: t=230 h, $R-2$: t=215 h and $R-3$: t=205 h) and for the saturated water permeabilities, namely, $k_{sv}^W = k_s^W$=1.0 x 10^{-6}, $2k_s^W$=2.0 x 10^{-6}, $5k_s^W$=5.0 x 10^{-6} and $10k_s^W$=1.0 x 10^{-5} m/s are shown in Figures 5.18(a) to (d), respectively. When the rainfall intensities are larger than the saturated water permeability, i.e. $I/k_{sv}^W > 1$, as for the cases with $k_{sv}^W = k_s^W$=1.0 x 10^{-6} and $2k_s^W$=2.0 x 10^{-6} m/s in Figures 5.18(a) and (b), respectively, the pore water pressures on the slope surface reached a value equal to zero. This is a result of the sufficient amount of water existing on the surface as explained previously. In these two cases, the pore water pressures increases along the soil profile from the ground surface and down to around 3 m in depth, according to the advance of the wetting front; the largest pore water pressures are presented for the case of rainfall pattern $R-1$, where the intensity of the major rainfall is equal to 10 mm/hr and its duration 30 h. Figures 5.18(a) and (b) also show that although the same amount of rainfall is applied to the slope (300 mm) by the three rainfall patterns, the pore water

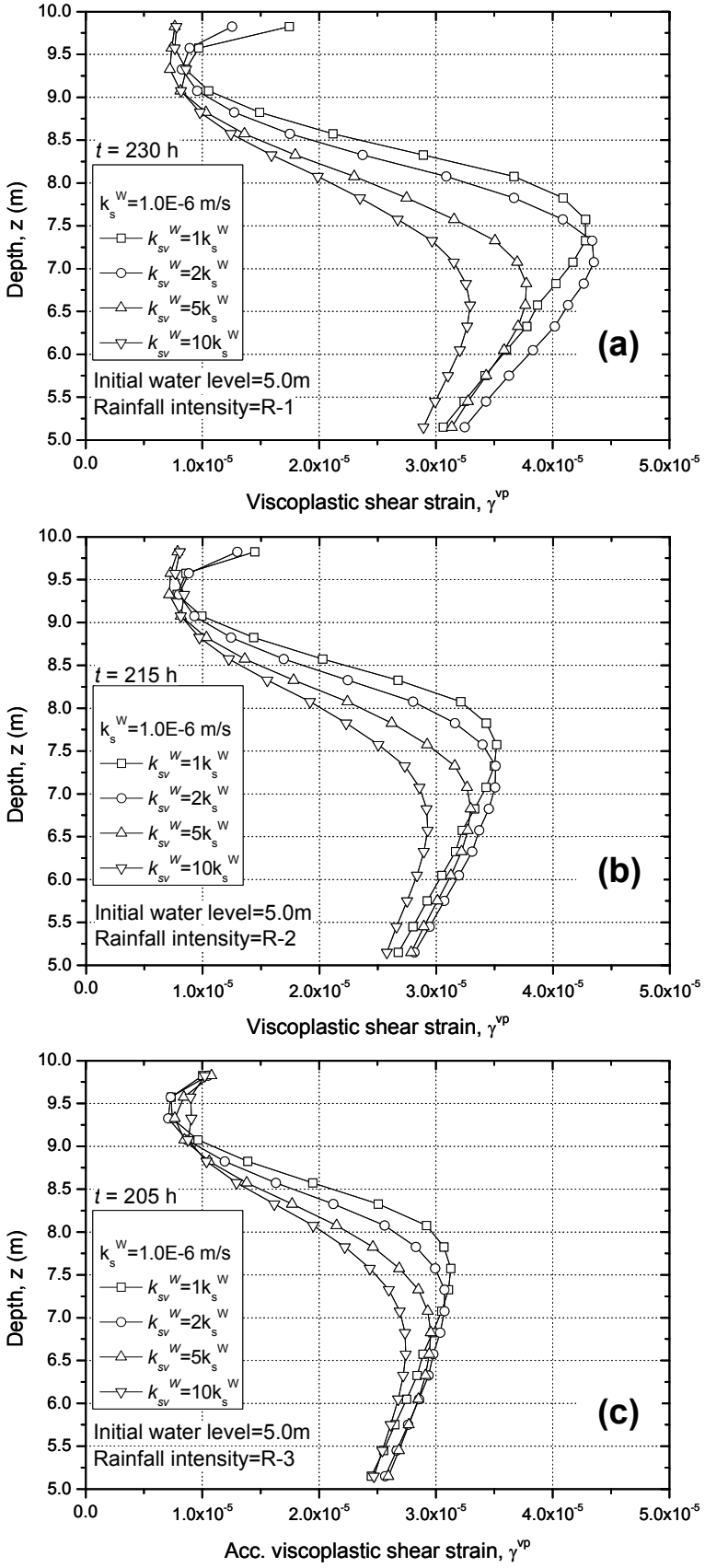

Figure 5.17 Viscoplastic shear strain profiles for different permeabilities. (a) Rainfall pattern $R-1$. (b) Rainfall pattern $R-2$. (c) Rainfall pattern $R-3$.

pressures developed for the rainfall patterns $R-2$ and $R-3$ are smaller when compared with the pore water pressures developed for the rainfall pattern $R-1$. This difference in the pore water pressure profiles can be explained by the different rainfall durations. Rainfall pattern $R-1$ generates larger pore water pressure along the profile because the major rainfall lasts for a longer time (30h) compared with the rainfall patterns $R-2$ and $R-3$ (15 h and 5 h, respectively). Rainfalls distributed over longer times on low permeable soils provide larger amount of water in the infiltration process. Consequently, it can be said that for relations $I/k_{sv}^{W} > 1$, the longer the rainfalls last, the greater the pore water pressures in low permeable soils.

Figures 5.18(c) and (d) show the pore water pressure profiles for the cases with k_{sv}^{W}=5k_{s}^{W}=5.0 x 10^{-6} and 10k_{s}^{W}=1.0 x 10^{-5} m/s, respectively. When these results of the pore water pressure are compared with the results obtained above in Figures 5.18(a) and (b), it is possible to see a different pattern in the pore water pressure profiles for the soil located close to the surface (z=10.0 to z=8.5 m). The pore water pressures on the soil close to the surface are larger for the rainfall pattern $R-3$ and smaller for the rainfall patterns $R-2$ and $R-1$, respectively. The smaller pore water pressure results obtained for $R-2$ and $R-1$ can also be explained by the relation between the rainfall intensity and the saturated water permeability as mentioned before. When the permeability increases and becomes larger than the rainfall intensity, the infiltration capacity of the soil is larger and the whole water infiltrates the soil; not accumulation or excess of water appears on the surface, maintaining the slope surface unsaturated. On the other hand, once the depth increases, i.e. below z= 8.5 m, the trend for the pore water pressure is inverted and they become larger for the rainfall pattern $R-1$ and reduce for rainfall patterns $R-2$ and $R-3$, respectively.

Comparison of Figures 5.18(a) to (d) shows that, regardless of the permeability and the rainfall pattern, the increase of pore water pressures due to the rainfall infiltration at shallow depths are more important than the increases of the pore water pressure at greater depths. It means that the rainfall patterns (different rainfall intensities and rainfall durations) have a more significant effect on the development of pore water pressures (reduction of suction) at shallow depth than at greater depths. This result is consistent with Au (1998) conclusion on the report of many soil failures during rainstorms in Hong Kong, that one of the most prominent ways by which the rainfall affects the instability of slopes is by the loss of pore water suction at shallow depths, which induces shallow and

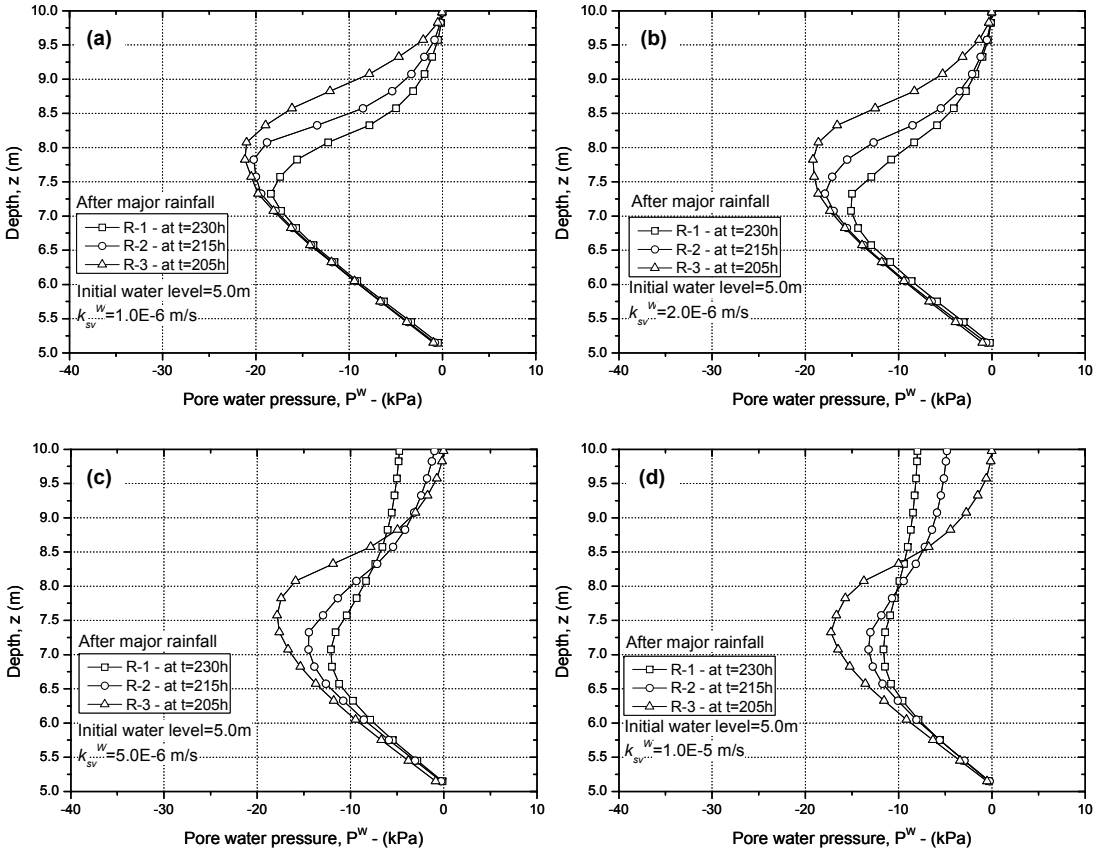

Figure 5.18 Comparisons of pore water pressure profiles for different rainfall patterns. (a) k_{sv}^{W}=1.0 x 10^{-06} m/s. (b) k_{sv}^{W}=2.0 x 10^{-06} m/s. (c) k_{sv}^{W}=5.0 x 10^{-06} m/s. (d) k_{sv}^{W}=1.0 x 10^{-05} m/s

small slope failures. Similarly, Rainfall-induced shallow landslides triggered by rainfall infiltration in Japan have also been reported by Matsushi et al. (2006). In Addition, Figures 5.18(a) to (d) show that the trend for the development of the pore water pressure at deeper soil is the same, regardless of the permeability. It is, the greater pore water pressures are obtained for the longer rainfall $(R-1)$ and the smaller pore water pressures are obtained for the shorter rainfalls $(R-2)$ and $(R-3)$. It suggests that longer rainfalls have a more important effect on the deeper soil. When the permeability of the soil increases and becomes larger that the rainfall intensity in Figures 5.18 (c) and (d), the effect of the rainfall patterns on the development of pore water pressure at shallow depths decreases.

The same infiltration characteristics described above by the pore water pressure profiles can be also obtained by the saturation profiles provided in Figures 5.19(a) to (d).

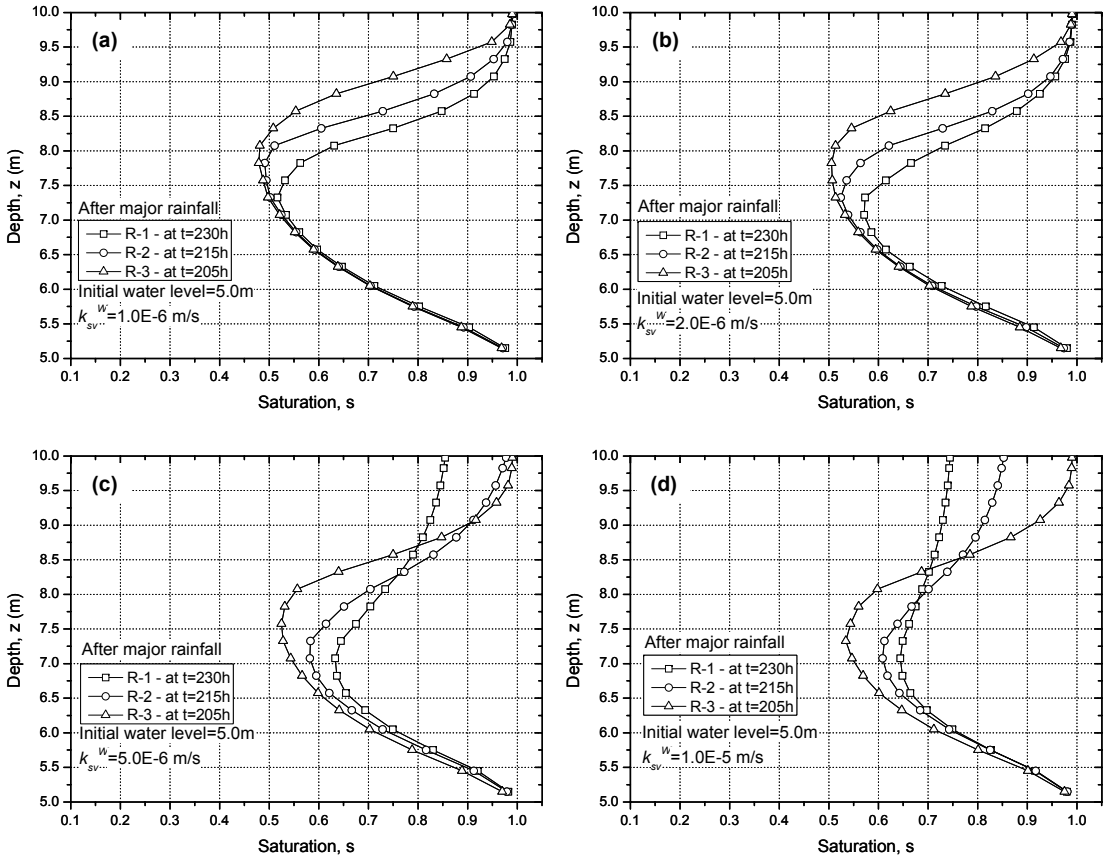

Figure 5.19 Comparisons of saturation profiles for different rainfall patterns. (a) k_{sv}^{W}=1.0 x 10^{-06} m/s. (b) k_{sv}^{W}=2.0 x 10^{-06} m/s. (c) k_{sv}^{W}=5.0 x 10^{-06} m/s. (d) k_{sv}^{W}=1.0 x 10^{-05} m/s

5.3.3.2 Lateral displacement and viscoplastic shear strain profiles

Figures 5.20(a) to (d) show a series of lateral displacement profiles with respect to the three different rainfall patterns, i.e. $R-1$, $R-2$ and $R-3$, and for the four permeabilities, namely, $k_{sv}^{W} = k_{s}^{W}$, $2k_{s}^{W}$, $5k_{s}^{W}$ and $10k_{s}^{W}$, respectively. Figures 5.20(a) and (b) present the comparison of the lateral displacement profiles among the three rainfall patterns for the saturated water permeabilities $k_{sv}^{W} = k_{s}^{W}$= 1.0 x 10^{-6} and $k_{sv}^{W} = 2k_{s}^{W}$= 2.0 x 10^{-6} m/s, respectively. The way in which the total amount of rainfall is distributed plays an important role in the development of the lateral displacement. In both figures, it is observed that the greatest lateral displacements along the profile are obtained for the rainfall pattern $R-1$. It is worth noting that the maximum lateral displacements are obtained for the case where the saturated water permeability is $k_{sv}^{W} = 2k_{s}^{W}$=2.00 x 10^{-6} m/s. As it was shown before, this permeability value is the closest to the applied rainfall intensity (I=10 mm/hr = 2.78 x 10^{-6} m/s, duration t=30h).

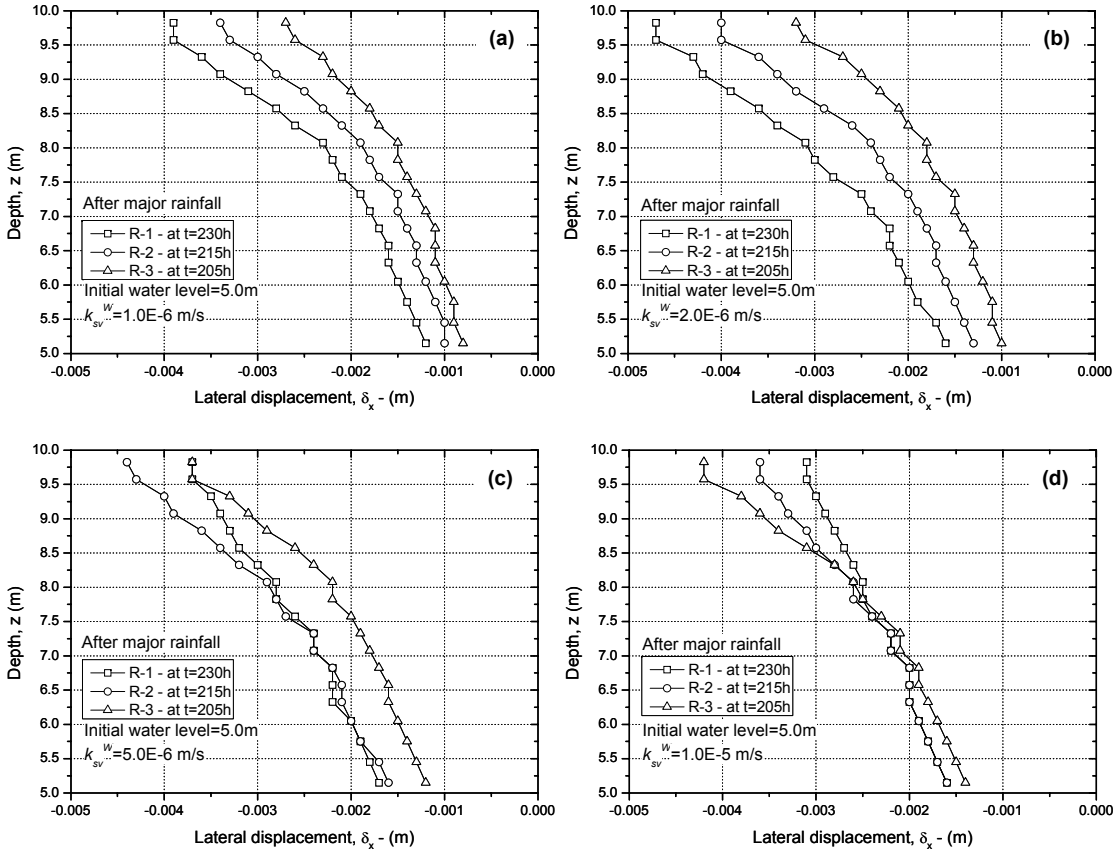

Figure 5.20 Comparisons of lateral displacement profiles for different rainfall patterns. (a) k_{sv}^{W}=1.0 x 10^{-06} m/s. (b) k_{sv}^{W}=2.0 x 10^{-06} m/s. (c) k_{sv}^{W}=5.0 x 10^{-06} m/s. (d) k_{sv}^{W}=1.0 x 10^{-05} m/s

Similarly, Figures 5.20(c) and (d) show the lateral displacement profiles for the cases with saturated water permeability $k_{sv}^{W} = 5k_{s}^{W}$= 5.0 x 10^{-6} and $k_{sv}^{W} = 10k_{s}^{W}$= 1.0 x 10^{-5} m/s, respectively. In these Figures, the maximum lateral displacements are obtained for the rainfall intensities $R-2$ (I=20 mm/hr = 5.56 x 10^{-6} m/s and duration t=15 h) and $R-3$ (I=60 mm/hr = 1.67 x 10^{-5} m/s, duration t=5 h), correspondingly. These intensities are the closest to the saturated water permeabilities of the soil. Therefore, the larger lateral displacements occur for the cases where the saturated water permeability is the closest to the rainfall intensity. It means that there is a critical rainfall intensity that develops the largest lateral deformations. It is the same result obtained by the comparison among the different permeabilities in Figures 5.16(a) to (c).

The comparison among the viscoplastic shear strains profiles after the major rainfall for the rainfall patterns $R-1$, $R-2$ and $R-3$, and for the four different permeabilities, namely, $k_{sv}^{W} = k_{s}^{W}$, $2k_{s}^{W}$, $5k_{s}^{W}$ and $10k_{s}^{W}$, are shown in Figures 5.21(a) to (d), respectively. Generally, the larger values for the viscoplastic shear strain along the profile below the

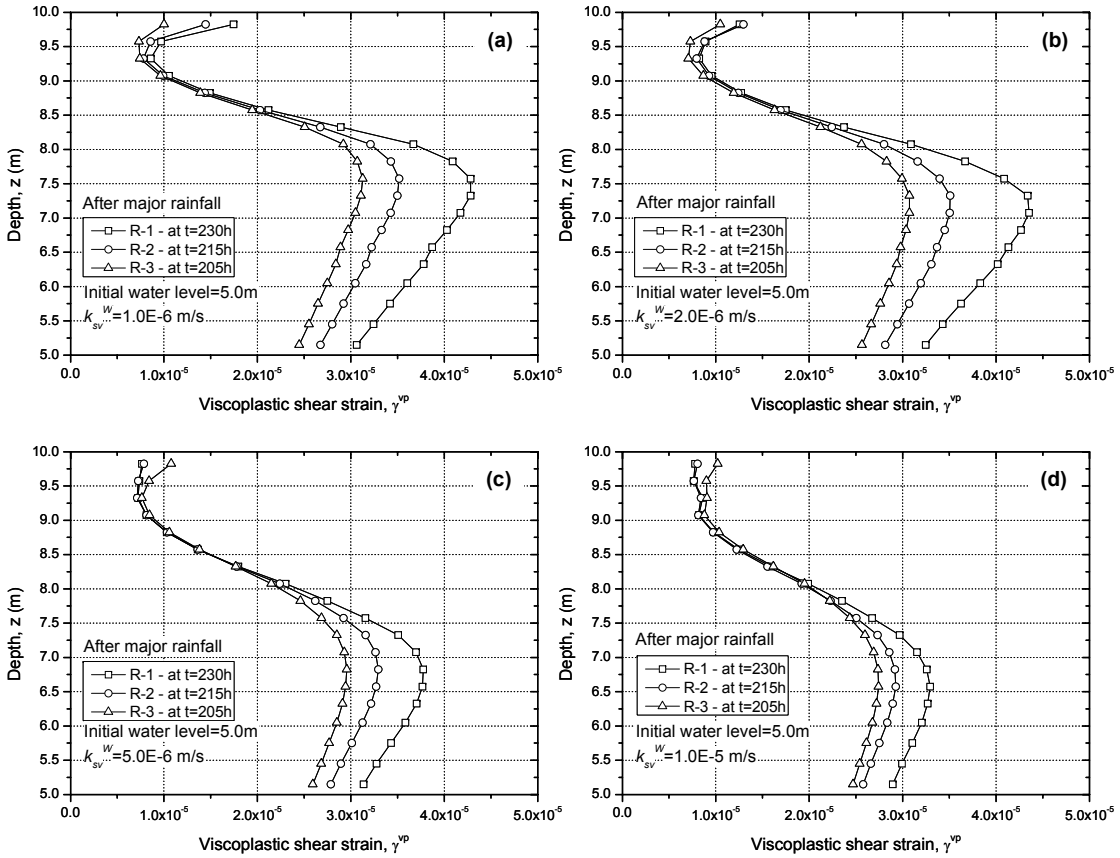

Figure 5.21 Comparisons of viscoplastic shear strain profiles for different rainfall patterns. (a) k_{sv}^{W}=1.0 x 10^{-06} m/s. (b) k_{sv}^{W}=2.0 x 10^{-06} m/s. (c) k_{sv}^{W}=5.0 x 10^{-06} m/s. (d) k_{sv}^{W}=1.0 x 10^{-05} m/s

crest of the slope are obtained in between z=7.5 and z=5.0 m. Comparison of these graphs show that, regardless of the permeability, the larger values of viscoplastic shear strain are obtained for the rainfall pattern $R-1$ (I=10 mm/h, duration t=30 h) and the smaller values are obtained for the rainfall patterns $R-2$ (I=20 mm/h, duration t=15 h) and $R-3$ (I=60 mm/h, duration t=5 h), respectively. It suggests that the longer the periods over which the 300 mm of the major rainfall is applied, the larger will be the shear viscoplastic strain. It indicates that rainfalls lasting for longer times or longer periods of rainfall have a more significant effect on the deformation of the slope due to the accumulation of larger deformation within the soil structure. The accumulation of deformation leads to the peak or the residual conditions within the soil triggering slope failures. It can explain the increase in the number of slope failures after long periods of rainfall.

5.4 Summary

A multiphase elasto-viscoplastic FE formulation based on the theory of porous media is used to describe the rainfall infiltration process into an unsaturated slope. The numerical analyses are focused on the effect of the different initial water levels, saturated water permeabilities, and rainfall distributions on the development of the pore water pressure and deformations. The calculated deformations are associated with the volume change of the soils as the saturation increases during the rainfall infiltration.

From the numerical analysis it was found that the initial water level (initial suction distribution) on an unsaturated slope subjected to rainfall infiltration has either a minimum or negligible effect on the hydraulic response at shallow depths. At the end of the major rainfall, similar pore water pressures are obtained close to slope surface for the different initial water levels. However, the initial water levels have a significant effect on the distribution of the pore water pressure below the wetting front. Additionally, larger deformations are obtained for the cases where the initial water levels are higher, which suggest that an unsaturated slope is more unstable if the initial suction distributions are smaller.

The simulations performed with different saturated water permeabilities show that larger pore water pressures are obtained at shallow depths when the saturated water permeabilities are smaller than the rainfall intensity; in contrast, in the case of permeabilities larger than the rainfall intensity, the pore water pressures at the surface are smaller. This behavior is inverted when the depth of the soil increases; at larger depths, the pore water pressures are larger for the soils with larger permeabilities. The analysis of the deformations shows that the maximum lateral displacements are obtained in the cases where the rainfall intensity is close to the saturated water permeability, i.e., $I/k_s^W \approx 1.0$. The ratio of the rainfall intensity to the saturated water permeability is a fundamental property in the deformation response of unsaturated soils subjected to rainfall infiltration.

From the comparison of the different rainfalls patterns it was observed that, regardless of the permeability, the entire rainfall patterns have a more significant effect on the increase of pore water pressures in the shallow depths than in the greater depths. Nevertheless, it was found that, the larger pore water pressures at greater depths are always presented for the case of the rainfall with longer duration. It means that rainfall lasting for longer times have a more significant effect on the generation of pore water pressures

at greater depths. For the deformation behavior due to the rainfall patterns, the larger values of viscoplastic shear strain are obtained for the rainfall pattern that lasted for a longer time, regardless of the permeability. It suggests that rainfalls lasting for longer times or longer periods of rainfall have a more significant effect on the deformation of the slope due to the accumulation of larger deformation within the soil structure.

Chapter 6

SIMULATION OF RAINFALL INFILTRATION AND SEEPAGE FLOW ON UNSATURATED EMBANKMENTS: TWO CASE STUDIES

6.1 Introduction

In recent years, frequent failures of river embankments have occurred in the world due to heavy rains and typhoons. Heavy rainfalls bring about a rise in the water level of the rivers as well as a rise in the ground water level within the river embankments. As a result, river embankments have been failed due to the rainfall infiltration and the generation of seepage flow. In addition, sometimes the upper parts of the river levees are connected to the surrounding mountains being exposed to the continuous seepage flow from the hilly areas. This, in turn, increases the pore water pressures within the river embankment leading to the degradation of the material (e.g., seepage-induced erosion). This deformation could trigger the progressive failure of the river embankments endangering the nearby structures.

In this chapter a study to clarify the effect of the rainfall infiltration and the seepage flow on the deformation of unsaturated river embankments is presented. To do that, two-dimensional numerical analyses have been performed for two common river embankments. The first case study, namely Seta River, corresponds to a three layered river embankment

which is subjected to both, the effect of the rainfall infiltration and the seepage flow from the mountain side. In the simulation, a rainfall record measured at the Seta River (Shiga Prefecture, Japan) and the variation of the water level measured at the right side of the embankment are used for the simulation, whereas the water level of the river is considered constant. In the Seta River case, the study of the effect of different water permeabilities for the upper layer on the seepage flow velocity and its effect on the surface erosion are emphasized. Furthermore, the effects of horizontal drains and degree of compaction on the generation of deformation are investigated. The second case study is a controlled experiment performed in an open laboratory, namely S River, and it corresponds to a river dike embankment used to protect the urban areas from the flooding triggered by the rainfall accumulation and the increase of the water level of the rivers. The analyses performed for this case are also based on the variation of the saturated water permeabilities of the soil layers. Constant rainfall infiltration is applied on the surface of the dike while the water level is increased and decreased to observe the effect of the seepage flow on the generation of pore water pressure and on the deformation of the embankment. The results obtained by the numerical analyses for the pore water pressure are compared with the existing measured field data.

The numerical analyses have been carried out using a seepage-deformation coupled method for unsaturated soil. Constitutive and hydraulic parameters that represent the soils found in the Seta River and S River embankments are employed in the simulations. The mechanism of the surface deformation and the strain localization on the embankment surface at the river side are discussed mainly with respect to the saturated water permeability of the soil. From the numerical results, it was observed that the deformation of the embankment significantly depends on the water permeability of the soil and it is localized on the slope surface at the river side. The larger the saturated water permeability of the soil, the larger the velocity of the seepage flow and the larger the deformation on the surface of the river embankment.

6.2 Numerical analysis

The elasto-viscoplastic model for unsaturated soil described in Section 2.3 and the multiphase finite element formulation described in Section 2.4 are used to simulate the rainfall infiltration and the seepage flow into the unsaturated river embankments. In this formulation, an updated Lagrangian method with the objective Jaumann rate of Cauchy stress

is adopted (Kimoto et al. 2004; Oka et al. 2006). The independent variables are the pore water pressure, the pore air pressure, and the nodal velocity. In the finite element formulation, an eight-node quadrilateral element with a reduced Gaussian integration is used for the displacement, and four nodes are used for the pore water pressure and the pore air pressure. The backward finite difference method is used for the time discretization.

6.3 Seta River case

6.3.1 Review of the existing data

The river embankment used for the study is located in Otsu city, Shiga prefecture, Japan. Figure 6.1 shows a sketch of the geomorphology of the study area and the location of the degradation of the Seta River embankment. As it is observed on the figure, the back of the embankment is surrounded by a hilly area. The embankment is located in a flat surface which is divided by small rivers that flow toward the Seta River. The study area was a farmland but nowadays has become a resident area. The soil investigation and the observation of the behavior of the embankment at Seta River have shown that the water infiltration from the surrounding mountains has been permanent and it has a significant impact on the damage and degradation of the soil close to the embankment surface at the river side. Figure 6.2 depicts the mechanics of the water flow and the degradation of the soil surface at the river side of the embankment. The fluctuation of the water level of the river at Seta River site is within one meter in a year. Figure 6.3 shows a detail of the kind of erosion occurred under the concrete face at the river side due to the seepage flow from the mountain and induced by the rainfall infiltration.

Figure 6.4 shows the rainfall record at Seta River and the ground water level observations at the right side of the embankment (mountain side) from January 2009 to February 2010. This figure shows that the ground water level changes over the time and increases when the rainfalls are presented. This is an indication of the appearance of seepage flow induced by the rainfall infiltration.

6.3.2 Geometry, boundary conditions and soil parameters

The cross section and the boundary conditions for the simulation of the rainfall infiltration and seepage flow into the unsaturated river embankment are shown in Figure 6.5. The top surface of the river embankment has an inclination of 0.95°. The slopes of the

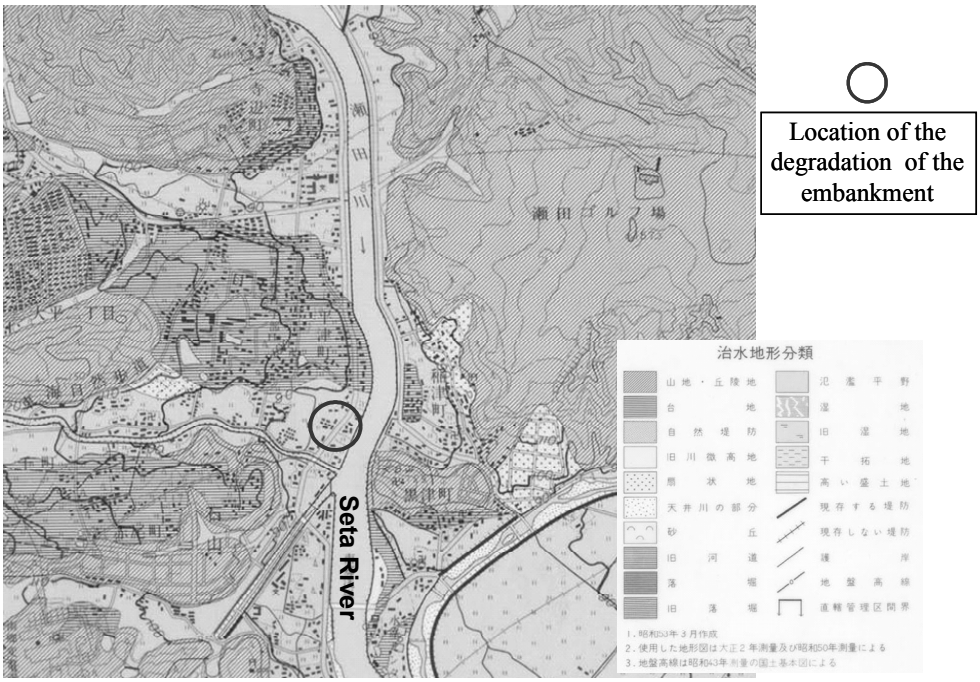

Figure 6.1 Geomorphology and location of the degradation of Seta River embankment

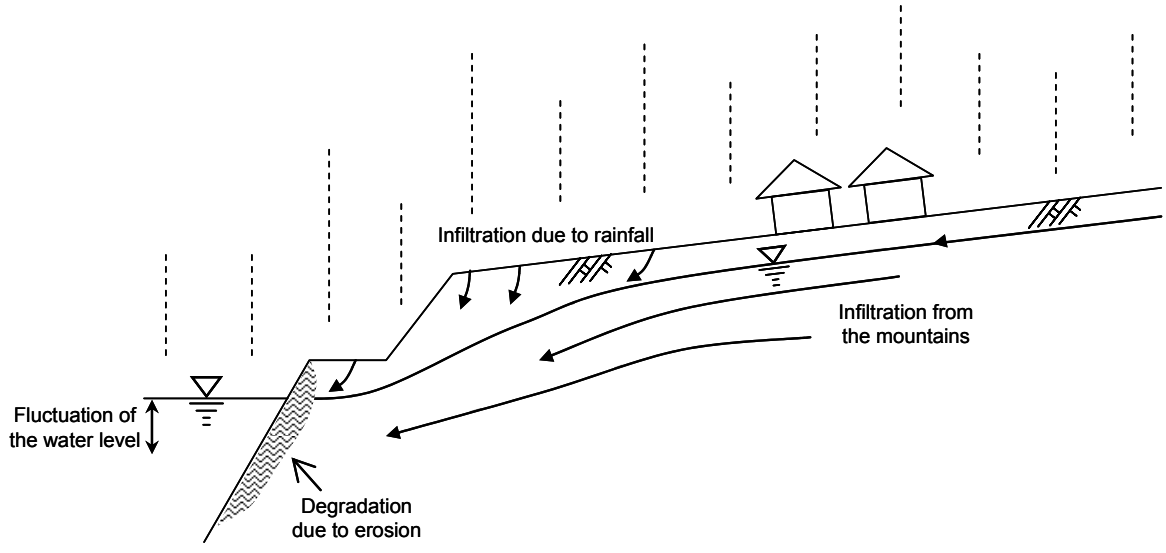

Figure 6.2 Mechanism of the water flow and degradation of the slope surface

Figure 6.3 Erosion below the concrete face at the right side of the Seta River (January 2007)

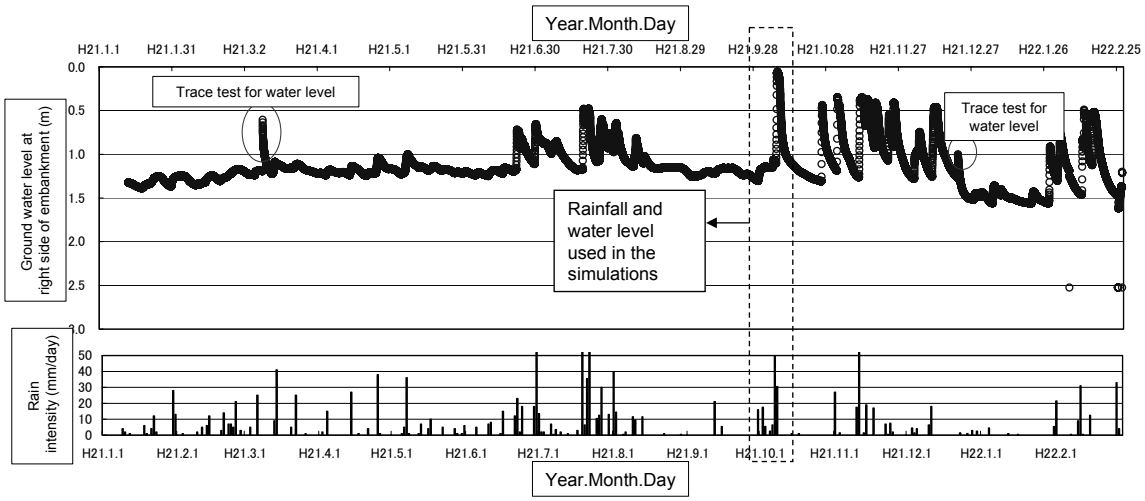

Figure 6.4 Rainfall and water level data from January 2009 to February 2010

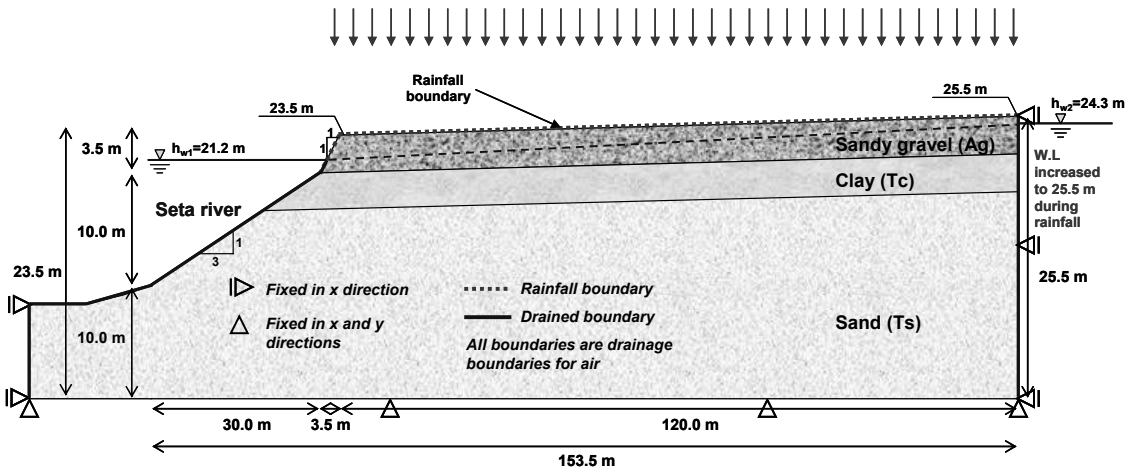

Figure 6.5 Cross section of the river embankment and boundary conditions

embankment have gradients of 1V:1H at the upper part and 1V:3H at the middle of the embankment. For displacement, the embankment is fixed at the bottom in both horizontal and vertical directions, the lateral boundaries are fixed only in horizontal direction. The initial negative pore water pressure distribution (suction) in the top sandy gravel layer is considered to be linear. The water level at the boundaries of the embankment are located at 21.2 m at the river side and at 24.3 m at the mountain side. The water level inside the embankment is linearly distributed according with the water levels at the river and montain sides, its inclination is about 1.5°. The flux of air is allowed for the entire boundaries and the initial air pressure, P_i^G, is assumed to be zero. The boundary conditions for water flux are described in this manner: an impermeable boundary is assigned to the bottom or soil foundation; for the lateral sides of the embankment below the water levels, the boundary is considered permeable; above the water levels the boundaries are initially impermeable, but it changes to be permeable if the pore water pressure turns positive; the slope and the top of the embankment are assumed to be rainfall boundaries. The rainfall boundary is the same described in Section 5.2.1. A detail of the mesh close to the slope of the embankment at the river side is shown in Figure 6.6. The mesh is finer close to the surface where the high hydraulic gradients due to the rainfall infiltration and seepage flow are expected.

The materials that compose the river embankment are assumed to be elasto-viscoplastic materials. The material parameters required by the constitutive model described in Section 2.3 are listed in Table 6.1. These parameters represent the three different soils found in the river embankment, namely, Sandy gravel (Ag), Clay (Tc), and Sand (Ts). The

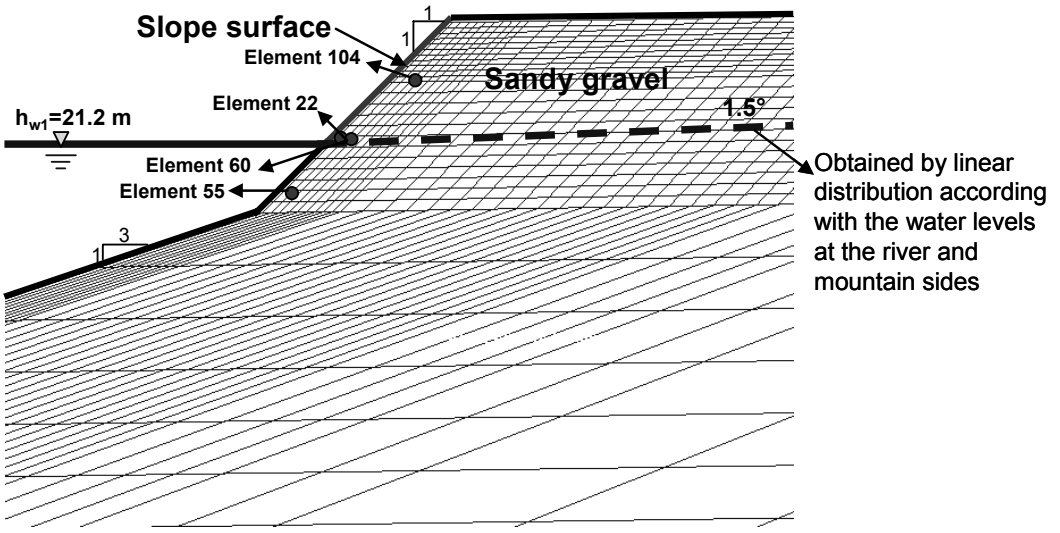

Figure 6.6 Finite element mesh at the slope of the embankment

upper sandy gravel layer is about 3.0 m in height and it overlies on a clay layer about 4.0 m in height; the bottom of the embankment is composed of a thick sand layer. The soil water characteristic curve considered to describe the suction-saturation relation of the upper sandy gravel layer is shown in Figure 6.7. The soil water characteristic curves for the clay and the sand layers are irrelevant because these soil stratums are below the water table, i.e., saturated soil.

In order to study the effect of the rainfall infiltration and seepage flow into the unsaturated river embankment, the rainfall record and the water level measured from October 2^{nd} to October 8^{th} 2009 corresponding to the Seta River site is used in the simulation. As it was shown in Figure 6.4 the water level measured during this time at the mountain side was the maximum, reaching almost the top of the embankment. An enlargement of the rainfall record and the water measured at that time are shown together in Figure 6.8. The total precipitation was 106 mm with a maximum hourly rainfall of 14 mm. According to the precipitation record, the rainfall was concentrated between the noon of October 7^{th} to the morning of October 8^{th} with a total rainfall of 97 mm (t=132 to t=152 h). During the simulation the non-uniform rainfall is applied on the top and the slope of the river embankment, while the water level is increased on the right side (mountain side). The initial degree of saturation for the unsaturated soil (sandy gravel layer) is considered to be about 60%.

Table 6.1 Material parameters for Sandy Gravel (Ag), Clay (Tc), and Sand (Ts)

Material parameters		Sandy Gravel (Ag)	Clay (Tc)	Sand (Ts)
Viscoplastic parameter	$m^{'}$	40.0	27.59	40.0
Viscoplastic parameter (1/s)	C_1	1.0 x 10^{-15}	2.0 x 10^{-14}	1.0 x 10^{-20}
Viscoplastic parameter (1/s)	C_2	2.0 x 10^{-15}	2.0 x 10^{-13}	2.0 x 10^{-20}
Stress ratio at critical state	M_m^*	1.27	1.25	1.27
Compression index	λ	0.0804	0.4910	0.0804
Swelling index	κ	0.0090	0.0760	0.0090
Initial elastic shear modulus (kPa)	G_0	3000	23000	20000
Initial void ratio	e_0	0.344	1.23	0.535
Structural parameter	β	5.0	15.0	0.0
Structural parameter	$\frac{\sigma_{maf}^{'}}{\sigma_{mai}^{'}}$	0.60	0.579	0.60
Ver. permeability of water s=1 (m/s)	k_{sv}^W	**	1.00 x 10^{-8}	1.00 x 10^{-6}
Hor. permeability of water s=1 (m/s)	k_{sh}^W	**	1.00 x 10^{-7}	1.00 x 10^{-5}
Permeability of gas at s=0 (m/s)	k_s^G	1.00 x 10^{-3}	1.00 x 10^{-3}	1.00 x 10^{-3}
Van Genuchten parameter (1/kPa)	α	0.10	0.13	2.00
Van Genuchten parameter	n'	4.0	1.65	1.20
Suction parameter	S_I	0.20	0.20	0.20
Suction parameter	s_d	0.20	5.00	0.20
Minimum saturation	s_{min}	0.0	0.0	0.0
Maximum saturation	s_{max}	0.97	0.99	0.99
Shape parameter of water permeability	a	3.0	3.0	3.0
Shape parameter of gas permeability	b	1.0	1.0	1.0

**The permeability of the sandy gravel layer depends on the simulation case

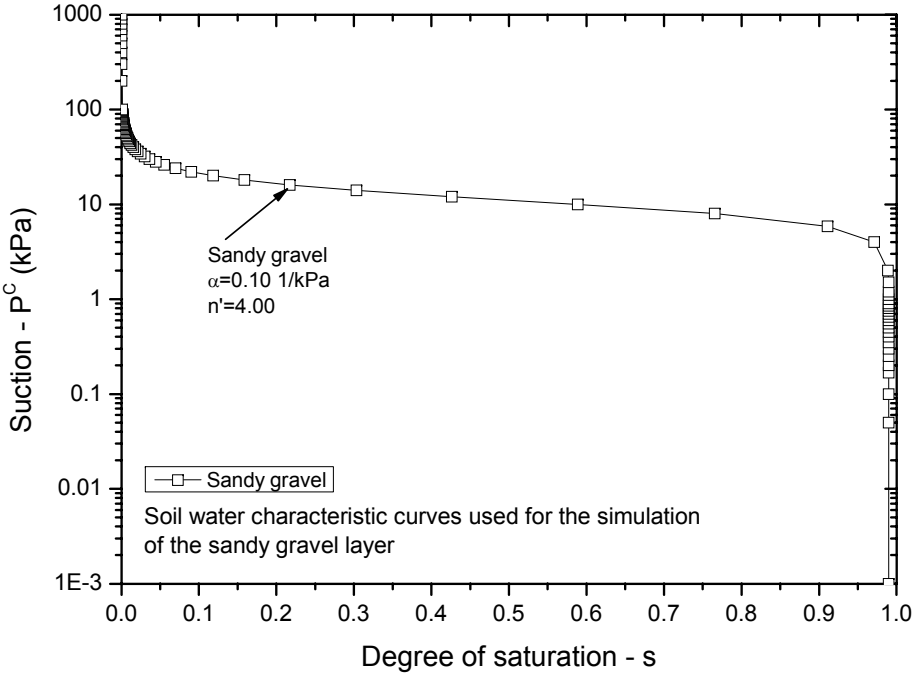

Figure 6.7 Soil water characteristic curve for the sandy gravel layer

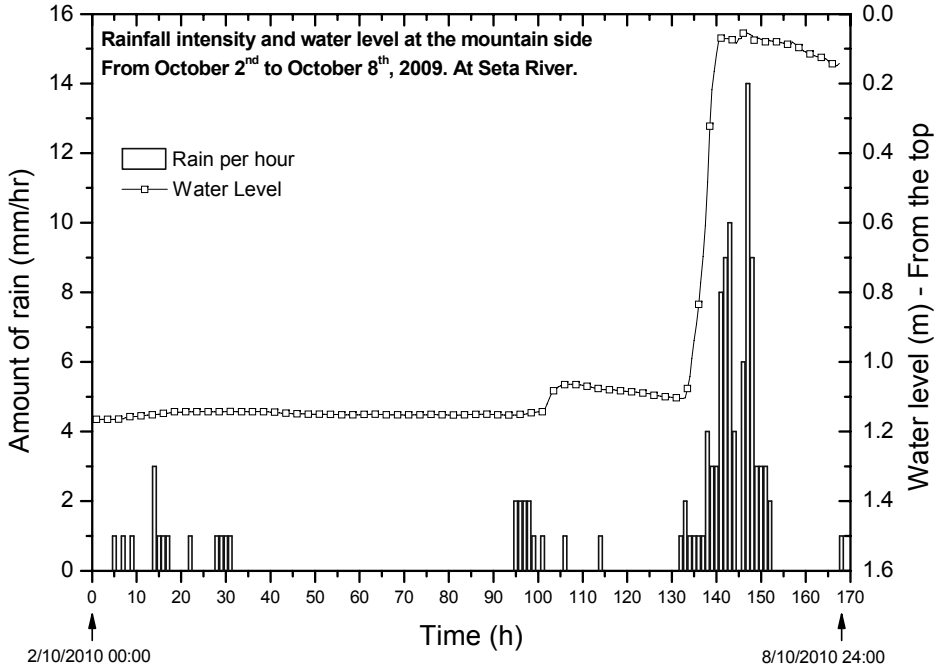

Figure 6.8 Rainfall record and water table history used for the simulations

According to the Figure 6.3, it was observed that the deformation of the river embankments is localized at the river side, just below the concrete face that covers the surface of the slope. It is thought that this localized erosion is triggered by a combined effect of the seepage flow due to the rainfall infiltration over the embankment surface, the seepage flow from the mountain side, and the difference in the permeabilities between the sandy gravel soil and the slope surface.

6.3.3 Effect of permeability

6.3.3.1 Simulation cases

To see the effect of the permeabilities on the seepage flow velocity and the development of deformation in the unsaturated river embankment, different cases are analyzed. The simulation cases are listed in Table 6.2. The analysis cases consist of different combinations of saturated permeabilities for the upper sandy gravel layer and the slope surface; the cases are divided in three groups. In Group I: Cases 1 to 4, the saturated permeability for the sandy gravel is increased, i.e. $k_{sv}^{W(G)}$ = 1.0 x 10^{-6}, 3.0 x 10^{-6}, 6.0 x 10^{-6}, and 1.0 x 10^{-5} m/s, respectively, while the permeability of the slope surface is kept constant, i.e. $k_{sv}^{W(S)}$ = 1.0 x 10^{-6} m/s. The lower permeability on the slope surface is used to consider the higher compaction at the surface. In Group II: Cases 5 to 8, both the saturated permeability of the sandy gravel and the saturated permeability of the slope surface are equal and they are increased simultaneously, namely, $k_{sv}^{W(G)}$ = 1.0 x 10^{-6}, 3.0 x 10^{-6}, 6.0 x 10^{-6}, and 1.0 x 10^{-5} m/s. In Group III: Cases 9 to 12, the saturated permeability for the sandy gravel is increased, i.e. $k_{sv}^{W(G)}$ = 1.0 x 10^{-6}, 3.0 x 10^{-6}, 6.0 x 10^{-6}, and 1.0 x 10^{-5} m/s, respectively, while the permeability of the slope surface is kept constant, i.e. $k_{sv}^{W(S)}$ = 1.0 x 10^{-7} m/s; in addition, the material of the slope surface is assumed to be an elastic material in order to simulate a concrete face over the slope of the embankment. For the elastic material the Elastic Young's modulus is considered to be E=1.0 GPa and the Poisson ratio ν=0.10.

6.3.3.2 Numerical results

One of the greatest uncertainties concerning the study of rainfall infiltration and seepage flow lies on the field values of the saturated water permeability. Because the erosion due to the seepage flow observed at the site is localized in the slope of the embankment (sandy gravel layer) and it is thought that this erosion is due to the water infiltration; the results presented herein are based on the variation of the permeabilities for the upper

Table 6.2 Saturated permeabilities for the analyses

Group	Cases	$k_{sv}^{W(G)}$ sandy gravel layer (m/s)	$k_{sv}^{W(S)}$ slope surface (m/s)	Rainfall record
Group I	Case 1	1.0 x 10^{-6}	1.0 x 10^{-6}	Measured at Seta River site
	Case 2	3.0 x 10^{-6}	1.0 x 10^{-6}	
	Case 3	6.0 x 10^{-6}	1.0 x 10^{-6}	
	Case 4	1.0 x 10^{-5}	1.0 x 10^{-6}	
Group II	Case 5	1.0 x 10^{-6}	1.0 x 10^{-6}	Measured at Seta River site
	Case 6	3.0 x 10^{-6}	3.0 x 10^{-6}	
	Case 7	6.0 x 10^{-6}	6.0 x 10^{-6}	
	Case 8	1.0 x 10^{-5}	1.0 x 10^{-5}	
Group III (Concrete face at the slope surface)	Case 9	1.0 x 10^{-6}	1.0 x 10^{-7}	Measured at Seta River site
	Case 10	3.0 x 10^{-6}	1.0 x 10^{-7}	
	Case 11	6.0 x 10^{-6}	1.0 x 10^{-7}	
	Case 12	1.0 x 10^{-5}	1.0 x 10^{-7}	

* The horizontal permeability is assumed to be 10 times the vertical permeability $k_{sh}^{W} = 10\, k_{sv}^{W}$

layer, namely, sandy gravel layer, as well as the permeabilities of the slope surface. The permeabilities of the clay layer and the sand layer were kept constant. The different case studies are given in Table 6.2. Different combinations among the permeabilities for the sandy gravel layer and for the slope of the embankment are used in order to find the permeability combinations that may lead to the localization of deformation at the slope of the embankment.

Cases 1 to 4 (Group I)

This series of simulation intends to evaluate the effect of the lower permeability existing on the slope surface due to the compaction during the construction process. Four different saturated water permeabilities for the sandy gravel layer are assumed in order to investigate the effects of the increase in the permeability of the top layer on the saturation, the pore water pressure, the horizontal hydraulic gradient, the water velocity, and the viscoplastic shear strain. The saturated water permeabilities are assumed to be $k_{sv}^{W(G)} =$ 1.0 x 10^{-6}, 3.0 x 10^{-6}, 6.0 x 10^{-6}, and 1.0 x 10^{-5} m/s, i.e., Cases 1 to 4, respectively. The permeability of the slope surface of the embankment is kept constant during the simulation, namely, $k_{sv}^{W(S)} = 1.0$ x 10^{-6} m/s.

Figure 6.9(a) and (b) show the comparison of the saturation and the pore water pressure profiles, respectively, corresponding to Cases 1 to 4 and obtained below the crest of the embankment. In these figures the results are shown at the time t=151 h, which corresponds to the time at the end of the major rainfall. The initial saturation and pore water pressure profiles are also included. From these figures it is observed that the greatest saturation and pore water pressure at the top of the embankment, z=22.5 to 23.5 m, are obtained for the case with the smaller saturated water permeability (Case 1) and they decrease as the saturated water permeability increases (Cases 2 to 4); however, the larger saturations and pore water pressures below 22.5 m are obtained for the cases with the larger saturated water permeabilities. Larger saturations and pore water pressures are obtained at shallow depths for smaller saturated permeabilities because the water infiltrated due to the rainfall is retained in the soil and it can not move easily downward; nevertheless, in the cases of larger saturation the water can flow more rapidly downward increasing the water table and the pore water pressure within the embankment.

Figure 6.10(a) and (b) show the comparison for Cases 1 to 4 of the time histories of the pore water pressure and the viscoplastic shear strain, respectively. These figures show the results for the element 22 located at the surface of the slope of the embankment as shown in Figure 6.6. Figure 6.10(a) presents the pore water pressure-time histories from October 2^{nd} to October 8^{th} (168 h). For the entire cases, the pore water pressure increases with time due to the rainfall infiltration and it changes from negative pore water pressure (suction) to the positive pore water pressure. The larger the permeability, the faster is the change from negative to positive pore water pressure. About 151 h after the simulation started, the pore water pressure in the element 22 reaches its maximum values, and these values correspond to the end of the major rainfall. The largest value for the pore water pressure at the time t=151 h is obtained for Case 4 (P^W=1.25 kPa). Figure 6.10(b) shows the viscoplastic shear strain-time histories for the same cases and during the time interval 140-168 h. It is seen that during the major rainfall the viscoplastic shear strain starts to increases rapidly for Cases 3 and 4 where the pore water pressures are larger. The larger viscoplastic shear strains are obtained for Case 4 in which the saturated water permeability of the sandy gravel layer is the largest.

Figure 6.11 shows the comparison of the distribution of the horizontal hydraulic gradient after the major rainfall (t=151 h) for Cases 1 to 4, respectively. It can be seen that the largest horizontal hydraulic gradient is obtained for the case with larger saturated

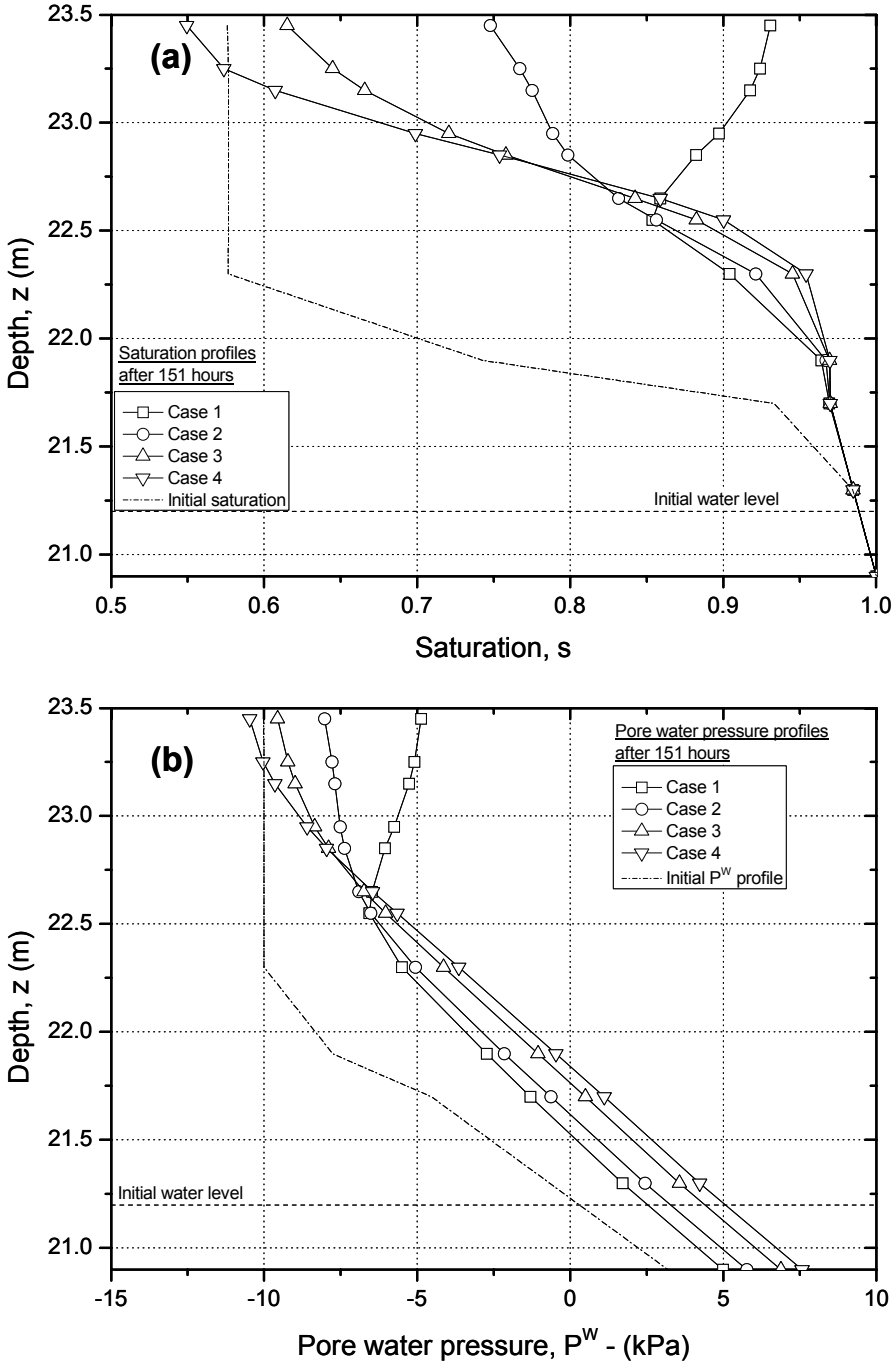

Figure 6.9 Effect of the permeability of the sandy gravel layer. (a) Saturation profile. (b) Pore water pressure profile

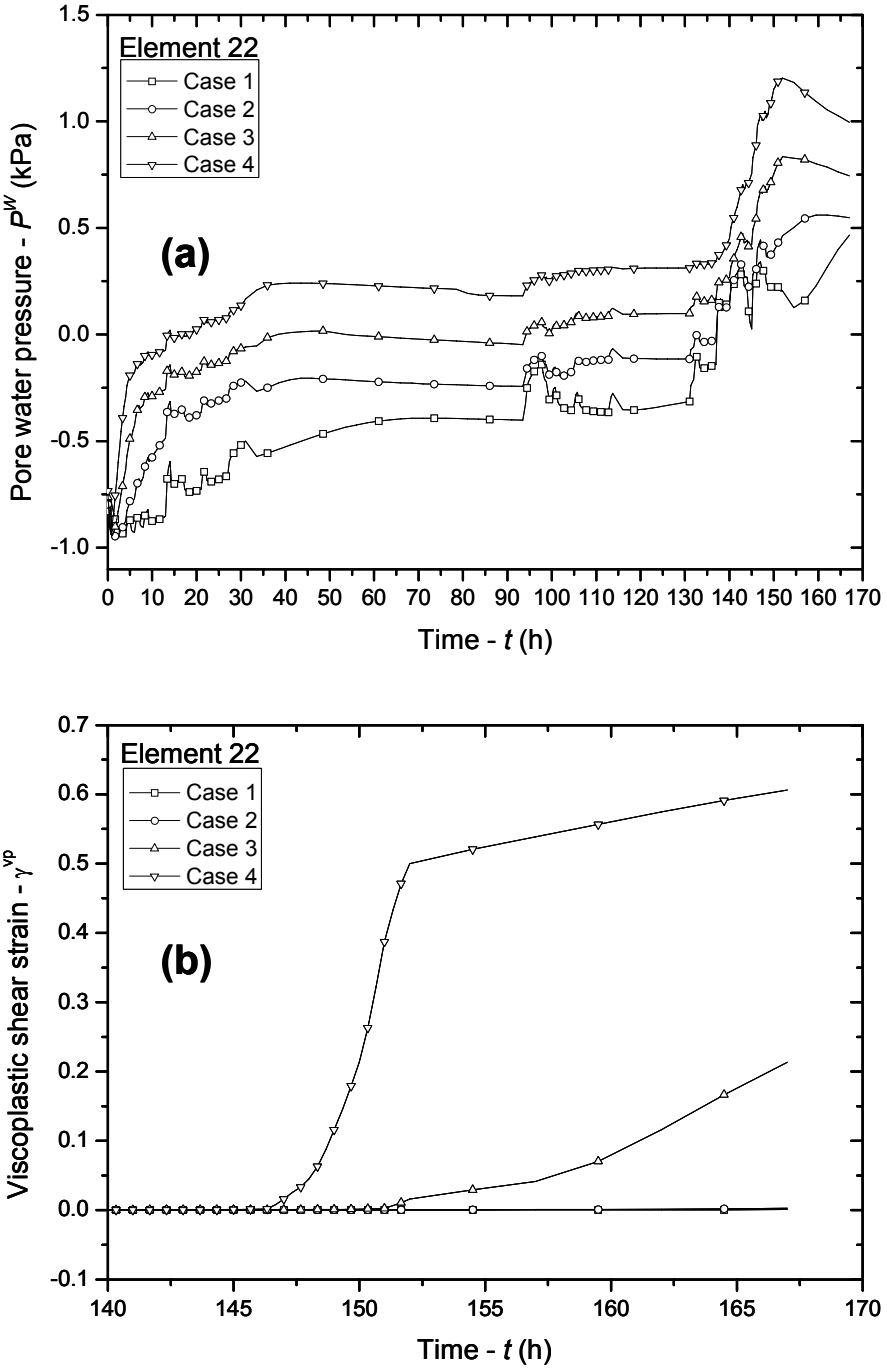

Figure 6.10 (a) Time history of pore water pressure (Element 22). (b) Time history of viscoplastic shear strain (Element 22)

permeability (Case 4: i =1.66) and it is presented on the slope of the embankment. This larger gradient is because of the larger pore water pressures presented behind the slope of the embankment caused by the accumulation of the water owing to the smaller permeability of the slope surface. In other words, the slope surface acts as a barrier that prevents the water flow outward the embankment toward the river. Figure 6.12 shows the comparison of the magnitude of the water velocity vectors for the four cases, Cases 1∼4 at the time t=151 h. The arrows show the vertical water infiltration on the top of the slope due to the rainfall infiltration and the lateral water infiltration toward the river side due to the seepage flow from the mountain side. It is seen that the velocity of the water flow increases when the permeability increases and it is more intense at the middle of the slope surface. Figure 6.13 presents the comparison of the distributions of accumulated viscoplastic shear strain ($\gamma^{vp} = \int d\gamma^{vp}$; $d\gamma^{vp} = \sqrt{de_{ij}^{vp} de_{ij}^{vp}}$) for the analyzed cases at the time t=151 h. It is shown that the accumulation of viscoplastic strain is generated on the slope of the embankment immediately above the river water level. Cases 1 to 3 show that the accumulated viscoplastic shear strains after the major rainfall are smaller; however, in Case 4 a large amount of accumulated viscoplastic shear strain (up to 38%) is generated on the slope surface. The water accumulated inside the embankment resulted in the accumulation of deformation on the middle of the slope (e.g., slope erosion may occur; however, erosion is not simulated in this study). This accumulation of deformation is induced not only by the rainfall infiltration but also by the generation of pore water pressure and seepage flow when the water table increases near the slope surface. Comparisons of Figures 6.11 to 6.13 show that the localization of deformation on the slope surface is related to the hydraulic gradient, the velocity of the water flow, and the permeabilities of the soil layer. The larger the saturated water permeability of the sandy gravel soil, the larger are the velocity of the seepage flow and the accumulation of deformation on the middle of the river embankment. Orense et al (2004) performed an experimental study on rainfall infiltration and seepage flow on small-scale unsaturated model slopes and reported a similar result that when the water table approach to the slope surface, a highly unstable zone developed in that area and slope failure may be induced.

Cases 5 to 8 (Group II)

In the previous cases (Cases 1 to 4) the saturated permeability of the slope surface was kept constant and it was equal or smaller than the permeability of the upper layer. Simulations 5 to 8 intend to show the effect of the saturated water permeability on an homogeneous

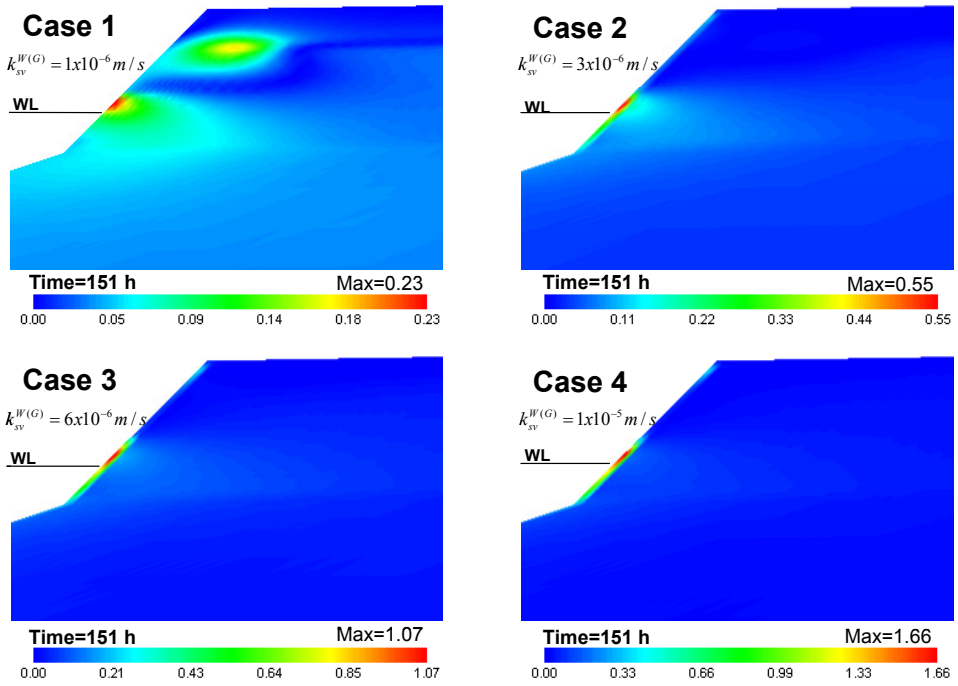

Figure 6.11 Distribution of the horizontal hydraulic gradient. Cases 1 to 4 (t=151 h).

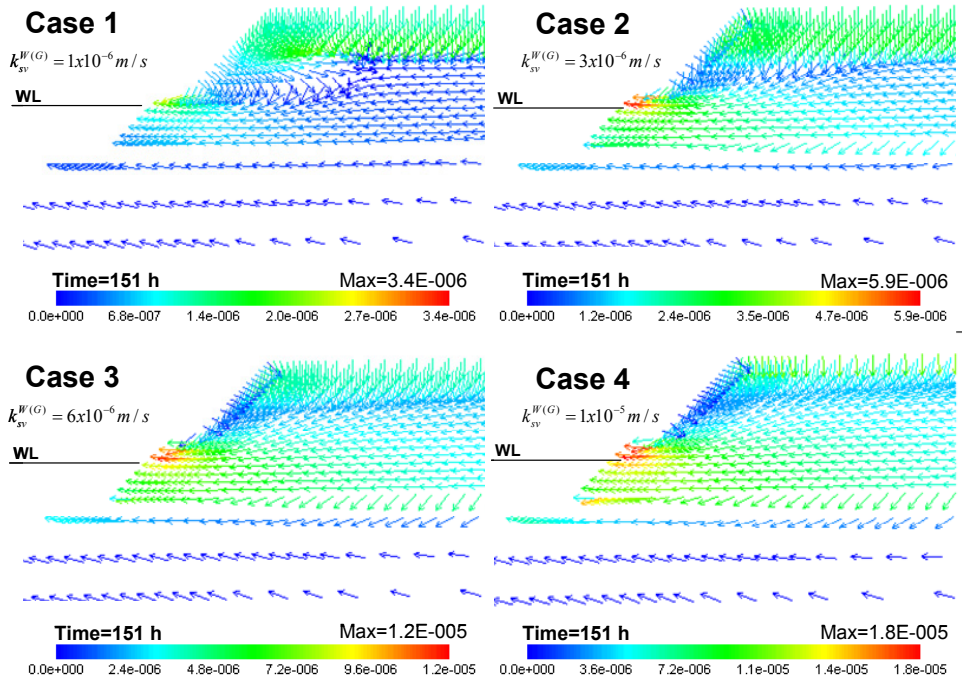

Figure 6.12 Distribution of the water velocity vectors. Cases 1 to 4 (t=151 h).

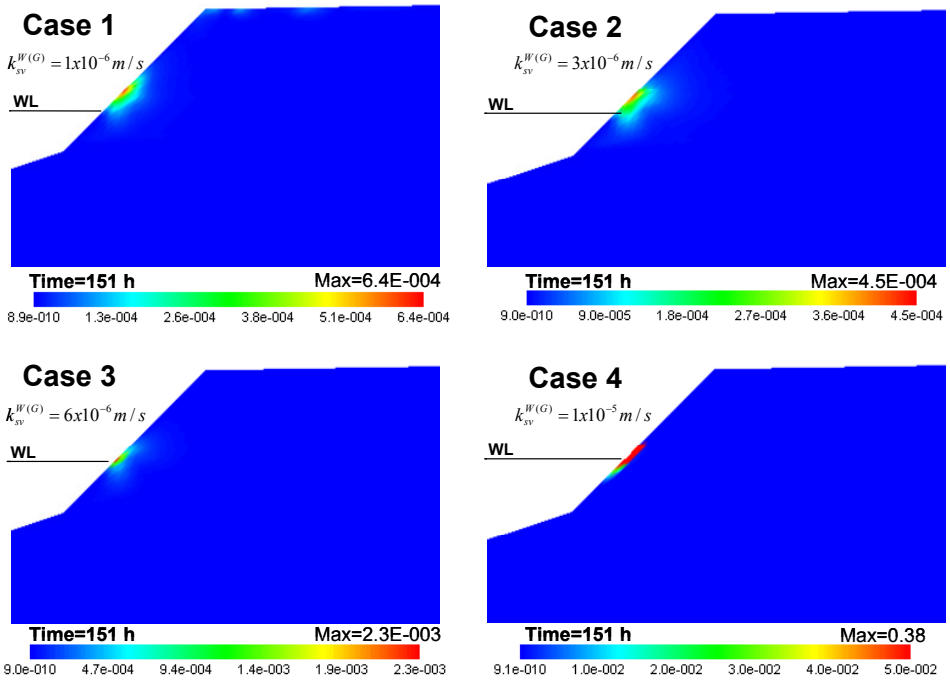

Figure 6.13 Distribution of the viscoplastic shear strain. Cases 1 to 4 (t=151 h).

soil; for these cases, the permeabilities assumed for both the slope surface and the sandy gravel layer are the same. Four values for the saturated permeabilities of the slope surface and the sandy gravel layer are assumed for Cases 5 to 8, namely, $k_{sv}^{W(S)} = k_{sv}^{W(G)} = 1.0$ x 10^{-6}, 3.0 x 10^{-6}, 6.0 x 10^{-6}, and 1.0 x 10^{-5} m/s, respectively, as shown in Table 6.2.

Comparison of the horizontal hydraulic gradient distributions near the slope of the embankment at the time t=151 h for Cases 5 to 8 is presented in Figure 6.14. This figure shows that the horizontal hydraulic gradient is very similar among the four cases, regardless of the permeability. Maximum values are obtained at the middle of the slope surface, immediately above the river water table. Contrary to Cases 1 to 4, these cases in which the saturated water permeabilities of the slope surface and the upper layer are the same, do not show the larger gradient at the slope surface. In addition, the horizontal hydraulic gradients are almost the same (between 0.23 to 0.26), regardless of the permeability. Figure 6.15 shows the comparison of the magnitude of the water velocity vectors for the four cases at the time t=151 h. Similarly to Cases 1 to 4, Cases 5 to 8 show that the velocity of the water flow increases when the permeability increases and it is intense at the middle of the slope surface. However, larger velocities were obtained for the cases where the permeability of the slope surface is equal to the permeability of the upper

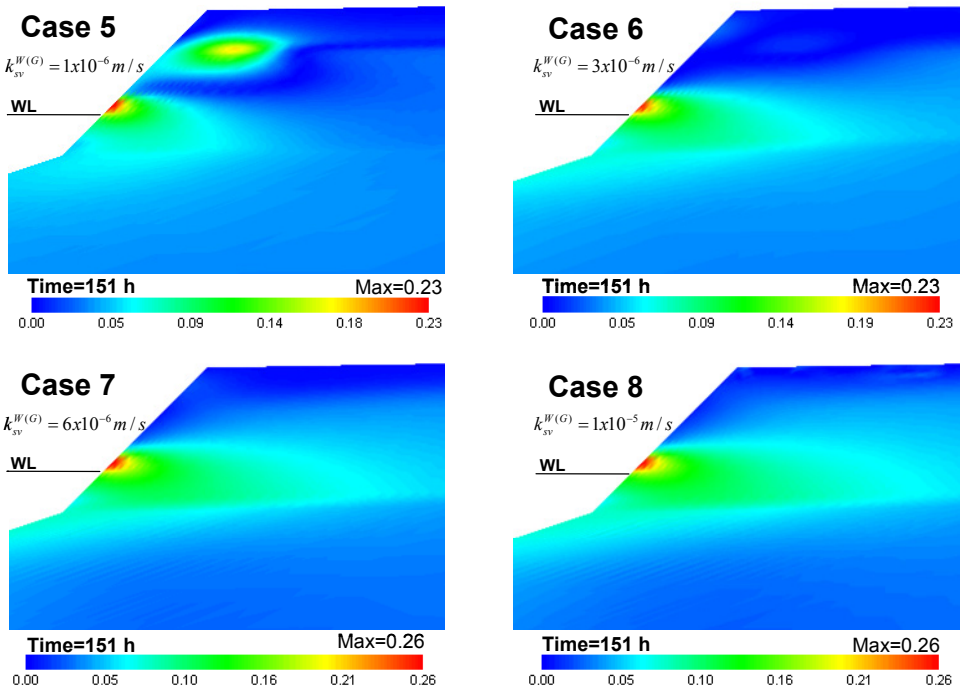

Figure 6.14 Distribution of the horizontal hydraulic gradient. Cases 5 to 8 (t=151 h).

layer (Cases 5 to 8) than for the cases where the permeability of the slope surface is smaller than the permeability of the upper layer (Cases 1 to 4). Comparison of the distributions of accumulated viscoplastic shear strain for the cases at the time t=151 h is shown in Figure 6.16. It is shown that the accumulation of viscoplastic shear strain is generated on the slope of the embankment immediately above the water level of the river. None of the cases show a large development of deformation on the slope of the embankment; however, a small accumulation of viscoplastic shear strain is evident above the water level near the slope surface. This is due to the larger hydraulic gradients presented on the surface of the slope above the water level. It can be said that due to homogeneity of the upper layer, the water can flow more easily toward the river side avoiding the increase of the pore water pressure inside the embankment.

Cases 9 to 12 (Group III)

From the results of Cases 1 to 4, we recognize that the effect of the permeability of the slope surface on the generation of viscoplastic shear strain is very significant. Smaller permeabilities on the slope surface bring about larger surface deformations immediately above the water level of the river. Consequently, it could lead to the local and general instability of the river embankment. This instability is due to the accumulation of the

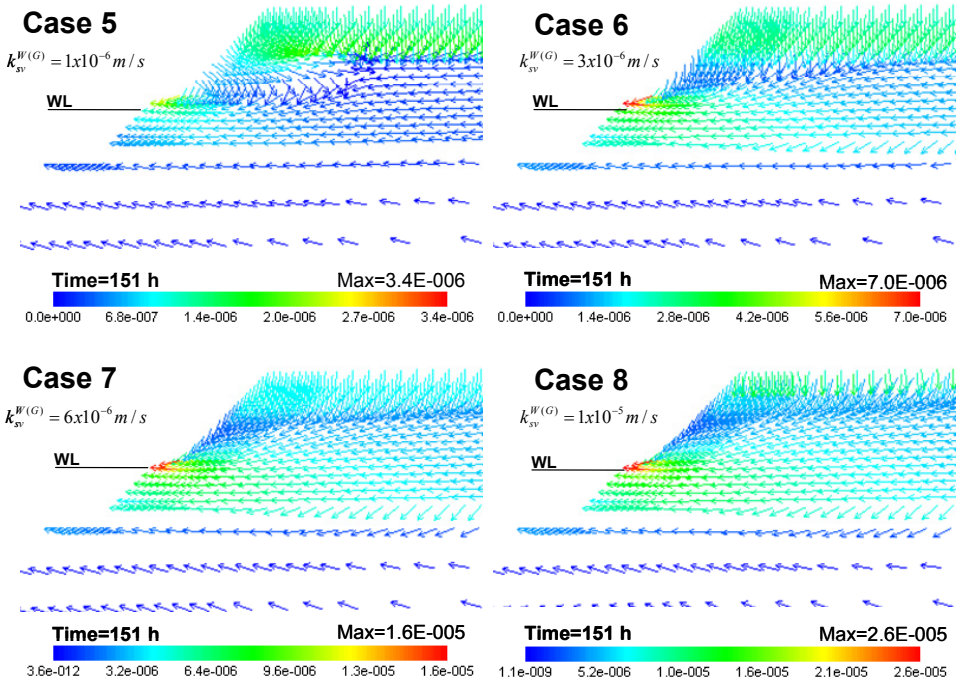

Figure 6.15 Distribution of the water velocity vectors. Cases 5 to 8 (t=151 h).

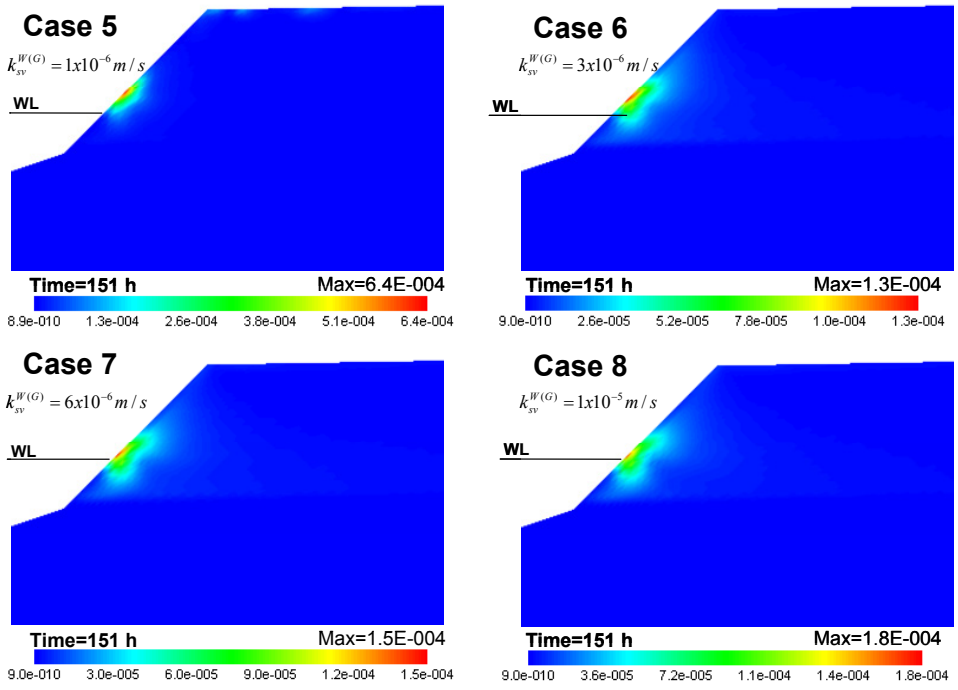

Figure 6.16 Distribution of the viscoplastic shear strain. Cases 5 to 8 (t=151 h).

water and the generation of pore water pressure at the back of the slope. To study more this behavior, the analysis of Cases 9 to 12 have been carried out in which a concrete face with small permeability is assumed at the slope surface. This is similar to the current case at Seta River site as shown in Figure 6.3. For the analyses, the concrete face is assumed as an elastic material (E=1 GPa, ν=0.1) and its saturated permeability is considered to be $k_{sv}^{W(S)}$ = 1.0 x 10^{-7} m/s. The saturated permeabilities for the sandy gravel layer are $k_{sv}^{W(G)}$ = 1.0 x 10^{-6}, 3.0 x 10^{-6}, 6.0 x 10^{-6}, and 1.0 x 10^{-5} m/s for Cases 9 to 12, respectively, as shown in Table 6.2.

Figure 6.17 shows the comparison of the distribution of the horizontal hydraulic gradient after the major rainfall (t=151 h) for Cases 9 to 12, respectively. Similarly to Cases 1 to 4, the horizontal hydraulic gradients increase with the increase of the permeability. However, larger gradient are obtained for the cases with the concrete face; it suggests a large accumulation of water and the generation of pore water pressures at the back of the concrete face. Figure 6.18 shows the comparison of the magnitude of the water velocity vectors for the same four cases at the time t=151 h. It is seen that the velocity of the water flow increases when the permeability increases and it is intense at the toe of the slope surface. Figure 6.19 presents the comparison of the distribution of viscoplastic shear strain for the cases at the time t=151 h. This figure shows that the accumulation of viscoplastic shear strain is localized below the concrete face. This result is very similar to the field data where soil erosion is presented below the concrete face in the embankment, as shown in Figure 6.3. Cases 9 to 11 show that the accumulated viscoplastic strains after the major rainfall are smaller; however, in Case 12 a large amount of accumulated viscoplastic strain (up to 49%) is generated. The water accumulated inside the embankment resulted in the accumulation of deformation of the soil on the back of the concrete face (internal erosion). Similarly to the cases with small permeabilities on the slope surface (Cases 1 to 4), comparison of Figures 6.17 to 6.19 shows that the localization of deformation below the concrete face is related to the hydraulic gradient, the velocity of the water flow, and the permeabilities of the soil layer.

Figure 6.20 shows the comparison of the viscoplastic shear strain-time histories for the elements 55, 60 and 104 between the times t=140 to t=168 h. The positions of the elements in the finite element mesh are shown in Figure 6.6, which correspond to the bottom, middle and middle-top of the slope at the back of the concrete face, respectively. It can be seen from this figure that the viscoplastic shear strain starts to increase in the

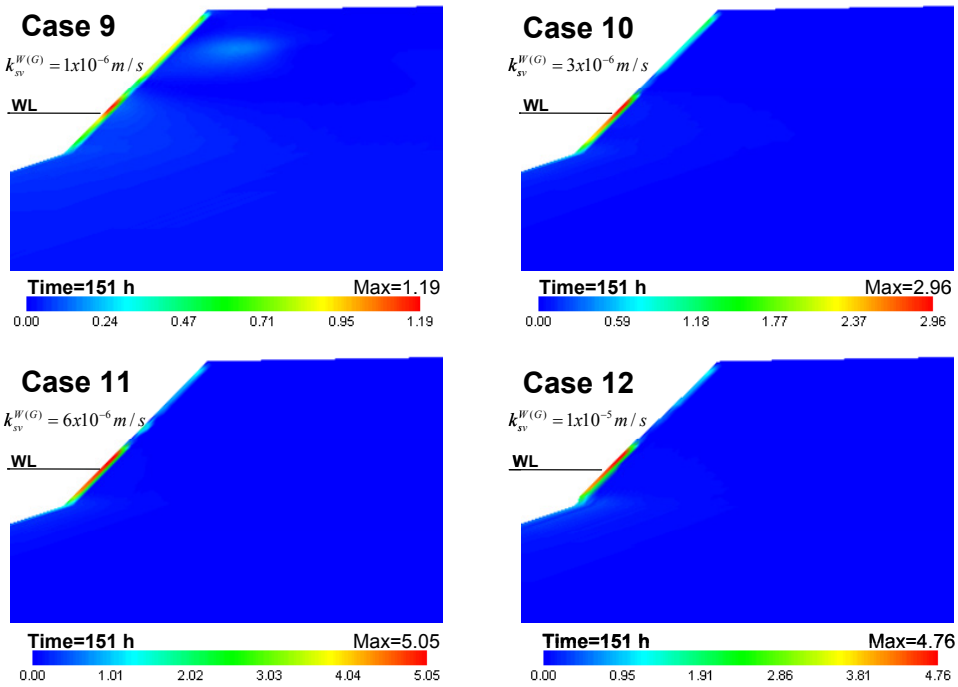

Figure 6.17 Distribution of the horizontal hydraulic gradient. Cases 9 to 12 (t=151 h).

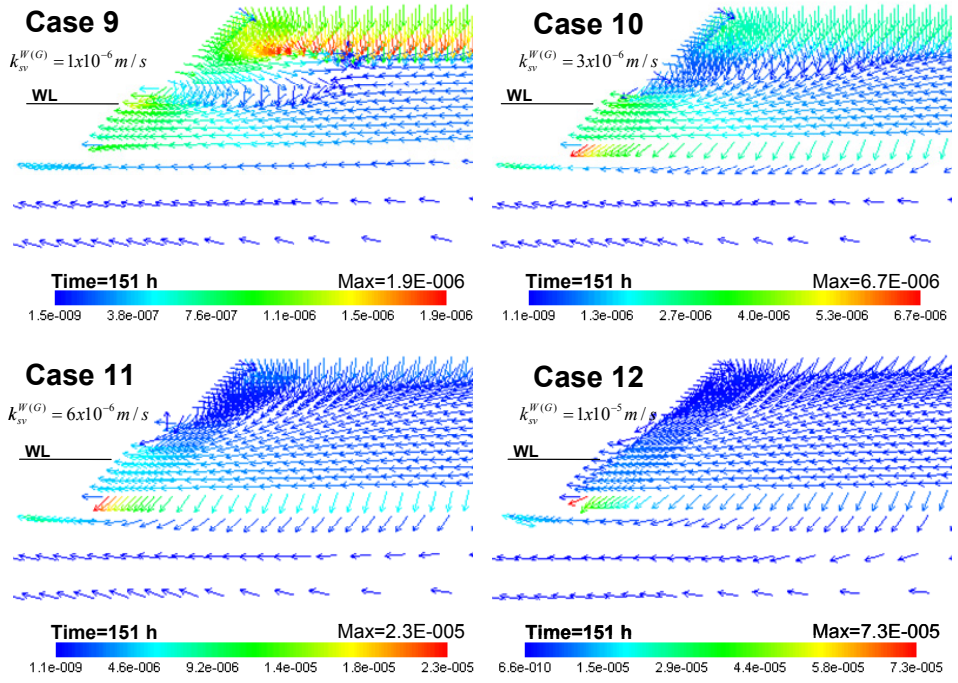

Figure 6.18 Distribution of the water velocity vectors. Cases 9 to 12 (t=151 h).

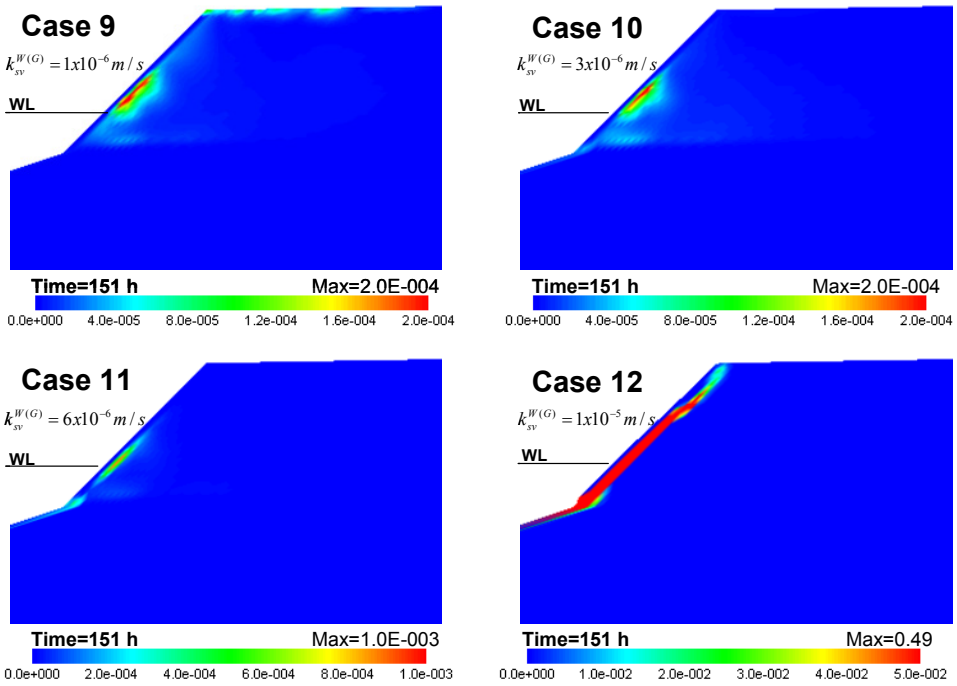

Figure 6.19 Distribution of the viscoplastic shear strain. Cases 9 to 12 (t=151 h).

elements 60 and 55 (middle and bottom of the slope) at time t=145 h. Later, at time t=147 h, it is possible to see that the development of viscoplastic shear strain appears at the middle-top of the embankment (element 104). This sequence in the development of viscoplastic shear strain shows that the localization of deformation starts below the middle high of the slope and rapidly propagates toward the crest of the embankment.

By comparing the results of Cases 5 to 8 and Cases 9 to 12 (Figures 6.14 to 6.19), it is possible to see that the effect of the permeability of the slope surface of a river embankment on its local instability is very significant. Larger hydraulic gradients and accumulated viscoplastic shear strains are obtained in the cases where the permeability of the slope surface is smaller compared to the permeability of the soil layer. It could be explained by the accumulation of the water behind the slope surface owing to the impediment of the water flow; as a result, larger pore water pressures and hydraulic gradients are generated at the back of the slope that may induce erosion at the surface. It suggests that some geotechnical measures to avoid the rainfall infiltration into the slopes, such as concrete faces and cement-soil mixtures, can be harmful for the local stability of the embankments if they are not accompanied by additional measures to reduce the water levels generated by the seepage flow from the hill sides during the rainfall infiltration. It supports the

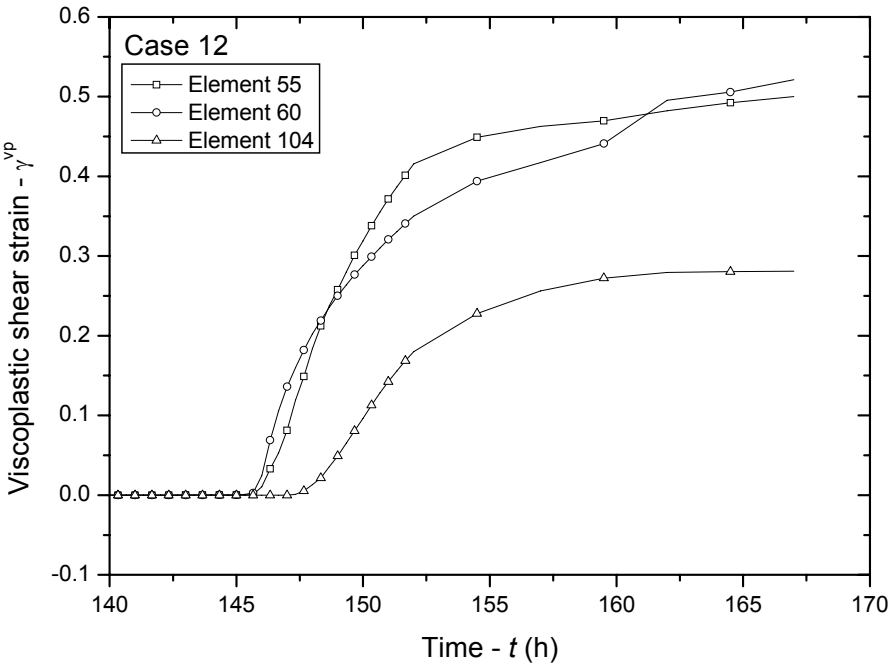

Figure 6.20 Time history of viscoplastic shear strain for elements 55, 60, and 104 (Case 12)

importance of the subsurface drainage of the soil structures in the improvement of their local and general stability.

6.3.4 Effect of horizontal drains

In the practical geotechnical problems, if a free drainage boundary condition prevails at the surface of an embankment, the excess of water resulting from the water infiltration drains out freely avoiding the increase of the water table and the increase of the pore water pressure (Cases 5 to 8). However, if the water can not flow out easily, it accumulates inside the embankment increasing the pore water pressure. Cases 1 to 4 and 9 to 12 showed that due to the rainfall infiltration and seepage flow, the water table rises within the river embankment and the pore water pressure increases. Moreover, once the pore water pressure develops at the back of the slope of the embankment, a highly unstable zone is developed in this area and the erosion or local failure occurs. It is evident that this problem could trigger larger instability zones due to the retrogressive advance in time of the erosion endangering the soil structure and inducing its global instability.

To overcome this problem it is convenient to allow the soil structure to dissipate the pore water pressure generated due to the build up of the water table. To do that, sub-

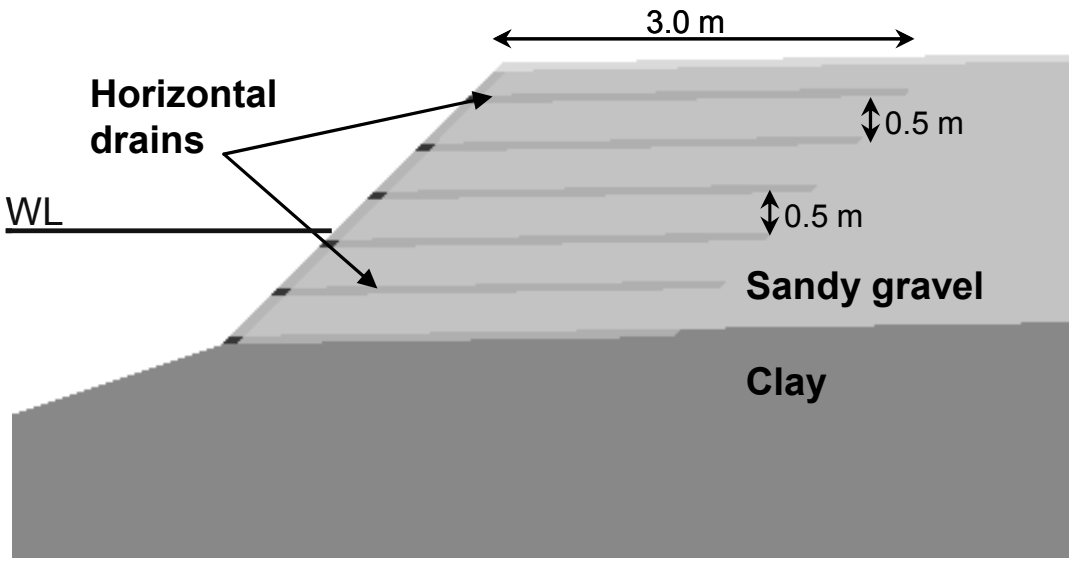

Figure 6.21 Location of the horizontal drains in the river embankment

surface drainage is recommended. Horizontal drains is one of the most common methods used for the subsurface drainage and it has been proved to be effective in preventing the development of pore water pressures due to the rainfall infiltration and seepage flow (e.g. Cai et al., 1998; Rahardjo et al., 2003; Ghiassian and Ghareh, 2008).

To show the effectiveness of the use of horizontal drains in the drainage of the excess of water generated inside the Seta River embankment, the same two cases in which the larger pore water pressures and larger deformations were presented (Cases 4 and 12) are simulated by using horizontal drains. These simulations are referred as Cases 21 and 22, respectively. The same parameters listed in Table 6.1 and the same finite element mesh configuration showed in Figure 6.6 are used; the location of the horizontal drains considered in the simulations are shown in Figure 6.21. Six rows of 3 m long horizontal drains spaced every 0.5 m are considered.

The horizontal drain is introduced in the simulation as a drained boundary line. Each horizontal drain is evaluated according to its location and the present pore water pressure at the nodes as follows:

- In the case the drain nodes are located below the water level, i.e., saturated zone: The pore water pressures at the nodes are adjusted to the pore water pressure calculated according the water level of the river. Consequently, the excess of water is drained out and there is not flow of water from the river into the embankment.

- In the case the drain nodes are located above the water level, i.e., unsaturated zone: If the pore water pressures at the nodes are negative (suction), the node is treated as a normal node; as a result, the excess of water moves throughout the embankment as if the drains were not installed. On the other hand, if the pore water pressure at the nodes is positive, the pore water pressure at the drain nodes is specified as a zero value. Therefore, the excess of water is drained out.

The drain nodes evaluated by the above boundary conditions allow the water to be drained out only in the case the surrounding soil is saturated.

The results of the distribution of the saturation at time t=151 h for the cases without drains, namely, Cases 4 and 12, and the cases with drains, namely, Cases 21 and 22, are shown comparatively in Figure 6.22. In these cases the same saturated water permeability for the sandy gravel layer is considered ($k_{sv}^{W(G)}$ = 1.0 x 10^{-5} m/s). When the numerical results are compared it is clearly shown by Cases 21 and 22 that the installation of the horizontal drains considerably reduces the saturation and accumulation of the infiltrated water in the upper part of the embankment. Figure 6.23 shows the comparison of the time histories of pore water pressure for the cases with and without drains. This figure show the results for the element 104 located at the back of the slope and above the initial water level as shown in Figure 6.6. From Figure 6.23 it can be seen that for the cases without drains, the pore water pressure increases in element 104 during the rainfall infiltration and it reaches its maximum value around the time t=151 h after the maximum rainfall intensity is applied. The maximum pore water pressure (or reduction in suction) was obtained for Case 12 (P^W=-0.18 kPa) where a concrete surface was assumed at the slope surface, it means that the water accumulates within the embankment increasing the level of the water table. For Case 4, in which a permeability larger than that used for Case 12 was assumed for the slope surface, the maximum value for the pore water pressure, P^W=-4.88 kPa, is attained at the time t= 151 h; after this time, the pore water pressure starts to dissipate. Cases 21 and 22 show the results of the pore water pressure when the drains are installed within the embankment. Similar results are obtained for both cases. From the figure it is seen that the pore water pressure remains almost constant between the times t=0 h and t=140 h. After t=140 h, the pore water pressure starts to increases and it shows its maximum value at the time t=147 h, P^W=-8.36 kPa, and it remains constant until the time t=151 h when the major rainfall is stopped, after this time the water pressure starts to decreases reaching a similar initial value. Comparison

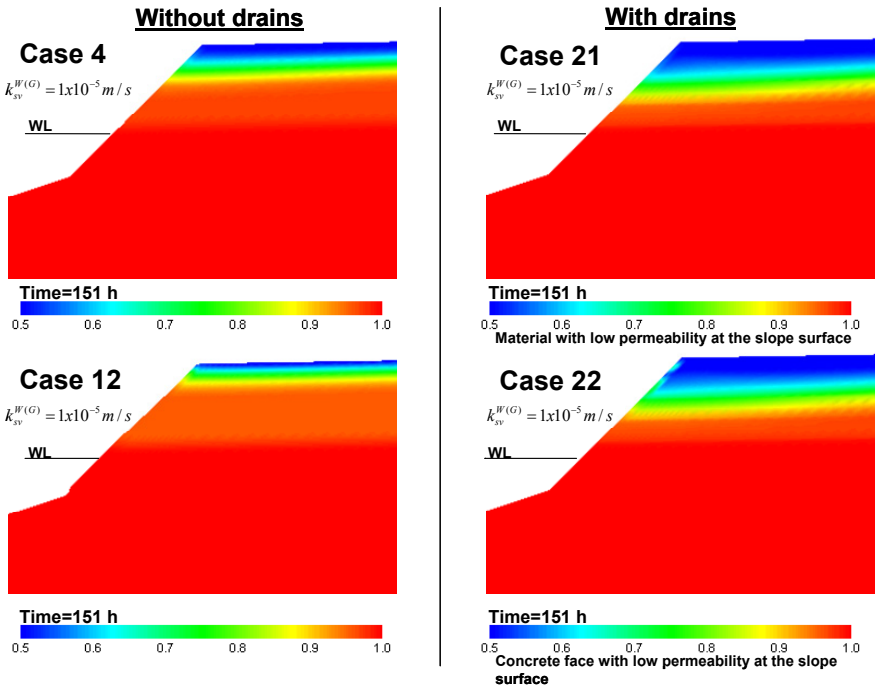

Figure 6.22 Distribution of saturation. Cases 4, 12, 21, and 22 (t=151 h).

of the results show that the horizontal drains keep the pore water pressure smaller during the infiltration process avoiding the build up of the water table; moreover, they allow the rapid drainage of the accumulated water after the rainfall is stopped.

A comparison of the magnitude of the water velocity vectors for the same cases described above at the time t=151 h are shown in Figure 6.24. Comparing the results, the analyses without drains (Cases 4 and 12) show a vertical water flow due to the rainfall infiltration at the top of the embankment, nevertheless, the direction of the flow changes rapidly to be horizontal toward the slope of the river embankment. In contrast, in the analyses with horizontal drains (Cases 21 and 22) it is observed that the water flow have a dominant vertical direction toward the drains where the infiltrated water can be drained out. The water flow direction shows that the drains located at the bottom of the river embankment attract both the water due to the rainfall infiltration and the seepage flow from the mountain side, it avoids the build up of the water table at the river side.

In order to investigate the effect of the horizontal drains on the strain localization due to the rainfall infiltration and seepage flow, the distributions of the viscoplastic shear strain at time t=151 h for the cases with drains are plotted together with those obtained for the cases without drains in Figure 6.25. As shown on the left side of Figure 6.25, the

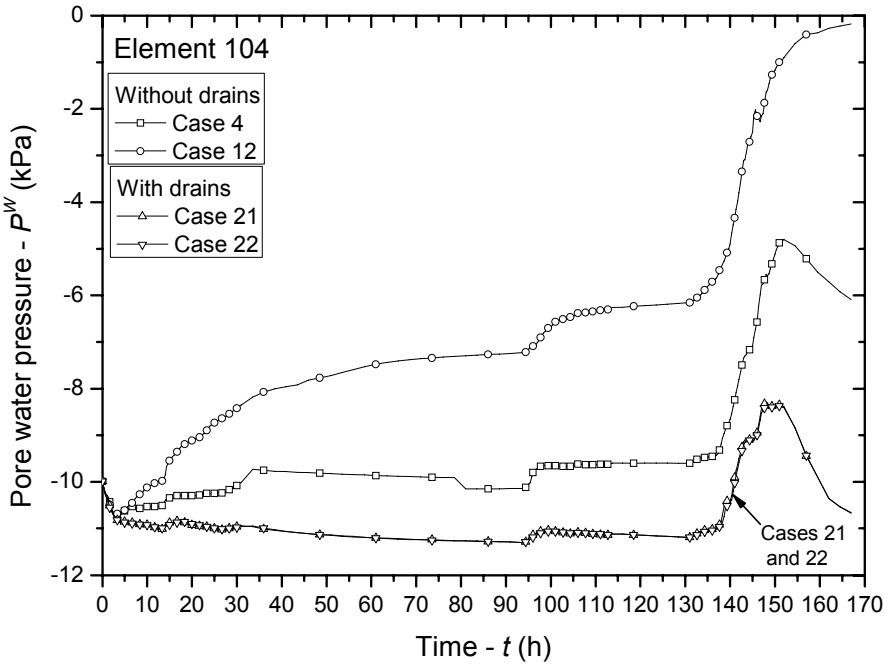

Figure 6.23 Time history of the pore water pressure, element 104. Cases 4, 12, 21, and 22.

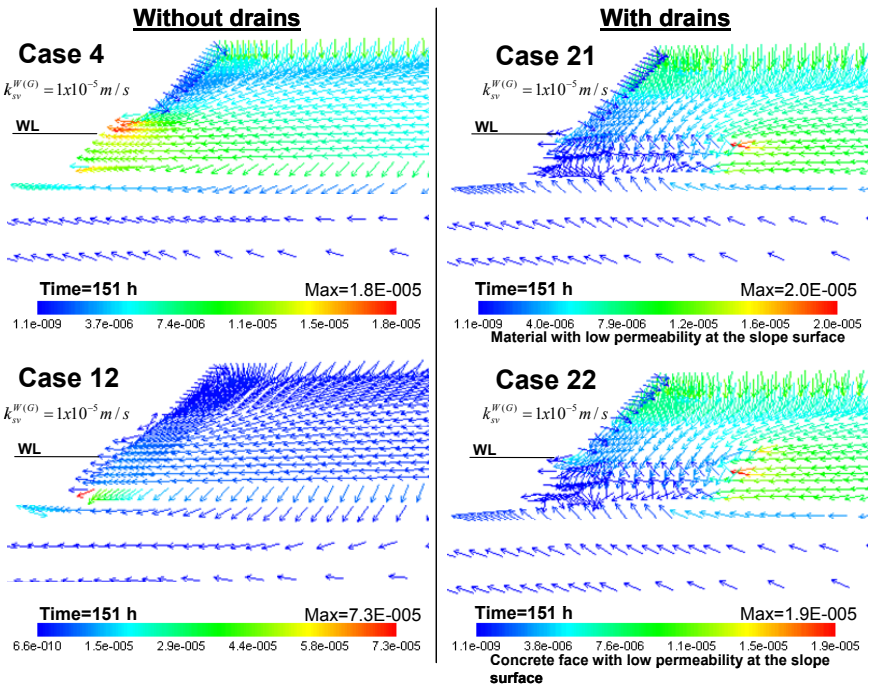

Figure 6.24 Distribution of the water velocity vectors. Cases 4, 12, 21, and 22 (t=151 h).

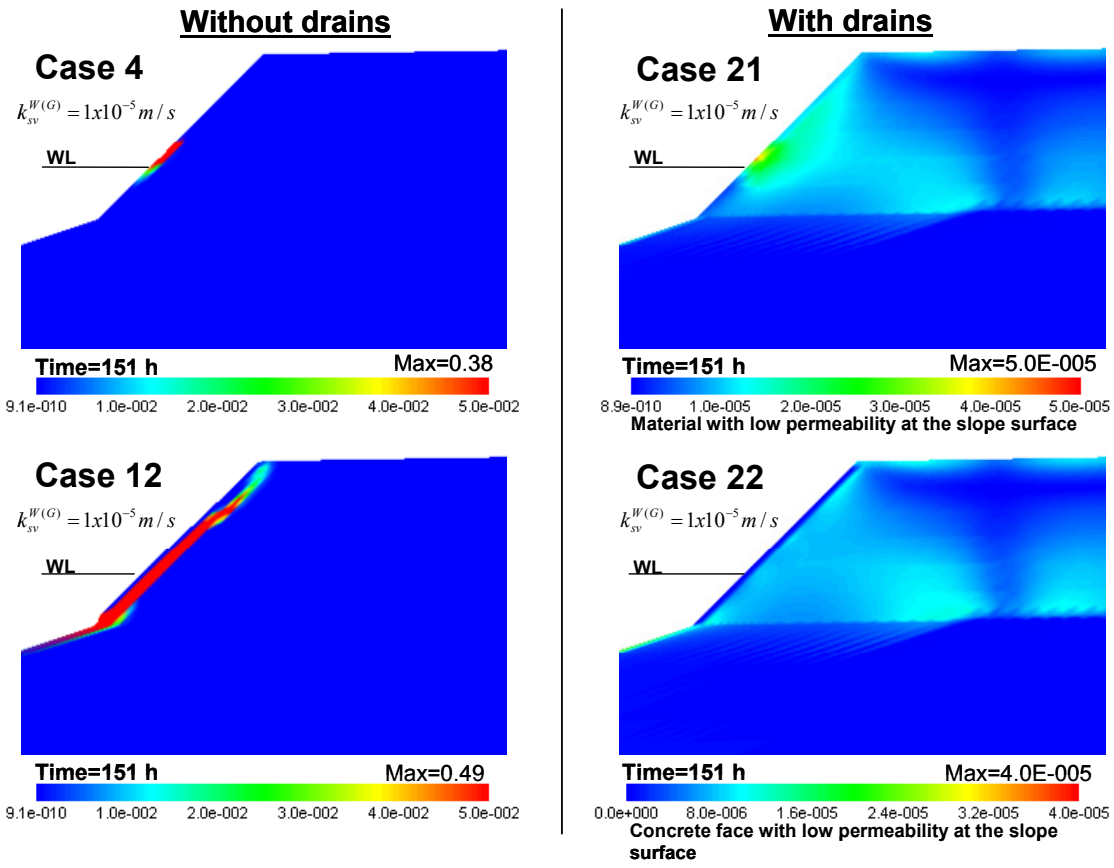

Figure 6.25 Distribution of the viscoplastic shear strain. Cases 4, 12, 21, and 22 (t=151 h).

accumulation of the viscoplastic shear strains for the cases without drains are localized at the middle high of the river embankment for Case 4 and all around the back of the concrete face for Case 12. The localization of the strain is due to the accumulation of water at the back of the slope as explained previously. For the analyses performed with the horizontal drains, right side of Figure 6.25, it is seen that the accumulation of the strains disappear at the slope of the embankment; in addition, only small accumulations of irrecoverable deformation are presented inside the river embankment (maximum values around 5.0 x 10^{-5}). It corroborates the effectiveness of the horizontal drains in avoiding the erosion and the instability of the river embankments due to the large seepage pressures that can be generated at the river sides owing to the infiltration processes.

6.3.5 Effect of compaction

One of the main parameters to determine the quality of the construction of the soil structures is the degree of compaction. Soil structures with larger degrees of compaction

Table 6.3 Material parameters for the study of the compaction effect

Material parameters		Case 12	Case 23	Case 24	Case 25
Initial elastic shear modulus (kPa)	G_0	3000	2300	1600	900
Viscoplastic parameter (1/s)	C_1	1.0×10^{-15}	1.0×10^{-13}	1.0×10^{-11}	1.0×10^{-9}
Viscoplastic parameter (1/s)	C_2	2.0×10^{-15}	2.0×10^{-13}	2.0×10^{-11}	2.0×10^{-9}

are expected to be more stable than those with smaller degrees of compaction. Larger degrees of compaction are associated with larger shear modulus and smaller development of strains. During the construction of embankments, however, it is very difficult to attain the compaction near the slope surfaces. This is because at the border of the embankments the soil is unconfined and the compaction is hard to be achieved. Therefore, any river embankment with a lack of compaction at the river side could develop larger deformation and consequently a more rapid failure during the seepage infiltration. This deformation could in turn lead to the damage or nearby structures.

This section addresses the problem of large deformation in the river embankments due to the low compaction of the soil close to the river side. The influences of both the rainfall and the seepage flow are considered. Four cases are analysed to show the effect of compaction on the development and the localization of strains, namely, cases 12, 23, 24, and 25. Case 12 in Table 6.2 is selected as the reference case. To simulate the material with smaller degrees of compaction, the initial elastic shear modulus G_0 is decreased while the viscoplastic parameters C_1 and C_2 are increased for the soil within the first three meters of the sandy gravel layer as shown schematically in Figure 6.26. The modified parameters used for the simulations are listed in Table 6.3. The remaining parameters are the same listed previously in Table 6.1.

Comparison of the viscoplastic shear strain distributions, corresponding to the four cases listed in Table 6.3, and for a rainfall infiltration time equal to 147.6 h is shown in Figure 6.27. The time t=147.6 h is chosen for the comparison because it is the time at which the simulation for case 25 is numerically unstable due to the divergence of the deformation. It can be seen that a large amount of viscoplastic shear strain is generated in the sandy gravel layer below the concrete face on the slope at the river side. This large strain extends from the bottom of the slope, and then progresses upward to the crest of the river embankment. By comparing the results of the analyses, we can observe that the viscoplastic shear strain increases as the material becomes weaker (smaller initial

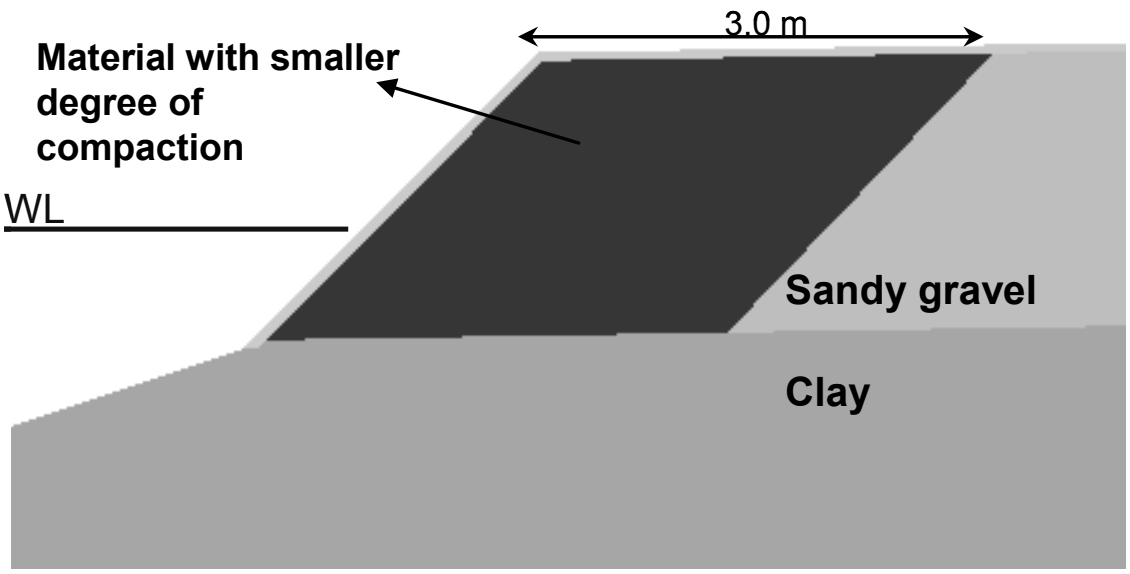

Figure 6.26 Location of the low compacted area

shear modulus and larger viscoplastic parameters, Cases 12, 23, 24 and, 25, respectively). The largest viscoplastic shear strain is obtained for case 25 (γ^{vp}=51%). This figure also shows that the shear zone is larger for Case 25. In this case, a second shear zone develops and progresses as a curve starting from the middle high of the slope of the embankment, which extends farther toward the upper part of the embankment. The results show the importance of achieving higher degrees of compaction during the construction process in order to improve the safety of the river embankments.

6.4 S River Case

In recent years, many natural disasters have occurred in the world associated with rains, typhoons and hurricanes. The tendency for these natural phenomena has been increasing nowadays. Torrential rains usually lead to the increase of the water level of the rivers triggering the failure of the river dike embankments due to seepage flow and overflow. In order to study the effect of the water infiltration due to the rise of the water level of the rivers on the river dikes, an experiment in the field has been performed. In the experiment constant rainfall intensity is applied on the surface of the river dike while the water level is increased and decreased to observe the effect of the seepage flow on the generation of pore water pressure and on the deformation of the embankment.

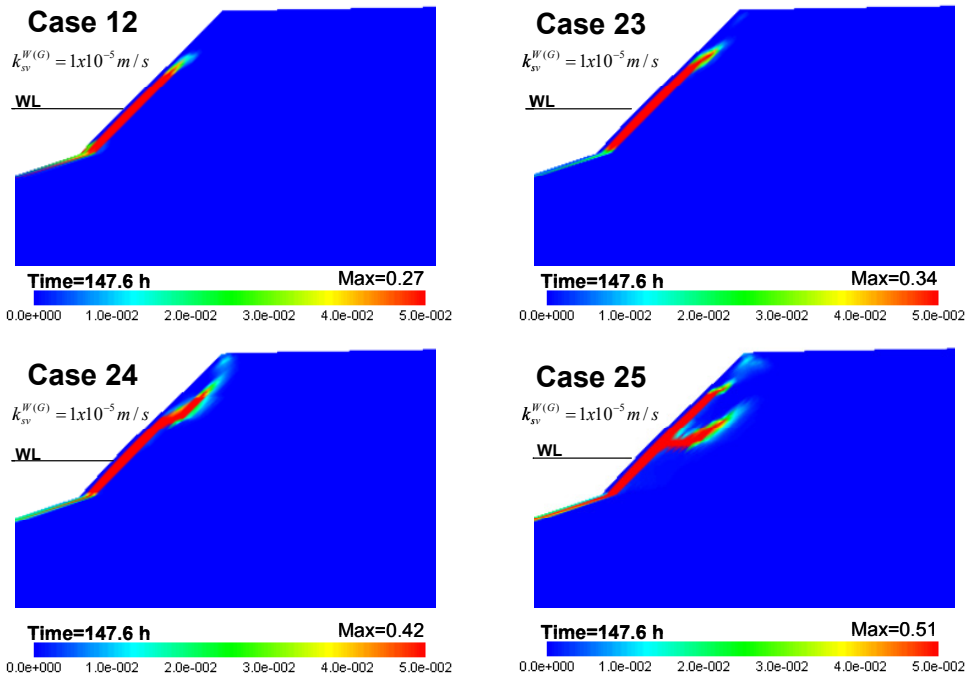

Figure 6.27 Distribution of the viscoplastic shear strain. Cases 4, 23, 24, and 25 (t=147.6 h).

6.4.1 Geometry and boundary conditions

The cross section, the finite element mesh, and the boundary conditions for the simulation of the rainfall infiltration and seepage flow into the unsaturated river dike are shown in Figure 6.28. The top of the river embankment is 4.0 m wide. The right and the left slopes of the embankment have a gradient about 1V:2H. The height of the embankment at the right side is 3.14 m and at the left side 2.3 m. The bottom of the embankment is 15.0 m wide. For displacement, the foundation of the embankment is fixed at the bottom in both horizontal and vertical directions, the laterals boundaries are fixed only in horizontal direction. The water level in the soil is assumed to be located at the right side toe of the river dike (z=2.5 m). The unsaturated embankment is considered to have a constant initial saturation equal to s=0.80, i.e., the initial negative pore water pressure is assumed to be constant. In the transition region between the initial water level and the constant saturation region, we assumed that the pore water pressure is linearly interpolated. The flux of air is allowed for the entire boundaries and the initial air pressure, P_i^G , is assumed to be zero. An impermeable boundary is assigned to the bottom of the soil foundation; for the lateral sides and the right top of the embankment foundation, the boundary is considered to be permeable. The right slope of the embankment is considered to be either a rainfall boundary if the water level is below the nodes or a drained boundary if the

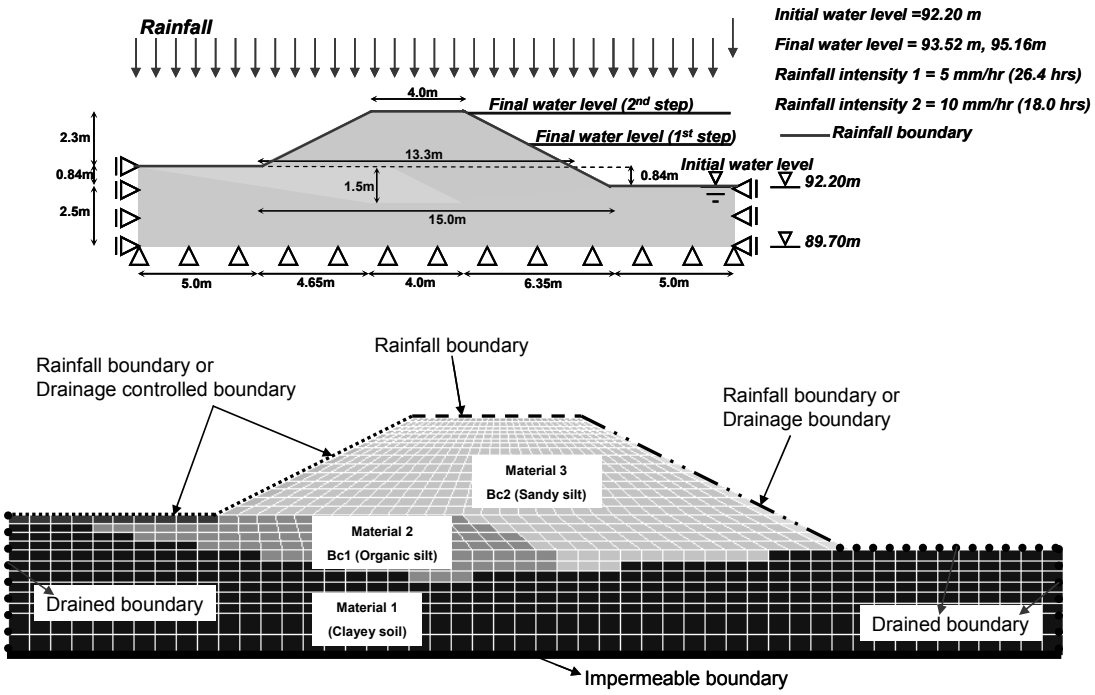

Figure 6.28 Cross section of the river embankment, element discretization, and boundary conditions

raising water reaches the nodes. Similarly, the left slope of the embankment and the left of the embankment foundation are considered to be either a rainfall boundary if the soil is unsaturated or a drained boundary in the case the pore water pressure becomes positive due to the seepage from the right side of the embankment. The top surface of the embankment is considered as a rainfall boundary. The rainfall boundary is the same as described in Section 5.2.1.

6.4.2 Soil profile

The river embankment is composed of three materials as shown schematically in Figure 6.28. These materials are considered to be elasto-viscoplastic materials. The same constitutive parameters are used for the three materials, except that the saturated water permeabilities of the Materials 2 (Bc1) and 3 (Bc2), are assumed to be different according the experimental tests. Bc1 indicates the middle stratum and it corresponds to organic silt, and Bc2 indicates the upper stratum and it corresponds to sandy silt, respectively. These soil layers overlie on a soil foundation composed of clayey soil (Material 1). The material parameters required for the simulation are listed in Table 6.4. These parameters represent the three soils found in the river embankment. The soil water characteristic curve considered to describe the suction-saturation relationship for the soils is shown in

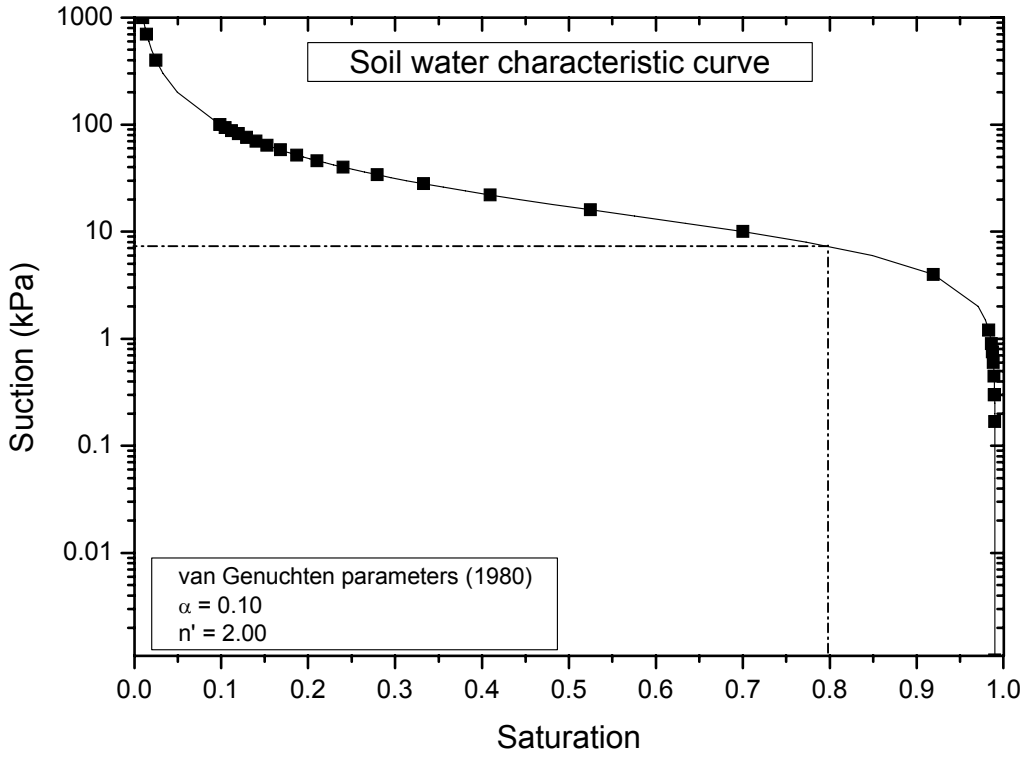

Figure 6.29 Soil water characteristic curve

Figure 6.29.

6.4.3 Experimental configuration

The configuration of the experiment is shown schematically in Figure 6.30. In the experiment two lateral and one longitudinal sheet piles were used to make a water tank in order to control the level of the water at the right side of the river embankment. The distant between the lateral sheet piles is 15.0 m, while the longitudinal sheet pile was located 4.0 from the toe of the embankment. The height of the sheet piles is 4.0 m measured from the soil foundation. To apply constant rainfall intensity, various perforated pipes located about 4.0 meters from the toe of the embankment were used. The field experiment was performed by both artificial rainfall and seepage flow from the rise of the water level at the right side of the embankment. The experimental program can be mainly explained in three steps as follows (Figure 6.30):

- Step 1: Constant rainfall intensity equal to 5 mm/h was applied on the surface of the embankment for a period of time of 26.4 h. At the time t=26.4 h the rainfall intensity was increased to be 10 mm/h and it continued during 8.1 h.

Table 6.4 Material parameters for S River simulation

Viscoplastic parameter	$m^{'}$	23.0
Viscoplastic parameter (1/s)	C_1	1.0 x 10^{-8}
Viscoplastic parameter (1/s)	C_2	1.0 x 10^{-8}
Stress ratio at critical state	M_m^*	0.947
Compression index	λ	0.03
Swelling index	κ	0.002
Initial elastic shear modulus (kPa)	G_0	28700
Initial void ratio	e_0	1.50
Structural parameter	β	0.0
Structural parameter	$\frac{\sigma_{maf}^{'}}{\sigma_{mai}^{'}}$	1.0
Vertical permeability of water s=1 (m/s)	k_{sv}^W	***
Horizontal permeability of water s=1 (m/s)	k_{sh}^W	***
Permeability of gas at s=0 (m/s)	k_s^G	1.00 x 10^{-3}
Van Genuchten parameter (1/kPa)	α	0.10
Van Genuchten parameter	n'	2.00
Suction parameter	S_I	0.20
Suction parameter	s_d	0.25
Minimum saturation	s_{min}	0.0
Maximum saturation	s_{max}	0.99
Shape parameter of water permeability	a	3.0
Shape parameter of gas permeability	b	1.0

***The permeability is variable, which depends on the soil layer and the simulation case

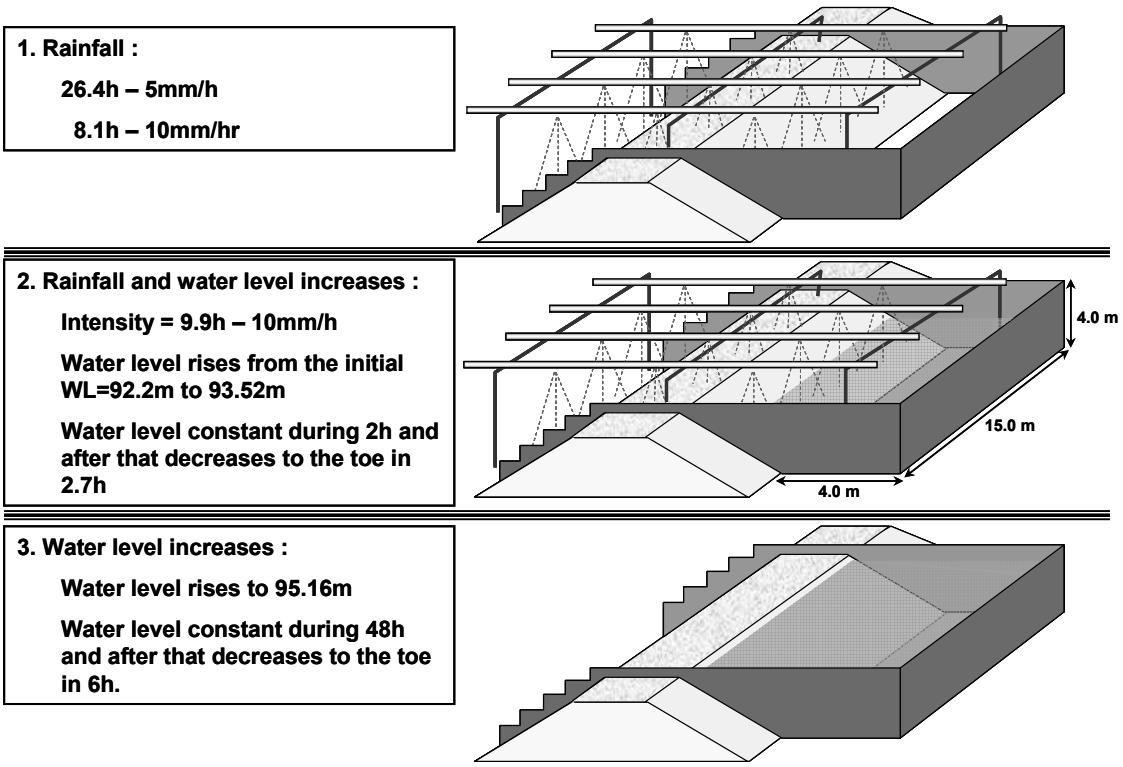

Figure 6.30 Sketch of the experimental configuration

- Step 2: The water level at the right side of the embankment was increased during 7.9 h from the toe of the embankment (datum, h=92.2 m, see Figure 6.28) to a height of 93.52 m and it was kept constant for 2 h. During the time the water level was increased and it was kept constant the previous rainfall intensity equal to 10 mm/h is continuously applied. Then, the rainfall was stopped and the water level was decreased to the initial water level during 2.7 h.

- Step 3: The water level is again increased for 17.7 h to a height of 95.16 m and then remains constant for 48 h. After that, the water level was decreased to its initial level in 6 h.

Figure 6.31 shows the rainfall pattern and the right water level-time histories during the experiment. For the rainfall, this figure shows that the first rainfall equal to 5mm/h is applied during the times t=0 h and t=26.4 h and the second rainfall equal to 10mm/h is applied between the times t=26.4 and t=44.4 h. The total amount of rainfall applied to the embankment was 312 mm. For the water level, it is possible to see during the experiment that the water level at the right side of the embankment started to be increased at the

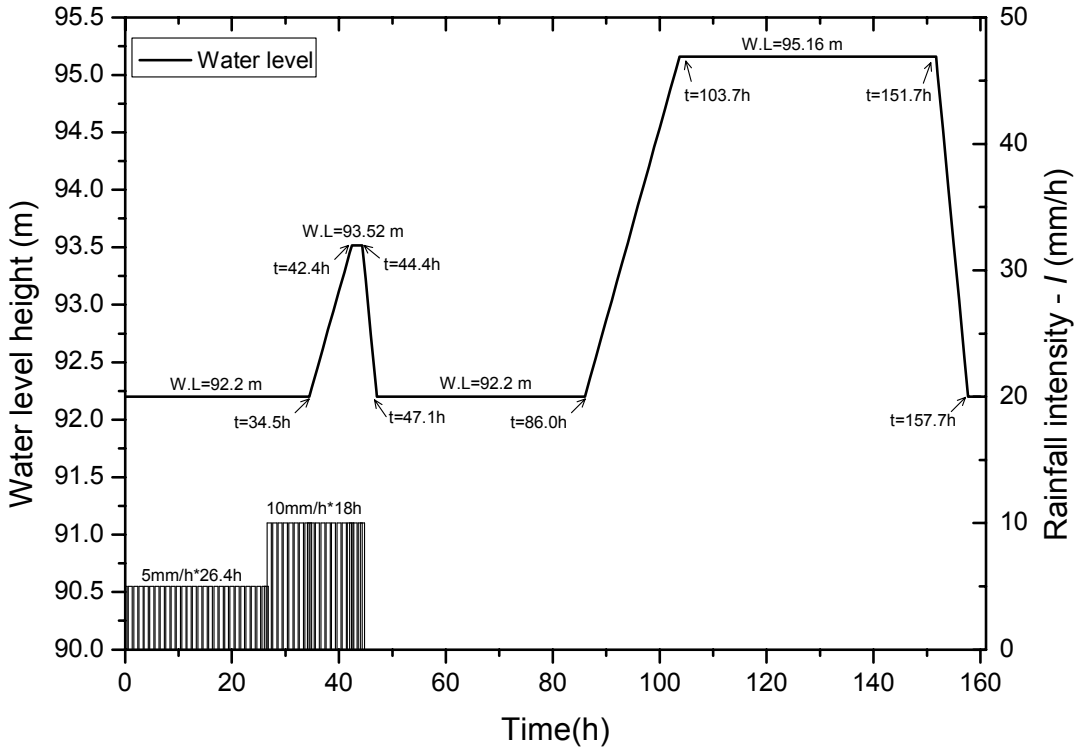

Figure 6.31 Experimental rainfall and water level hitories

time t=34.5 h, after 7.9 h the water level reached a height equal to 93.52 m and remained constant for 2 h; at the time t=44.4 h the water level was decreases in 2.7 h to its initial water level and it was kept constant for 38.9 h. At the time t=86.0 h the water level started to be increased for 17.7 h until the height of 95.16 m was reached at the time t=103.7 h and it remained constant for 48.0 h. Finally, at the time t=151.7 h the water level started to be decreased to its initial level in 6 h.

6.4.4 Simulation cases

As mentioned before, one of the greatest uncertainties concerning the study of rainfall infiltration and seepage flow lies on the field values of the saturated water permeability. Figure 6.32 shows a summary of the experimental results for the saturated permeabilities obtained by the laboratory tests, the field measurements, and those estimated by the gradation of the soils. The results are shown for materials 2 and 3, respectively. From Figure 6.32 it can be seen that the permeabilities obtained by the laboratory tests and those obtained by field measurements significantly differ among them. In general, the laboratory permeabilities are much smaller than those obtained by the field measurements. These

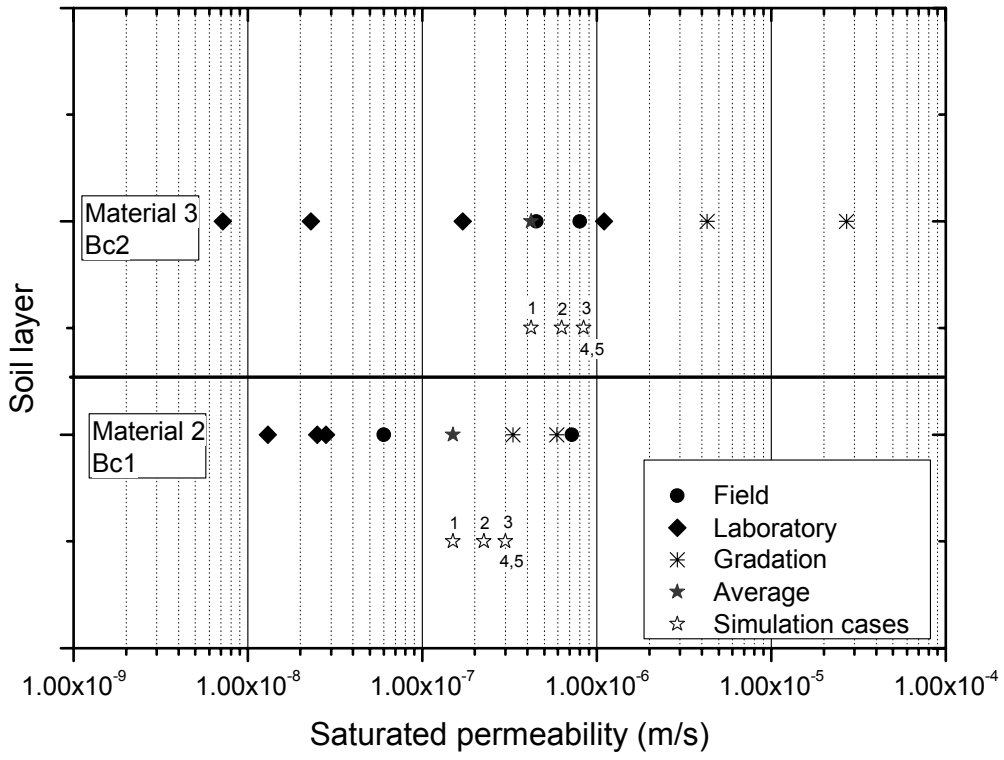

Figure 6.32 Summary of the measured saturated water permeabilities

differences can be explained by the heterogeneity of the material and the disturbance of the soil samples during the laboratory tests. Figure 6.32 also shows the average saturated permeabilities which were calculated by averaging all the results. Because of the high variability of the results obtained for the permeabilities of the soils, it is necessary to perform a parametric analysis to seek for the permeability values that can represent the soils. Therefore, in order to compare the results of the water levels obtained in the simulation with the results of the field measurements, different permeabilities were used for the layers Bc1 and Bc2.

Five cases are considered in the parametric analysis. These cases consist mainly of the combination of different saturated permeabilities for the middle and the upper layers. The range of the permeabilities used for the analysis varies from the average permeabilities (Bc1: k_{sv}^{W}=1.5 x 10^{-07} m/s, Bc2: k_{sv}^{W}=4.2 x 10^{-07} m/s) to two times the average permeabilities. The simulation program is outlined in Table 6.5. The horizontal permeability is considered to be 10 times the vertical permeability for Cases 1 to 3 and 7.5 times the vertical permeability for Cases 4 and 5. The initial water level (minimal water level in the simulations) is assumed to be 92.2 m, except for Case 5 where it is assumed to be

Table 6.5 Saturated water permeabilities and simulation case

Case No.	Average permeability (m/s)		Magnification	Permeability used in the simulation (m/s)		Rainfall intensity (mm/hr)	
	Layer Bc1	Layer Bc2		Layer Bc1	Layer Bc2		
1			1	1.50×10^{-7}	4.20×10^{-7}	1.5	$k_{sh}^{W}=10k_{sv}^{W}$; WL=92.2m
2			1.5	2.25×10^{-7}	6.30×10^{-7}	2.3	$k_{sh}^{W}=10k_{sv}^{W}$; WL=92.2m
3	1.50×10^{-7}	4.20×10^{-7}	2	3.00×10^{-7}	8.40×10^{-7}	3.0	$k_{sh}^{W}=10k_{sv}^{W}$; WL=92.2m
4			2	3.00×10^{-7}	8.40×10^{-7}	3.0	$k_{sh}^{W}=10k_{sv}^{W}$; WL=92.2m
5			2	3.00×10^{-7}	8.40×10^{-7}	3.0	$k_{sh}^{W}=10k_{sv}^{W}$; WL=91.9m

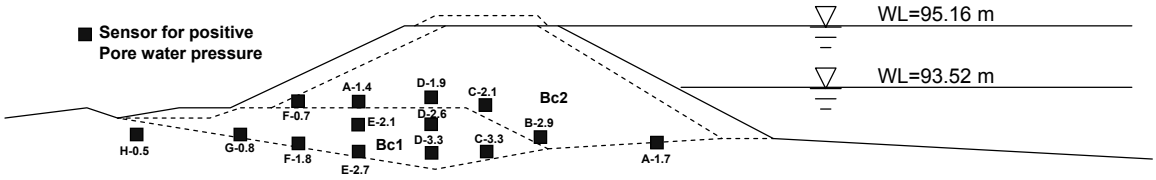

Figure 6.33 Sensor location for the measurement of pore water pressure

91.9 m. The rainfall intensity applied on the embankment is assumed to be equal to the saturated permeability of the soil, meaning that the excess of rainfall is considered to be dissipated as run off.

During the test, the positive pore water pressure response was monitored by installing pore water pressure sensors within the river embankment. A total of 14 sensors were placed at different elevations and closer to the toe of the embankment as shown schematically in Figure 6.33. The sensors were connected to a computer-based data acquisition system. The pore water pressures measured by the sensors were automatically converted to the water heights. In the sensor labels presented in Figure 6.33, the number indicates the depth of the location of the sensor projected vertically from the surface of the river embankment.

Figure 6.34 shows the measured results of the change of the water levels (change in positive pore water pressures) at the sensor locations in Figure 6.33. This graph shows that when the rainfall was applied, only a small accumulation of water is observed at the bottom of the embankment. However, when the water level at the right side of the embankment was increased to the heights of 93.52 m and 95.16 m, the water infiltrated into the soil increasing the pore water pressures at the bottom of the embankment. The water levels are higher at the right side of the embankment and gradually decrease toward

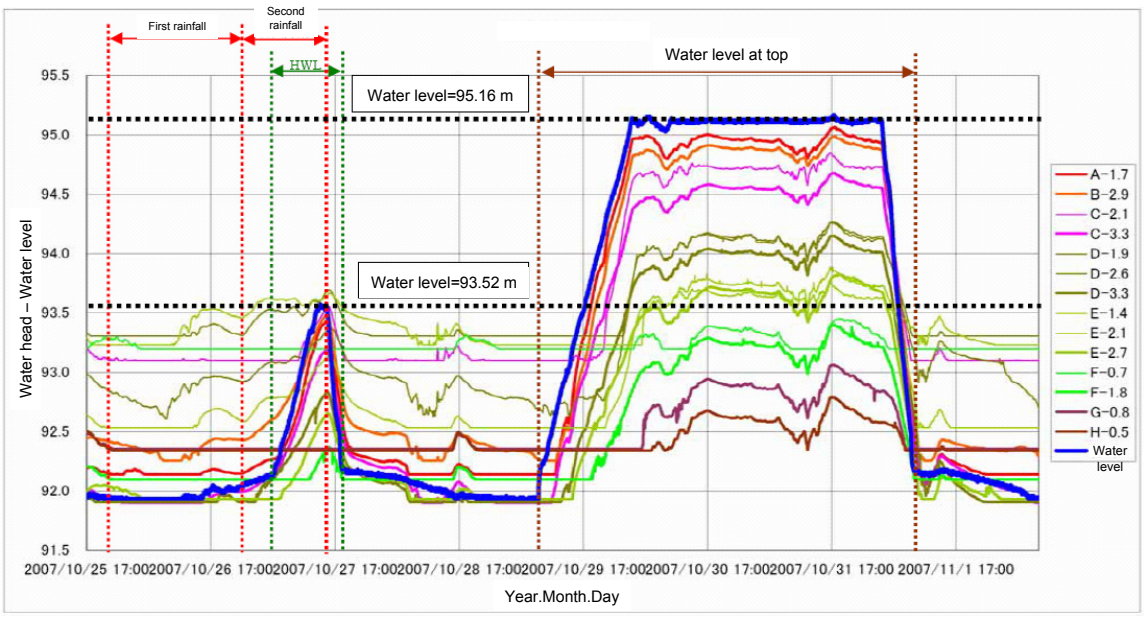

Figure 6.34 Histories of the measurement of water levels

the left side of the embankment.

6.4.5 Numerical results

Figure 6.35 shows the calculated pore water pressure profiles below the crest of the embankment at the right side for Case 5 and at the time intervals 0, 5, 10, 20, 30, 44, 50 and 80 h during the rainfall infiltration and seepage process. The initial state of t=0 h corresponds to the initial conditions at which the unsaturated soil presents an initial maximum suction of -7.2 kPa (corresponding to the saturation s=0.8). Next, after $t = 0$, the rainfalls start to be applied and the pore water pressure is generated in the embankment. The suction is reduced on the top of the embankment and the pore water pressure starts to increase at the bottom due to the accumulation on the rainfall infiltration. The pore water pressure profile at the end of the rainfall infiltration and before the water level started to decrease is shown as the line corresponding to the time t=44.4 h. The pore water pressure profiles at times t=50 h and t=80 h present the results after the water level reaches its initial condition and before it starts to increase again to the height of 95.16 m, respectively. The results show that, during this time, the water close to the surface moves downward toward the water table increasing the water level within the river embankment.

The results of the saturation distribution for the same case at the times when the water level is constant at the height h=93.52 m (t=44.4 h), the water level starts to increase at

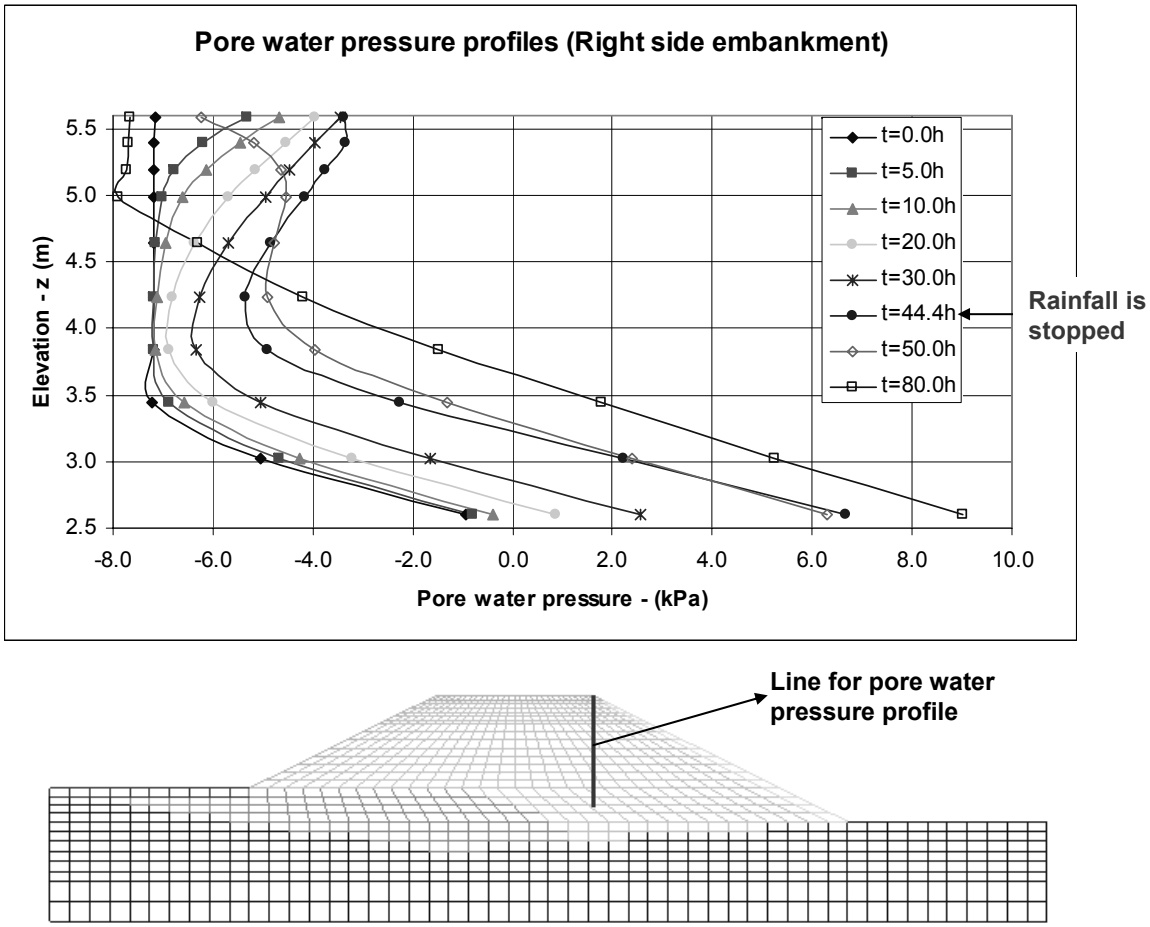

Figure 6.35 Pore water pressure profiles from times t=0 h to t=80 h.

86.0 h to the height h=95.16 m, the water level is at the crown of the embankment at t=103.7 h, and before the water level decreased at t=151.7 h are shown together in Figure 6.36. Figure 6.36(a) shows the saturation distribution when the water level on the river side reaches the height h=93.52 m and remained constant for 2 h. A saturated zone is observed at the right side of the embankment due to the seepage flow infiltrated within the soil from the river side. It is also observed that most of the embankment is unsaturated; however, its saturation increases due to the rainfall infiltration and the advance of the water front. The saturation distribution just before the water level is increased to the height h=95.16 m is presented in Figure 6.36(b), the results shows the accumulation of the water at the bottom of the embankment due to the rainfall infiltration and the seepage flow. Figures 6.36(c)-(d) show the saturation distributions when the water level reached the crest of the embankment and after it remained constant for 48 h at that level, respectively. It can be seen that, after 48 h the water level was at the crest of

the embankment, most of the soil within the embankment became saturated due to the seepage flow from the river side.

Figures 6.37-6.39 shows the simulation results of the water levels with the elapsed time for the Cases 1, 3 and, 5, respectively. The position of the soil elements in the mesh is approximately the same position of the sensors within the embankment (Figure 6.33). From the figure it is possible to see that the water levels within the embankment (positive pore water pressures) increase meanly when the water level increases at the right side of the embankment. The results do not show a significant effect of the rainfall at the beginning of the simulation on the increase of the water level. This is consistent with the measurements results by the positive pore water pressure sensors installed within the embankment. It can be explained by the low permeability of the soil which does not allow the water to move rapidly downward, toward the water table.

From the numerical analysis, it was observed that the case with the permeability combinations and the initial water level that lead to better results when compared with the field measurements corresponds to Case 5. Case 5 show a better agreement in the increase of the water levels inside the slope when the water level is increased at the right side of the river embankment. The comparison between the water levels measured by the sensors during the experiment and the water levels obtained by the simulation of Case 5 is show in Figure 6.40. The comparison is made between the times t=86 h and t=160 h, when the water level at the right side of the embankment was increased to the height h=95.16 m and it was kept constant for 48 h as shown in Figure 6.31. This comparison shows that the water levels in the simulation increase slower than the water levels measured in the field. Nevertheless, the general trend of the increase of the water level within the embankment and the final results obtained by the simulation show a very good agreement. It was not possible to simulate the rapid build up of the ground water table as well as the rapid dissipation of the pore water pressure at the left side of the embankment during the field test. These differences can be explained by the heterogeneity of the material which plays an important role on the permeability function of the soil and on the flow paths for the infiltrated water. It suggests that more accurate information about the permeabilities of the soil, the soil-water characteristic curves, and their hysteretic behavior during the wetting and drying paths are necessary to improve the simulation results. It emphasizes the significance of the experimental tests and field data related to infiltration on unsaturated soils in the improvement of the numerical models

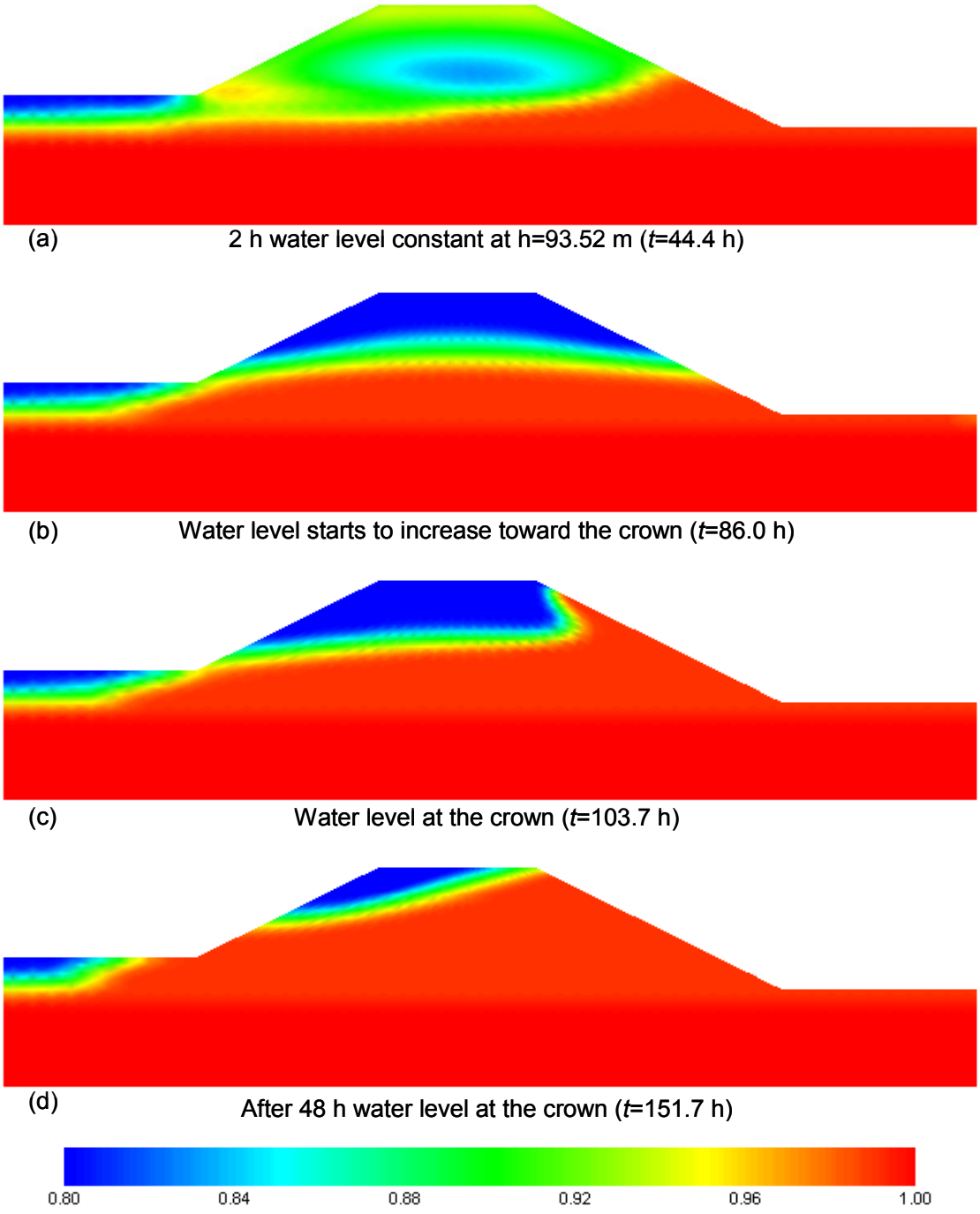

Figure 6.36 Distribution of saturation during the infiltration process

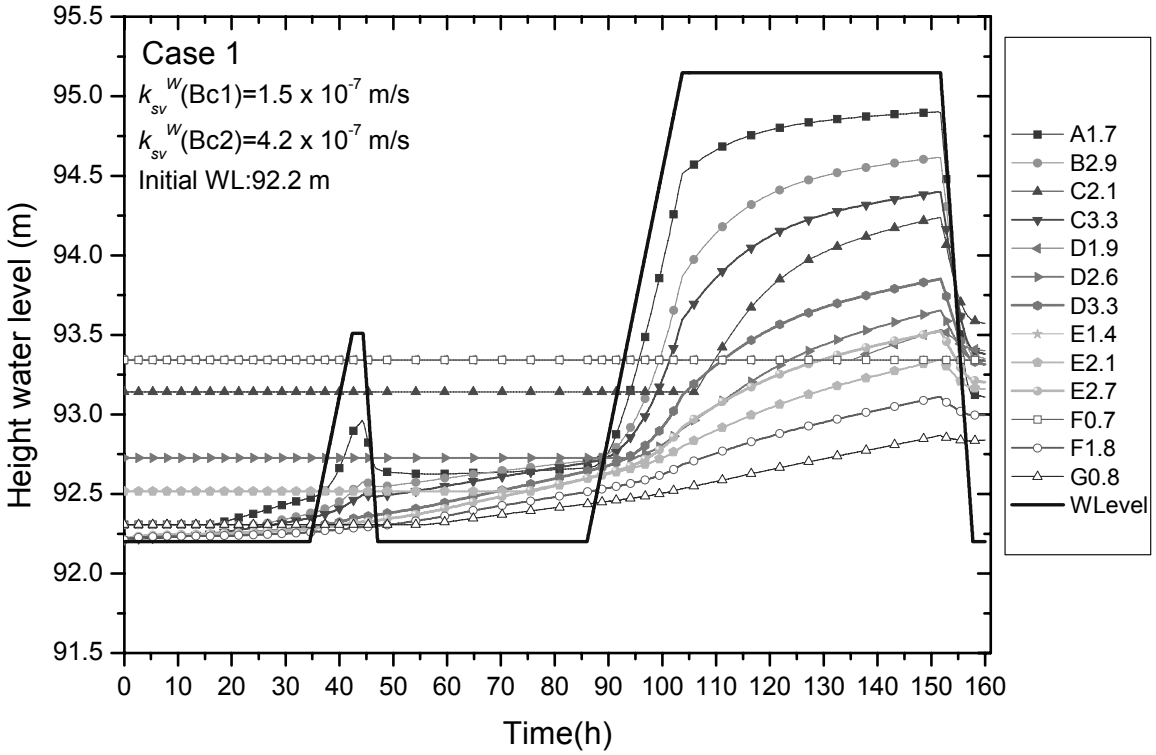

Figure 6.37 Histories of the increase of water level at the sensors location (Case 1)

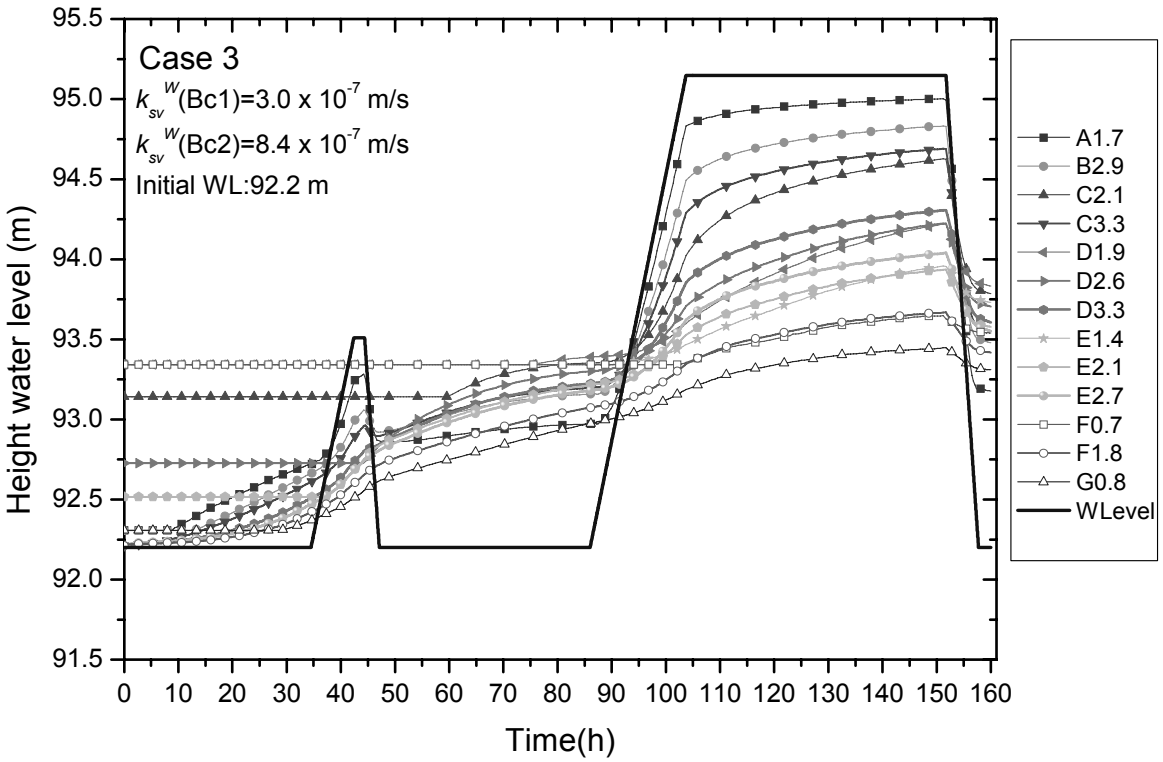

Figure 6.38 Histories of the increase of water level at the sensors location (Case 3)

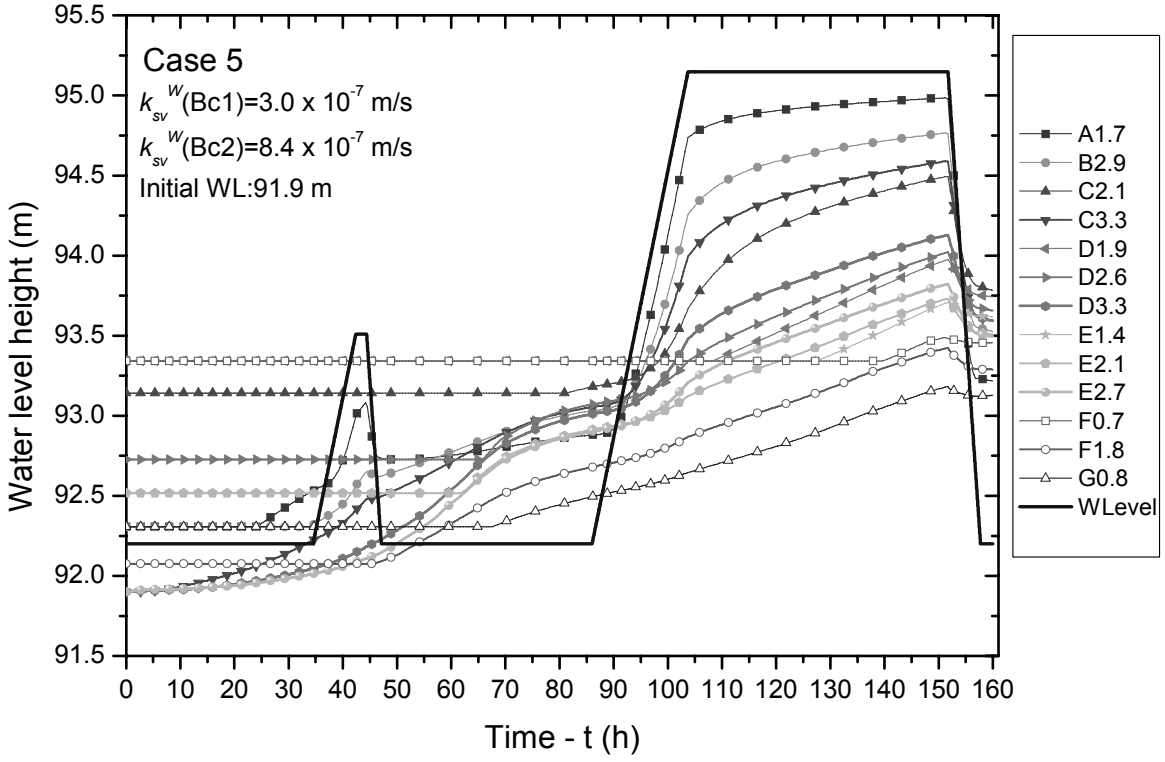

Figure 6.39 Histories of the increase of water level at the sensors location (Case 5)

to understand the complex response of unsaturated soils.

Figure 6.41 presents the horizontal gradient distributions at the times the first rainfall finishes (t=26.4 h), the water level starts to increase to the height h=93.52 m (t=34.5 h), the water level is increased for the second time to the height h=95.16 m (103.7 h), and after the water level is constant at the height h=95.16 m for 48 h (t=151.7 h). Figures 6.41(a) and (b) show that during the rainfall infiltration, the horizontal hydraulic gradients at the right side of the embankments are equal to 0.75 at the time t=26.4 h and 0.66 at the time t=35.4 h, respectively. These hydraulic gradients indicate that the seepage flow from inside to outside of the embankment is concentrated at the right of the embankment foundation. At the toe of the right slope, the soil is being saturated owing to the accumulation of water from the rainfall infiltration. The horizontal hydraulic gradient is larger at the right side of the embankment because this side is closer to the initial water level (higher initial saturation); while the left side is at a higher level (lower initial saturation). Figure 6.41(c) shows the distribution of the horizontal hydraulic gradient at the time t=103.7 h, it is seen that the maximum value (2.15) is obtained at the upper part of the right side of the embankment and it is due to the water infiltration from the

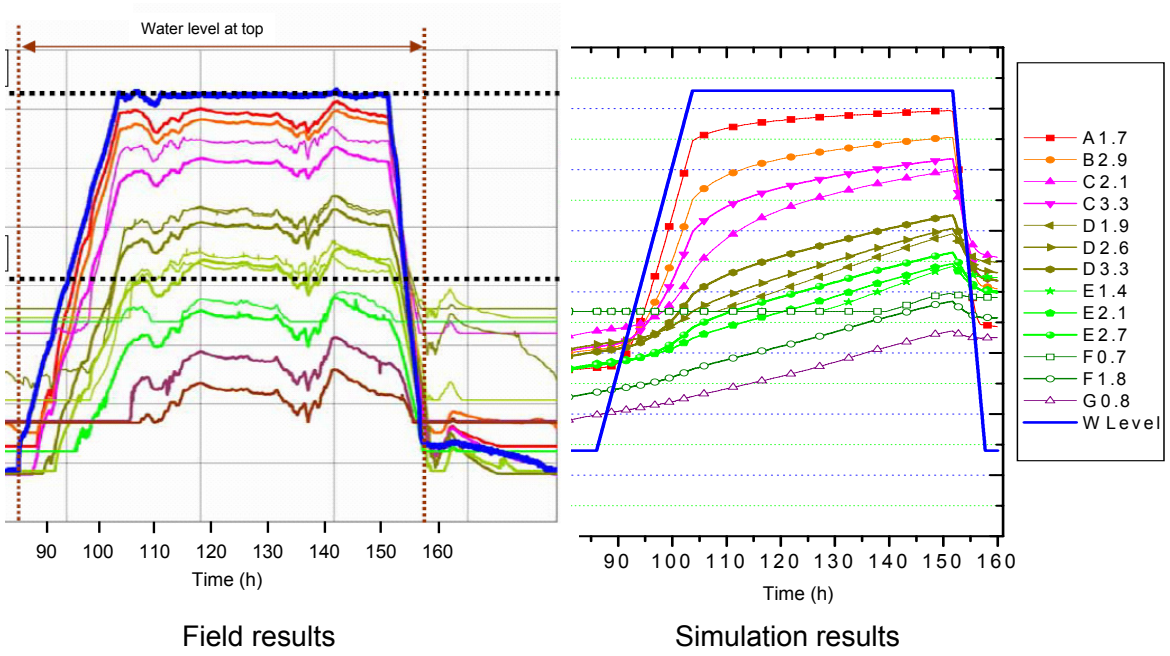

Figure 6.40 Comparison of the water levels. Field measurements and simulations Case 5

increase of the water level. The horizontal hydraulic distribution after 48 h the water level has been constant at the height h=95.16 m (t=151.7 h) is shown in Figure 6.41(d). This figure shows that the maximum value for the horizontal gradient (0.75) is presented at the left side of the embankment in the soil foundation when the seepage flow from the right side of the embankment reaches this zone.

Similarly, Figure 6.42 shows the distribution of the viscoplastic shear strain for the same case and the same time intervals described above. From the figure it is seen that the viscoplastic shear strain develops prominently at the right side of the embankment during the rainfall infiltration. The viscoplastic strain reaches a maximum value of 9.8% after 34.5 h of rainfall infiltration (Figure 6.42(b)). Figures 6.42(c) and (d) show the viscoplastic shear strain attained at the time intervals t=103.7 h and t=151.7 h, respectively. These Figures show that the accumulation of the deformation at the right side of the embankment increases to a maximum viscoplastic shear strain of 12.1%. It can be said in this case, that the accumulated viscoplastic shear strain at the toe of the embankment is mainly due to the seepage flow from the rainfall infiltration at the right slope of the embankment.

The corresponding distribution of the pore air pressure with time is shown in Figure 6.43. In this figure, it is possible to see that the pore air pressure increases while the

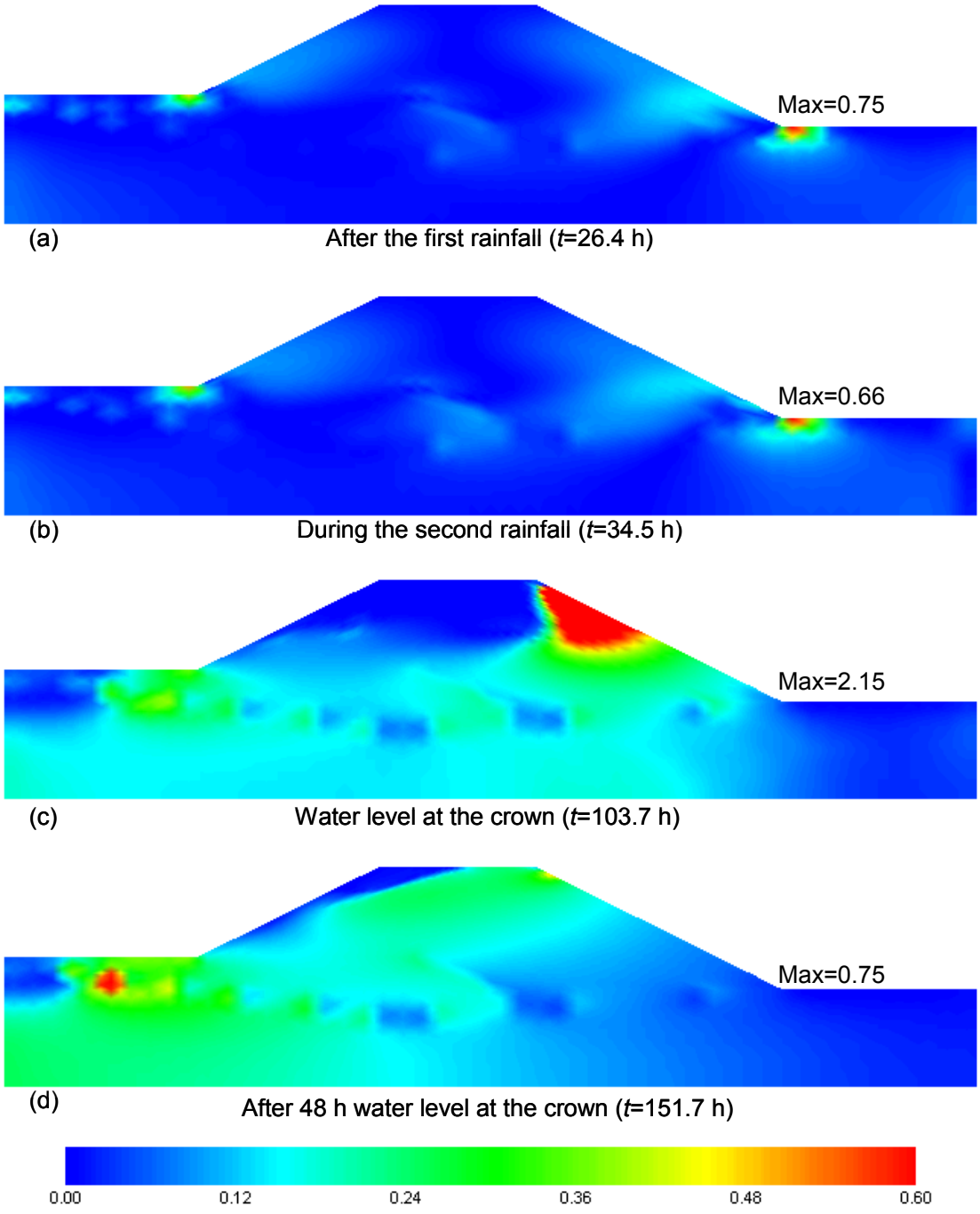

Figure 6.41 Distribution of the horizontal hydraulic gradient during the infiltration process

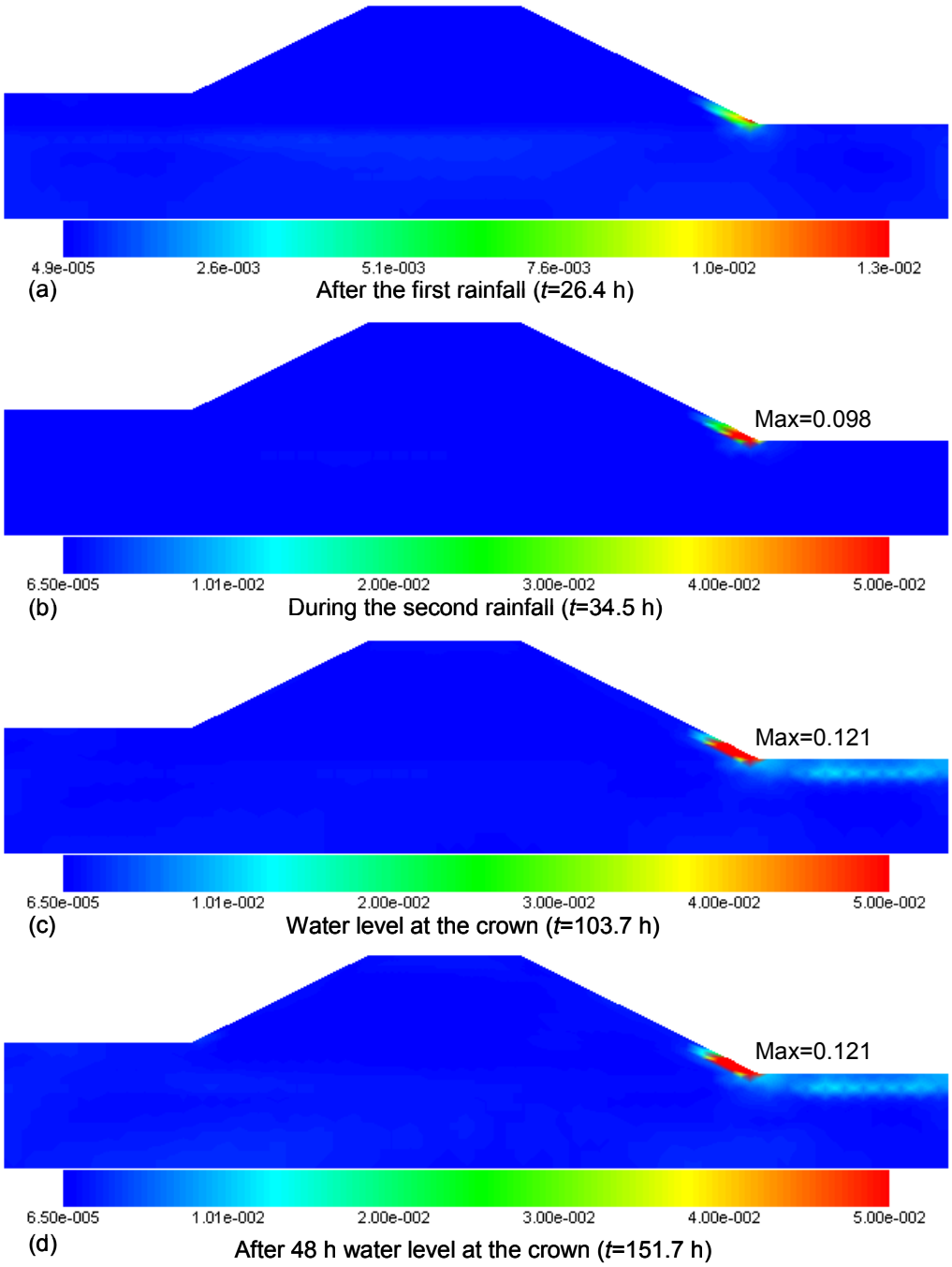

Figure 6.42 Distribution of the viscoplastic shear strain during the infiltration process

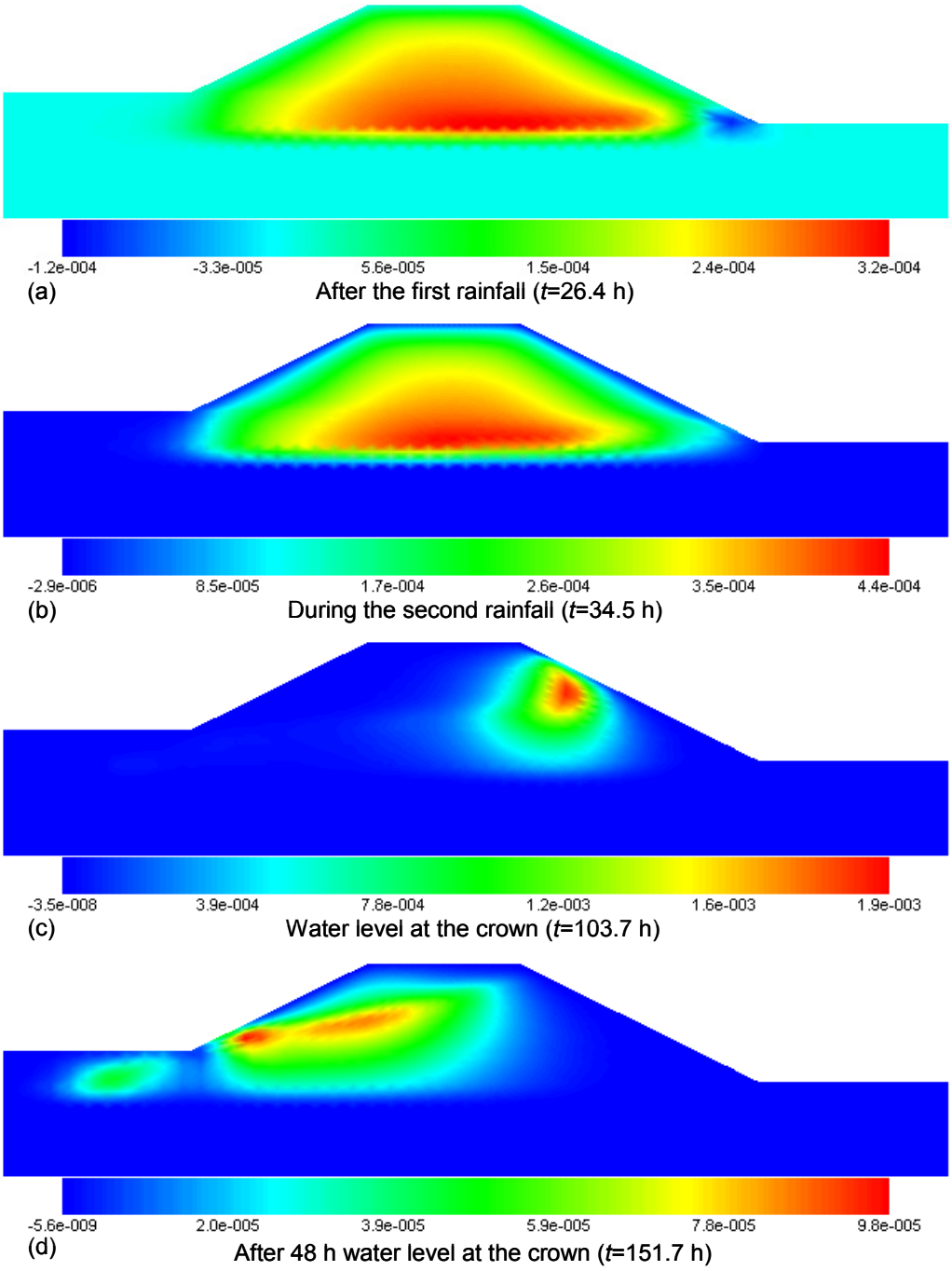

Figure 6.43 Distribution of the pore air pressure during the infiltration process

rainfall is applied on the surface of the embankment (Figures 6.43(a) and (b)). This is because the existing air within the embankment is compressed when the water moves downward toward the water table. The pore air pressures calculated when the water level increases are presented in Figures 6.43(c) and (d). These figures show that the maximum pore air pressure ($1.9\text{x}10^{-3}$ kPa=1.9 Pa) is obtained at the time the water level reaches the crown of the river. The seepage flow from the right side of the embankment compresses and displaces the air toward the left side increasing the pore air pressure inside the embankment. The magnitude of the calculated air pressure is relatively small during the infiltration process but it is reasonably simulated by the analysis method.

6.5 Summary

In this chapter, two-dimensional numerical simulations of two case studies of unsaturated river embankments subjected to rainfall infiltration and seepage flow were carried out. The distribution of the pore water pressures and the pattern of deformations were investigated. In the analyses, the mechanism of the surface deformation and the strain localization on the embankment surface at the river side were discussed mainly with respect to the saturated water permeability of the soil. From the numerical results, it was found that the deformation of the embankment significantly depends on the water permeability of the soil and it is localized on the slope surface at the river side. The larger the saturated water permeability of the soil, the larger the velocity of the seepage flow and the larger the deformation on the surface of the river embankment.

In the Seta River case, different simulations were performed to study the effects of the permeability, the subsurface drainage, and the degree of compaction on the deformation of unsaturated river embankments. The results of the analyses of the river embankment with smaller permeabilities at the slope surface (e.g., concrete face) showed that larger hydraulic gradients and larger accumulated viscoplastic shear strains are obtained at the back of the slope surface. This deformation was induced by the accumulation of the water behind the slope surface owing to the impediment of the water to flow toward the river. However, the deformation of the slope surface was avoided when the horizontal drains were used in the simulations. The horizontal drains showed to be very effective in avoiding the erosion and the local instability of the river embankments caused by the large seepage pressure presented at the river sides during the infiltration processes. From the simulations of the embankments with different compaction levels, larger deformations were

obtained for the soil with smaller degrees of compaction. It emphasizes the importance of achieving larger degrees of compactions during the construction process in order to improve the safety of the river embankments.

A comparison between the simulation results for the water levels within the embankment and the field measurement values yields a good agreement and indicates that the calculation method adopted here can be effectively used to study the practical seepage-deformation coupled problems on unsaturated soils. However, there is a need of more field and experimental data related to the hydraulic and deformation behavior of unsaturated soils in order to improve the numerical model and the simulation processes.

Chapter 7

CONCLUSIONS AND FUTURE WORK

7.1 Concluding remarks

In the present study, the deformation behavior of unsaturated soil subjected to water infiltration was investigated through an instability analysis and the simulation of the one-dimensional infiltration problem by using an elasto-viscoplastic seepage-deformation coupled method. In addition, two-dimensional simulations of rainfall infiltration and seepage flow were carried out on unsaturated soil slopes and unsaturated river embankments. The generation of pore water pressure and the localization of deformation were studied. The conclusions obtained in each chapter are described below.

In **Chapter 2**, an elasto-viscoplastic constitutive model and a seepage-deformation coupled method for unsaturated soils were used (Oka et al., 2006). In the constitutive model, the skeleton stress and suction were adopted as the basic stress variables. The collapse behavior was considered with the shrinkage of the overconsolidation boundary surface, the static yield function, and the viscoplastic potential surface. This multiphase finite element formulation was used for the numerical analysis of the one-dimensional and the two-dimensional infiltration problems.

In **Chapter 3**, the effect of parameters and state variables on the unstable behavior of unsaturated materials when they are subjected to a wetting process was theoretically and numerically studied. A theoretical investigation was conducted with a one-dimensional unsaturated coupled linear instability analysis using a simplified viscoplastic model. The

growth rate of the fluctuation was discussed, and it was determined that in both hardening and softening ranges, the unsaturated material can be unstable if the initial suction and the specific moisture capacity increase. Moreover, the onset of the instability was increased when the strain rate was negative and the behavior of the material was contractive. As for the numerical study on the one-dimensional infiltration problem, it was found that the elasto-viscoplastic material system is more unstable when parameters α and n' are large, namely, for large values of the slope of the soil water characteristic curve (specific moisture capacity). For the effect of the suction, it was observed that the instability significantly increases when the initial suction of the unsaturated material is increased. These trends were consistent with the theoretical results obtained by the linear instability analysis. In addition, the simulated settlements showed that for smaller parameters α and n', the material behavior is expansive. Nevertheless, when these parameters became large, the expansive behavior of the soils changes to a compressive one (contractive). Parameters α and n' indicated a great effect on the development of the deformation. The greater the parameters α and n', the larger the settlements obtained. Larger rates of settlement were also obtained for higher levels of initial suction. This suggests that rapid transitions from unsaturated to saturated states and higher levels of suction lead to compressive or contractive behavior and instability; e.g., a wetting-induced collapse.

In **Chapter 4**, a parametric analysis to study the effects of the hydraulic parameters on the infiltration and deformation of unsaturated soil was performed. It was observed that parameters α and n' have a significant effect on the one-dimensional infiltration process. The steady states were reached faster for soils where parameter α is smaller, as well as for soils where parameter n' is larger. It could be seen that the initial saturation in the column is important in regards to the time it takes to attain the steady state and it is controlled by these two parameters. Rainfall intensity also had a significant effect on the infiltration process; the higher the rainfall infiltration, the greater the pore water generated along the column. Parameters s_{max} and a do not show a significant effect on the infiltration process. As for the deformation behavior, the results show a trend in larger negative volumetric strains for the higher pore water pressures. In contrast, when the pore water pressure is smaller, either the negative volumetric strain is smaller or it changes to be positive. Moreover, it is shown that the generation of the pore water pressure and the volumetric strain is mainly controlled by material parameters α and n' that describe the soil water characteristic curve. This shows that the deformation behavior of unsaturated soils is strongly dependent on the hydraulic behavior, which emphasizes the importance

of seepage-deformation coupled methods for the analysis of rainfall infiltration.

From the results obtained through the simulations, it could be seen that the proposed multiphase finite element analysis can describe very well the characteristics observed during the experiments of the one-dimensional water infiltration into layered unsaturated columns. The model is useful for the study of the unsaturated response of multiple layered soils that are commonly found in practical geotechnical problems related to water infiltration such a rainfall- and seepage-induced instability.

In **Chapter 5**, two-dimensional numerical analyses to describe the rainfall infiltration process into unsaturated soil slopes were conducted. The numerical analyses are focused on the effects of the different initial water levels, saturated water permeabilities, and rainfall distributions on the development of pore water pressure and deformations. From the numerical analyses it has been found that the effect of the initial water level on an unsaturated soil slope subjected to rainfall infiltration has either a minimum or negligible effect on the hydraulic response at shallow depths. However, the initial water levels have a significant effect on the distribution of the pore water pressure below the wetting front. Additionally, larger deformations were obtained for the cases where the initial water levels are higher, which suggest that an unsaturated slope is more unstable when the initial suction distributions are smaller. The simulations performed with different saturated water permeabilities show that larger pore water pressures are obtained at shallow depths when the saturated water permeabilities are smaller than the rainfall intensity; in contrast, in the case of permeabilities larger than the rainfall intensity, the pore water pressures at the surface are smaller. This behavior is inverted when the depth of the soil increases; at larger depths, the pore water pressures are larger for the soils with larger permeabilities. The analysis of the deformations shows that the maximum lateral displacements are obtained in the cases where the rainfall intensity is close to the saturated water permeability, i.e., $I/k_s^W \approx 1.0$. Finally, from the comparison of the different rainfalls patterns it is observed that, regardless of the permeability, the entire rainfall patterns have a more significant effect on the increase of pore water pressures in the shallow depths than in the greater depths. Nevertheless, it is found that, the larger pore water pressures at greater depths are always presented for the case of the rainfall with longer duration. For the deformation behavior due to the rainfall patterns, the larger values of viscoplastic shear strain are obtained for the rainfall pattern that lasted for a longer time, regardless of the permeability. It suggests that rainfalls lasting for longer

times or longer periods of rainfall have a more significant effect on the deformation of the soil slope due to the accumulation of larger deformation within the soil structure.

In **Chapter 6**, two-dimensional numerical simulations of two case studies of unsaturated river embankments subjected to rainfall infiltration and seepage flow were carried out. The distribution of the pore water pressures and the pattern of deformations were investigated. In the analyses, the mechanism of the surface deformation and the strain localization on the embankment surface at the river side were discussed mainly with respect to the saturated water permeability of the soil. From the numerical results, it was found that the deformation of the embankment significantly depends on the water permeability of the soil and it is localized on the slope surface at the river side. The larger the saturated water permeability of the soil, the larger the velocity of the seepage flow and the larger the deformation on the surface of the river embankment.

In the Seta River case, different simulations were performed to study the effects of the permeability, the subsurface drainage, and the degree of compaction on the deformation of unsaturated river embankments. The results of the analyses of the river embankment with smaller permeabilities at the slope surface showed that larger hydraulic gradients and larger accumulated viscoplastic shear strains are obtained at the back of the slope surface. This deformation was induced by the accumulation of the water behind the slope surface owing to the impediment of the water flow toward the river. However, the deformation of the slope surface was avoided when the horizontal drains were used in the simulations. The horizontal drains showed to be very effective in diminishing the strain localization at the slope surface and the local instability of the river embankments caused by the large seepage pressure presented at the river sides during the infiltration processes. From the simulations of the embankment with different compaction levels, larger deformations were obtained for the soil with smaller degrees of compaction. It emphasizes the importance of achieving higher degrees of compactions during the construction process in order to improve the safety of the river embankments.

In the S River case, a comparison between the simulation results for the water levels within the embankment and the field measurement yields a good agreement and indicated that the calculation method adopted here can be effectively used to study the common practical seepage-deformation coupled problems on unsaturated soils.

7.2 Recommendation for future work

Further investigations on seepage-deformation behavior of unsaturated soil are required in order to clarify the complex non-linear relation among the constitutive parameters including the hydraulic parameters in the infiltration problem in unsaturated soil. The topics of research that deserve future investigation are listed below.

In this study, the role of the initial suction and the specific moisture capacity on the instability of unsaturated soil subjected to a wetting process was investigated. However, the instability of unsaturated soil is a complex problem which requires further analysis. For instance, it is necessary to extend the study to the effects of the constitutive parameters and the water and gas permeabilities on the instability of the unsaturated soil. Moreover, the theoretical and numerical instability of unsaturated soil in triaxial conditions needs to be examined.

One of the main problems related to the simulation of practical cases in unsaturated soils is little existing information about the constitutive parameters, the saturation-suction relationship, and the permeability functions of unsaturated soils. Experimental and field data allow the calibration and verification of numerical models used to investigate the behavior of unsaturated soils. Therefore, it is necessary for the full validation of the seepage-coupled methods to perform tests on infiltration in unsaturated soils with complete measurement of the hydraulic and the deformation characteristics.

In this study, simulations of soil slopes and river embankments subjected to rainfall and seepage flow have been performed. However, these cases are only an example of the geotechnical problems regarding the water infiltration in unsaturated soils. It is necessary therefore, to perform numerical analyses considering other cases, different geometries and boundaries, and different initial conditions, e.g., road embankments, cut slopes, reinforced-soil structures, etc. Additionally, the combined effect of infiltration in unsaturated soil and the dynamic loads is an interesting topic that needs to be study.

In the seepage-deformation coupled method, a van Genuchten type of soil water characteristic curve was adopted. It was assumed that the saturation-suction relationship was the same for the wetting and drying paths. However, the soil water characteristic curve is dependent of the void ratio, the stress state, and it follows different paths for the wetting and drying processes during the rainfall infiltration, i.e. the soil exhibits hysteretic be-

havior. Thus, it is desired to consider these features of the soil water characteristic curve in the analysis of unsaturated soil, especially in the case the soil is subjected to several wetting and drying processes.

References

Alonso, E.E., Gens, A., & Josa, A., (1990). A constitutive model for partially saturated soils, *Géotechnique*, **40**(3), 405–430.

Alonso, E.E., Gens, A., & Delahaye, C.H., (2003). Influence of rainfall on the deformation and stability of a slope in overconsolidated clays: a case study, *Hydrogeology Journal*, **11**, 174–192.

Atkin, R.J. & Craine, R.E., (1976). Continuum theories of mixtures: basic theory and historical developments, *The Quarterly Journal of Mechanics and Applied Mathematics*, **29**(2), 209–244.

Au, S.W.C., (1993). Rainfall and slope failure in Hong Kong, *Engineering Geology*, **36**, 141–147.

Au, S.W.C., (1998). Rain-induced slope instability in Hong Kong, *Engineering Geology*, **51**, 1–36.

Barden, L., McGown, A., & Collins, K., (1973). The collapse mechanism in partly saturated soil, *Engineering Geology*, **7**, 49–60.

Bathurst, R., Ho, A., & Siemens, G., (2007). A column apparatus for investigation of 1-d unsaturated-saturated response of sand-geotextile systems, *Geotechnical Testing Journal*, **30**(6), 1–9.

Biot, M.A., (1941). Three-dimensional theory of consolidation, *Journal of Applied Physics*, **12**(2), 155–164.

Biot, M.A., (1962). Mechanics of deformation and acoustic propagation in porous media, *Journal of Applied Physics*, **33**(4), 1482–1498.

Bishop, A.W., (1960). The measurement of pore pressure in the triaxial test, In: *Proc. Conf. Pore Pressure and Suction in Soils*, Butterworths, London, pp. 38–46.

Bishop, A.W. & Donald, I.B., 1961. The experimental study of partly saturated soil in the triaxial apparatus, In: *Proc. 5th Int. Conference on Soil Mechanics and Foundation Engineering*, Paris, France, pp. 13–21.

Bishop, A.W. & Eldin, G., (1950). Undrained triaxial tests on saturated sand and their significance in the general theory of shear strength, *Géotechnique*, **2**, 13–32.

Boer, R.D., (1998). Theory of porous media - past and present, *Zeitschrift fur Angewandte Mathematik und Mechanik*, **78**(7), 441–466.

Bolzon, G., Schrefler, B.A., & Zienkiewicz, O.C., (1996). Elastoplastic soil constitutive laws generalized to partially saturated states, *Géotechnique*, **46**(2), 279–289.

Bowen, R.M., (1976). Theory of mixtures, In: *Continuum Physics, Vol. III*, Eringen, A.C. ed. Academic Press, New York, pp. 1–127.

Buscarnera, G. & Nova, R., (2009a). Modelling the onset of instability in oedometric tests on unsaturated bounded soils, In: *First International Symposium on Computational Geomechanics, Juan-les-Pins, France*, Pietruszczak, S., Pande, G.N., Tamagnini, C. and Wan, R. eds. ComGeo I, pp. 226–238.

Buscarnera, G. & Nova, R., (2009b). Modelling instabilities in triaxial testing on unsaturated soil specimens, *International Journal for Numerical and Analytical Methods in Geomechanics*, **doi: 10.1002/nag.832**.

Cai, F. & Ugai, K., (2004). Numerical analysis of rainfall effects on slope stability, *International Journal of Geomechanics*, **4**(2), 69–78.

Cai, F., Ugai, K., Wakai, A., & Li, Q., (1998). Effects of horizontal drains on slope stability under rainfall by three-dimensional finite element analysis, *Computers and Geotechnics*, **23**(4), 255–275.

Chen, H., Dadson, S., & Chi, Y.G., (2006). Recent rainfall-induced landslides and debris flow in nothern Taiwan, *Geomorphology*, **77**, 112–125.

Cho, S.E. & Lee, S.R., (2001). Instability of unsaturated soil slopes due to infiltration, *Computers and Geotechnics*, **28**, 185–208.

Coleman, J.D., (1962). Stress/strain relations for partly saturated soils, *Géotechnique*, **12**, 348–350.

Coussy, O., (2004). *Poromechanics*, John Wiley & Sons, London.

Cui, Y.J. & Delage, P., (1996). Yielding and plastic behavior of an unsaturated compacted silt, *Géotechnique*, **46**(2), 291–311.

Cunningham, M.R., Ridley, A.M., Dineen, K., & Burland, J.B., (2003). The mechanical behaviour of a reconstituted unsaturated silty clay, *Géotechnique*, **53**(2), 183–194.

Ehlers, W., (2003). Continuum and numerical simulation of porous materials in science and technology chapter 9, In: *Modeling and Mechanics of Granular and Porous Materials*, Capriz, G., Ghionna, V.N. and Giovine, P. eds. Birkhauser.

Ehlers, W. & Volk, W., (1998). On theoretical and numerical methods in the theory of porous media based on polar and non-polar elasto-plastic solid materials, *International Journal of Solids and Structures*, **35**(34,35), 4597–4617.

Ehlers, W., Graf, T., & Amman, M., (2004). Deformation and localization analysis of partially saturated soil, *Computer Methods in Applied Mechanics and Engineering*, **193**, 2885–2910.

Feng, H., (2007). Multiphase deformation analysis of elasto-viscoplastic unsaturated soil and modeling of bentonite, Ph.D. thesis, Kyoto University, Department of Civil & Earth Resources Engineering.

Feng, H., Kimoto, S., Oka, F., Kodaka, T., & Suzuki, H., (2006). Three dimensional multiphase analysis of elasto-viscoplastic unsaturated soil, In: *Proc. 19th KKCNN Symp. on Civil Engng.*, Kyoto, Japan, pp. 449–452.

Fredlund, D.G. & Morgenstern, N.R., (1977). Stress state variables for unsaturated soils, *Journal of the Geotechnical Engineering Division*, **103**(GT5), 313–321.

Fredlund, D.G. & Rahardjo, H., (1993). *Soil mechanics for unsaturated soils*, Wiley, New York.

Garcia, E.F., Gallage, C.P.K., & Uchimura, T., (2007). Function of permeable geosynthetics in unsaturated embankments subjected to rainfall infiltration, *Geosynthetics International*, **14**(2), 89–99.

Garcia, E., Oka, F., & Kimoto, S., (2010). Numerical analysis of a one-dimensional infiltration problem in unsaturated soil by a seepage-deformation coupled method,

International Journal for Numerical and Analytical Methods in Geomechanics, **doi: 10.1002/nag.908**.

Gens, A., (1995). Constitutive laws, In: *Modern Issue in Non-Saturated soils*, Gens, A., Jouanna, P. and Schrefler, B.A. eds. Vienam Austria. Sprinter, pp. 129–158.

Ghiassian, H. & Ghareh, S., (2008). Stability of sandy slopes under seepage conditions, *Landslides*, **5**, 397–406.

Gitirana, G.J., Fredlund, M.D., & Fredlund, D.G., (2005). Infiltration-runoff boundary conditions in seepage analysis, In: *Proceedings of the 58th Canadian Geotechnical Conference*, GeoSask2005, Saskatoon, S.K., Canada, p. 8.

Griffiths, D.V. & Lu, N., (2005). Unsaturated slope stability analysis with steady infiltration or evaporation using elasto-plastic finite elements, *International Journal for Numerical and Analytical Methods in Geomechanics*, **29**, 249–267.

Higo, Y., (2003). Instability and strain localization analysis of water-saturated clay by elasto-viscoplastic constitutive models, Ph.D. thesis, Kyoto University, Department of Civil & Earth Resources Engineering.

Higo, Y., Oka, F., Jiang, m., & Fujita, Y., (2005). Effects of transport of pore water and material hetereogeneity on strain localization of fluid-saturated gradient-dependent viscoplastic geomaterial, *International Journal for Numerical and Analytical Methods in Geomechanics*, **29**, 495–523.

Higo, Y., Oka, F., Kodaka, T., & Kimoto, S., (2006). Three dimensional strain localization of water-saturated clay and numerical simulation using an elasto-viscoplastic model, *Philosophical Magazine*, **86**, 3205–3240.

Horton, R.E., (1933). The role of infiltration in the hydrologic cycle, *Transactions, American Geophysical Union*, **14**, 446–460.

Houlsby, G.T., (1997). The work input to an unsaturated granular material, *Géotechnique*, **47**(1), 193–196.

Jennings, J.E.B. & Burland, J.B., (1962). Limitations to the use of effective stress in partly saturated soils, *Géotechnique*, **12**, 125–144.

Jommi, C., (2000). Remarks on the consitutive modeling of unsaturated soil, In: *Experimental evidence and Theoretical Approaches in Unsaturated Soils*, Tarantino, A., and Mancuso, C. eds., Balkema, pp. 139–153.

Kato, R., Sunami, S., Oka, F., Kimoto, S., & Kodaka, T., (2009). A multi-phase elasto-viscoplastic analysis of a unsaturated river embankment associated with seepage flow, In: *Proc. of the International Symposium on Prediction and Simulation Methods for Geohazard Mitigation, Kyoto, Japan*, Oka, F., Murakami, A., and Kimoto, S. eds. Taylor and Francis Group: London, UK, pp. 401–407.

Khalili, N. & Khabbaz, M.H., (1998). A unique relationship for χ for the determination of the shear strength of unsaturated soils, *Géotechnique*, **48**(5), 681–687.

Khalili, N., Geiser, F., & Blight, G.E., (2004). Effective stress in unsaturated soils: Review with new evidence, *International Journal of Geomechanics*, **4**(2), 115–126.

Kim, Y.S., (2004). Elasto-viscoplastic modeling and analysis for cohesive soil considering suction and temperature effects, Ph.D. thesis, Kyoto University, Department of Civil & Earth Resources Engineering.

Kim, Y., Kimoto, S., Oka, F., & Kodaka, T, (2005). Numerical simulation of the triaxial compression behavior of unsaturated silt using and elastoviscoplastic model, In: *Proceedings of the 11th international Conference of IACMAG, AGI*, Barla, G., Barla, M. eds. Patron Editore, vol. 1, pp. 361–368.

Kimoto, S. & Oka, F., (2005). An elasto-viscoplastic model for clay considering destructuralization and consolidation analysis of unstable behavior, *Soils and Foundations*, **45**(2), 29–42.

Kimoto, S., Oka, F., & Higo, Y., (2004). Strain localization analysis of elasto-viscoplastic soil considering structural degradation, *Computer Methods in Applied Mechanics and Engineering*, **193**, 2845–2866.

Kimoto, S., Oka, F., Fushita, T., & Fujiwaki, M., (2007). A chemo-thermo-mechanically coupled numerical simulation of the subsurface ground deformations due to methane hydrate dissociation, *Computer and Geotechnics*, **34**, 216–228.

Kimoto, S., Oka, F., & Fushita, T., (2010). A chemo-thermo-mechanically coupled analysis of ground deformation induced by gas hydrate dissociation, *International Journal of Mechanical Sciences*, **52**(2), 365–376.

Kogho, Y., Nakano, M., & Miyazaki, T., (1993). Theoretical aspects of constitutive modeling for unsaturated soils, *Soils and Foundations*, **33**(4), 49–63.

Kogho, Y., Asano, I., & Hayashida, Y., (2001). An elastoplastic model for unsaturated soils bases on cyclic plasticity, In: *Proc, Int. Workshop on Deformation of Earth Materials*, Oka, F. ed., TC34 of ISSMGE. , Sendai, Japan, pp. 129–140.

Lade, P. & Boer, R., 1997. The concept of effective stress of soil, concrete and rock, *Géotechnique*, **47**(1), 61–78.

Laloui, L. & Nuth, M., 2009. On the use of the generilised effective stress in the consitutive modelling of unsaturated soils, *Computers and Geotechnics*, **36**, 20–23.

Lambe, T.W. & Whitman, R.V., (1969). *Soil mechanics*, Wiley, New York.

Liakopoulos, A., (1964). Transient flow through unsaturated porous media, Ph.D. thesis, University of California at Berkeley.

Lloret, A. & Alonso, E.E., (1980). Consolidation of unsaturated soils including swelling and collapse behaviour, *Géotechnique*, **30**(4), 449–477.

Loret, B. & Khalili, N., (2000). A three phase model for unsaturated soils, *International Journal for Numerical and Analytical Methods in Geomechanics*, **24**, 893–927.

Loret, B. & Prévost, J.H., (1991). Dynamic strain localization in fluid-saturated porous media, *Journal of Engineering Mechanics*, **117**, 907–922.

Lu, N. & Likos, W.J., (2004). *Unsaturated soil mechanics*, Wiley, New Jersey.

Matsushi, Y., Ayalew, L., Hattanji, T., & Matsukura, Y., (2006). Mechanisms of shallow landslides on soil-mantled hillslopes with permeable and impermeable bedrocks in the Boso Peninsula, Japan, *Geomorphology*, **76**, 92–108.

Matyas, E.L. & Radhakrishna, H.S., (1968). Volume change characteristics of partially saturated soils, *Géotechnique*, **18**, 432–448.

Nakata, Y., Liu, D., Hyodo, M., Yoshimoto, N., & Kato, Y., (2010). Numerical simulation of an expressway embankment slope failure, In: *Unsatuarted Soils, Theoretical and Numerical Advances in Unsaturated Soil Mechanics*, Buzzi, O., Fityus, S. and Sheng, D ed., Taylor and Francis Group: London, U.K., pp. 719–724.

Ng, C.W.W. & Shi, Q., (1998). A numerical investigation of the stability of unsaturated soil slopes subjected to transient seepage, *Computers and Geotechnics*, **22**(1), 1–28.

Nuth, M. & Laloui, L., (2008). Effective stress concept in unsaturated soils: Clarification and validation of a unified framework, *International Journal for Numerical and Analytical Methods in Geomechanics*, **32**, 771–801.

Oka, F., (1982). Elasto-viscoplastic constitutive equation for overconsolidated clay, In: *Proceedings of the 1st International Symposium on Numerical Models in Geomechanics.*, Dungar, R., Pande, G.N., and Studer, J.A. eds. Zurich: Balkema, pp. 147–156.

Oka, F., (1988). The validity of the effective stress concept in soil mechanics, In: *Micromechanics of Granular Materials*, Satake, M. and Jenkins, J.T. eds. Elsevier Science Publihsers B.B., Amsterdam, pp. 207–214.

Oka, F., (1992). A cyclic elasto-viscoplastic constitutive model for clay based on the non linear kinematic hardening rule, In: *Proc. 4th. Int. Symposium on Numerical Model in Geomecahnics*, Pande, G.N. and Pietruszczak, S. eds., Swansea, UK, Balkema: Rotterdam, vol. 1, pp. 105–114.

Oka, F., (1996). Validity and limits of the effective stress concept in geomechanics, *Mechanics of Cohesive-Frictional Materials*, **1**, 219–234.

Oka, F., (2002). Effect of dilatancy on the strain localization of water-saturated elasto-viscoplastic soil, *International Jounal of Solids and Structures*, **39**, 3625–3647.

Oka, F., (2004). Thermo-hydro-mechanically coupled finite element analysis of cohesive soil using an elasto-viscoplastic model, In: *Computational Mechanics (abstracts), WCCM 4 in conjuntion with APCOM'04*, Beijing, China.

Oka, F., Yashima, A., & Kohara, I., (1992a). A finite element analysis of clay foundation based on finite elasto-viscoplasticity, In: *Proc. 4th. Int. Symposium on Numerical Model in Geomecahnics*, Pande, G.N. and Pietruszczak, S. eds., Swansea, UK, Balkema: Rotterdam, pp. 915–922.

Oka, F., Adachi, T., & Yashima, A., (1994). Instability of an elasto-viscoplastic constitutive model for clay and strain localization, *Mechanics of Materials*, **18**, 119–129.

Oka, F., Adachi, T., & Yashima, A., (1995). A strain localization analysis using a viscoplastic softening model for clay, *International Journal of Plasticity*, **11**(5), 523–545.

Oka, F., Kodaka, T., Kimoto, S., Kim, Y.-S., & Yamasaki, N., (2006). An elasto-viscoplastic model and multiphase coupled FE analysis for unsaturated soil, In: *Proceedings of the fourth international conference on unsaturated soils*, Miller, G.A., Zapata, C.E., Houston, S.L. and Fredlund, D.G. eds. Geotechnical Special Publication, ASCE, Carefree, Arizona, vol. 147(2), pp. 124–131.

Oka, F., Feng, H., Kimoto, S., Kodaka, T., & Suzuki, H., (2008). A numerical simulation of triaxial tests of unsaturated soil at constant water and air content by using and elasto-viscoplastic model, In: *Proc. of the First European Conference on Unsaturated Soils, E-UNSAT 2008, Durham, United Kingdom*, Toll, D.G., Augarde, C.E., Gallipoli, D., and Wheeler, S.J. eds. Taylor and Francis Group: London, UK, pp. 735–741.

Oka, F., Kimoto, S., Takada, N., & Higo, Y., (2009). A multi-phase elasto-viscoplastic analysis of a unsaturated river embankment associated with seepage flow, In: *Proc. of the International Symposium on Prediction and Simulation Methods for Geohazard Mitigation, Kyoto, Japan*, Oka, F., Murakami, A., and Kimoto, S. eds. Taylor and Francis Group: London, UK, pp. 127–132.

Oka, F., Kodaka, T., Suzuki, H., Kim, Y.S., Nishimatsu, N., & Kimoto, S., (2010). Experimental study on the behavior of unsaturated compacted silt under triaxial compression, *Soils and Foundations*, **50**(1), 27–44.

Okada, K. & Sugiyama, T., (1994). A risk estimation method of railway embankment collapse due to heavy rainfall, *Structural Safety*, **14**, 131–150.

Orense, R., Shimona, S., Maeda, K., & Towhata, I., (2004). Instrumented model slope failure due to water seepage, *Journal of Natural Disaster Science*, **26**(1), 15–26.

Perzyna, P., 1963. The constitutive equations for work-hardening and rate sensitive plastic materials, *Proc. Vibrational Problems*, **4**(3), 281–290.

Pierce, D., Shih, C.F., & Needleman, A., (1984). A tangent modulus method for rate dependent solids, *Computers and Structures*, **18**, 875–887.

Pinder, G.F. & Gray, W.G., (2008). *Essentials of multiphase flow and transport in porous media*, John Wiley and Sons, Inc., Hokoben, New Jersey.

Rahardjo, H., Hritzuk, K.J., Leong, E.C., & Rezaur, R.B., (2003). Effectiveness of horizontal drains for slope stability, *Engineering Geology*, **69**, 295–308.

Rahardjo, H., Ong, T.H., Rezaur, R.B., & Leong, E.C., (2007). Factors controlling instability of homogeneous soil slopes under rainfall, *Journal of Geotechnical and Geoenvironmental Engineering*, **133**(12), 1532–1543.

Rice, J.R., (1975). On the instability of dilatant hardening for saturated rock masses, *Journal of Geophysical Research*, **80**(11), 1531–1536.

Schrefler, B.A., (2002). Mechanics and thermodynamics of saturated/unsaturated porous materials and quantitative solutions, *Applied Mechanics Reviews*, **55**(4), 351–388.

Schrefler, B.A. & Gawin, D., (1996). The effective stress principle: incremental of finite form, *International Journal for Numerical and Analytical Methods in Geomechanics*, **20**(11), 785–814.

Schrefler, B.A., Majorana, C.E., & Sanavia, L., (1995). Shear band localization in saturated porous media, *Archives of Mechanics*, **47**(3), 577–599.

Sheng, D., Sloan, W., Gens, A., & Smith, D.W., (2003). Finite element formulation and algorithms for unsaturated soils part i: Theory, *International Journal for Numerical and Analytical Methods in Geomechanics*, **27**, 745–765.

Simons, N.E. & Menzies, B.K., (1974). A note on the principle of effective stress, *Géotechnique*, **24**, 259–262.

Srivastava, R. & Jim Yeh, T.-C., (1991). Analytical solutions for one-dimensional, transient infiltration toward the water table in homogeneous and layered soils, *Water Resources Research*, **27**(5), 753–762.

Terzaghi, K., (1936). The shearing resistance of saturated soils and the angle between the planes for shear, In: *International Conference on Soil Mechanics and Foundation Engineering*, Harvard University Press: Cambridge, MA., pp. 54–56.

Terzaghi, K., (1943). *Theoretical soil mechanics*, John Wiley & Sons.

Thomas, H.R. & He, Y., (1998). Modeling the behaviour of unsaturated soil using and elastoplastic constitutive model, *Géotechnique*, **48**(5), 589–603.

Truesdell, C., (1984). Thermodynamics of diffusion, In: *Rational Thermodynamics*, Truesdell, C. eds., 2nd ed., Springer-Verlag, New York, pp. 219–236.

Tsaparas, I., Rahardjo, H., Toll, D.G., & Leong, E.C., (2002). Controlling parameters for rainfall-induced landslides, *Computers and Geotechnics*, **29**, 1–27.

Van Genuchten, M. Th., (1980). A closed-form equation for predicting the hydraulic conductivity of unsaturated soils, *Soil Science Society of America Journal*, **44**, 892–899.

Wheeler, S.J. & Karube, D., (1996). State of the art report: Constitutive modeling, In: *Proc. 1st Int. Conference on Unsaturated Soils, Paris*, Alonso, EE. and Delage, P. eds. Balkema, Rotterdam, vol. 3, pp. 1323–1356.

Wheeler, S.J. & Sivakumar, V., (1995). An elasto-plastic critical state framework for unsaturated soil, *Géotechnique*, **45**(1), 35–53.

Wheeler, S.J., Sharma, R.S., & Buisson, S.R., (2003). Coupling of hydraulic hysteresis and stress-strain behaviour in unsaturated soils, *Géotechnique*, **53**(1), 41–54.

Wu, L.Z. & Zhang, L.M., (2009). Analytical solution to 1D coupled water infiltration and deformation in unsaturated soils, *International Journal for Numerical and Analytical Methods in Geomechanics*, **33**, 773–790.

Yamagishi, H., Horimatsu, T., Kanno, T., & Hatamoto, M., (2004). Recent landslides in Niigata Region, Japan, In: *Proceedings of the 4th Asian Symposium on Engineering Geology and the Enviroment, Hong Kong*, Free, M. and Ayding, A. eds. Geological Society of Hong Kong, Hong Kong, p. 7.

Yamagishi, H., Watanabe, N., & Ayalew, L., (2005). Heavy-rainfall induced landslides on july 13, 2004, in Niigata Region, Japan, In: *Monitoring, Prediction and Mitigation of Water Related Disasters*, Takara, K., Tachikawa, Y. and Bandara N.M.N.S eds. Disaster Prevention Research Institute (DPRI), Kyoto University, Kyoto, p. 6.

Yang, H., Rahardjo, H., Wibawa, B., & Leong, E.-C., (2004). A soil column apparatus for laboratory infiltration study, *Geotechnical Testing Journal*, **27**(4), 347–355.

Yang, H., Rahardjo, H., & Leong, E.-C., (2006). Behavior of unsaturated layered soil columns during infiltration, *Journal of Hydrologic Engineering, ASCE*, **11**(4), 329–337.

Ye, G., Zhang, F., Yashima, A., Sumi, T., & Ikemura, T., (2005). Numerical analyses on progressive failure of slope due to heavy rain with 2D and 3D FEM, *Soils and Foundations*, **45**(2), 1–15.

Yoshida, Y., Kuwano, J., & Kuwano, R., (1991). Rain-induced slope failures caused by reduction in soil strenth, *Soils and Foundations*, **31**(4), 187–193.

Zhan, L.T. & Ng, C.W.W., (2004). Analytical analysis of rainfall infiltration mechanism in unsaturated soils, *International Journal of Geomechanics*, **4**, 273–284.